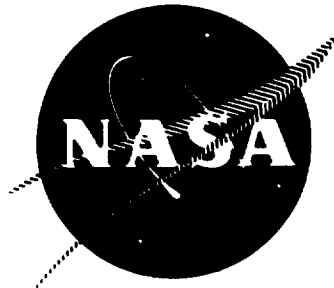


**CASE FILE
COPY**

NASA CR-72705
R-8266

N71-25801



**SPACE STORABLE
REGENERATIVE COOLING INVESTIGATION**

by
R. P. Pauckert



prepared for
NATIONAL AERONAUTICS AND SPACE ADMINISTRATION

NASA Lewis Research Center
Contract NAS 3-11191
John W. Gregory, Project Manager

NOTICE

This report was prepared as an account of Government-sponsored work. Neither the United States, nor the National Aeronautics and Space Administration (NASA), nor any person acting on behalf of NASA:

- A.) Makes any warranty or representation, expressed or implied, with respect to the accuracy, completeness, or usefulness of the information contained in this report, or that the use of any information, apparatus, method, or process disclosed in this report may not infringe privately-owned rights; or
- B.) Assumes any liabilities with respect to the use of, or for damages resulting from the use of, any information, apparatus, method or process disclosed in this report.

As used above, "person acting on behalf of NASA" includes any employee or contractor of NASA, or employee of such contractor, to the extent that such employee or contractor of NASA or employee of such contractor prepares, disseminates, or provides access to any information pursuant to his employment or contract with NASA, or his employment with such contractor.

NASA CR-72705
R-8266

FINAL REPORT
SPACE STORABLE REGENERATIVE COOLING INVESTIGATION

by
R. P. Pauckert

ROCKETDYNE
A Division of North American Rockwell Corporation
6633 Canoga Avenue
Canoga Park, California 91304

prepared for

NATIONAL AERONAUTICS AND SPACE ADMINISTRATION

June 1970

CONTRACT NAS3-11191

Technical Management
John W. Gregory
NASA Lewis Research Center
Cleveland, Ohio
Liquid Rocket Technology Branch

ACKNOWLEDGMENTS

The contributions of the following personnel are gratefully acknowledged:
R. Tobin and J. Shoji, heat transfer analysis, L. Russell, R. Rowland,
and R. Wilkinson - design and fabrication; F. Hoehn, M. Cole, and
L. Allison - injector design, testing and performance data analysis;
H. Griggs, E. Monteath, and W. Anderson - program management advice
and direction.

FOREWORD

The results of the analytical and experimental studies conducted by Rocketdyne, a division of North American Rockwell Corporation, under Contract NAS3-11191 are presented in this report. Technical direction of the program was supplied by John W. Gregory of the NASA Lewis Research Center.

The analyses and experiments were conducted from July 1967 through May 1970.

ABSTRACT

Analyses were conducted to determine the regenerative cooling limits of the light hydrocarbons with FLOX and OF_2 over a wide range of operating conditions. Methane was shown to be the most attractive fuel. Performance and heat transfer characteristics were experimentally determined for triplet and concentric element injectors at chamber pressures of 500 to 900 psia (345 to 620 N/cm^2) and propellant mixture ratios of 3.5 to 7.6 using water-cooled hardware. Both injectors performed well with the concentric injector producing lower heat fluxes in the combustion zone. A regeneratively cooled thrust chamber with a 60:1 expansion area ratio nozzle was fabricated using an electroforming fabrication technique. The chamber was operated from 500 to 640 psia (345 to 440 N/cm^2) and mixture ratios of 2.8 to 5.7. Other concentric element injectors were tested in water-cooled and regeneratively cooled thrust chambers at pressures as low as 46 psia (32 N/cm^2) to demonstrate throttling capability.

CONTENTS

Acknowledgments	iii
Foreword	v
Abstract	vii
Introduction	1
Summary	3
Task I Heat Transfer Analysis	3
Task II Hardware Design	5
Task III & IV Injector Characterization and Altitude Test	6
Task V Regeneratively Cooled Tests	7
Task VI Throttling Injector Design	7
Task VII Throttling Tests	8
Conclusions and Recommendations	11
Section I Regenerative Cooling Analysis	13
Parametric Analysis	13
Detailed Analysis	25
Section II Hardware Design and Fabrication	29
Injectors	29
Performance Analyses	30
Injector Face Heat Transfer Analyses	32
Full Scale Injectors	36
Thrust Chambers	56
Solid and Water-Cooled Chambers	58
Regeneratively Cooled Thrust Chamber	77
Section III Injector Characterization and Altitude Tests	95
Cold Flow Tests	95
Impinging Element Tests	95
Concentric Element Tests	105
Injector Cold Flow Tests	117
Hot Firing Tests	124
Experimental Equipment	124
Test Facility	125
Instrumentation	132

Data Recording	136
Test Summary	138
Test Results	147
Conclusions	177
Section IV Regenerative Cooling Tests	179
Test Facility and Equipment	179
Propellant Storage and Feed Systems	179
Test Procedures	181
Instrumentation and Data Recording	183
Test Summary	183
Test Results	190
Performance	190
Heat Transfer	192
Conclusions	201
Section V Throttling Tests	203
Test Facility and Equipment	203
Propellant Storage and Feed Systems	203
Test Procedures	205
Instrumentation	206
Test Summary	207
Test Results	216
Performance	216
Heat Transfer	228
Pressure Drops and Stability	248
Conclusions	257
References	261
<u>Appendix A</u>	
Injector Performance Design Analysis	A-1
<u>Appendix B</u>	
Injector Face Heat Transfer Analysis	B-1
<u>Appendix C</u>	
Correlation of Recessed Post Injector Data	C-1

<u>Appendix D</u>	
Nozzle Contour Analysis and Design	D-1
<u>Appendix E</u>	
Water-Cooled Thrust Chamber Design Analysis	E-1
<u>Appendix F</u>	
Solution for the Penetration of a Liquid Stream into a Gas Stream	F-1
<u>Appendix G</u>	
Data Reduction and Performance Calculations	G-1
<u>Appendix H</u>	
Regenerative Coolant Flowrate Characteristics	H-1
<u>Appendix I</u>	
Distribution	I-1

ILLUSTRATIONS

1. Thrust Influence Coefficient.	15
2. Chamber Pressure Influence Coefficient.	16
3. Area Ratio Influence Coefficients	17
4. Gas-Side Wall Temperature Influence Coefficient . .	18
5. Heat Transfer Rate Reduction for Various Hydrocarbons	20
6. Injector Element Types	31
7. Combustion Efficiency as a Function of Combustion Length for Various Mean Dropsizes . . .	33
8. Combustion Efficiency as a Function of Mean FLOX Drop Size	34
9. Combustion Efficiency As a Function of Mixing Parameter	35
10. Pentad Injector Face Pattern and Element Detail . .	38
11. Pentad Injector	39
12. Triplet Injector Drawing	40
13. Triplet Injector	41
14. Concentric Element Injector.	43
15. Components of Concentric Element Injector.	44
16. Concentric Element Injector, Rear View	45
17. Concentric Injector with Solid Copper Face	46
18. Heat Exchanger Element	47
19. Heat Exchanger Injector Components	49
20. Recessed Post Injector Element	50
21. Recessed Post Injector Components.	51
22. Recessed Post Injector - Front of FLOX Body.	53
23. Recessed Post Injector; Back of FLOX Body.	54
24. Recessed Post Injector Assembly.	55
25. Recessed Post Injector Face.	57
26. Water-Cooled Thrust Chamber.	59
27. Copper Liner for Electroformed Thrust Chamber. . . .	60
28. Electron Beam Weld Sample and Actual Joint	63

ILLUSTRATIONS (continued)

29.	Components of Water Cooled Thrust Chamber	65
30.	Pre-Weld Assembly of Water Cooled Thrust Chamber. .	66
31.	Final Assembly of Water Cooled Thrust Chamber . . .	67
32.	Electroformed Thrust Chamber Extension Before Assembly	68
33.	Water Cooled Nozzle Extension	69
34.	Uncooled Nozzle Wall Temperature as a Function of Time, $P_C = 500$ psia (345 N/cm ²)	71
35.	Uncooled Nozzle Wall Temperature as a Function of Time, $P_C = 1000$ psia (690 N/cm ²).. . . .	72
36.	Water-Cooled Nozzle	73
37.	Thrust Chamber and Nozzle Fabrication Flow Chart. .	75
38.	Solid Electroformed Nozzle.	76
39.	Temperature Distribution in Nickel Thrust Chamber Wall	78
40.	Electroformed Thrust Chamber.	79
41.	Effect of Heat Flux Level on the Regeneratively- Cooled Nozzle, Hot-Gas Wall Temperature Profile . .	82
42.	Hot Wall Temperature Profiles; Combustion and Coolant Sides	84
43.	Coolant Temperature Profile	85
44.	Coolant Pressure Profiles	86
45.	Heat Flux Profile	87
46.	Regeneratively Cooled Combustion Chamber.	89
47.	Regeneratively Cooled Thrust Chamber After Electroforming and Machining.	90
48.	Assembled Regeneratively Cooled Combustion Chamber ;	91
49.	Cutting Channels on the Regeneratively Cooled Nozzle	93
50.	Regeneratively Cooled Thrust Chamber	94

ILLUSTRATIONS (continued)

51.	Liquid Mass Distribution for the Triplet Element.	100
52.	Liquid Mass Distribution for the Fan Injector Element.	101
53.	Liquid Mass Distribution for the Pentad Injector Element	102
54.	Mass Distribution as a Function of Jet Penetration.	104
55.	Combustion Efficiency as a Function of Jet Penetration	106
56.	Concentric Injector FLOX ΔP vs Swirler Area Ratio	107
57.	FLOX Tube Simulation Corresponding to 500 psia Chamber Pressure	108
58.	FLOX Tube Simulation Corresponding to 1000 psia Chamber Pressure.	109
59.	Heat Exchanger Element Cold Flow, Recess = 0, $\dot{w}_f = 0$	112
60.	Heat Exchanger Element Cold Flow, Recess = 0.107 in., $w_f = 0$	113
61.	Heat Exchanger Element Cold Flow Recess = 0, $\dot{w}_f = 0.022$ lb/sec	114
62.	Heat Exchanger Element Cold Flow, Recess = 0.107 inches $\dot{w}_f = 0.022$ lb/sec.	115
63.	Heat Exchanger Element Cold Flow Recess = 0.500 inches, $\dot{w}_f = 0.022$ lb/sec	116
64.	Injector Water Calibration Data	118
65.	Water Flow of Triplet Injector	119
66.	Water Flow of Pentad Injector	120
67.	Concentric Element Injector Cold Flow Test	121
68.	Mixture Ratio Distribution in Recessed Post Injector	122
69.	Mixture Ratio Distribution in Modified Heat Exchanger Injector	123

ILLUSTRATIONS (continued)

70.	Propulsion Research Area	126
71.	Facility Schematic	127
72.	Diffuser Schematic	130
73.	Self-Pumping Diffuser With High Area Ratio Thrust Chamber	131
74.	Instrumentation Location	133
75.	C* Efficiency of Triplet Injector at 500 psia (345 N/cm ²) Chamber Pressure.	149
76.	Comparison of Triplet and Concentric Injector Performance	150
77.	Propellant Injection Momentum Ratio.	152
78.	Concentric Element Injector Performance vs Injection Velocity Difference	153
79.	Experimental Heat Flux Profiles with Triplet Injector	155
80.	Comparison of Experimental and Theoretical Heat Transfer Coefficient Profiles	156
81.	Heat Flux Profiles for Various Mixture Ratios with Triplet Injector	158
82.	Experimental Heat Flux Profiles.	159
83.	Experimental Peak Heat Fluxes.	160
84.	Concentric Injector Axial Heat Flux Profiles	162
85.	Experimental Heat Inputs	163
86.	Combustion Chamber Heat Inputs	164
87.	Nozzle Heat Transfer Coefficient Distribution at P _c = 500 psia (345 N/cm ²).	165
88.	Nozzle Heat Transfer Coefficient Distribution at P _c = 700 psia (485 N/cm ²)	167
89.	Nozzle Heat Transfer Coefficient Distribution at P _c = 900 psia (620 N/cm ²)	168
90.	Circumferential Temperature Profile Near Concentric Injector	169

ILLUSTRATIONS (continued)

91. Wall Temperature Profile	174
92. Coolant Bulk Temperature Profiles	175
93. Coolant Pressure Profiles	176
94. Facility Schematic	180
95. Comparison of Start Model and Actual Start	184
96. Combustion Chamber Heat Inputs	194
97. Combustion Chamber Pressure Drop Relations	196
98. Concentric Element Injector Pressure Drops	200
99. Facility Schematic	204
100. Pressure Drops for FLOX Side of Recessed Post Injector	220
101. Effects of Recess and Mixture Ratio on Recessed Post Injector Performance	221
102. Effects of Injection Velocities and Mixture Ratio on Recessed Post Injector Performance	223
103a. Performance of Recessed Post Injector Based on Test Data and Correlations	225
103b. Performance Correlation for the Heat Exchanger Injector	225
104. Circumferential Variation of Outer Wall Temperature	230
105. Water Temperature Rise Transient	233
106. Heat Flux Distribution - Carbon Layer Influence	235
107. Comparison of Heat Flux Profiles for Coaxial Injectors	236
108. Peak Heat Flux Variation with Chamber Pressure	237
109. Total Heat Input to Combustion Chamber	239
110. Recessed Post Injector Face Temperatures	241
111. Combustion Chamber Contours	242
112. Combustion-Side Heat Transfer Coefficient Distribution	244
113. Design Channel Geometric Dimensions vs Axial Length	245
114. Combustion-Side Wall Temperature Variation with Chamber Pressure	247
115. Influence of Reduced Injector Region Heat Transfer Coefficient	249
116. Fuel Side Pressure Drops for Throttling Injectors	252

ILLUSTRATIONS (continued)

117.	Oxidizer-Side Pressure Drop for Heat Exchanger Injector	254
118.	Fuel Jacket and Crossover Duct Pressure Drop Correlations	255
119.	Correlation of Chugging Amplitude with FLOX Subcooling, Recessed Post Injector	258

TABLES

1.	Ranges of Operating Parameters	14
2.	Operating Conditions for Q_{ref}	19
3.	Heat Absorption Capabilities	22
4.	Coolant Jacket Discharge Temperatures	23
5.	Design Conditions and Constraints.	29
6.	Injector Element Configurations and Temperatures	36
7.	Weld-Sample Test Results	64
8.	Summary of Results of Channel Geometry Variation Study.	81
9.	Regeneratively Cooled Combustion Chamber Operating Characteristics.	88
10.	Cold Flow Impinging Element Configurations	98
11.	Heat Exchanger Element Flow Tests.	111
12.	Instrumentation List for Tasks III-IV Tests.	134, 135
13.	Sea Level Tests In Solid Wall Chamber.	139
14.	Sea Level Tests In Water Cooled Chamber With Injector T24.	140
15.	Altitude Tests - Water-Cooled Chamber and Solid Nozzle - Concentric Injector.	141
16.	Water-Cooled Test Performance Summary	148
17.	Maximum Wall Temperatures, Tapered Chamber.	172
18.	Instrumentation for Task V Tests	185, 186
19.	Altitude Tests in Regeneratively Cooled Chamber, Concentric Element Injector	187
20.	Regeneratively Cooled Test Performance Summary	191
21.	Heat Transfer Results for Regeneratively Cooled Thrust Chamber	193
22.	Regeneratively Cooled Chamber Wall Temperatures.	195

TABLES (continued)

23.	Concentric Injector Oxidizer Delta P	198
24.	Concentric Element Injector Fuel Delta P	199
25.	Throttling Test Summary.	208, 209
26.	Throttling Test Performance Summary.	217
27.	Thrust-Based Performance: Throttling Tests	226
28.	Throttling Regenerative Cooling Data	229
29.	Throttling Injector Pressure Drop Summary	250
30.	Regenerative Coolant Pressure Drops	256

INTRODUCTION

Previous investigations have established the performance and regenerative cooling capabilities of the light hydrocarbon fuels with FLOX mixtures for space propulsion applications involving low chamber pressures and relatively low thrust levels. The present effort was undertaken because of the expanded interest in application of these propellants to larger space propulsion systems and to pump-fed engines. The overall goal of the investigation was to provide analytical data, with experimental verification, to define the regenerative cooling capabilities of the light hydrocarbons, when used with FLOX mixtures or OF_2 , at higher thrust levels and chamber pressures.

The program, conducted at Rocketdyne, was directed to provide this data for the expanded range of variables. In order to obtain valid experimental heat transfer data in the combustion chamber and throat regions, it was necessary to conduct the tests with a high performance injector. Accordingly, the second goal of this program was to provide an injector capable of delivering a characteristic exhaust velocity (C^*) of 96 percent of the theoretical value for the conditions tested. A final goal was to provide an injector capable of high performance and stable operation over a 10:1 throttling range.

The specific objectives of the program were as follows:

1. To specify the regenerative cooling limits for a wide variety of operating conditions (propellants, chamber pressure, thrust chamber geometric parameters) based on a comparison of the total heat transferred to the thrust chamber with the thermal capacity of the light hydrocarbon coolants.
2. To conduct detailed design analysis in order to specify the regenerative cooling limits on the basis of such additional factors as: minimum coolant passage dimensions, coolant pressure drop, coking of the coolant, and maximum heat flux allowable for transition from nucleate to film boiling for subcritical cooling of the chamber.

3. a. To design, fabricate, and test an injector capable of delivering a C* efficiency of at least 96 percent.
- b. To design, fabricate, and test an injector capable of stable operation over a 10:1 throttling ratio with 98 percent efficiency at full thrust and 96 percent at minimum thrust.
4. To design and fabricate a water-cooled thrust chamber with truncated nozzle to test the injector at sea level conditions to obtain heat transfer and injector performance data.
5. To design and fabricate a high area ratio nozzle, and to test the nozzle in conjunction with the water-cooled thrust chamber at simulated altitude conditions to obtain nozzle heat transfer and performance data.
6. To design and fabricate a regeneratively cooled thrust chamber using advanced fabrication techniques, and to demonstrate regenerative cooling under hot firing conditions with the chamber.

SUMMARY

The present study was undertaken to analytically define the limits of regenerative cooling with light hydrocarbon fuels and to experimentally verify the analytical results. The effort was divided into seven tasks as outlined below to include analytical, design, fabrication, and test efforts.

TASK I - REGENERATIVE COOLING ANALYSIS

This task was divided into two subtasks. First, regenerative cooling limits were determined on the basis of coolant decomposition temperature and bulk boiling limits. These analyses were conducted for a wide range of variables: methane, methane-ethane blend, ethane, propane, and 1-butene as fuels; OF_2 and FLOX as oxidizers; thrust levels of 1000 to 20,000 pounds (4500 to 89,000 N) chamber pressures of 100 to 2000 psia (35 to 690 N/cm^2); chamber contraction area ratios of 2 to 4; expansion area ratios of 40 to 100; combustion-side wall temperatures of 1700 to 3200 F (1200 to 1900 K); and propellant mixture ratios of 70 to 100 percent of the optimum values. Additionally, the effects of a potential combustion-side carbon layer were evaluated.

All of the fuels were found to be suitable coolants based on thermal decomposition limits under practically all conditions investigated if the assumed carbon layer exists. Without this carbon layer only methane did not decompose under all conditions. The other fuels required some compromise in operating conditions to prevent decomposition at high chamber pressures and low thrust levels. Regenerative cooling at low chamber pressures is limited by bulk boiling constraints but is possible for most of the coolants by proper selection of operating conditions. Methane could be used at low pressures under all conditions investigated.

Based on the results of the above analyses the following propellants and thrust levels were selected for more detailed heat transfer analyses: FLOX/methane at 1000, 5000, and 20,000 pounds (4500, 22000, and 89,000 N); OF_2 /propane at 5000 and 20,000 pounds (22,000 and 89,000 N); and OF_2 /1-butene at 1000 (4500 N) pounds. These detailed analyses were used to determine additional regenerative cooling limits based on coolant jacket pressure drop, coolant decomposition on the wall of the passages, and minimum passage dimensions to facilitate fabrication. The same range of chamber pressures and wall temperatures were investigated. The contraction and expansion area ratios were fixed at 4 and 100 respectively and the optimum propellant mixture ratio was assumed initially. The effects of compromising the latter two parameters on the range of regenerative cooling capability were studied.

Regenerative cooling with methane was found to be applicable over practically the entire range of thrust levels and chamber pressures at nominal mixture ratio and an area ratio of 100. Propane could be used as a regenerative coolant at all pressures at 20,000 pounds (89,000 N) thrust or for chamber pressures below 750 psia (520 N/cm^2) at 5000 pounds (22,000 N). At higher pressures, with no combustion-side carbon layer, a reduction in mixture ratio is required to prevent the channels from becoming too small. A similar condition was encountered with 1-butene at chamber pressures of 500 psia (345 N/cm^2) or greater. In the case of 1-butene, propellant decomposition also occurred at high pressures without the presence of a carbon layer. Reduction of propellant mixture ratio again resulted in acceptable channel dimensions and coolant temperatures.

The results of the Task I analyses indicated that, in general, the light hydrocarbons, particularly methane, are suitable for regenerative cooling applications. The results of this task were published as Reference 1.

TASK II - DESIGN AND ANALYSIS OF HARDWARE FOR HIGH PRESSURE TESTS

The results of the analytical studies indicated that the FLOX/methane propellant combination was the most attractive candidate for experimental verification. The hardware for these experiments was designed in Task II for operation at 500 to 1000 psia (345 to 690 N/cm²) chamber pressure with corresponding altitude thrust levels of 5,000 to 10,000 pounds (22,000 to 89,000 N). This hardware included injector elements; injectors; and solid, water-cooled, and regeneratively cooled thrust chambers and nozzles.

Single injector elements were designed for the cold flow test program. Various configurations of triplet, impinging fan, pentad, and concentric elements were designed. Three basic complete injectors were designed: a 72 element triplet; a 91 element pentad; and a 61 element concentric injector. These injectors had solid copper faces. A version of the concentric element injector with a Rigimesh face was also designed.

A water cooled thrust chamber was designed with a machined copper liner and an electroformed nickel outer shell. The circumferential cooling passages were designed to provide good axial heat flux profile data. Circumferential heat flux profile data was obtained by thermocouples in the wall between coolant passages. The contraction and expansion area ratios of the chamber were both 4.0. A water cooled cylindrical thrust chamber extension was also designed using the same concept to increase the L* from approximately 30 to 50 inches (76 to 127 cm).

Three nozzles were designed. A short ($\epsilon = 4-6$) water-cooled extension was designed to provide a relatively sharp edged nozzle exit to minimize base pressure effects on thrust measurements. A solid electroformed nickel nozzle was designed to extend the area ratio from 4 to 60. A completely electroformed water-cooled nozzle of the same contour ($\epsilon = 4-60$) was also designed.

A regeneratively cooled thrust chamber was designed in two sections with the same contours as the water-cooled and solid hardware. Both the chamber and nozzle sections were completely electroformed with the exception of the flanges which also served as inlet and outlet manifolds. Coolant channels were milled into the electroformed nickel.

TASKS III and IV - INJECTOR CHARACTERIZATION AND ALTITUDE TESTS

These tasks included cold flow tests, hardware fabrication, and sea level and altitude tests at chamber pressures of 500 psia (345 N/cm^2) and greater. The cold flow tests were conducted using various configurations of triplet, impinging fan, and pentad elements. Comparison of spray distribution results indicated that all three elements should yield acceptable (≥ 96 percent) C^* efficiencies with the pentad giving the highest performance. Cold flow testing of a FLOX element of the concentric element injector was conducted to determine the FLOX pressure drop, cone angle, and stability with various hydraulic swirler configurations.

Nineteen hot firing tests were conducted with the triplet injector with low area ratio ($\epsilon = 4$) thrust chambers at chamber pressures of 480 to 500 psia (330 to 345 N/cm^2) and propellant mixture ratios of 3.6 to 7.6. C^* efficiencies of 94 to 100 percent were measured (98.5 percent at $O/F = 5.25$). Heat fluxes in the combustion zone were considerably higher than predicted. The heat fluxes in the converging and diverging regions agreed with analytical boundary layer predictions. The pentad injector was damaged on its first test.

Ten tests were conducted with the concentric element injector in the water cooled thrust chamber and solid-wall high area ratio nozzle. These tests were conducted at chamber pressures ranging from 500 to 890 psia (345 to 620 N/cm^2) and propellant mixture ratios of 3.5 to 5.7. Measured C^* efficiencies ranged from 95 to 101 percent (98 percent at 500 psia (345 N/cm^2) and 5.25 O/F). Heat fluxes in the combustion zone were much lower than those measured with the triplet injector. Heat fluxes in the throat region were similar to those measured with the triplet injector. The peak heat flux at 500 psia (345 N/cm^2) chamber pressure and 5.25 mixture ratio was $17 \text{ Btu/in}^2\text{-sec}$. The heat flux profile in the nozzle agreed fairly well with theoretical predictions.

TASK V - REGENERATIVELY COOLED TESTS

Water flow and methane blowdowns were conducted on the regeneratively cooled thrust chamber and nozzle to verify the predicted pressure drops and establish chilldown characteristics. Two dump cooled tests were conducted to demonstrate the thrust chamber steady state regenerative cooling capability under less severe start transient conditions. The thrust chamber was operated during the second test for 5.5 seconds at 525 psia (360 N/cm^2) chamber pressure and 5.0 propellant mixture ratio while the coolant flowrate corresponded to a mixture ratio of 4.5 at that pressure.

A series of 5 tests was then conducted in the regeneratively cooled mode. Chamber pressure and mixture ratio ranges were 510 to 640 psia (350 to 440 N/cm^2) and 2.8 to 5.6 respectively for the regeneratively cooled test series.

TASK VI - THROTTLING INJECTOR DESIGN AND FABRICATION

An injector was designed with 61 concentric elements to provide 10:1 throttling capability by reducing the FLOX injection pressure drop variation. This was done by recessing the FLOX posts to provide part of the pressure drop in the "cup" region where the pressure drop has been found, on previous programs, to be significantly less sensitive to flowrate than the normal hydraulic pressure drop. A copper face was bonded to an Inconel structural body in this design. The injector had provisions for varying the FLOX post recess and for changing the restriction at the inlet of each FLOX element.

An injector using a heat exchanger principle to vaporize the FLOX in the elements was available from another program. This injector was modified to reduce the heat flux to the chamber near the injector. The modifications consisted of increasing the FLOX post recess and adding small fuel showerhead orifices near the chamber wall.

TASK VII - THROTTLING INJECTOR TESTS

Nine sea level tests were conducted with both injectors in the regeneratively cooled chamber at chamber pressures ranging from 76 to 330 psia (52 to 228 N/cm²). Propellant mixture ratios ranged from 3.7 to 15.2. Three of the tests demonstrated 2:1 dynamic throttling and provided two data points per test. The chamber was damaged during a test at high mixture ratio. Twenty-three tests were then conducted in the water-cooled thrust chamber No. 2 (identical to chamber No. 1) using both injectors. Six of the tests were dynamic throttling tests. Chamber pressures of 46 to 522 psia (32 to 360 N/cm²) and propellant mixture ratios of 2.8 to 10.8 were tested.

Performance correlations were obtained for both injectors indicating that high performance could be obtained over all or most of the throttling range. Approximately 100 percent injector efficiency was obtained on several of the tests. The heat exchanger injector was stable over the full throttling range. The recessed post injector chugged at throttling ratios of greater than 6:1.

Axial heat flux profiles were obtained for both injectors with the water-cooled chamber over the ranges of chamber pressures and mixture ratios tested. Circumferential wall temperature distributions were obtained on the regeneratively cooled chamber. The heat flux profile with the heat exchanger injector was significantly lower than that with the recessed post injector at all locations except near the injector face. Both injectors exhibited satisfactory heat flux profiles for regenerative cooling (with a long chamber life) at nominal mixture ratio from nominal chamber pressure to approximately the 5:1 throttle point. At lower pressures the bulk temperature rise of the methane coolant would be excessive with the recessed post injector, and the heat flux near the heat exchanger injector would result in unacceptable wall temperatures. Regenerative cooling

over the 10:1 throttling range would be possible with either injector if the mixture ratio were reduced from 5.25 at approximately 100 psia (69 N/cm^2) to 4.5 at a chamber pressure of 50 psia (35 N/cm^2). Regenerative cooling at nominal mixture ratio could be accomplished with the heat exchanger injector with local heat flux reduction and with general heat flux reduction for the recessed post injector.

CONCLUSIONS AND RECOMMENDATIONS

The following conclusions and recommendations are based upon the results of the analytical and experimental investigations conducted during the present study.

1. Regenerative cooling with the light hydrocarbons, with FLOX or OF_2 as the oxidizer, is feasible over a wide range of operating conditions.
2. Methane is the most attractive coolant of the hydrocarbons considered.
3. Regenerative cooling with methane has been demonstrated at chamber pressures of 46 to 640 psia.
4. The concentric element injector results in lower heat fluxes in the combustion zone than the triplet although heat fluxes in the throat region are similar.
5. High injector performance ($\eta_{c*} \geq 98$ percent) is obtainable using triplet or coaxial element injectors with the FLOX/methane propellant combination.
6. Specific impulse values of 400 seconds can be achieved at a chamber pressure of 500 psia, mixture ratio of 5.25, and nozzle area ratio of 60.
7. Fabrication of a thrust chamber without using tubes is feasible using an electroforming technique.
8. Further component and integration studies leading to development of a FLOX/methane engine should be undertaken.

9. Additional thrust chamber and injector tests should be conducted to demonstrate
 - a) dynamic stability
 - b) heat flux reduction techniques
 - c) recessed post injector modifications to suppress chugging
 - d) flightweight hardware fabrication and operating characteristics

SECTION I

REGENERATIVE COOLING ANALYSIS

A detailed report on this Task was presented in Ref. (1), the Interim Report. The results are summarized in this section. Task I was divided into two subtasks. A broad parametric analysis was first conducted to establish regenerative cooling limits based only on coolant temperature restrictions. This was followed by analyses which were narrower in scope but were more detailed and involved actual thrust chamber coolant circuit designs.

PARAMETRIC ANALYSIS

The purpose of the Parametric Analysis was to determine regenerative cooling limits, based upon coolant temperature restrictions, for a wide variety of operating parameters. These parameters and the ranges investigated are shown in Table 1.

The total heat input to the chamber was first calculated without considering a combustion-side carbon layer. Little variation in heat input with propellant combination or propellant mixture ratio was found. The total heat inputs calculated for the various combinations of thrust, chamber pressure, expansion and contraction area ratios, and gas-side wall temperature are presented in Fig. 1 through 4 in the form of influence coefficients. These coefficients illustrate the effect of a single variable on the heat input and, as such, they are useful in showing the significance of variations of a particular parameter with respect to the heat input. Furthermore, they provide a convenient means of approximating the total heat input for any given set of conditions. The total heat input, Q , in terms of the reference value, Q_{ref} , and influence coefficient, η , is:

$$Q = Q_{refN} \times \eta_{FN} \times \eta_{PCN} \times \eta_{TWG} \times \eta_{\epsilon} + Q_{refCZ} \times \eta_{FCZ} \times \eta_{PC CZ} \times \eta_{TWG} \times \eta_{\epsilon}$$

TABLE 1
RANGES OF OPERATING PARAMETERS

Fuels: Methane (CH₄)
 Ethane (C₂H₆)
 Blend of 45 percent Ethane and 55 percent Methane
 Propane (C₃H₈)
 Butene (C₄H₈)

Oxidizers: FLOX (optimum mixture)
 OF₂

Chamber Pressure, psia: 100, 250, 500, 750, 1000
 N/cm²: 69, 172, 345, 417, 690

Vacuum Thrust, pounds: 1000, 2500, 5000, 10,000, 20,000
 Newtons: 4,500, 11,000, 22,000, 44,500, 89,000

C* Efficiency: 96 percent of theoretical shifting equilibrium

Mixture Ratio, O/F: 70, 80, 90 and 100 percent of optimum

Contraction Ratio: 2:1, 3:1, 4:1

Chamber Characteristic Length (L*), inches (cm): 30 (76.2)

Nozzle Area Ratio (Regeneratively Cooled Portion): 40:1, 60:1, 100:1

Combustion-Side Wall Temperature, F: 1700, 2100, 3200
 K: 1200, 1400, 1900

Combustion-Side Carbon Resistance: none, (Ref. 2)

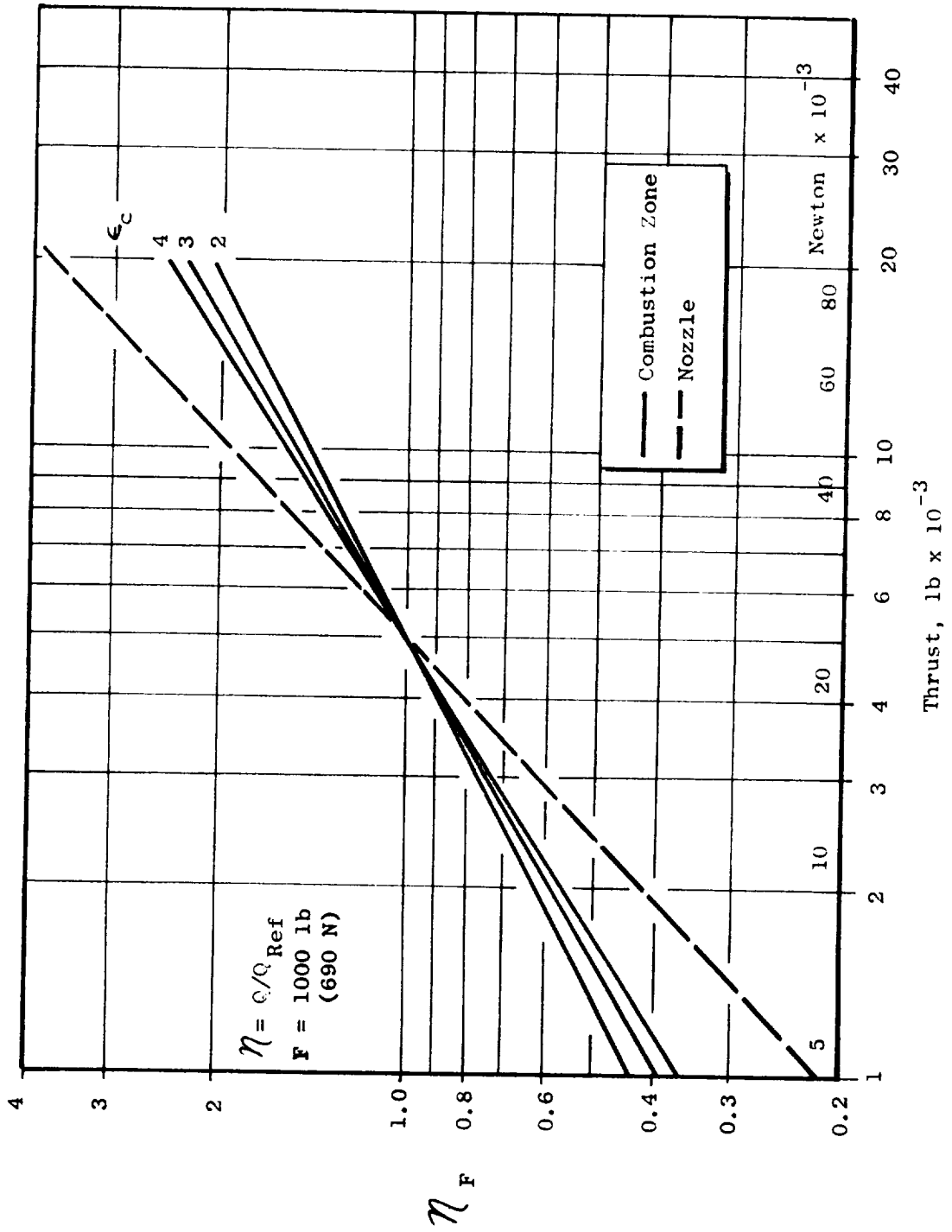


Figure 1 Thrust Influence Coefficient

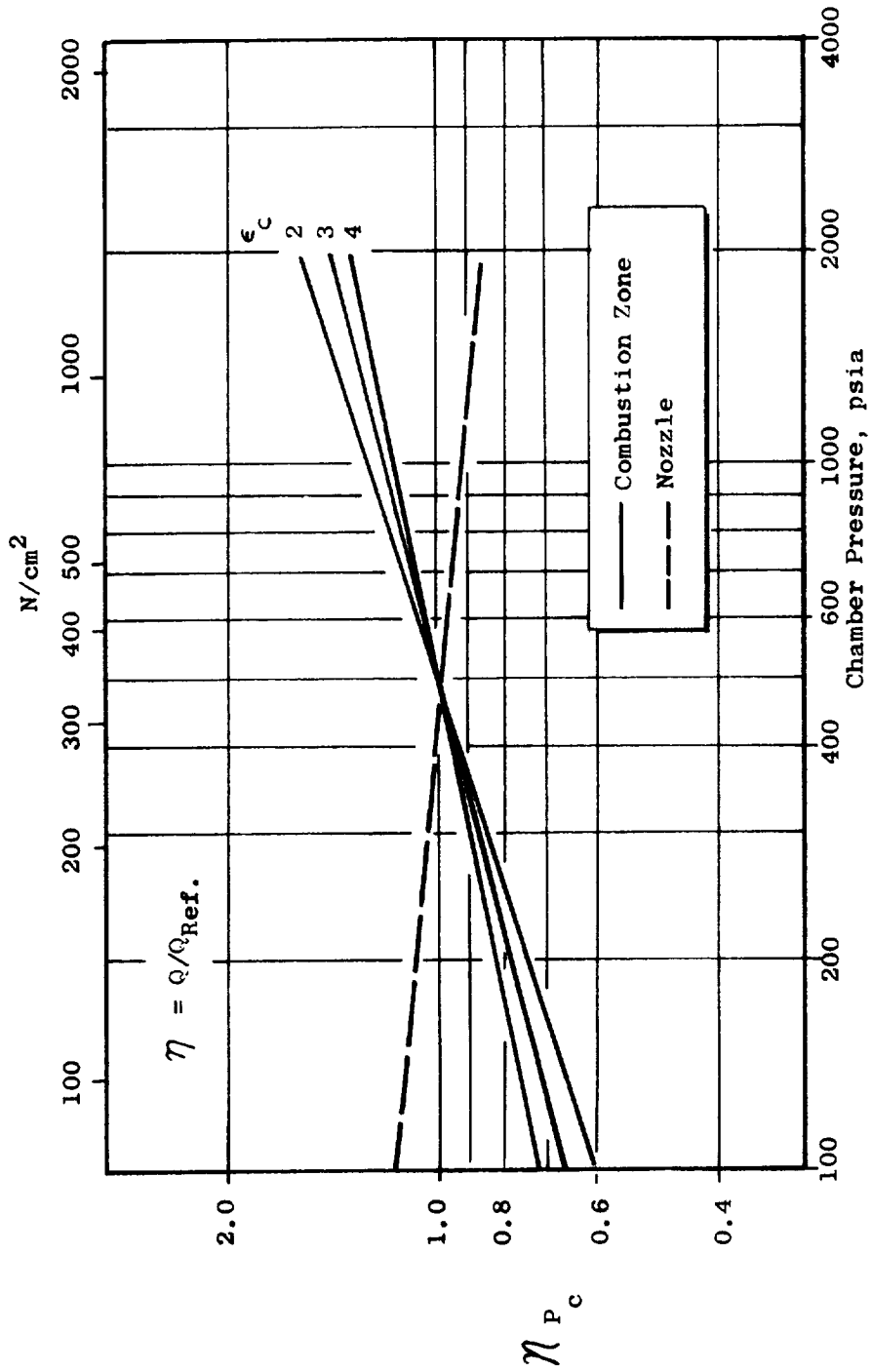


Figure 2 Chamber Pressure Influence Coefficient

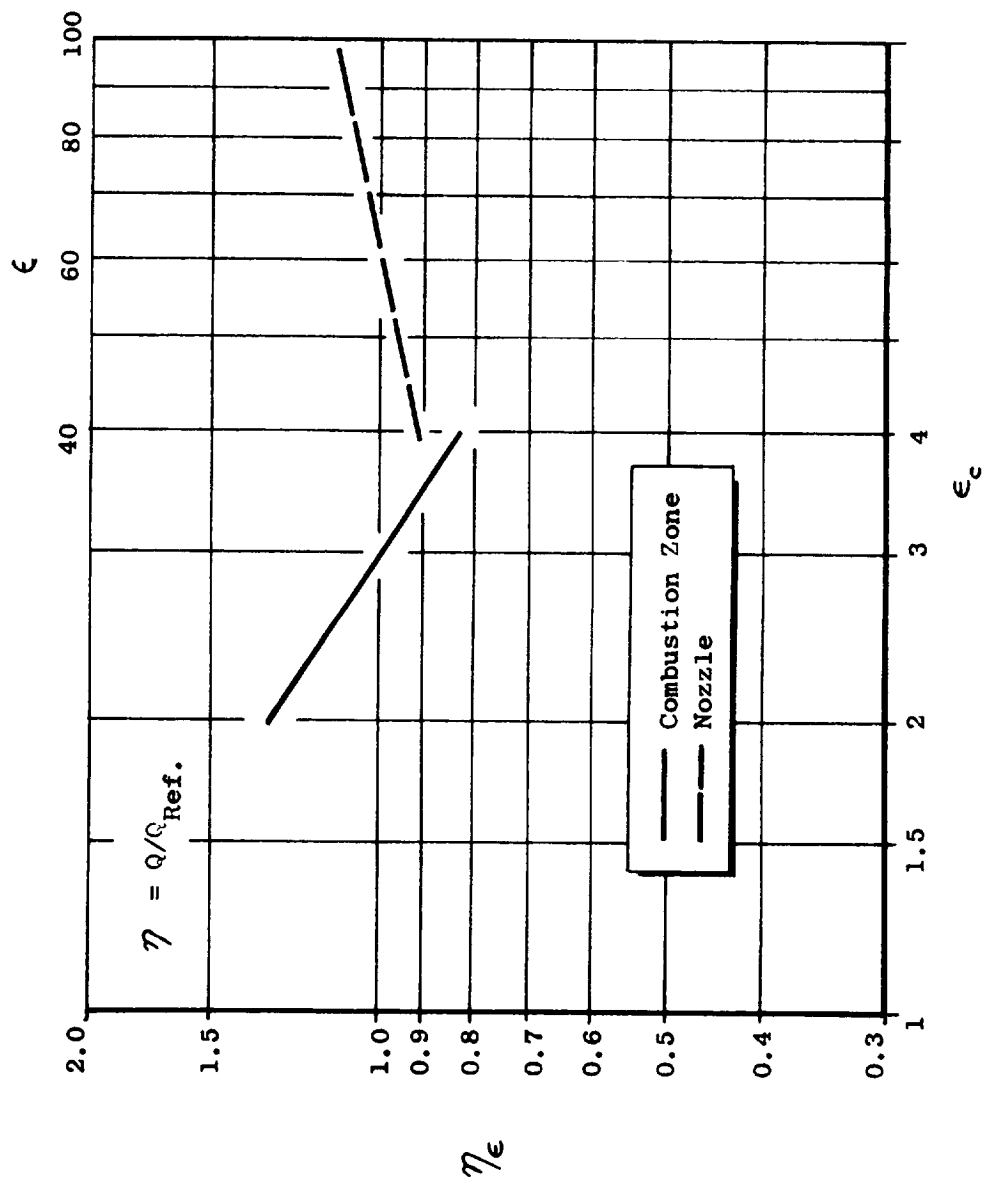


Figure 3 Area Ratio Influence Coefficients

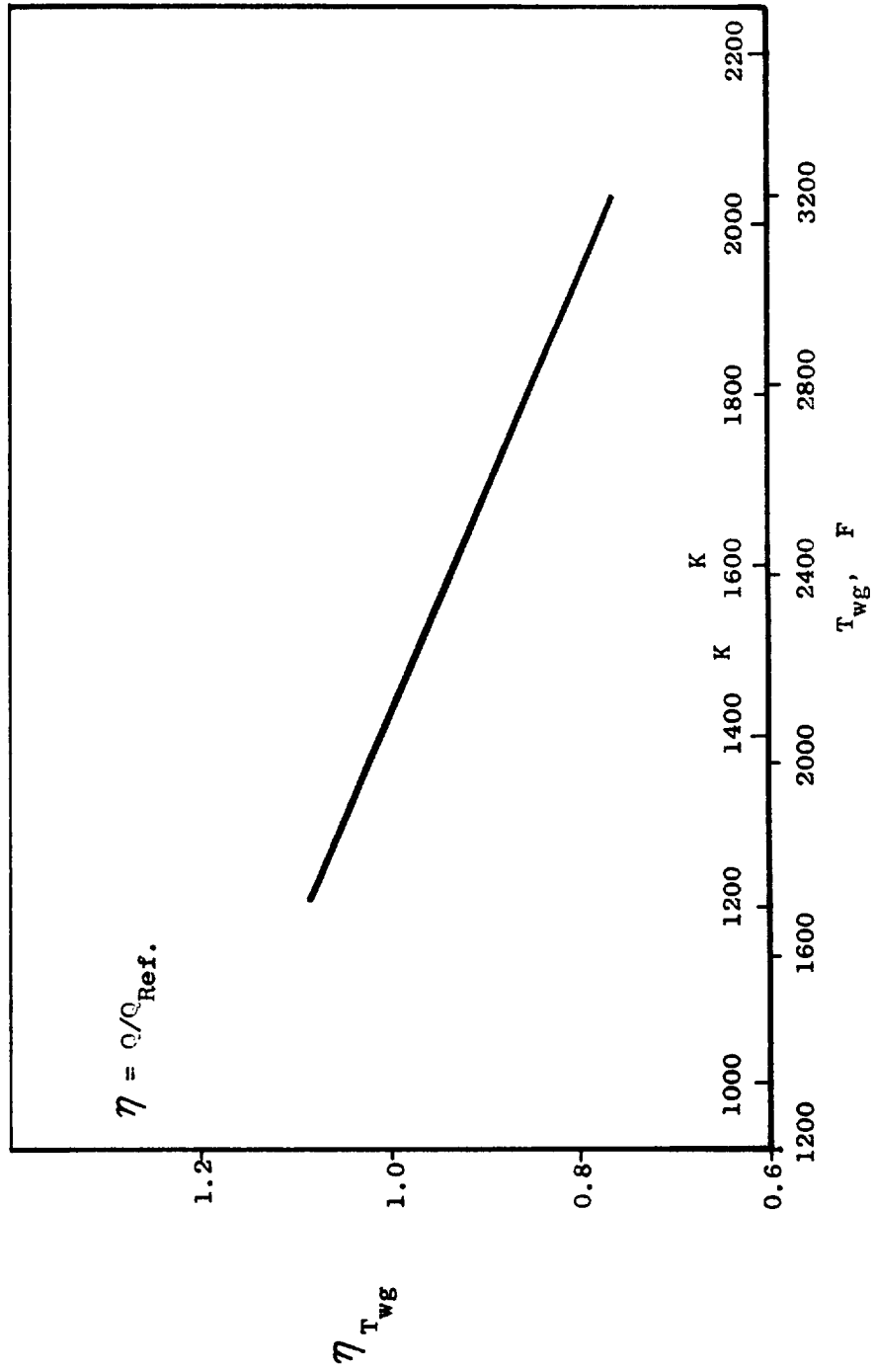


Figure 4 Gas-Side Wall Temperature Influence Coefficient

The subscript CZ refers to the thrust chamber region upstream of the throat and the subscript N refers to the region downstream. The value of Q_{ref}^N was 649 Btu/sec (686 kW) and Q_{ref}^{CZ} was 846 Btu/sec (895 kW). The reference values of total heat input were calculated for the conditions shown below:

TABLE 2
OPERATING CONDITIONS FOR Q_{ref}

Propellants	FLOX (82.6)/Methane
Mixture Ratio	5.7
Thrust, pounds (Newtons)	5000 (22,200)
Chamber pressure, psia (N/cm^2)	500 (345)
Nozzle Area Ratio	60
Contraction Area Ratio	3
Gas-side Wall Temperature, F(K)	2100 (1422)
Carbon Layer	None

Experimental data taken at 100 psia ($69N/cm^2$) chamber pressure and relatively low characteristic velocity efficiency from Ref. 2 were then correlated with total heat input determined by application of the analytical model to the experimental conditions. Significant heat input reductions were found and the ratio of experimental-to-analytical values of heat input was nearly linear with the hydrogen-to-carbon atomic ratio of the fuel as shown in Fig. 5. No significant trends in propellant mixture ratio effects on the carbon layer effectiveness were found.

The heat absorption capability of the regenerative coolants was based upon the enthalpy change of the coolant between the inlet and exit of the coolant jacket. The inlet enthalpy was evaluated at 10F (5.6K) above the freezing point of the fuel. The exit enthalpy depended upon the allowable maximum bulk temperature of the fuel which, in turn, depended upon either the pressure at the coolant jacket exit or the decomposition temperature of the fuel.

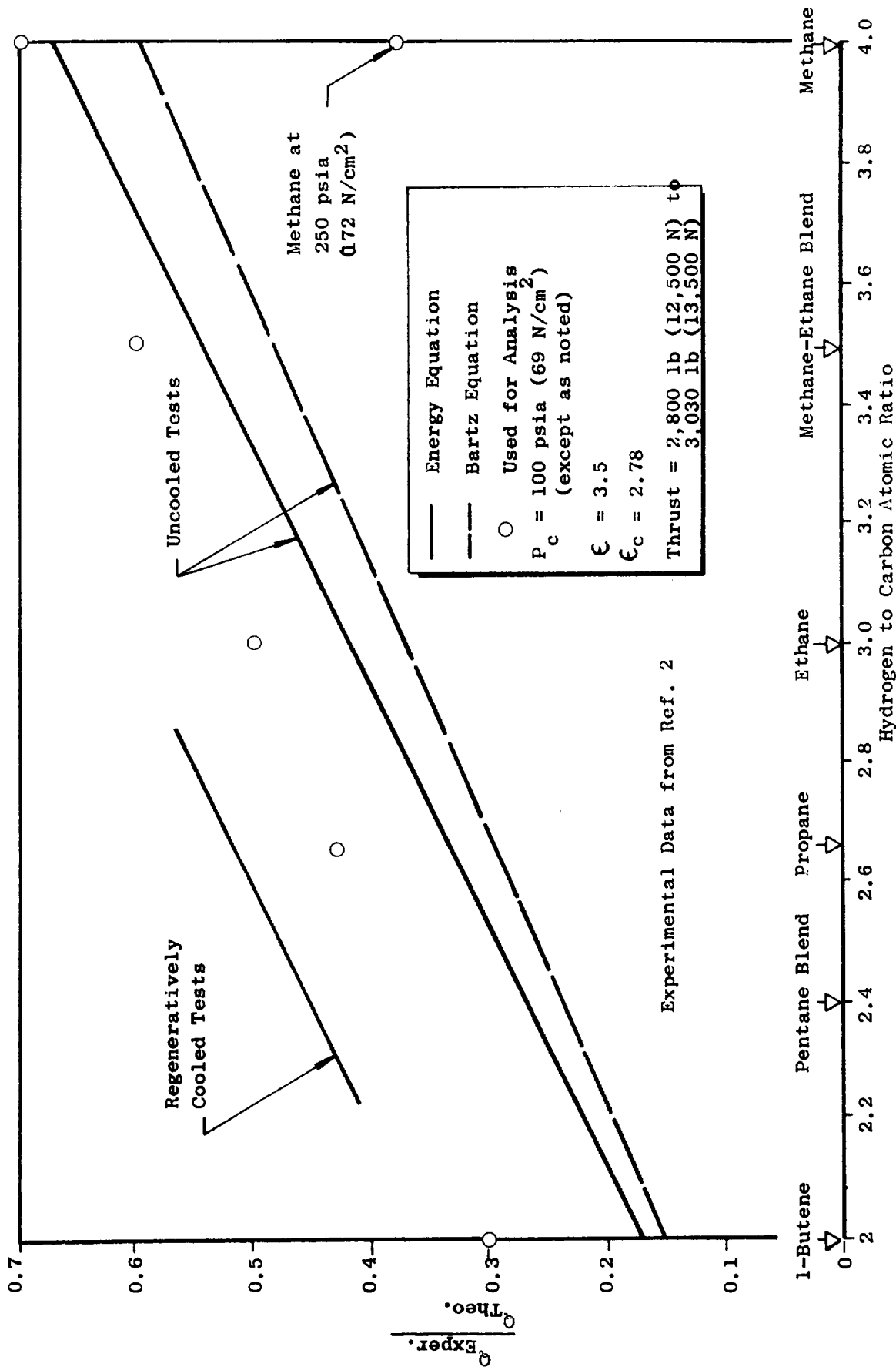


Figure 5 Heat Transfer Rate Reduction for Various Hydrocarbons

For high chamber pressure operation, the limiting temperature was that which resulted in decomposition of the fuel. A literature search was conducted to determine the most accurate values of kinetic constants with which to relate decomposition rates to coolant bulk temperature. Decomposition temperatures used in the analysis were: methane, 1500F (1082K); ethane and the methane-ethane blend, 900F (758K); propane, 850F (730K); and 1-butene, 800F (702K).

For low-chamber-pressure operation the conditions in the coolant jacket were subcritical and the restriction that bulk boiling should not occur limited the exit temperature to the saturation value. The saturation temperature was based upon a pressure which was 20 percent higher than chamber pressure to account for a reasonable injector pressure drop, i.e., saturation pressures were 120 and 300 psia (82 and 206N/cm²) for chamber pressures of 100 and 250 psia (69 and 172N/cm²) respectively. Heat absorption capacities are shown in Table 3.

Removal of the saturation temperature limit at low pressures was also investigated. However, it was then required that (1) complete vaporization of the fuel be accomplished to avoid mixed-phase flow in the injector, and (2) that bulk boiling be confined to the low flux (< 1 Btu/in²-sec) region of the nozzle. A nucleate boiling flux of 3 Btu/in²-sec (440W/cm²) was established as a practical maximum value.

A comparison of the heat inputs and the heat absorption capabilities was then made to determine the conditions under which regenerative cooling could be accomplished. Regenerative cooling was found to be applicable to practically all combinations of parameters investigated on the basis of propellant decomposition if the assumed gas-side carbon layer was present. Maximum propellant bulk temperatures under quite severe operating conditions are shown in Table 4. The temperature of the 1-butene at the exit of the coolant jacket was furthest below the decomposition temperature.

TABLE 3

HEAT ABSORPTION CAPABILITIES

Propellants	Optimum Propellant Mixture Ratio	Maximum Heat Absorption Capability, Q/F					
		Decomposition Limit Btu/lb-sec	W/kg	$P_{sat} = 120$ psia Btu/lb-sec	$P_{sat} = 83$ N/cm ² W/kg	$P_{sat} = 300$ psia Btu/lb-sec	$P_{sat} = 207$ N/cm ² W/kg
FLOX/Methane	5.70	0.61	1420	0.028	65	0.040	93
FLOX/Methane-Ethane	5.33	0.40	930	0.038	88	0.051	119
FLOX/Ethane	4.82	0.40	930	0.063	147	0.078	181
FLOX/Propane	4.50	0.40	930	0.093	216	0.111	258
FLOX/Butene-1	3.85	0.40	930	0.130	302	0.157	165
OF ₂ /Methane	5.30	0.65	1510	0.030	70	0.043	100
OF ₂ /Methane-Ethane	5.00	0.42	980	0.040	93	0.054	126
OF ₂ /Ethane	4.60	0.41	950	0.065	151	0.081	188
OF ₂ /Propane	4.60	0.39	910	0.090	210	0.107	249
OF ₂ /1-Butene	3.85	0.40	930	0.129	300	0.156	363

TABLE 4
COOLANT JACKET DISCHARGE TEMPERATURES

Propellants	Discharge Temperature	
	F	K
FLOX/CH ₄	1005	814
FLOX/CH ₄ -C ₂ H ₆	795	697
FLOX/C ₂ H ₆	635	608
FLOX/C ₃ H ₈	430	494
FLOX/C ₄ H ₈	300	422
OF ₂ /CH ₄	935	775
OF ₂ /CH ₄ -C ₂ H ₆	750	672
OF ₂ /C ₂ H ₆	610	594
OF ₂ /C ₃ H ₈	445	503
OF ₂ /C ₄ H ₈	310	428

Operating Conditions

Thrust, pounds (Newtons)	1000 (4450)
Chamber Pressure, psia (N/cm ²)	1000 (690)
Propellant Mixture Ratio	Optimum
Combustion Efficiency, percent	96
Contraction Area Ratio	3
Expansion Area Ratio	60
Gas Side Wall Temperature, F (K)	1700 (1200)
Carbon Layer Resistance	Figure 5

The exit temperature of the methane-ethane blend was closest to the decomposition value. Without the carbon layer, methane could still be used as a regenerative coolant under all conditions if the contraction area ratio were 4. For the other fuels, however, reduction of propellant mixture ratio and/or nozzle area ratio additionally would be required to prevent propellant decomposition at low thrust levels and high chamber pressures, or the gas-side wall temperature would have to be raised to 3200F (2033K).

Combinations of parameters may be selected for the chamber pressures which result in subcritical pressure operation (100 and 250 psia (69 and 172N/cm²) chamber pressures were investigated) which will permit use of regenerative cooling with all of the fuels at most thrust levels. Methane can be used as a regenerative coolant with complete vaporization under all conditions. The same conclusions apply to the methane-ethane blend except that the minimum thrust level is approximately 3500 pounds (17,400N) at 250 (172N/cm²) psia chamber pressure if a carbon layer does not exist. Ethane can be used as a liquid at the higher thrust levels and completely vaporized at the low thrust levels if a carbon layer exists. Without a carbon layer, ethane can be vaporized at all thrust levels but is decomposition-limited to thrust levels above 3500 pounds (17400N) at 250 psia (172N/cm²) chamber pressure. Propane may be used as a liquid at all thrust levels with a carbon layer and may be completely vaporized without decomposition at all thrust levels above 5000 pounds (22,250N) without a carbon layer. Butene may be used at all thrust levels with a carbon layer as a liquid and may be completely vaporized at all thrust levels without a carbon layer at 100 psia (69N/cm²) chamber pressure. Regenerative cooling without a carbon layer at 250 psia (172N/cm²) chamber pressure is limited to the 20,000 (89,000N) pound thrust level for 1-butene.

DETAILED ANALYSIS

The purpose of the Detailed Analysis was to further investigate regenerative cooling limits for propellant combinations which were the most attractive on the basis of performance and the results of the Parametric Analysis. Detailed analysis and designs were accomplished for FLOX/methane at thrust levels of 1000, 5000 and 20,000 pounds (4450, 22,250 and 89,000N) for OF_2 /propane at 5000 and 20,000 pounds (22,250 and 89,000N), and for OF_2 /1-butene at 1000 (4450N) pounds. Channel-type coolant passages in nickel, stainless steel (CRES), and Hastelloy X walls were assumed. The nickel and CRES operated at a maximum gas-side wall temperature of 1700F (1200K), the Hastelloy X at 2100F (1420K). The case of a refractory coating operating at 3200F (2033K) on a nickel wall chamber was also evaluated. Analyses were again conducted both with and without the assumption of a gas-side carbon layer. A contraction ratio of 4, a nozzle area ratio of 100, and optimum propellant mixture ratio were generally assumed. Single-pass counterflow coolant circuits were found to be practical for most cases.

Regenerative cooling limits were based upon coolant jacket pressure drop, minimum channel dimensions, and coking of the coolant. The allowable pressure drop varied linearly from 100 psi (69N/cm²) at a chamber pressure of 100 psia to 500 psi (69-345N/cm²) at 1000 psia (690N/cm²). Minimum channel dimensions occurred near the throat where the channels were square for dimensions greater than 0.040 inches (0.10 cm) and a variable depth with 0.040 inches (0.10 cm) width for smaller channels. A minimum depth of 0.025 inches (0.063 cm) was selected on the basis of manufacturing tolerances and plugging considerations. Coolant-side wall temperatures were limited to 1500F (1080K) for propane and 1-butene and to 2000F (1370K) for methane to prevent coking of the coolant.

Regenerative cooling was practical for the FLOX/methane propellant combination with nickel walls at all chamber pressures and thrust levels investigated whether or not a gas-side carbon layer exists. Only at the

most severe condition (1000 psia ($690\text{N}/\text{cm}^2$) chamber pressure and 1000 pounds (4550N) thrust level with no carbon layer) were the pressure drop and minimum channel dimension limits slightly exceeded. The refractory coating was approximately as effective as the gas-side carbon layer in reducing the heat flux.

Pressure drop limits were slightly exceeded for the OF_2 /propane propellant combination only at 1000 psia ($690\text{N}/\text{cm}^2$) chamber pressure with no carbon layer. The carbon layer was more effective in reducing the heat flux than the 3200F (2033K) coating. The 1500F (1080K) decomposition temperature limit on the coolant-side wall did not permit use of the 2100F (1420K) capability of the Hastelloy X. The gas-side wall temperatures of all materials were established by nucleate boiling conditions for subcritical pressure operation with a carbon layer. Minimum channel dimensions were less than 0.025 inches (0.063cm) at chamber pressures greater than 750 psia ($159\text{N}/\text{cm}^2$) with no carbon layer. Propellant mixture ratio reductions (to as low as 74 percent of the optimum value at 1000 psia ($69\text{N}/\text{cm}^2$) chamber pressure) would be required to maintain a minimum channel depth of 0.025 inch (0.063cm). Regenerative cooling is therefore practical for OF_2 /propane at all chamber pressures and thrust levels if the assumed gas-side carbon layer exists. Regenerative cooling is possible without the carbon layer but operating parameters are sometimes restricted.

The OF_2 /1-butene propellant combustion can be regeneratively cooled at the 1000-pound (4450N) thrust level for all chamber pressures and materials investigated if the assumed gas-side carbon layer exists. Without the carbon layer, pressure drops with a nickel wall were generally acceptable, although slightly above the 500 psi ($345\text{N}/\text{cm}^2$) limit at the highest (1000 psia) chamber pressure analyzed. Use of CRES or Hastelloy X would result in even higher pressure drops at the high chamber pressures. The minimum channel dimensions were satisfactory for subcritical operation without a

carbon layer but were below the limit under supercritical operating conditions. The exit temperature of the coolant was above the decomposition value, 800F (702K), for all chamber pressures without a carbon layer or refractory coating. Application of a coating to increase the gas-side wall temperature to 3200F (2033K) or reduction of propellant mixture ratio would prevent coolant decomposition.

Nickel 200 was found to be the most suitable material for thrust chamber walls at high flux levels, i.e., high chamber pressures with no carbon layer. Hastelloy X was slightly superior at moderate heat flux conditions. CRES was inferior to the other two materials because of its low thermal conductivity and operating temperature. However, under low heat flux conditions, the differences between the three materials was not sufficient to base a selection on the regenerative cooling characteristics.

As a general conclusion, it may be stated that regenerative cooling with the light hydrocarbons appears practical over the ranges of chamber pressures and thrust levels investigated in this study. Regenerative cooling is, generally, greatly facilitated by the presence of a gas-side carbon layer.

SECTION II
HARDWARE DESIGN AND FABRICATION

The FLOX/methane propellant combination was selected for experimental verification of performance and heat transfer characteristics on the basis of the results of the regenerative cooling analyses conducted in Task I and because of the high performance of the combination. In Task II injectors, thrust chambers, and nozzles were designed to accomplish this verification at chamber pressures in the 500 to 1000 psi region (345 to 690N/cm²). In Task VI injectors were designed and fabricated to operate over chamber pressures ranging from 50 to 500 psia (35 to 345 N/cm²). Design conditions and constraints are tabulated below.

TABLE 5
DESIGN CONDITIONS AND CONSTRAINTS

Propellants	FLOX (82.6 percent F ₂)/Methane
Mixture Ratio	a. 4.0 to 5.7 b. 5.25
Nozzle Area Ratio	60
Chamber Pressure, psia (N/cm ²)	a. Task II, 500 to 1000 (345 to 690) b. Task VI, 50 to 500 (35 to 345)
Thrust Level, pounds (Newtons)	a. 5000 to 10,000 (22,200 to 44,500) b. 500 to 5000 (2220 to 22,200)
Injector Efficiency, percent	a. 96 or greater b. 96 to 98 or greater
Water-cooled Thrust Chamber	Steady-state operation
Regeneratively Cooled Thrust Chamber	Advanced fabrication method a. - Task II b.- Task VI

Flight-weight configurations were not a goal in these designs. Hardware interchangeability and flexibility were emphasized.

INJECTORS

Injector configurations and designs were based on the use of liquid FLOX as

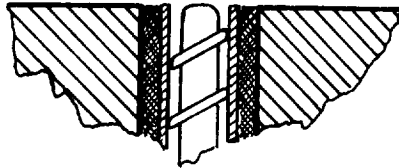
the oxidizer and supercritical methane (heated in the regenerative cooling circuit) as the fuel. The design approach was to first determine analytically the injector atomization and mixing requirements for high performance. Single element cold flow tests were then conducted with element types which have been successfully used on previous Rocketdyne programs to determine how well these element types could be expected to meet the requirements. Finally, heat transfer analysis for the injector faces were conducted to determine the relative safety of the various element types and to assist in specifying the overall injector face pattern for each element type. The types of elements considered are shown schematically in Fig. 6.

Combustion stability comparisons were made between the triplet and concentric elements during the early phases of the J-2 engine program at Rocketdyne. The rating was based on the minimum hydrogen injection temperature at which combustion was stable. The minimum temperatures for the triplet element injectors were generally higher than for the concentric element injectors, i.e., the concentric element injectors tended to be more stable.

Performance Analysis

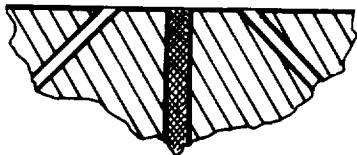
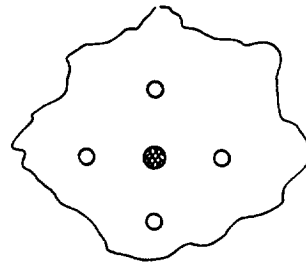
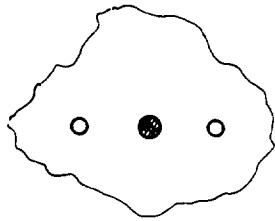
Analyses were conducted to estimate and compare performance of the impinging jet elements, considering such factors as atomization, vaporization, mixing, and chemical reaction. For these propellants the latter is not rate-controlling.

A one-dimensional, steady-state, combustion model was used to predict combustion characteristics as a function of propellant dropletsizes and combustor geometry. Details of the analysis are given in Appendix A. The loss in efficiency due to incomplete propellant vaporization was calculated for the FLOX/methane propellant combination as a function of FLOX dropletsizes from 10 to 100 microns, chamber lengths from 5 to 12 inches (12.7 to 27.5 cm) and contraction ratios from 2 to 6.

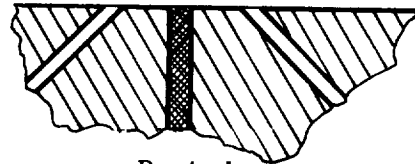


○ Oxidizer
● Fuel

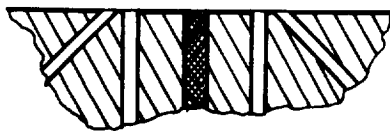
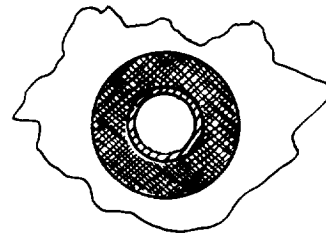
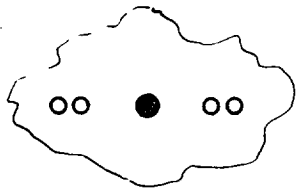
Heat Exchanger



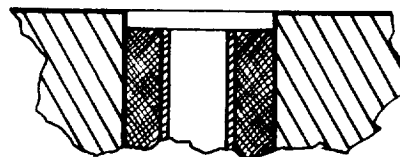
Triplet



Pentad



Impinging Fan



Concentric and Recessed Post

Figure 6. Injector Element Types

Combustion efficiency, degraded only for FLOX vaporization losses, is shown in Fig. 7 as a function of combustion length and average drop size. The results indicate that, for a reasonable combustion chamber design, high efficiencies are obtainable with dropsizes of 80 microns or less, as shown in Fig. 8. Dropsizes calculations and the photographs taken during the cold flow tests indicate that dropsizes of much less than 80 microns should be obtainable with any of the elements tested. Therefore, injector performance will depend more on uniform mixing than on vaporization and chemical reaction losses.

The effect of mixing on combustion performance was determined employing a stream tube analysis program in which the chamber cross section was divided into discrete "tubes" of differing mixture ratio and percent mass. Overall performance was then defined as a function of departure from the ideal distribution (or mixing) by computing the integrated C* level obtainable, assuming no inter-stream-tube mixing.

The results of the analysis (Appendix A) are shown in Fig. 9. Although combustion efficiency losses depend quite strongly on the uniformity of mixing, typical mixing efficiencies for injectors tested under Contract NAS 8-19 indicate that either the triplet ($E_m = 0.875$) or fan ($E_m = 0.93$) could achieve the 96 percent C* efficiency goal. The fan would be more likely to have a higher performance. The pentad would be expected to be similar to the fan; perhaps even higher performing, in practice, because the pentad would be less sensitive to oxidizer jet misimpingement resulting from manufacturing tolerances.

Injector Face Heat Transfer Analysis

Analyses were conducted to estimate the face temperature and, thus, the relative safety of several injector configurations. Pentad and concentric elements were analyzed for solid copper and nickel face injectors and for injectors with transpiration-cooled faces. The analyses are described in Appendix B. The results of these analyses indicated that the injector

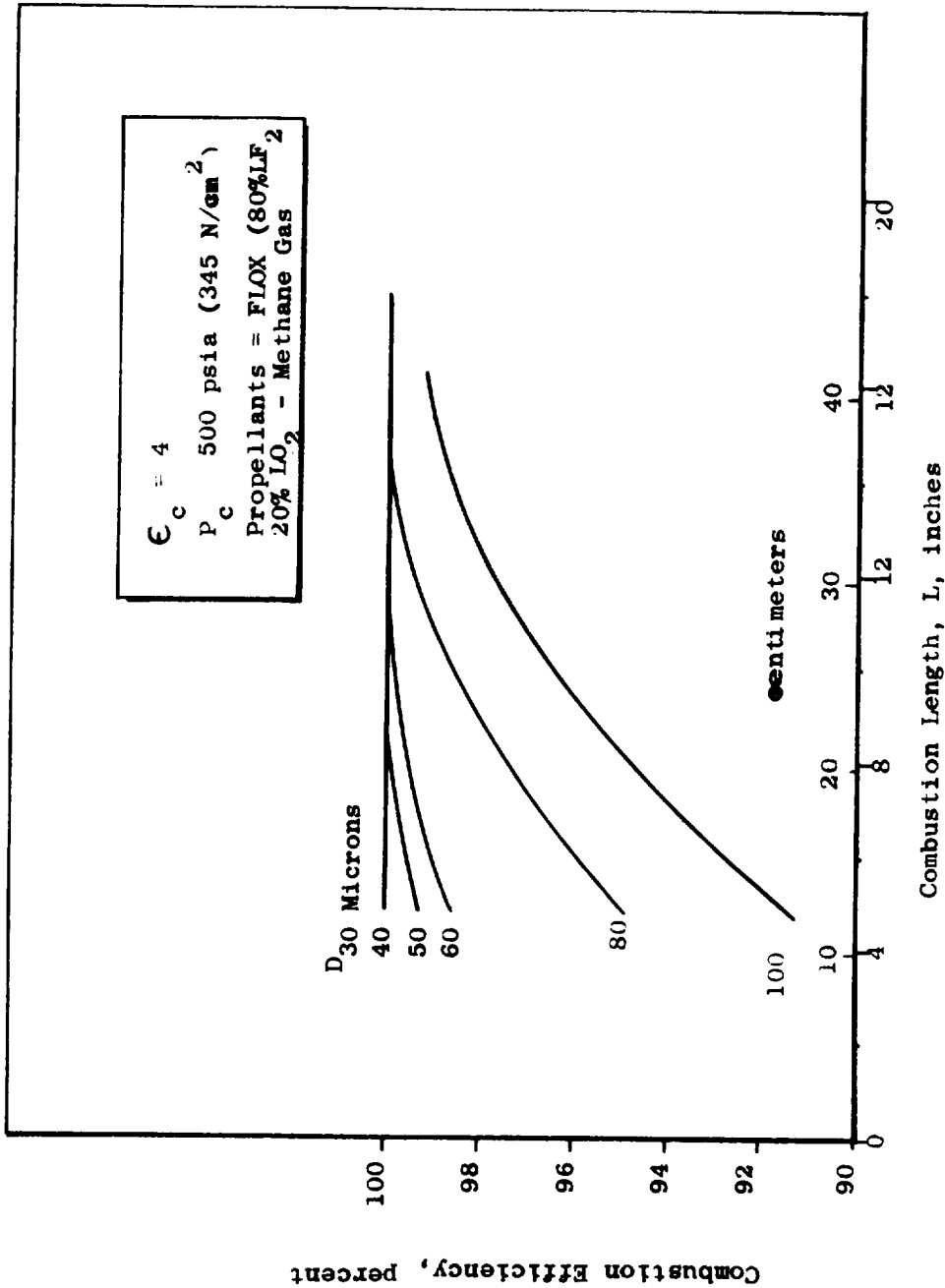


Figure 7 . Combustion Efficiency as a Function of Combustion Length for Various Mean Drop Sizes.

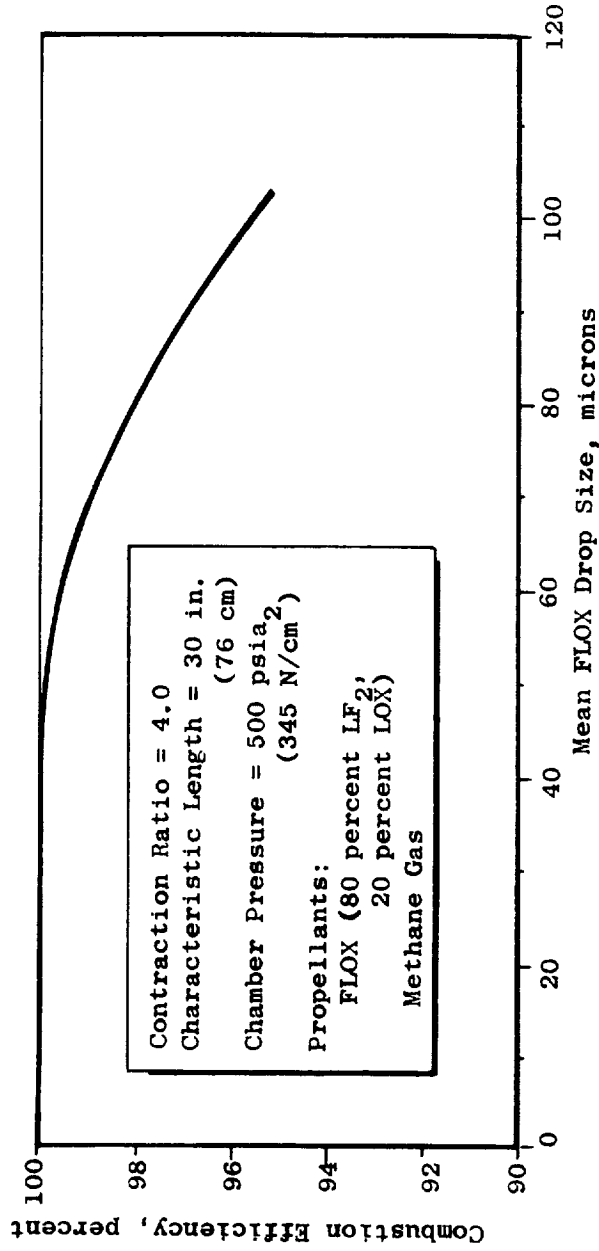


Figure 8 Combustion Efficiency as a Function of Mean FLOX Drop Size

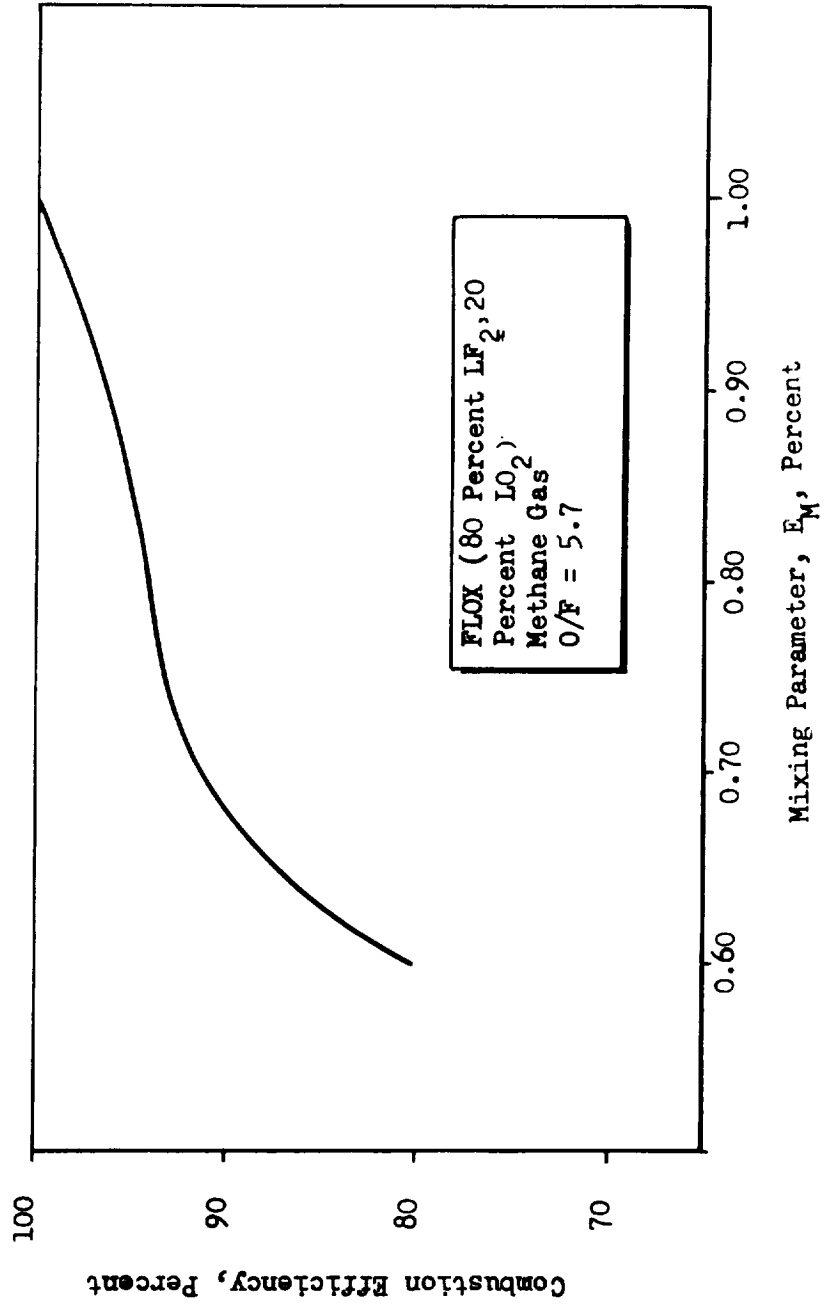


Fig. 9. Combustion Efficiency As a Function of Mixing Parameter

with nickel concentric elements surrounded by a transpiration-cooled face was the safest design. The designs are listed below in order of decreasing safety of operation at 1000 (690 N/cm²) psia chamber pressure.

TABLE 6

INJECTOR ELEMENT CONFIGURATIONS AND TEMPERATURES

<u>Element</u>	<u>Face</u>	<u>Maximum Temperature</u>	
		F	K
Concentric	Nickel/Transpiration	1340	1000
Pentad	Solid Copper	1200	920
Pentad	Nickel/Transpiration	2000	1370
Concentric	Solid Copper	1970	1350
Pentad	Solid Nickel	2360	1560

Heat fluxes were based on applying a safety factor of approximately 2 to the values calculated for the chamber wall near the injector. The same heat flux values were used for both elements whereas previous experience and subsequent experience on this contract indicated that the concentric element injector heat flux would be lower. Thus it was thought that the prediction of poor safety for the solid copper concentric injector was unduly pessimistic. This was subsequently verified by safe operation of the injector at approximately 900 psia (623 N/cm²) chamber pressure.

Full Scale Injectors

Based on these analytical studies and the cold flow tests conducted in Task III the solid copper pentad and the rigimesh face concentric element injectors were selected for detailed design. Subsequently designs featuring a solid copper face with concentric elements and triplet elements included and are also discussed. These injectors were designed with a 5.18 inch (13.2 cm) diameter face for operation at 500 to 1000 psia (345 to 690 N/cm²) chamber pressure with FLOX/methane at propellant mixture ratios of 5.7 (nominal) to 4.0. Concentric element heat exchanger and recessed

post injectors were later designed for operation at 50 to 500 psia (35 to 345 N/cm²) chamber pressure and 5.25 + 0.50 propellant mixture ratio.

Pentad. An injector face pattern containing 91 elements (four oxidizer on one fuel) was selected to promote uniformity of propellant distribution consistent with reasonable manufacturing tolerances for the feeder manifolds. The elements were arranged in six concentric rings based on equal area coverage for each element. The injector face pattern and typical element detail are shown in Fig. 10. The FLOX feeder manifolds were sealed with electron beam welded plugs and supplied with FLOX from the back of the injector body. The methane feeder manifolds were supplied from a ring manifold at the circumference of the injector body. An attempt was made to electrochemically deburr the orifices at the feeder manifolds by inserting electrodes into the manifolds and plating copper from the injector onto the electrodes. No significant improvement in discharge coefficients was determined. Figure 11 is a photograph of the completed pentad injector.

Triplet. The triplet injector is attractive from the standpoint of fabrication simplicity. A drawing of the 73 element triplet (two oxidizer on one fuel) injector with a solid copper face is shown in Fig. 12. The assembly is similar to that of the pentad injector: the inner body containing the orifices and feeder manifolds is electron beam welded to the outer body which closes out the fuel manifold and contains the bolt holes for assembly to the thrust chamber and the FLOX dome. The completed triplet injector is shown in Fig. 13. The spots on the face are braze dots to indicate incipient overheating conditions.

Three triplet injectors were fabricated. The oxidizer and fuel orifice diameters were as follows:

Injector	CH ₄ diameter,		FLOX diameter,	
	inches	cm	inches	cm
TI	0.070	0.178	0.0469	0.119
T2	0.073	0.185	0.052	0.132
T3	0.073	0.185	0.050	0.127

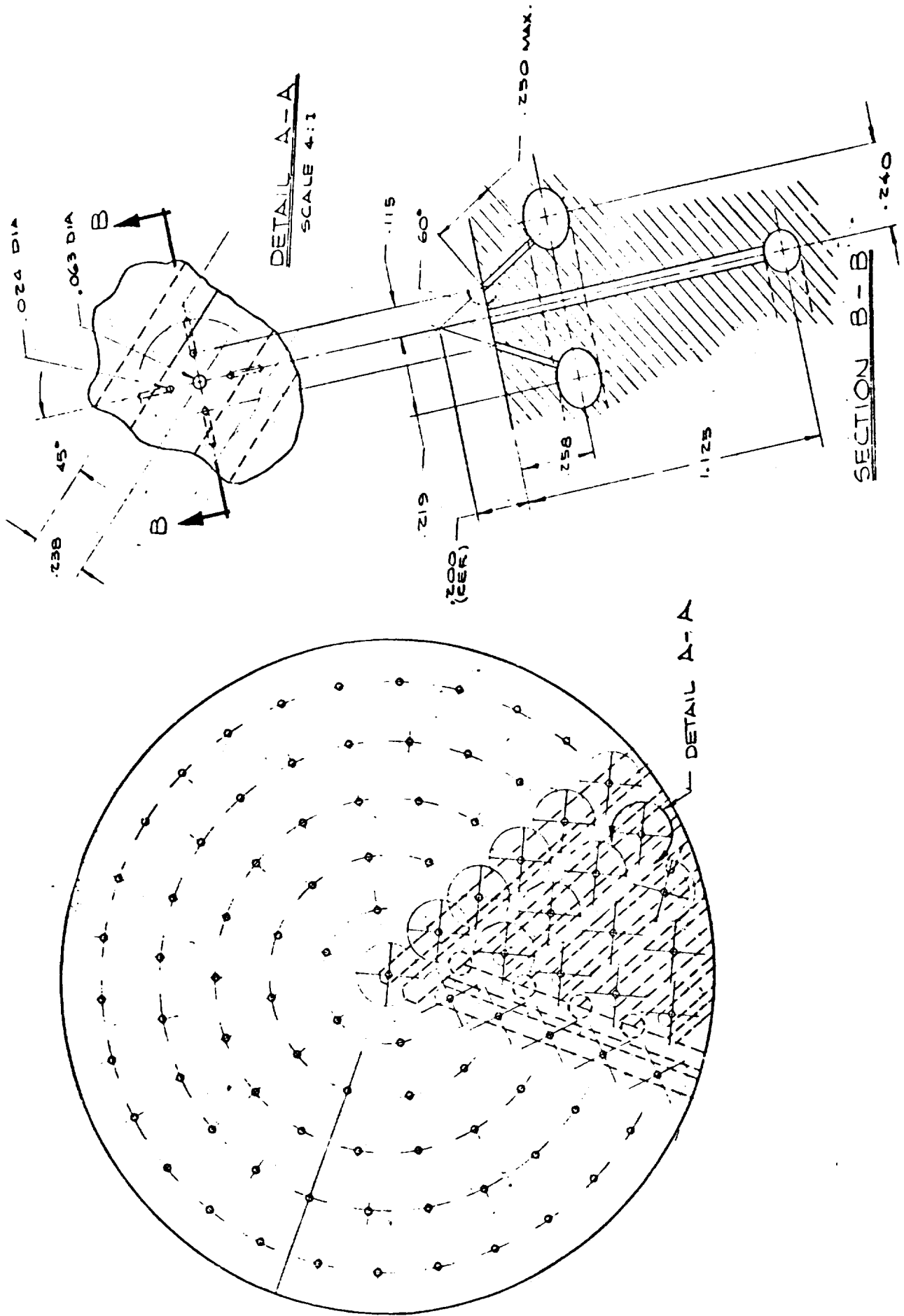
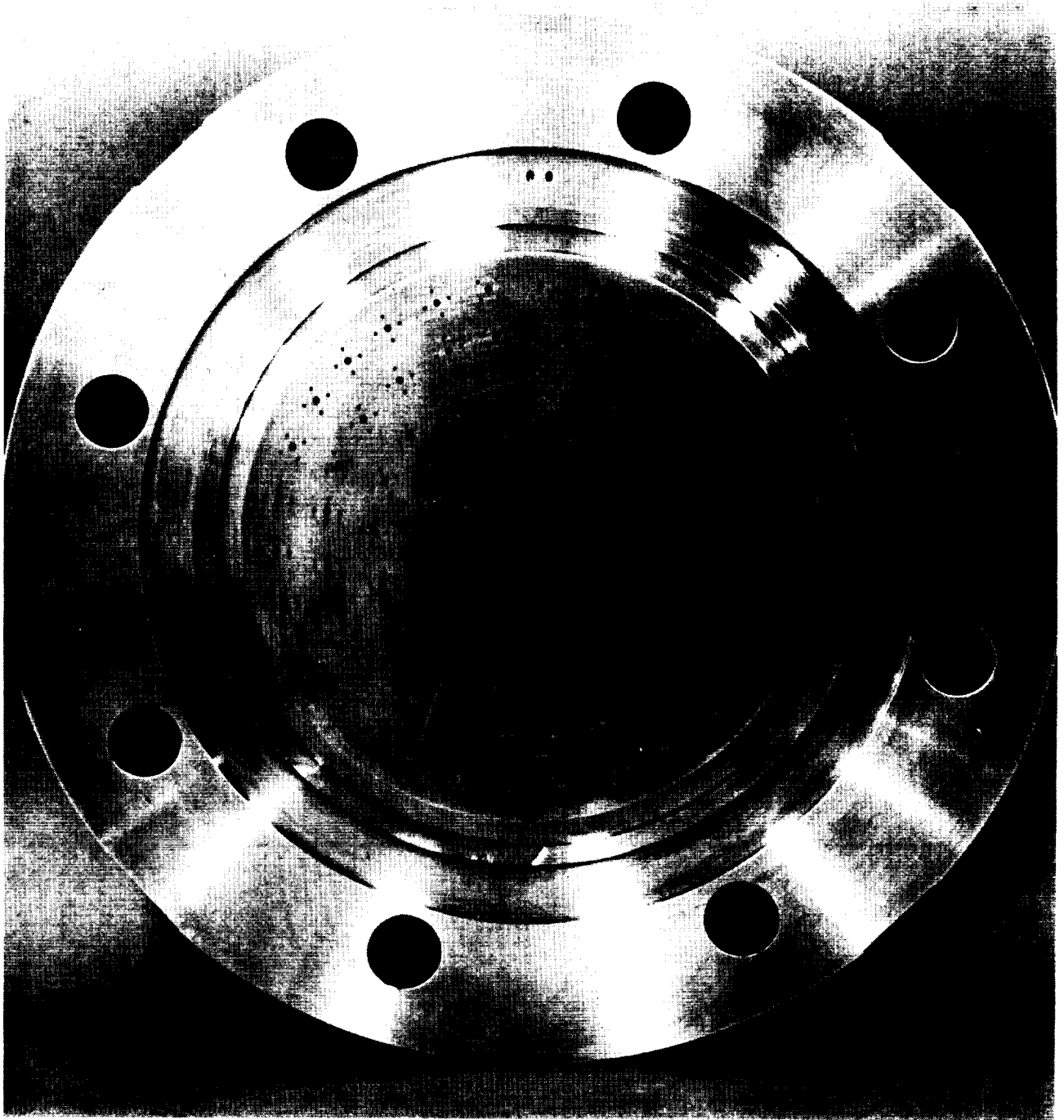


Figure 10. Pentad Injector Face Pattern and Element Detail



1XX42-5/14/68-C1D

Figure 11. Pentad Injector

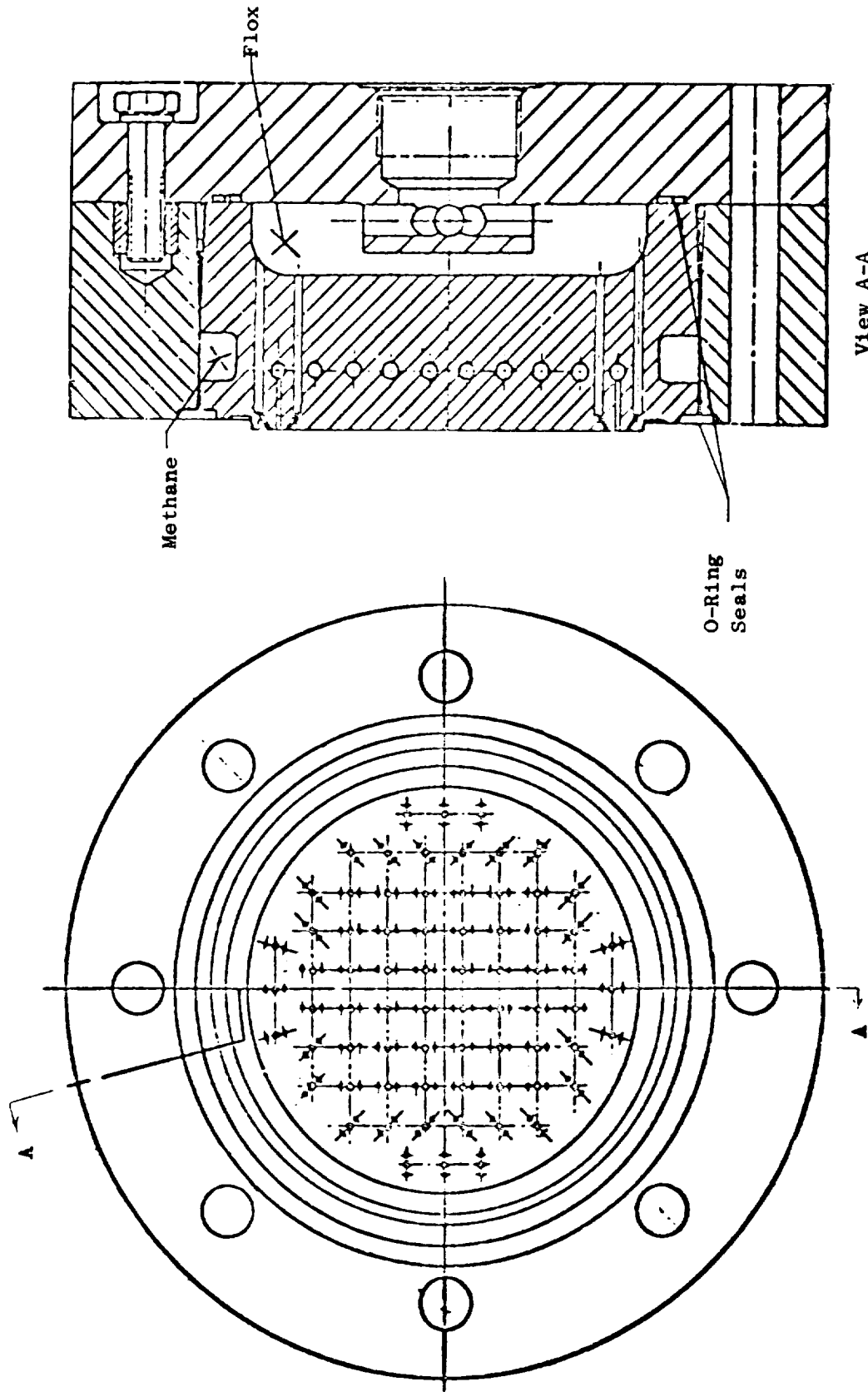
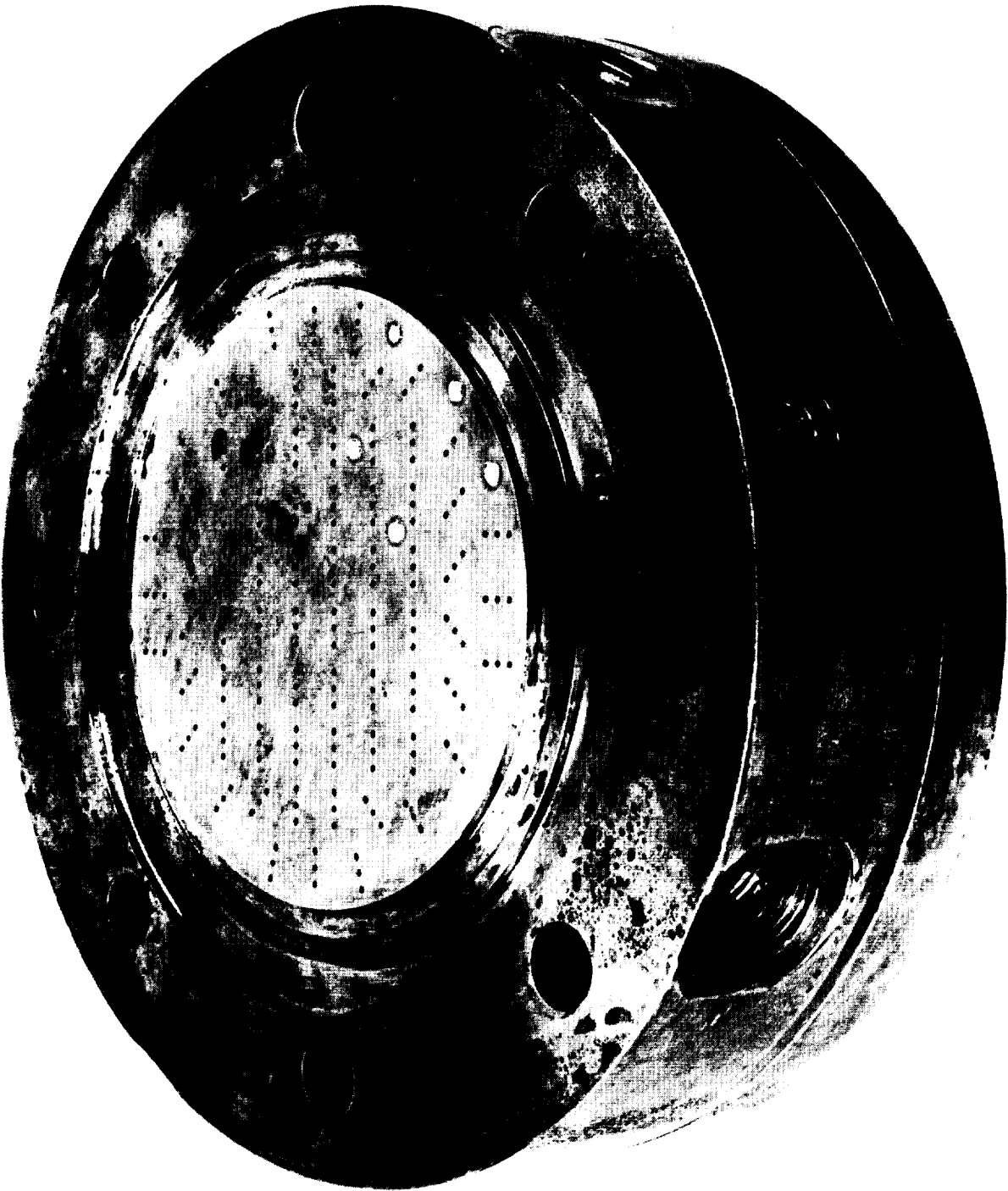


Figure 12 . Triplet Injector Drawing



LXW32-7/2/68-C1D

Figure 13. Triplet Injector

During the test program 12 showerhead fuel orifices (0.031 inches diameter) were added near the circumference of injector T1 and were included on T2 and T3. Eight of the outer elements on T2 and T3 were converted to fuel showerheads by closing the FLOX orifices. The FLOX orifice diameters were reduced on T2 to lower the inlet pressure to meet facility limits. An intermediate diameter was used on T3 to provide adequate pressure drop at low pressure, low mixture ratio operating conditions.

Concentric. Figure 14 is a drawing of the 61 concentric element injector. This injector is assembled in five pieces: 1) The FLOX dome is the same as used with the pentad and triplet injectors, 2) The oxidizer body contains the FLOX tubes, hydraulic swirlers, and interbody pressure cavity. Several swirler configurations were cold-flow tested and a two-port (0.055 inch diameter) tangential entry swirler was selected. The hydraulic swirlers assure FLOX flow on the inner wall of the FLOX tube to cool the tube. The swirlers also cause the oxidizer to leave the tube as a hollow cone spray, which promotes mixing with the methane. The FLOX tubes are 304 CRES with an O.D. of 0.250 inches (0.63 cm) and an I.D. of 0.120 inches (0.25 cm). The tubes are doubly brazed into the FLOX body. A positive GN_2 pressure in the interbody pressure cavity assures that failure of either or both braze joints will not result in an interpropellant reaction, 3) The interbody spacer locates the tip of the FLOX tube with respect to the injector face. The FLOX tube recess depth can be controlled to balance performance and face heating effects and to influence the injection pressure drops. The nominal recess was 0.117 inches, 4) The fuel body is stainless steel with a rigimesh face welded to the circumference and also supported by tubular members on several elements. Approximately 5 percent of the fuel flows through the 200 cfm rigimesh face for cooling. The methane tubes are secured on either end by flares and are precision broached to maintain the annular gap between the FLOX tube and the methane tube. The methane tubes were made of CRES because of the availability of this material, 5) An insertion depth spacer (not shown in Fig. 14) controls the distance of the injector face from the thrust chamber throat.

Figures 15 and 16 show the component parts of the concentric injector. A solid copper fuel body was designed and fabricated. Low heat fluxes at the injector face resulted in successful operation of this injector. The solid face concentric injector assembly is shown in Fig. 17. One 0.032 inch

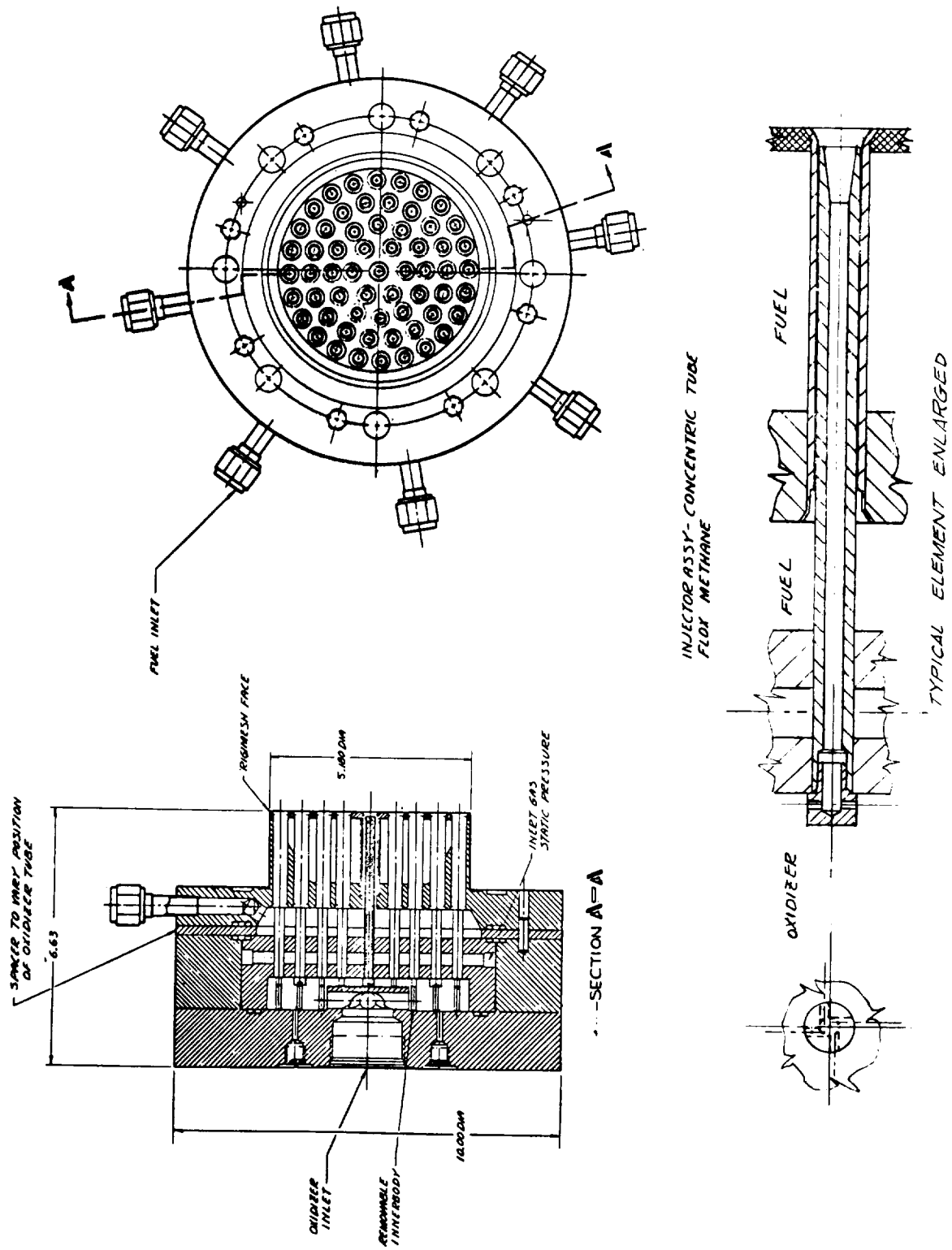
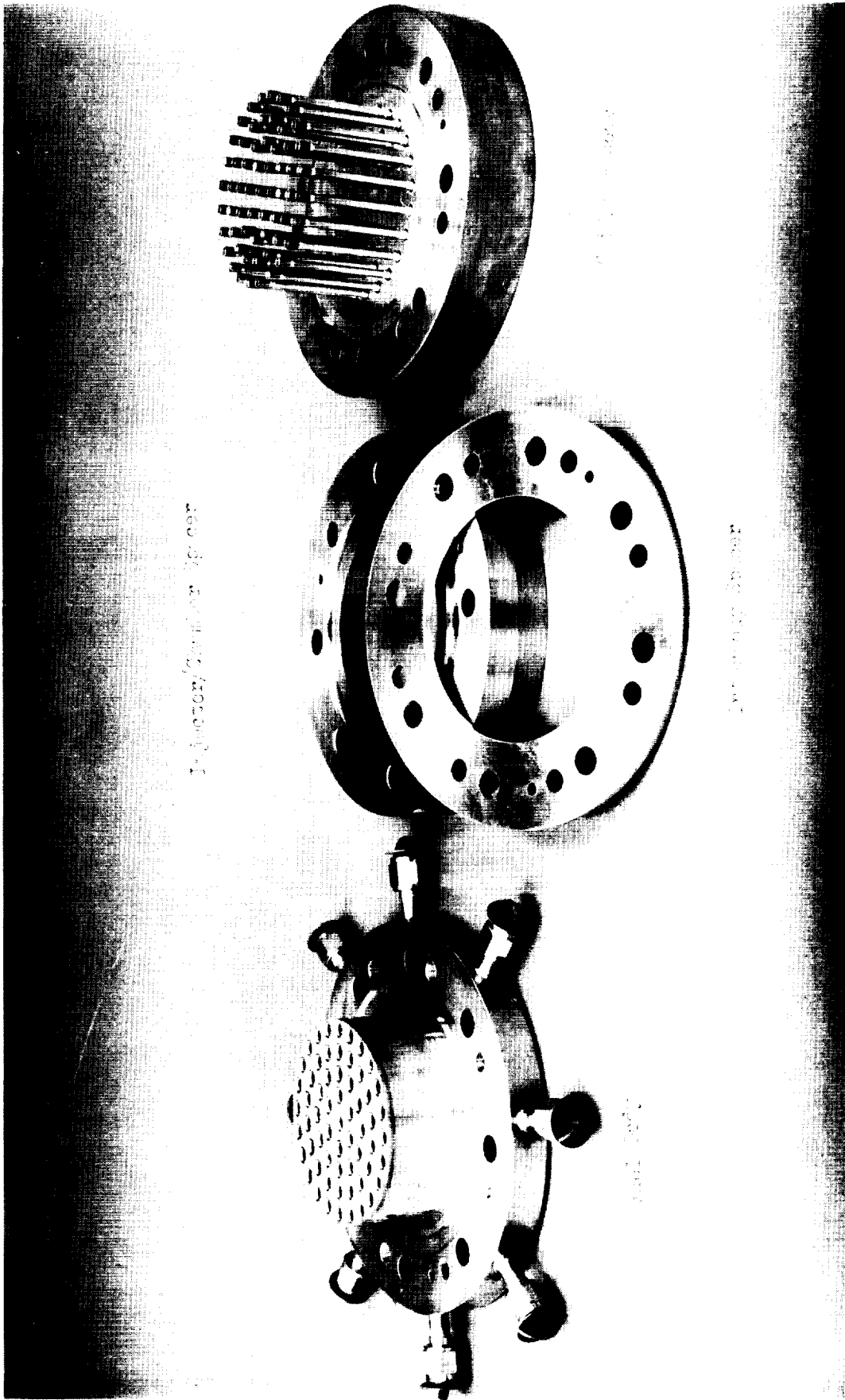
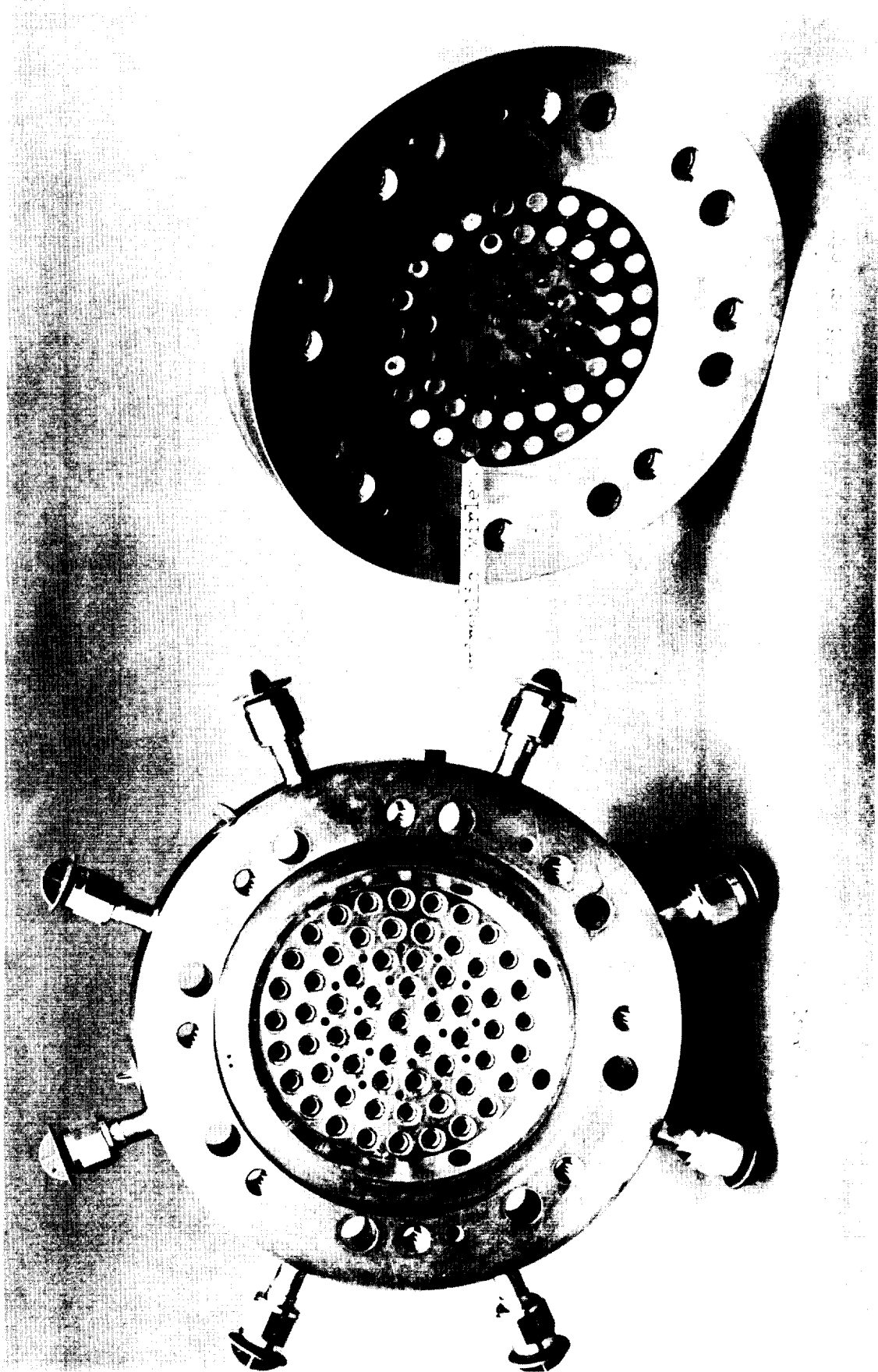


Figure 14 . Concentric Element Injector



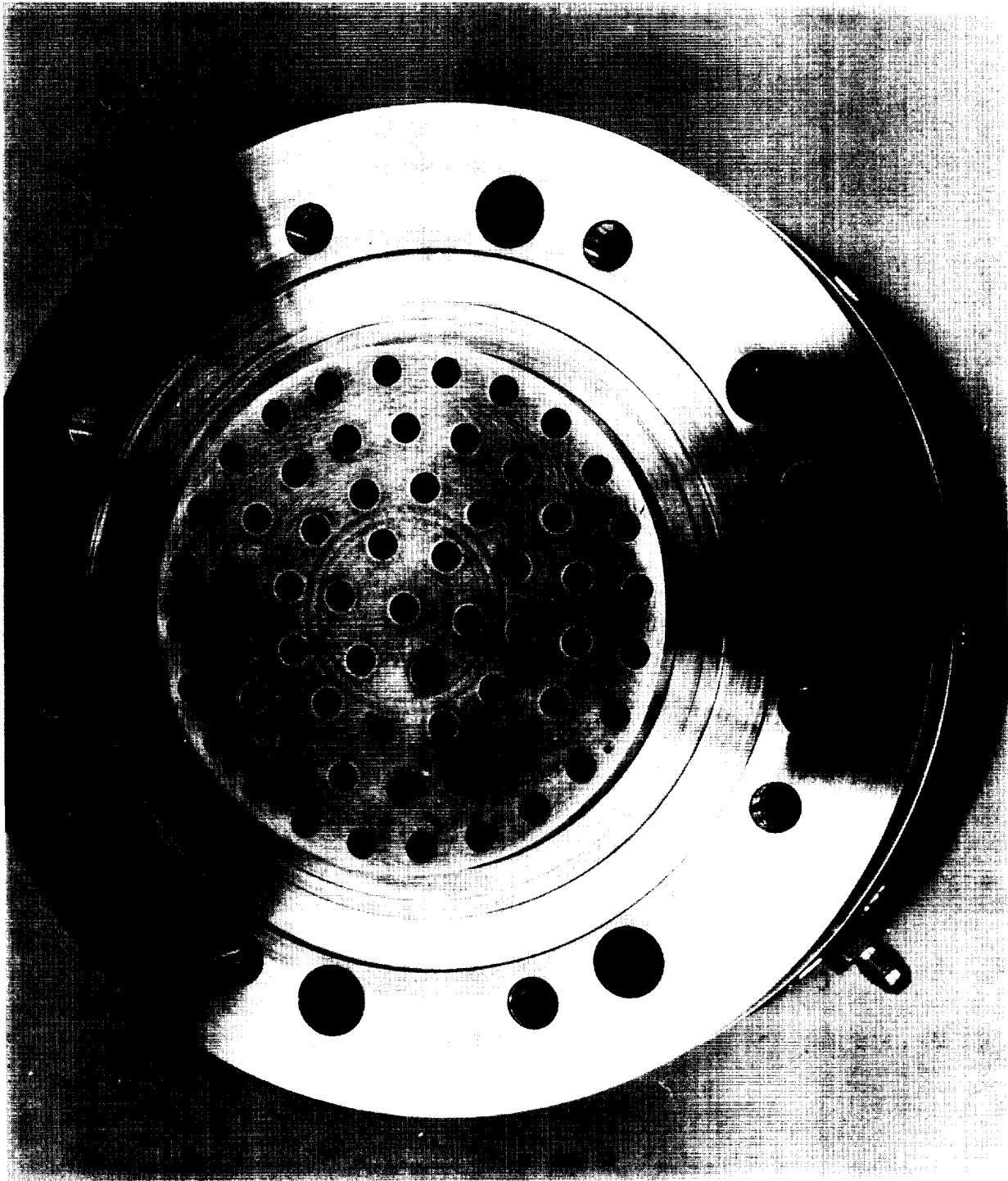
1XX42-9/23-68-C1A

Figure 15. Components of Concentric Element Injector



LXX42-9/23/68-CIB

Figure 16. Concentric Element Injector, Rear View



1XX42-12/6/68-C1B

Figure 17. Concentric Injector with Solid Copper Face

(0.081 cm) diameter fuel orifice was added between each element in the outer row and the outside diameter of the injector after the Task IV tests. This was done to provide a more uniform circumferential mixture ratio distribution.

Heat Exchanger. This injector was designed and fabricated under an IR&D study and has the same face pattern and propellant manifolding system as the concentric element injector described above except for the details of the elements. The FLOX flows through a central spiral passage in each element. Three sides of the passage are formed by a spiral grooved copper rod. A nickel tube of 0.017 inch (0.030 cm) thickness forms the heat transfer side of the passage. Hot methane flowing through the annular gap (0.010 inches) between the nickel tube and the fuel body heats and vaporizes the FLOX in the element. At high thrust levels little vaporization of the FLOX occurs. The temperature of the methane entering the injector increases as the thrust chamber is throttled and the pressure of the FLOX decreases so that the amount of FLOX vaporized increases. The net result is that the FLOX injection pressure drop does not follow the hydraulic square law, and relatively high pressure drops are maintained at low flow rates which promote stability. Concentricity of the elements is provided by flutes broached into the copper fuel body.

The length of the element over which heat transfer occurs was conservatively designed to be 2.5 inches (6.3 cm). The cross sectional area for FLOX flow in each element is 0.0063 in.² (0.041 cm²). A drawing of one of the elements is shown in Fig. 18.

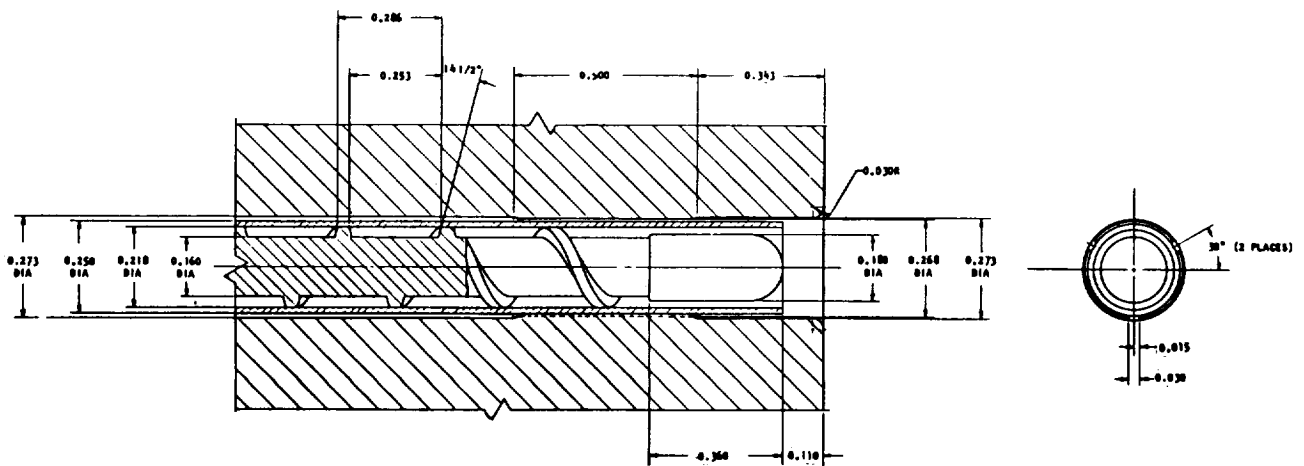


Figure 18. Heat Exchanger Element

The same fuel body and oxidizer dome were designed for use with this injector as with the concentric element injector described above and has the same variable recess feature. Figure 19 is a photograph of the injector components. A FLOX swirler and tube are shown in the foreground. The tubes were roughened on both sides to enhance the heat transfer coefficients. Fuel showerhead orifices were added after initial tests indicated oxidizer-rich conditions on the combustion chamber wall. One 0.040 inch (0.10 cm) diameter orifice was electrodischarge machined into the fuel body on the outside of each element in the outer row.

Recessed Post. The first indications that concentric tube elements possessed unique throttling advantages appeared at Rocketdyne during the J-2 engine development program. Early concentric tube injector designs for the J-2 incorporated oxidizer center posts, which were flush with the injector face, surrounded by a fuel annulus formed between the outside of the oxidizer center post and the inside diameter of the fuel passage.

Flow data obtained from these original injectors showed that the oxidizer sides of the injectors were following the normal square law for ΔP vs w over the range of chamber pressure variation. As the development program progressed, it became apparent that significant performance advantages could be realized if the injector elements were designed such that the end of the center post was recessed back into the injector some small distance. The region at the end of concentric tube elements between the end of the oxidizer center post and the injector face was named the "cup" region.

Flow data obtained from injectors having recessed oxidizer center posts could not be correlated using standard square law relationships. It was found that the pressure drop of the oxidizer system was higher for injectors with recess than for injectors with flush posts at a given flow rate (oxidizer post recess being the only difference between the injectors). Further, it was found that the oxidizer pressure drop varied with mixture ratio at a fixed value of oxidizer flow. It was, therefore, concluded that the interaction of oxidizer and fuel within the confines of the cup was producing pressure losses at the element exit.



1XX42-3/24/69-C1E

Figure 19. Heat Exchanger Injector Components

Subsequent study of data and related analysis produced a correlation which rationalized the flow data from recessed post injectors. The correlation, unlike the simple square law, involved the flow parameters of both the oxidizer and fuel systems. Thus, mixture ratio, fuel properties, and element geometry enter into the calculation of oxidizer pressure drop.

The hydraulic characteristics of the concentric tube elements incorporating cup recess were such that the pressure drop range exhibited over a given flow rate range was significantly less than that predicted by the standard square law. This behavior is highly beneficial for throttleable injector application.

Although the physics of the flow interactions are not sufficiently defined to permit precise prediction of the pressure drop in the cup region, assumptions of the general nature of the flow field have resulted in reasonable correlations of experimental data and predictions of pressure drop. Details of the correlations are given in Appendix C.

The element geometry, based on these analyses and on J-2 injector experience, is shown in Fig. 20.

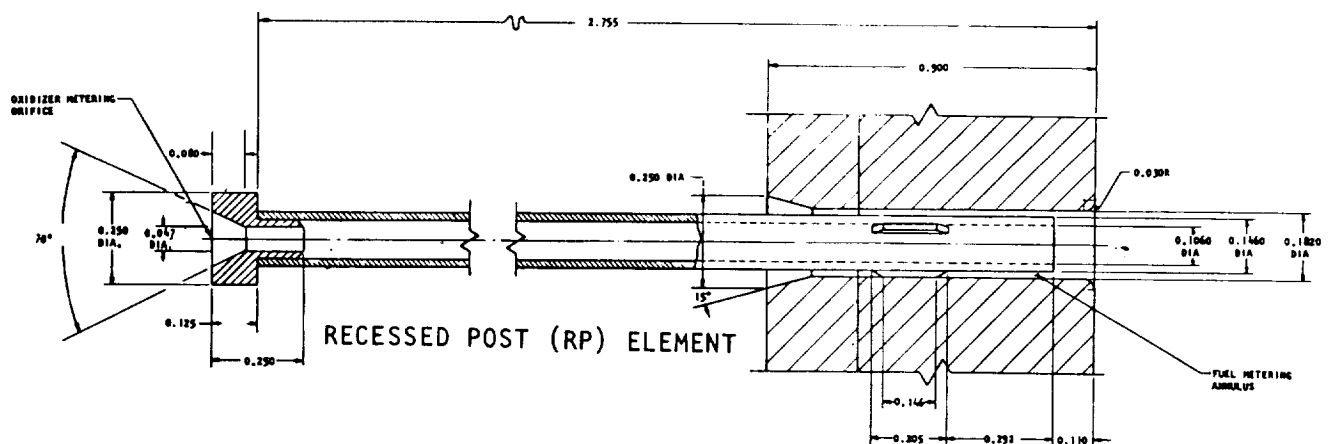


Figure 20. Recessed Post Injector Element

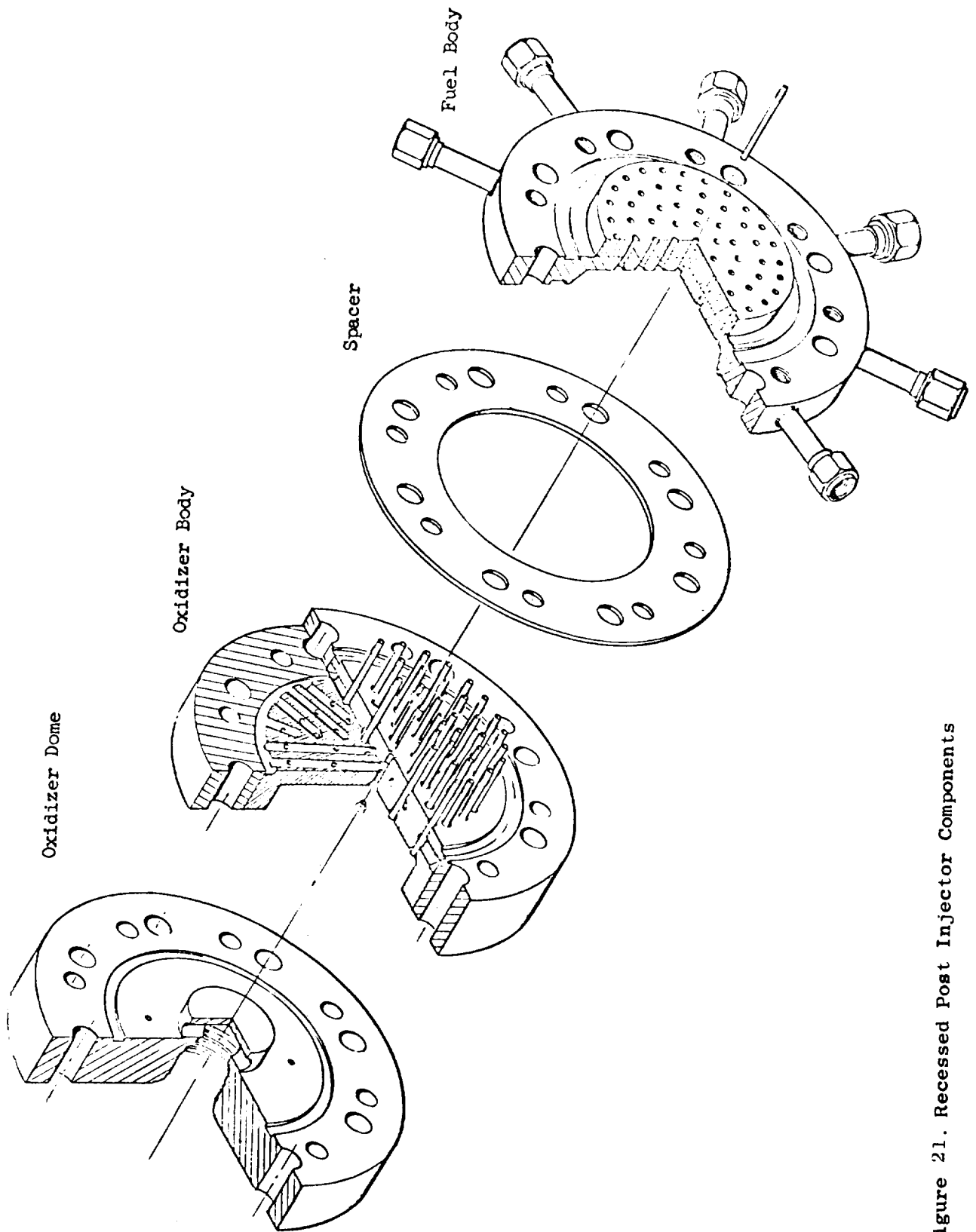
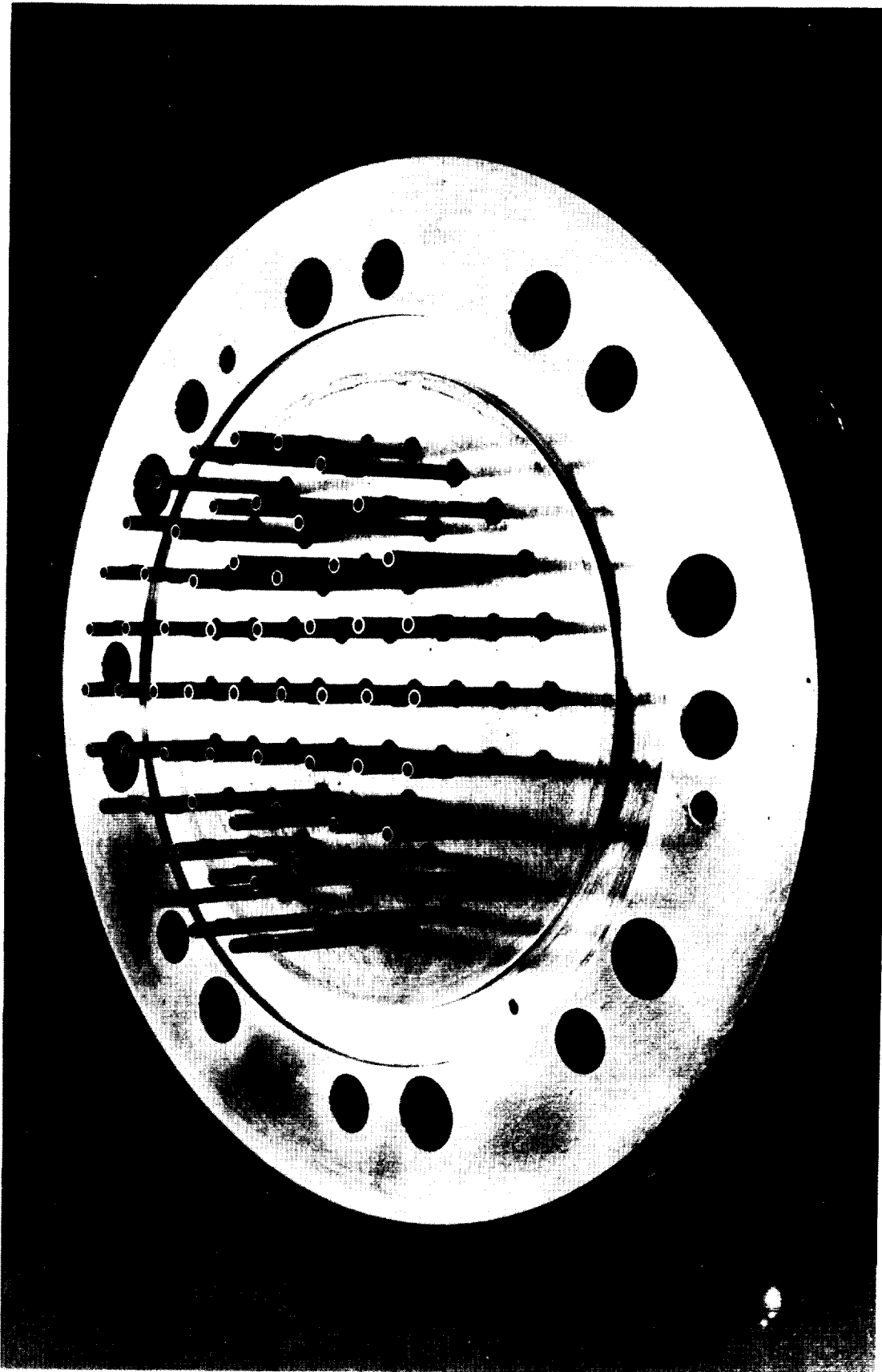


Figure 21. Recessed Post Injector Components

The components of the injector are generally similar to the other concentric injectors and are shown in Fig. 21. In fact, the FLOX dome and spacers from the other injectors are used. The oxidizer body is identical to the previous design with the exception that the FLOX tube dimensions are different. Also, the FLOX tubes each have three lands to provide concentricity (the other injectors have the lands on the copper fuel body). Putting the lands on the steel tube has two advantages: 1) The steel lands are more durable than the copper lands, 2) the lands can be located at the optimum distance from the tip of the FLOX tube (support distance vs fuel wake closure around the land) for all recess positions. CRES 304 tubes are used to closely approximate the thermal conductivity of the cast Inconel tubes planned for the flight design. The inside and outside diameters of the FLOX tubes are 0.106 and 0.146 inches (0.270 and 0.370 cm) respectively.

The fuel body is a composite structure using Inconel 625 as a structural member and copper for the face to conduct the heat back to the methane. The copper face is brazed to the Inconel body. The diameter of the fuel holes is 0.182 inches (0.461 cm) which results in an annular gap of 0.018 (0.046 cm) inches. The restrictors are pressed into the back of the FLOX body and can be easily replaced by other restrictors or hydraulic swirlers. The FLOX post recess is varied by using spacers of various thicknesses between the FLOX and fuel bodies.

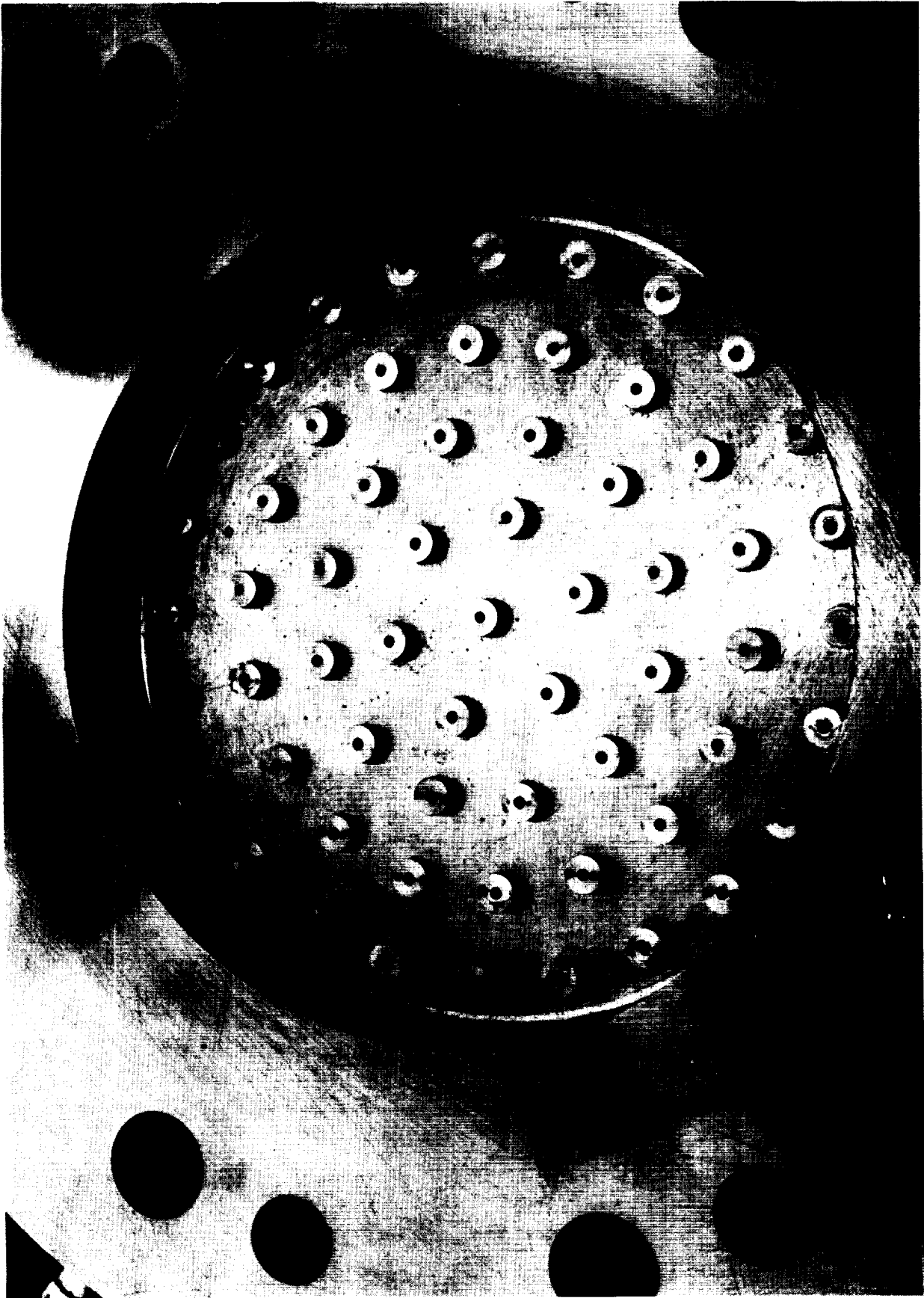
Figure 22 is a photograph of the FLOX body showing the brazed tubes. The positioning flutes can be seen on each tube. The double seal groove and the groove pressurization port can also be seen in this photo. The port in the right foreground is for pressurizing the internal cavity which prevents interpropellant mixing. The back side of the FLOX body is shown in Fig. 23, where the FLOX orifice restrictors are shown. Figure 24 is a photograph of the injector assembly, excluding the FLOX dome. The assembly is shown in the zero-recess position, i.e., with the tips of the FLOX posts flush with the face of the fuel body. Only six of the eight fuel inlet tubes were initially used as fuel inlets. The others were used to bring out the injector face thermocouple wires. Two thermocouples were brazed into the injector to provide face temperature data. One thermocouple is located near an element in the outer row. The other thermocouple is between rows where the distance between elements is greatest. All eight inlets were finally used to improve uniformity of fuel injection. Two holes were

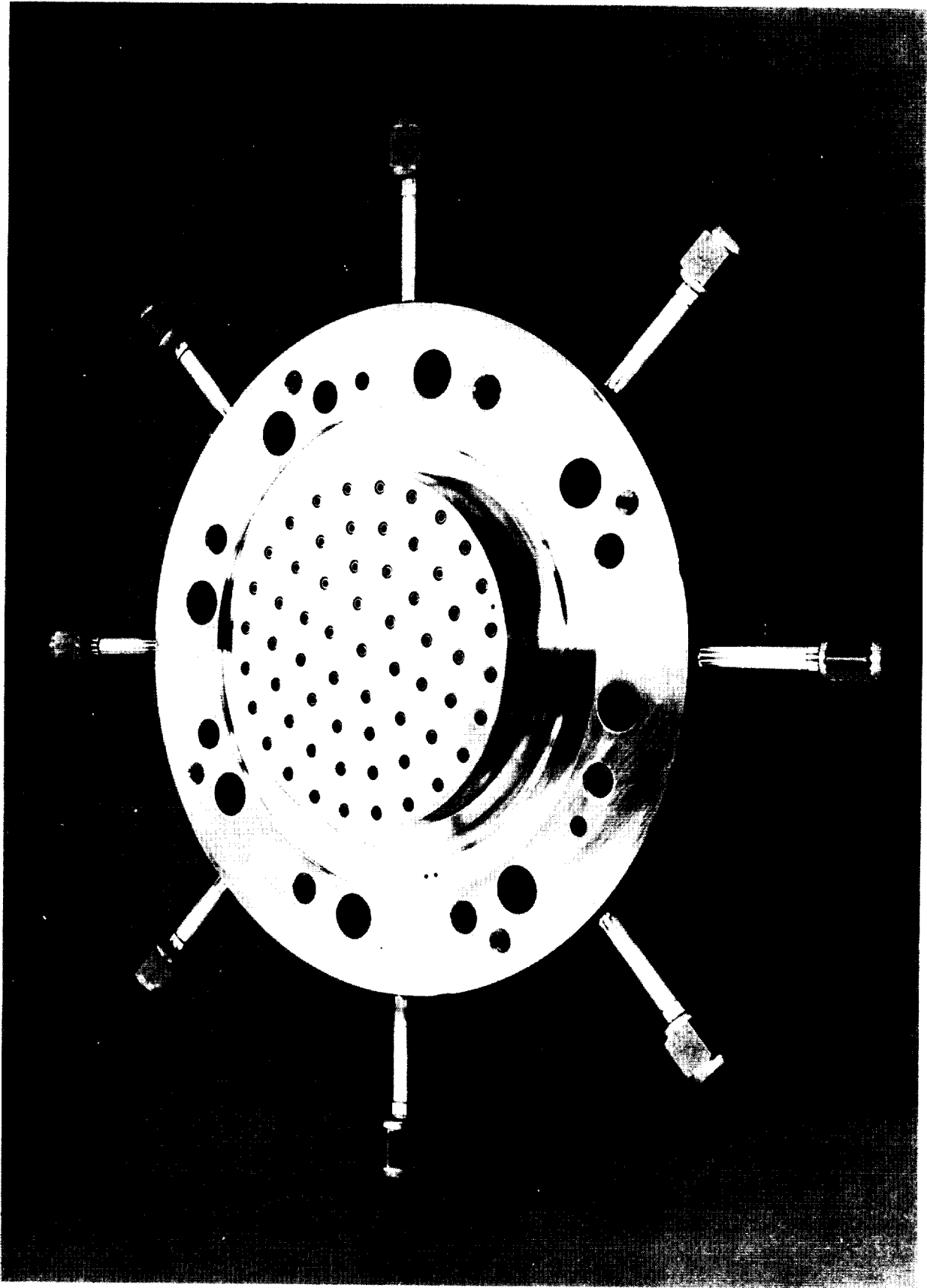


1XX42-10/22/69-CLC

Figure 22. Recessed Post Injector - Front of FLOX Body

Figure 23. Recessed Post Injector; Back of FLOX Body





1XX42-10/22/69-CLF

Figure 24. Recessed Post Injector Assembly

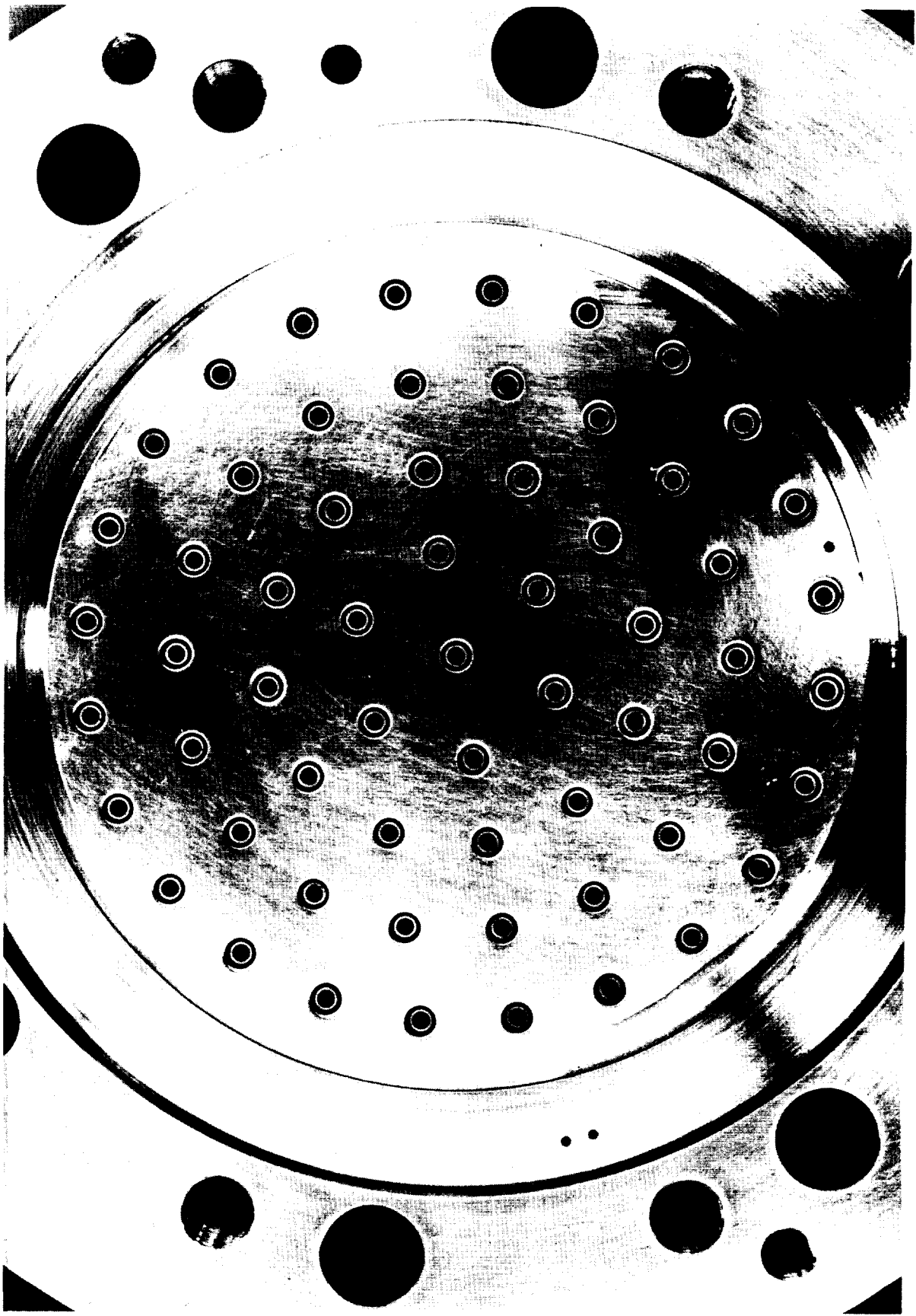
drilled to intersect each of the existing holes and for a Y-shaped entrance into the fuel manifold. The good concentricity of the elements is illustrated in the closeup view of the injector face shown in Fig. 25.

THRUST CHAMBERS

Solid, water-cooled, and regeneratively cooled hardware was designed and fabricated for the experimental program. The thrust chamber was designed in three sections: the combustion chamber which included the divergent nozzle to ϵ^{-4} ; a combustion chamber extension to increase the L^* from 30 to 50 inches (76 to 127 cm), and the nozzle which extended the area ratio to 60. The three piece construction achieves considerable operating flexibility through hardware interchangeability.

The combustion chamber is 2.6 inches (6.6cm) in diameter at the throat and 5.2 inches (13.2 cm) in diameter at the injector end. The cylindrical section of the chamber is 5.4 inches (13.7 cm) long with a total distance of 9.6 inches (24.4 cm) from the throat to the injector end. The nozzle convergence angle is 20 degrees and the divergence angle is 36 degrees. The combustion chamber extension is a 5-inch (12.7 cm) long cylinder 5.2 inches (13.2 cm) in diameter. The combustion chamber was designed and fabricated prior to final selection of the nozzle area ratio. The 36 degree divergence angle is optimum for an 80 percent length bell nozzle with an area ratio of 100 while the final design area ratio was 60. The nozzle contour was optimized subject to this constraint as discussed in Appendix D. The resultant nozzle had a predicted efficiency of approximately 0.8 percent less than that for an optimum 80 percent length bell nozzle.

The advanced fabrication technique utilized to construct the regeneratively cooled chamber was to machine passages in an electroformed chamber liner, and electroform the closeout (outer wall) for the chamber. This method was selected after considering other techniques such as welding, brazing, spinning, etching, powder metallurgy, and casting. The electroforming process results in a chamber which has a contiguous and smooth wall which



1XX42-10/22-69-C1D

Figure 25. Recessed Post Injector Face

is beneficial with respect to potential hot gas leakage problems and heat transfer. Contour and channel design changes can be made with relative simplicity and cost compared to chambers using conventional tube bundles.

Solid and Water-Cooled Chambers

Combustion Chamber. A solid wall thrust chamber was available from a previous program and was modified slightly for the injector checkout tests. This chamber was made in two parts: 1) a cylindrical section with a steel shell and copper liner and, 2) a throat section with a steel shell and graphite liner.

A water-cooled thrust chamber was designed to permit extended duration tests at chamber pressures as high as 1000 psia (690 N/cm^2) and to obtain an accurate profile of the heat fluxes throughout the chamber. The heat flux distribution data was required to verify the analyses of Task I and to determine the heat transfer characteristics of the injectors. In order to accomplish these goals the hardware was designed with circumferential water coolant grooves having individual inlets and outlets. A sectioned view of the combustion chamber is shown in Figure 26.

The thermal design studies were based on the results of Task 1 analyses assuming no combustion-side carbon layer. The high heat fluxes in the combustion chamber resulted in the selection of copper for the combustion-side wall material. These thermal design studies, described in Appendix E, resulted in a combustion chamber liner fabricated by machining 22 circumferential grooves into an OFHC billet to form a combustion side wall thickness of 0.125 inches (0.28 cm). The grooves were filled with wax and nickel was electroformed on the outer surface to close out the channels and provide structural material to resist forces generated by chamber pressure and coolant water pressure. Previous company sponsored research had indicated that excellent copper-nickel bonds would be obtained in this manner. Figure 27 is a photograph of the copper liner after it had been grooved and waxed.

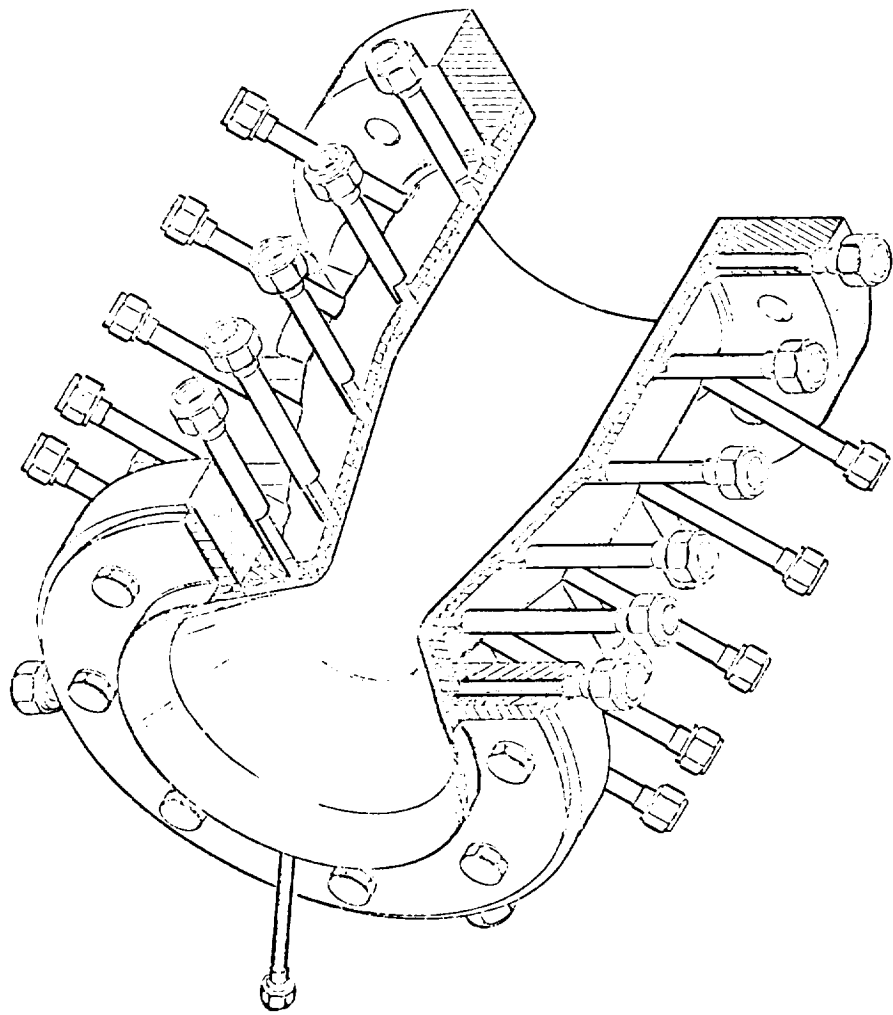


Figure 26 . Water-Cooled Thrust Chamber



1XW32-4/9/68-CIA

Figure 27. Copper Liner for Water-Cooled Thrust Chamber

Electroforming over the annular grooves presents a condition not encountered on any of the previously-fabricated thrust chambers with axial coolant channels. The initial electroforming is applied at low temperature to establish a strong copper-nickel bond. The temperature is subsequently increased to obtain reasonably rapid deposition rates. The ends of the channels are left open, in the axially oriented designs, to provide for expansion of the wax when the temperature of the bath is raised. It was, therefore, not surprising when samples made by electroforming over a closed-end trough ruptured when the bath temperature was increased, while other samples electroformed at the initial temperature only and examined microscopically showed good bonds.

Three methods were successfully used to prevent rupture of the initial layer. 1) Plastic tubing was laid in the grooves before waxing and dissolved after the wax was removed. 2) Plastic tubing was laid in the grooves before waxing with the ends exposed. After waxing, hot water was flushed through the tubes which melted the wax at the tube surface. The tubes were pulled out and the holes in the wax were patched. 3) A new wax having a very low coefficient of expansion and excellent machining properties was used. A single curved panel having the same curvature profile as the thrust chamber in the throat region was electroformed to determine the degree of non-uniformity of deposition. The non-uniformity is caused by electric field variations resulting from the variable distance between the nickel anode and the surface of the chamber. The sample panel resulted in approximately three times the deposition rate at the $\epsilon = 4$ point as at the throat. The deposition rate profile was used to design selective shielding to accomplish a more uniform deposition on the actual thrust chamber.

The water-cooled thrust chamber utilizes an electroformed nickel structural shell with 321 stainless steel flanges electron beam welded to each end. Strength data were not available for the nickel-to-stainless steel weld or for the weld-affected zone of the nickel shell. The joint design and shell thickness were, therefore, conservatively sized based on annealed Nickel 200 properties. A design yield strength of 13 ksi (9kN/cm^2) was used. To verify the structural integrity of the joint, samples were fabricated which simulate

the thrust chamber configuration as shown in Fig. 28. The sample was conservative in that the actual flange joint has a second weld on the opposite side of the flange. Each sample consisted of a strip of electroformed Nickel, 0.200 inches thick, electron beam welded between two 321 stainless steel end pieces. Eight samples were tested (16 joints).

Two weld penetration depths were tested. A 0.5 (1.27 cm) inch depth was designed to produce failure in the weld affected zone of the nickel sheet. The shallower, 0.3 inch (0.76 cm) weld was designed to minimize the weld affected zone in the nickel while still providing an adequate weld strength. Tests were run at room temperature and 550 F. The 550F tests simulate the average working temperature of the nickel shell. The test results are shown in Table 8. The 0.5 inch (1.27 cm) weld joint exhibited higher ultimate strength than the 0.3 inch (0.76 cm) weld. The 0.5 inch (1.27 cm) weld joint also has acceptable yield strength at the working temperature and was used on the thrust chamber.

The flanges, coolant water tubes, and chamber pressure instrumentation bosses were welded to the chamber after electroforming and removal of wax. The chamber, after electroforming and machining, is shown in Fig. 29 with other parts of the assembly. The assembly of the chamber and flanges, including the split rings for the aft flange, is shown in Fig. 30. Figure 31 is a photograph of the final assembly showing the water tubes and chamber pressure instrumentation ports. Two water-cooled chambers were completed. The second chamber did not have an aft flange because it was designed for sea level testing only without a nozzle extension. A cylindrical water-cooled extension was fabricated for the combustion chamber to increase the L^* from 30 to 50 inches (76 to 127 cm). The electroformed extension is shown in Fig. 32 prior to assembly. The L^* of the chamber was later reduced from 30 to 22 inches (76 to 55 cm) by cutting a section of the forward end and welding on a new flange. A short water-cooled nozzle extension ($\epsilon = 6$) was designed to provide a relatively sharp-edged exit to minimize base pressure effects on thrust measurements during sea level operation. This extension, shown in Fig. 33, was machined from OFHC copper.

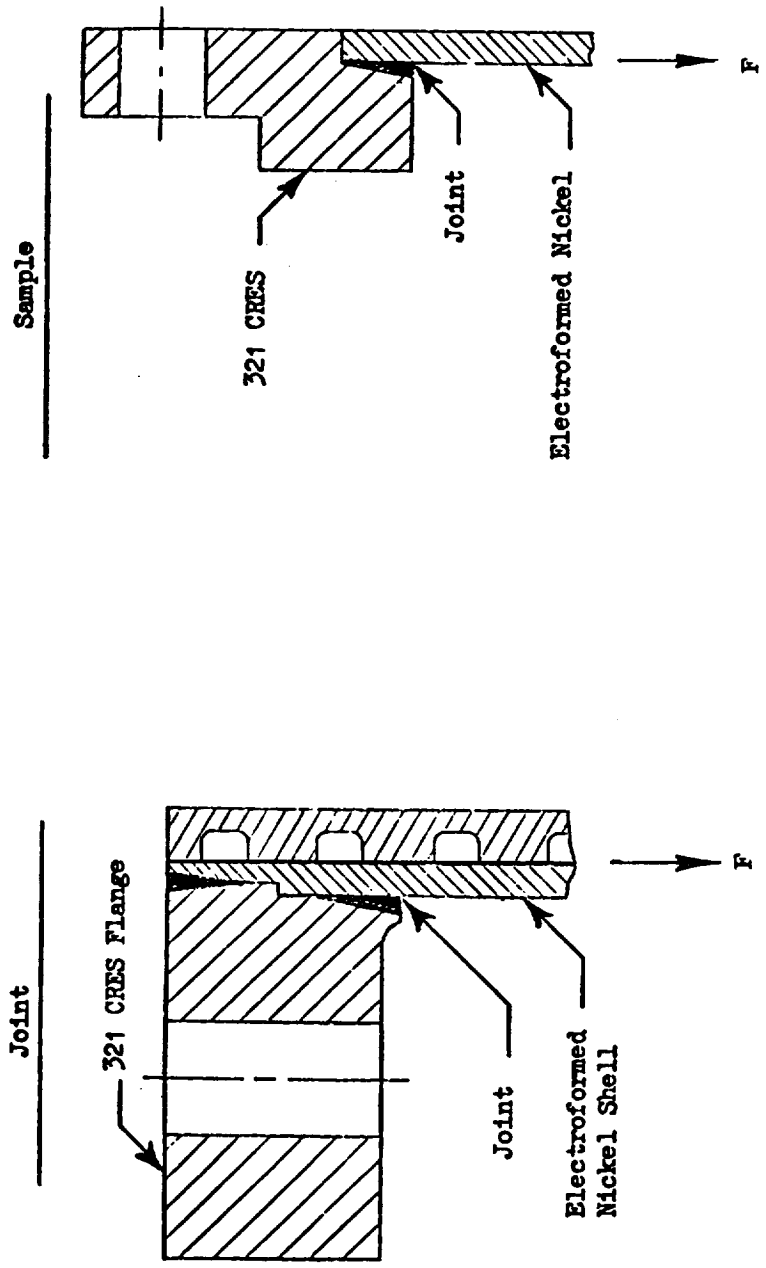


Figure 28 . Electron Beam Weld Sample and Actual Joint

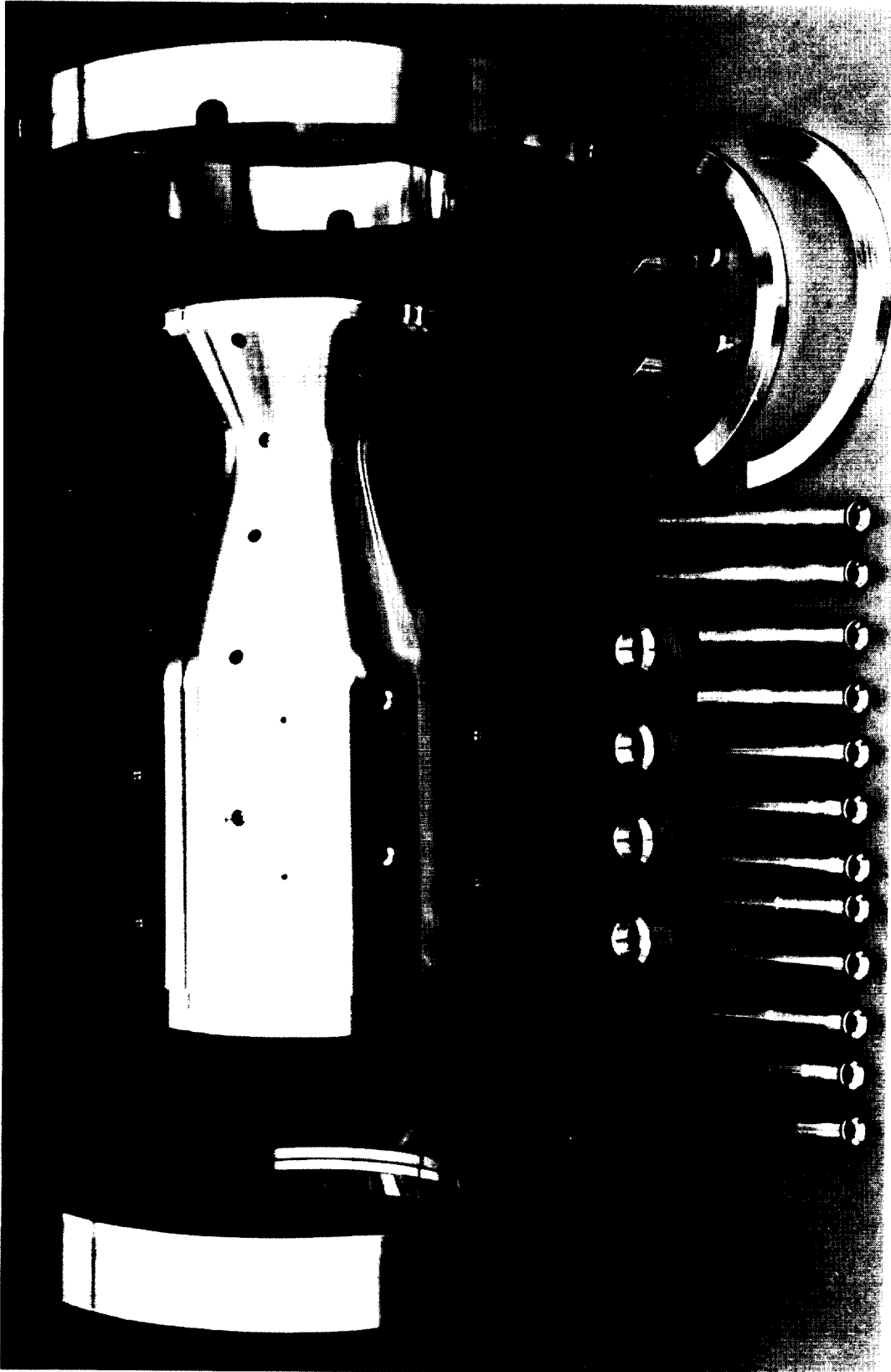
TABLE 7

WELD-SAMPLE TEST RESULTS

Weld Penetration, inches	cm	Test Temperature		0.2 Percent Yield	UTS,		Elongation, percent	Failure Mode	
		F	K		ksi	N/cm ²			
0.5	1.3		R.T.	23	15,900	55.7	38,400	*	Nickel
0.5	1.3		R.T.	46	31,700	57.1	39,400	**	Lap Shear
0.5	1.3		R.T.	30	20,700	64.8	94,000	21	Nickel
0.5	1.3	550	561	18	12,400	38.6	26,600	52	Nickel
0.5	1.3	550	561	17	11,700	40.2	27,700	30	Nickel
0.3	0.76		R.T.			29.2	20,100	**	Lap Shear
0.3	0.76		R.T.	23	15,900	32.6	22,500	**	Lap Shear
0.3	0.76		R.T.	27	18,600	57.6	39,700	*	Nickel

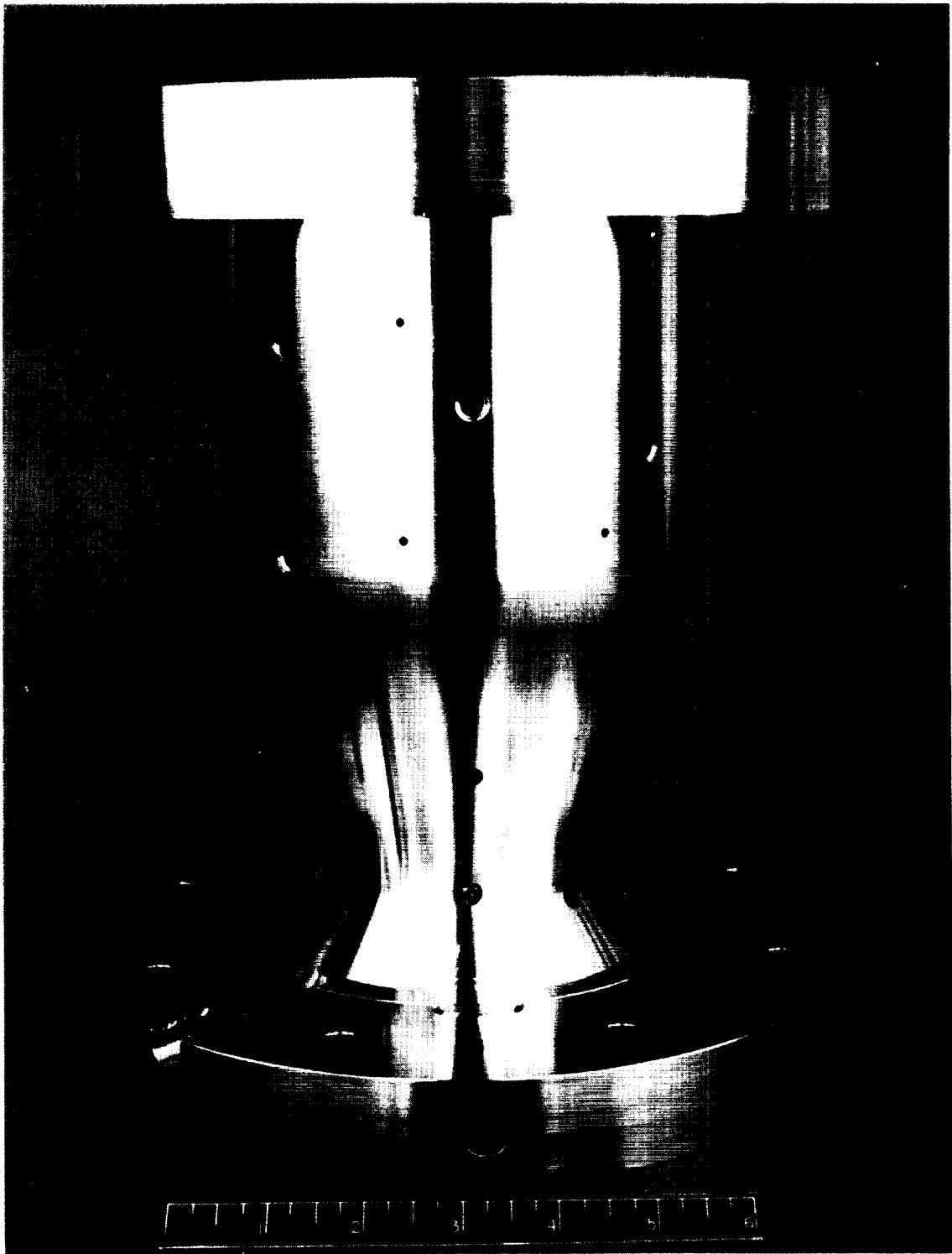
* Too much bending to measure elongation.

** Lap Shear failure.



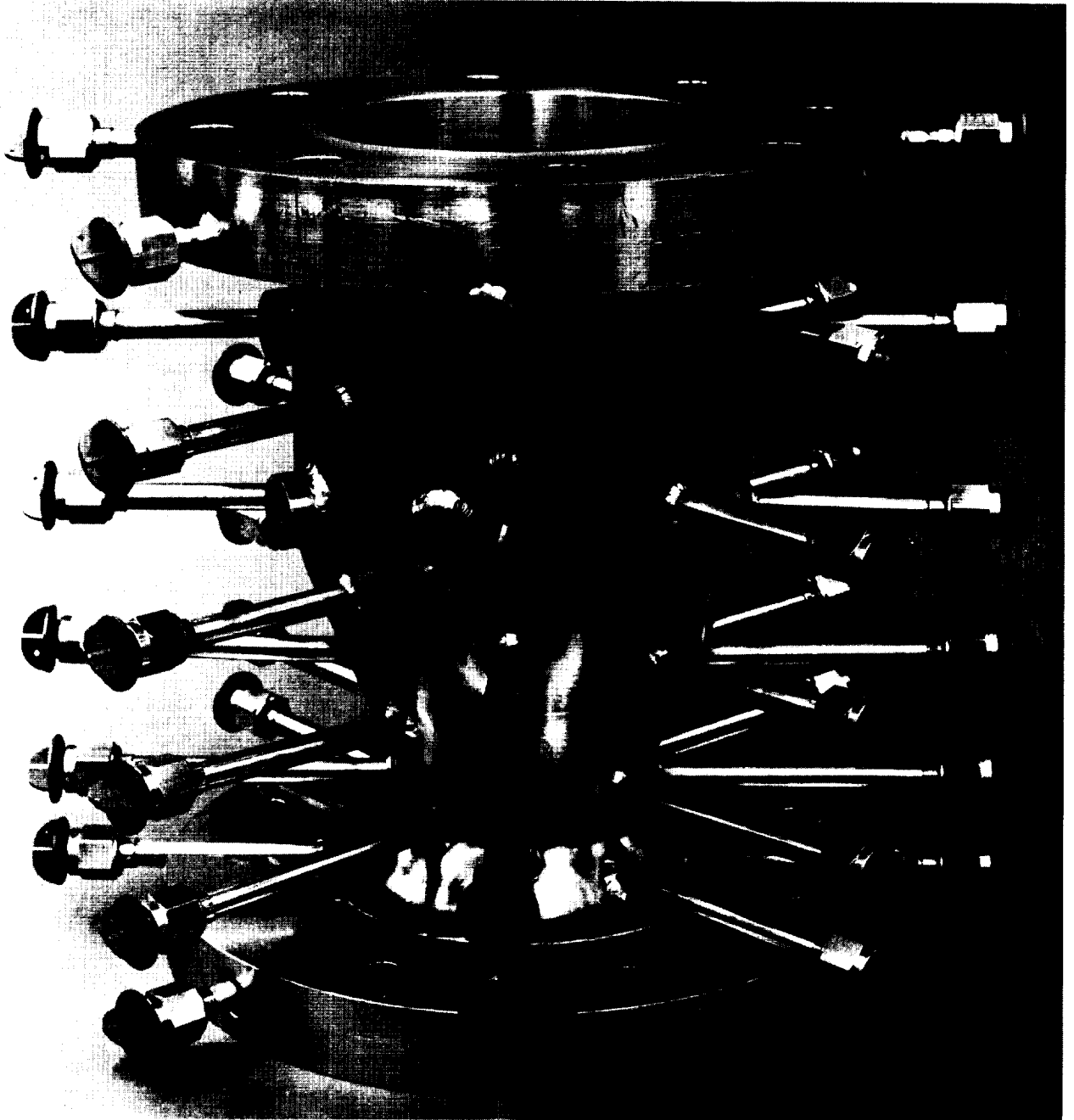
1XW32-10/23/68-C2A

Figure 29 Components of Water Cooled Thrust Chamber



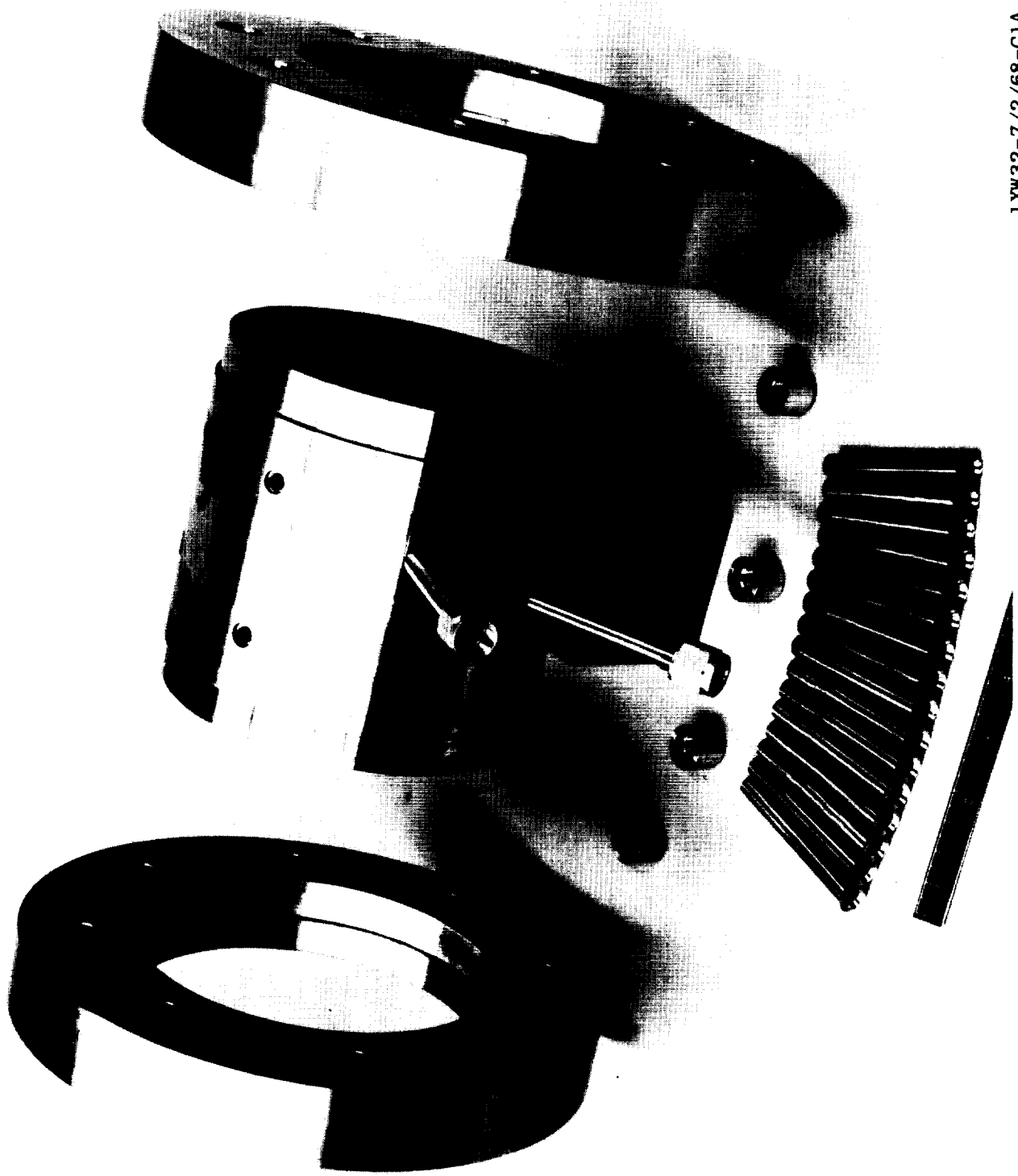
1XW32-10/23/68-C2D

Figure 30. Pre-Weld Assembly of Water Cooled Thrust Chamber



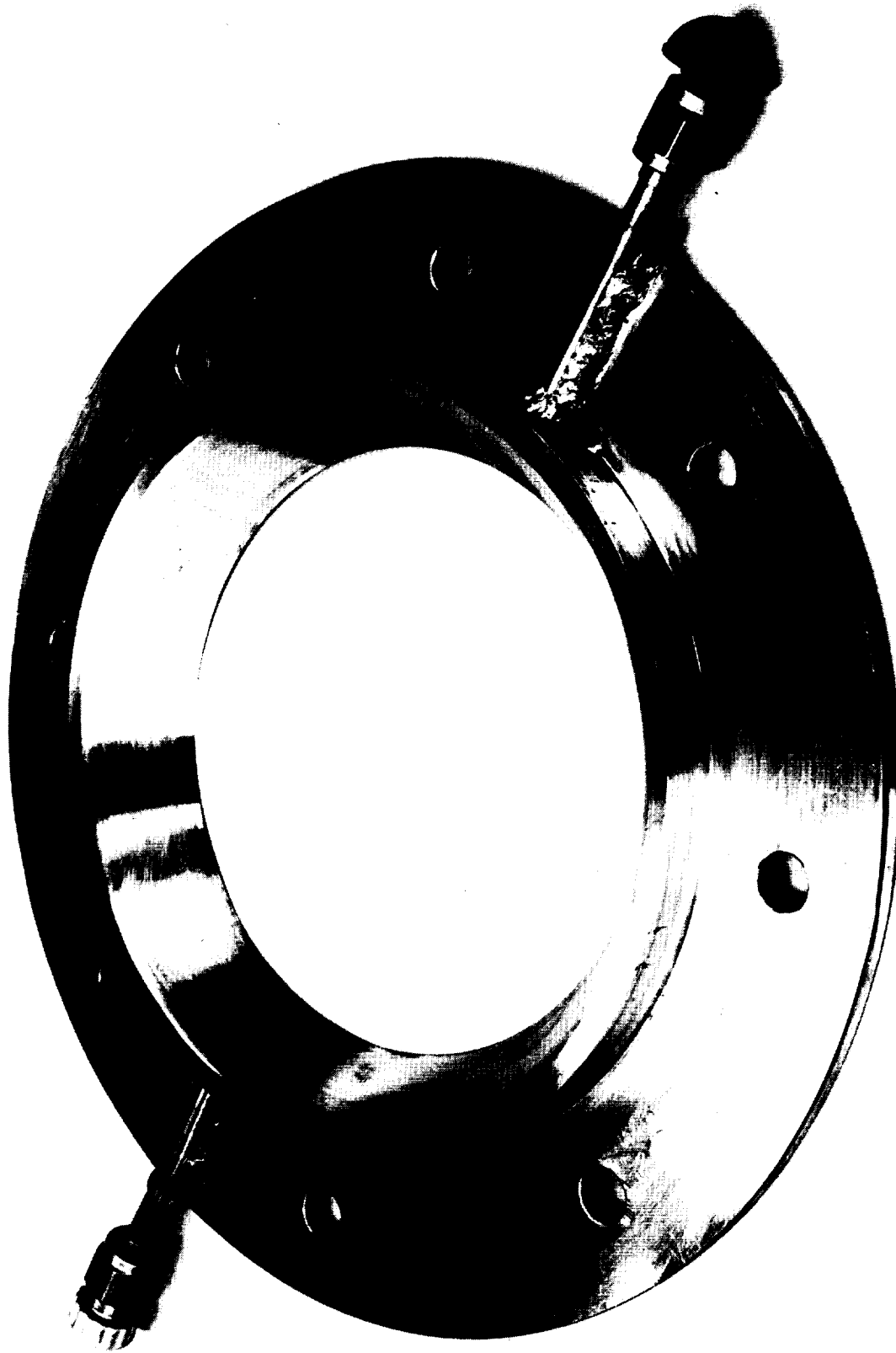
1XW32-10/3/68-C1C

Figure 31. Final Assembly of Water Cooled Thrust Chamber



1XW32-7/2/68-C1A

Figure 32. Electroformed Thrust Chamber Extension Before Assembly



LXW32-7/2-68-C1C

Figure 33. Water Cooled Nozzle Extension

Nozzles. Solid and water-cooled nozzles were designed to extend the area ratio from 4 to 60. Heat fluxes are sufficiently low in this region to permit use of nickel for both nozzles. The thickness of the solid wall nozzle determines the allowable operating duration as shown in Figs. 34 and 35 for chamber pressures of 500 and 1000 psia (345 and 690 N/cm^2), respectively. The 0.375 inch (0.95 cm) thick nozzle could be operated for approximately 3 seconds at 1000 psia (690 N/cm^2) or 6 seconds at 500 psia (345 N/cm^2). This is somewhat conservative because it ignores the cooling effect of the flange which extends from $\epsilon = 4$ to $\epsilon = 7$. At $\epsilon = 7$ the combustion-side temperature of a 0.250 inch (0.63 cm) thick wall would be 1550F (1056K) after 3 seconds operation at 1000 psia (690 N/cm^2). Thus the nozzle thickness was 0.250 inches (0.63cm) except under the flange where the thickness was 0.375 inches (0.95 cm) to reduce fabrication time and nozzle weight. Pressure taps were provided near the nozzle exit and at the exit flange to verify full flow conditions.

The dimensions of the channels and wall thickness of the water-cooled nozzle were based on tradeoffs between stress, instrumentation requirements, facility flow and pressure capabilities, operational ease, and fabrication simplicity. Nominal channel height and combustion-side wall thickness of 0.100 inches (0.254 cm) were selected based on stress and ease of fabrication. The channel widths (dimension along X-axis) and land widths were determined as described in Appendix E. A total of 28 channels was established. The 16 channels at low area ratio were 0.250 inches (0.63 cm) wide; the remaining channels were 0.500 (1.27cm) inches wide. Figure 36 is a drawing of the water-cooled nozzle.

Schedules and costs were reviewed for a decision on the initial fabrication technique to be used for the three high area ratio nozzle extensions (solid, water-cooled, regeneratively cooled). The candidate techniques were spinning and electroforming. The former method would consist of rolling and welding a sheet of nickel 200 into a cone and then spinning it to the required contour. The alternative method was to electroform nickel onto a mandrel of suitable contour. Either of these processes would result in the final solid-wall nozzle (except for flanges, instrumentation, etc.). The water-

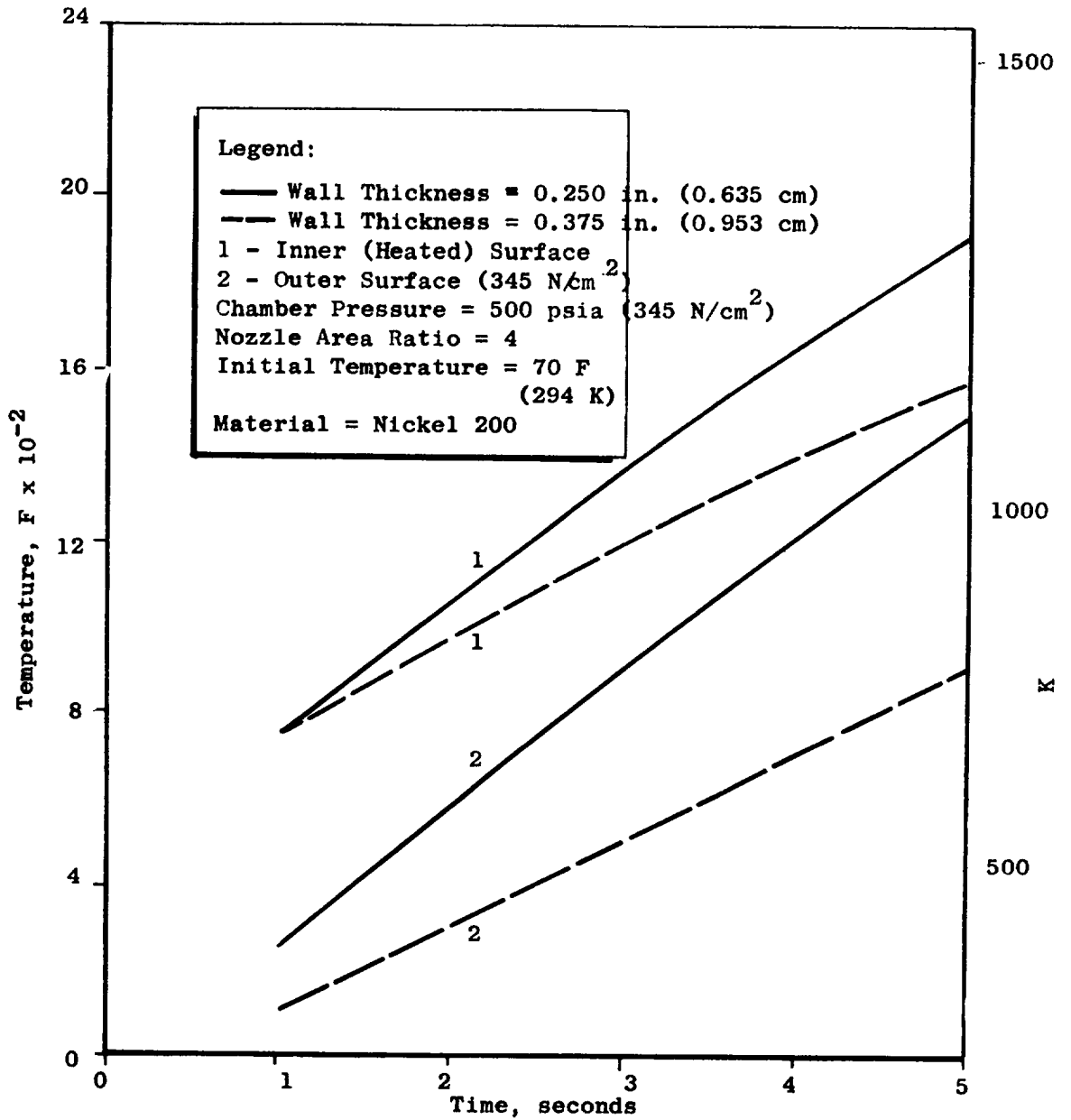


Figure 34. Uncooled Nozzle Wall Temperature as a Function of Time
 $P_c = 500 \text{ psia } (345 \text{ N/cm}^2)$

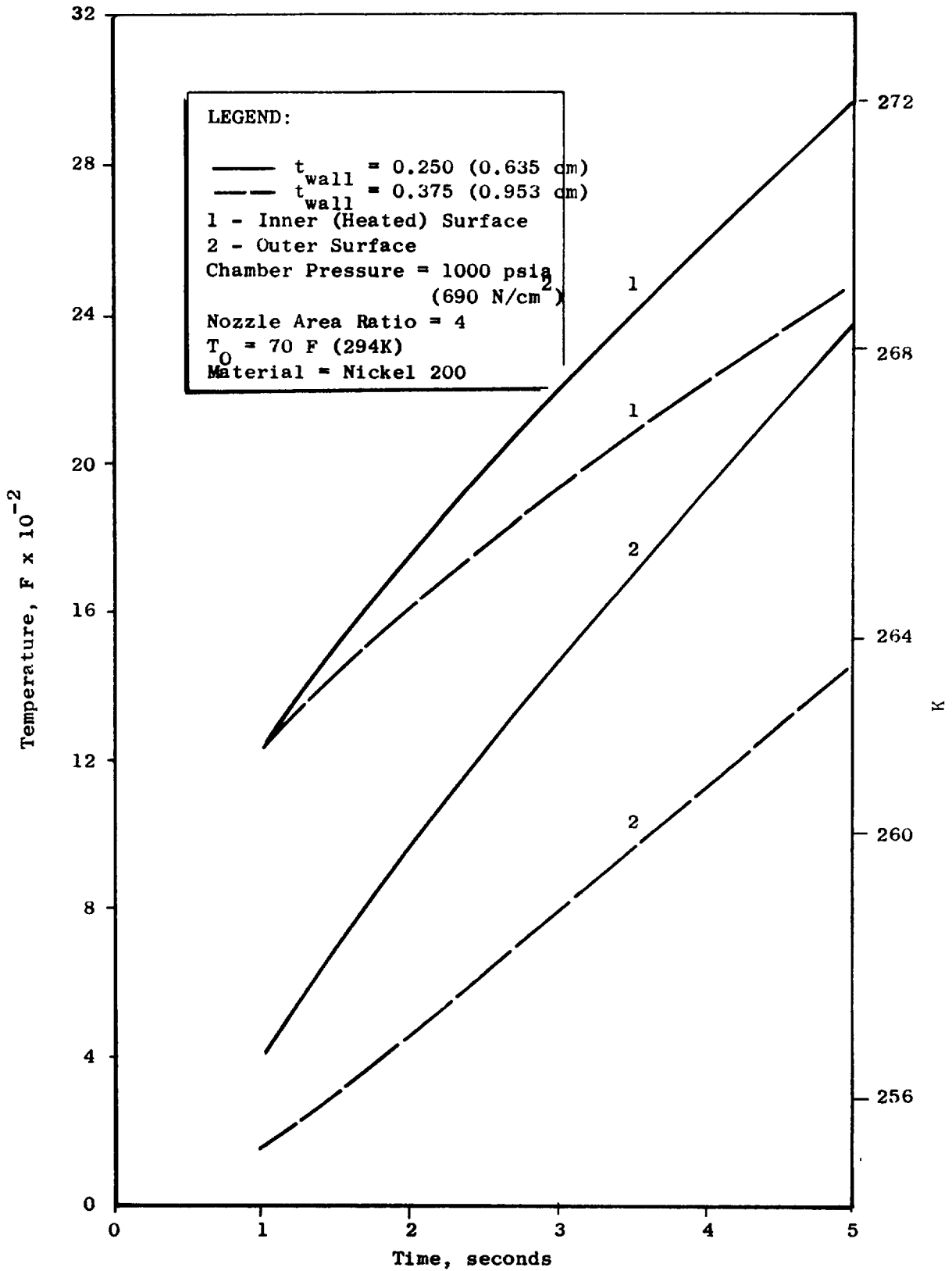


Figure 35 . Uncooled Nozzle Wall Temperature as a Function of Time, $P_c = 1000$ psia (690 N/cm²).

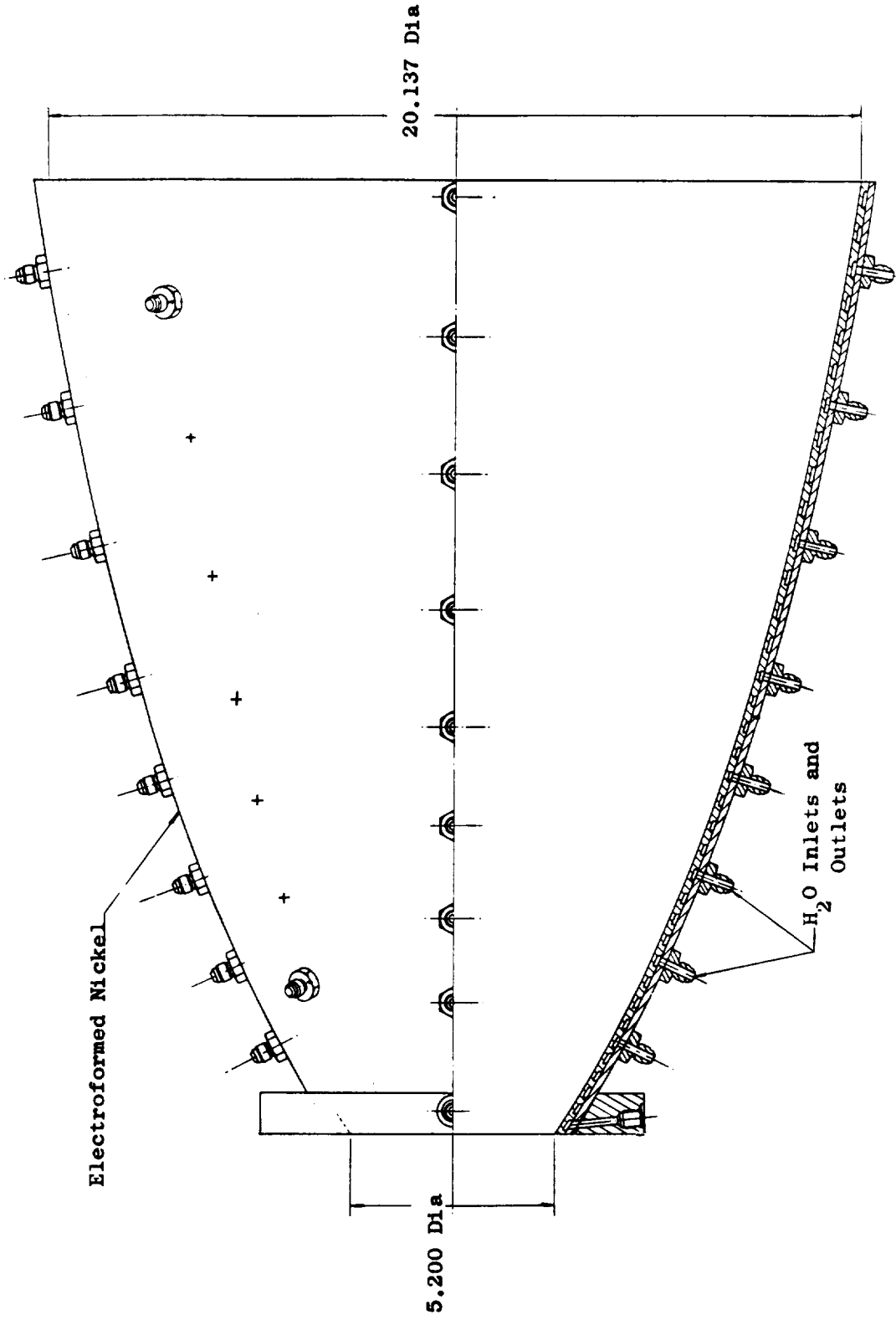


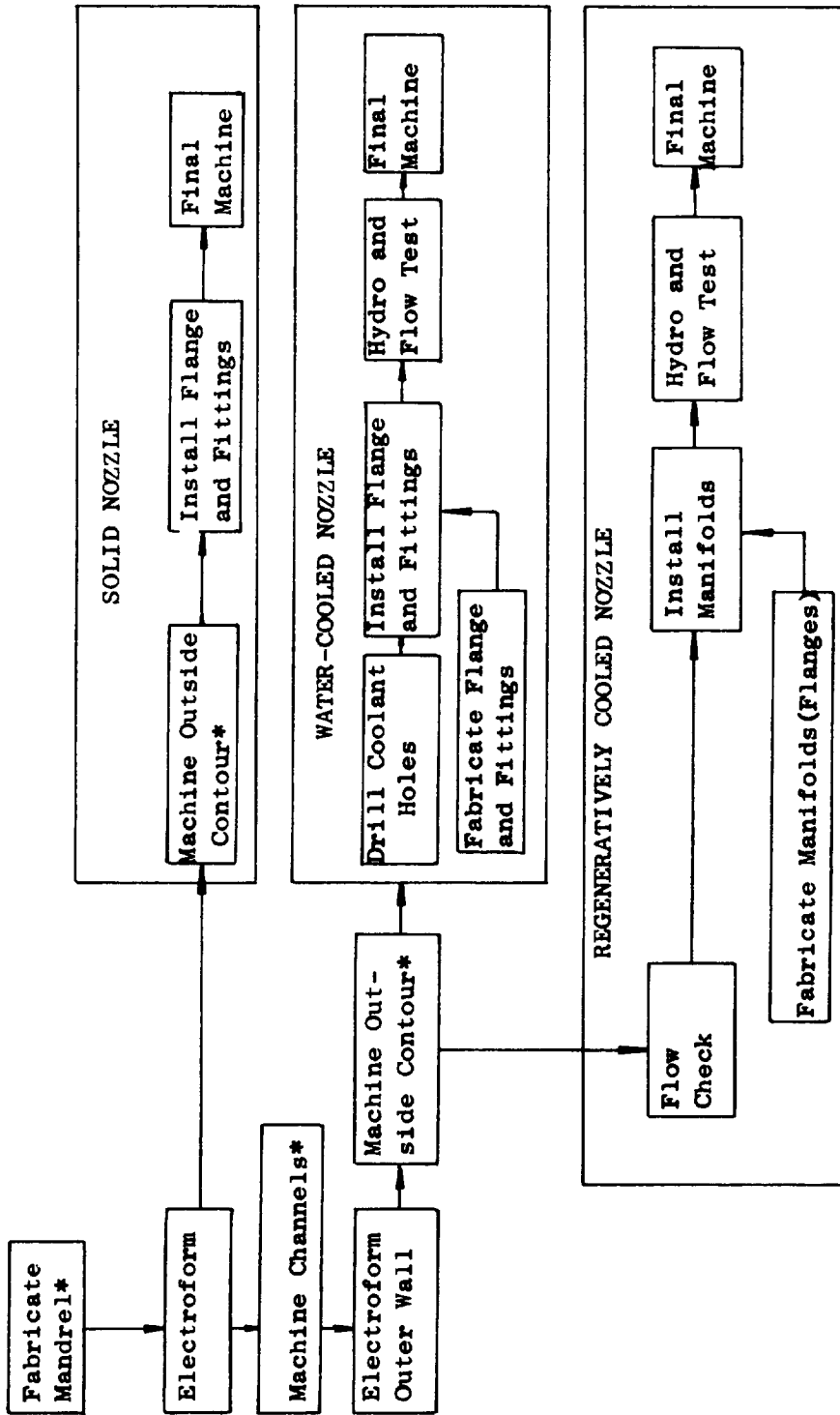
Figure 36 . Water-Cooled Nozzle

cooled and regenerative-cooled nozzles would then be grooved to form the coolant passages. The outside closure of the grooves in both cooled nozzles would be made by electroforming nickel over the outside contour after filling the grooves with wax.

The electroforming costs were slightly lower than the spinning costs. Although the actual fabrication time for the spinning process was slightly shorter than for the electroforming process, the spinning vendor's start date (due to backlog) would result in later delivery dates than the electroforming process. These factors, as well as the advantage of using a single process instead of two different processes for each nozzle, led to the selection of electroforming as the means of fabricating the inner shells of the water-cooled and regeneratively cooled nozzles as well as the solid wall nozzle.

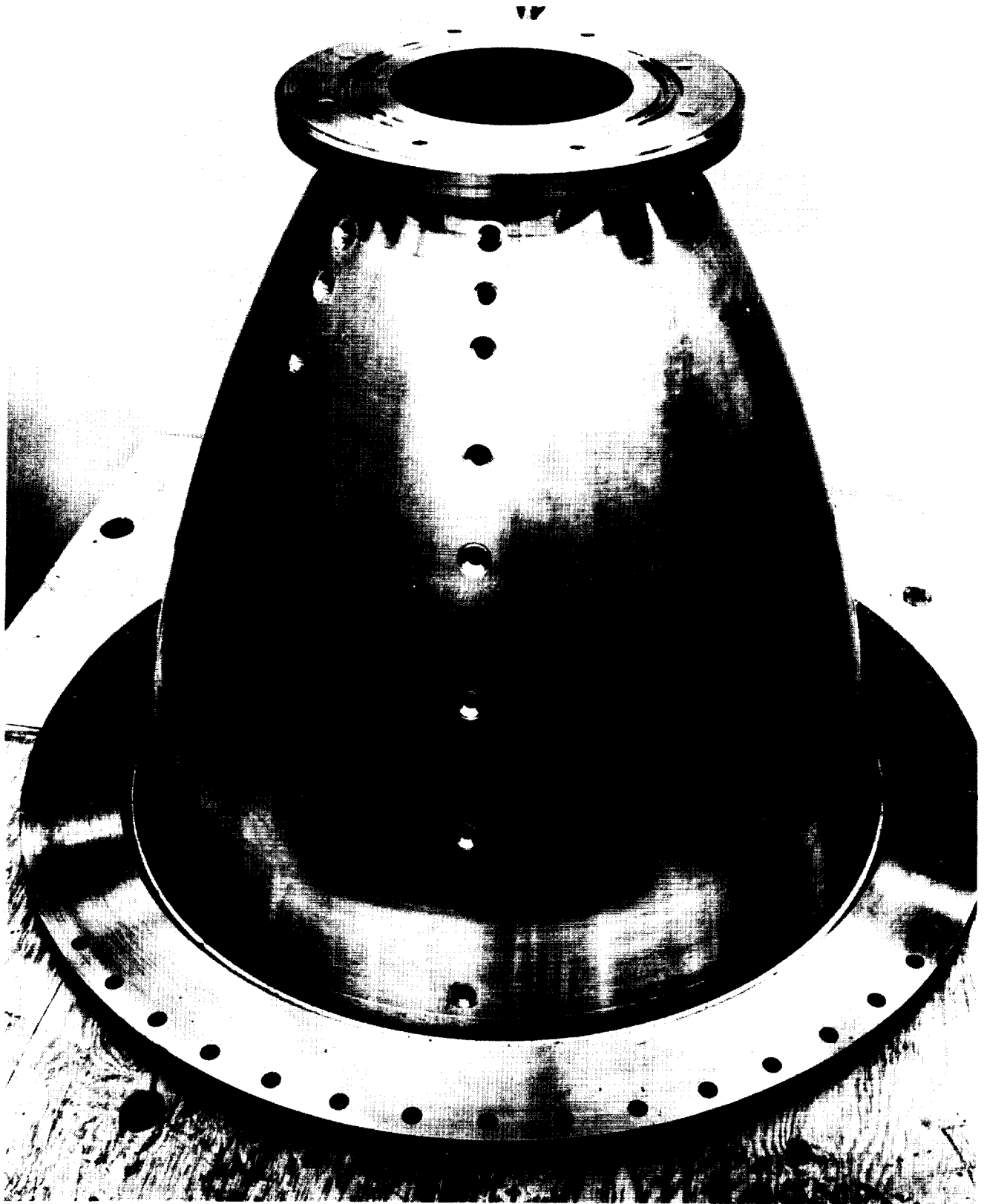
The step-by-step fabrication processes for the solid and water-cooled nozzles, are shown in Fig. 37. The same electroforming mandrel could be used for all nozzles. However, since this mandrel also serves as a machining mandrel, schedule constraints required that two mandrels be made. The initial electroforming operation provided the nickel material for the hot gas wall and the lands of the cooled nozzle. Only one electroforming operation was required for the solid wall nozzle.

After electroforming, the solid nozzle required machining of the outside contour and attachment of fittings and flanges. The completed solid wall nozzle is shown in Fig. 38. The two rows of ports shown in the figures are for installation of thermocouples. Constant width and depth circumferential channels were machined into the initial electroformed nickel for the water-cooled nozzle. After machining, the channels were filled with wax and the final electroform accomplished. Fabrication of the water-cooled nozzle was stopped at this point because of schedule requirements. Analysis indicated that, although operating durations would be limited, satisfactory nozzle heat transfer data could be obtained with the solid wall nozzle.



*Accurate Dimensional
Check and Documentation

Figure 37 . Thrust Chamber and Nozzle Fabrication Flow Chart



1XW32-1/10/69-C1C

Figure 38. Solid Electroformed Nozzle

Regeneratively Cooled Thrust Chamber

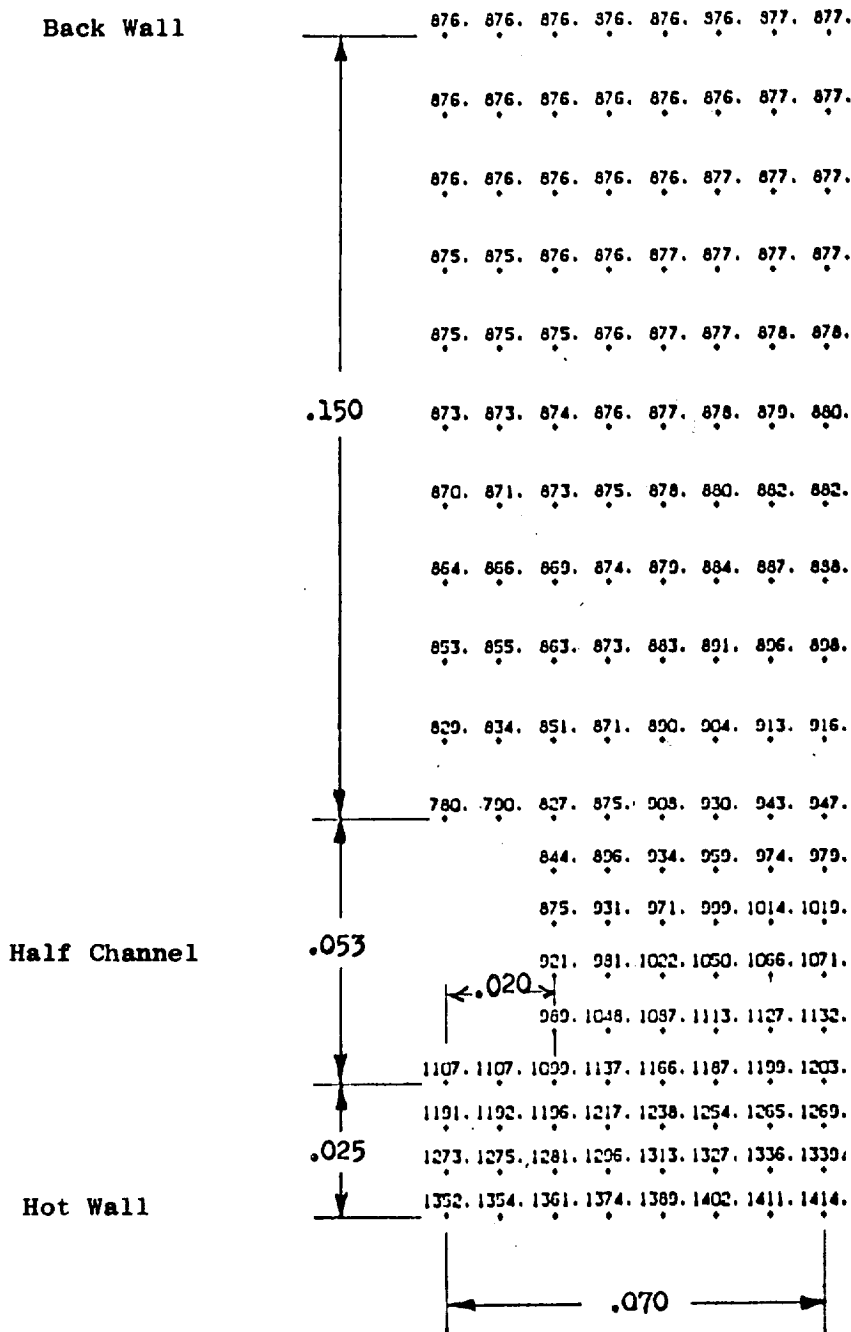
A single pass counterflow regeneratively cooled thrust chamber was designed to operate between chamber pressures of 500 and 800 psia (345 and 553 N/cm²). A two piece nickel chamber was designed which separates at $\epsilon = 4$ and is completely electroformed. The heat flux profile in the combustion chamber was based on early water-cooled test data with the triplet injector. Subsequent water-cooled chamber tests at higher chamber pressures and propellant mixture ratios with the concentric injector resulted in higher heat fluxes in the convergent and throat sections and lower heat fluxes in the cylindrical section than anticipated from the early triplet injector tests. The coolant-side heat transfer coefficients were calculated by the method described in Appendix F.

Two-dimensional heat transfer analyses were conducted for the start-of-convergence and throat regions. The results of two-dimensional analyses agreed well with those of one-dimensional analyses predicting the combustion-side wall temperatures at the throat. Two-dimensional wall temperatures at the start of convergence were considerably higher than the one-dimensional values because of the greater land width at this location. A printout of the results of a typical two-dimensional calculation is shown in Fig.39.

Figure 40 is a drawing of the combustion chamber. The L^* of the chamber is 30 inches (76 cm) but the insertion depth of the concentric element injector reduces the L^* to approximately 28 inches (71 cm). The injector-to-throat distance is 9.1 inches (23.1 cm). The thickness of the combustion-side wall in the combustion chamber is 0.025 inches (0.063 cm). The 120 channels are 0.040 inches (0.10cm) wide and of variable height. The height tapers linearly from 0.150 inches (3.75 cm) at $\epsilon = 4$ to 0.034 inches (0.086 cm) at the throat and then tapers linearly to 0.053 inches (0.134 cm) at the cylindrical section. This height is maintained in the cylindrical section until near the injector end where the height flares to 0.069 inches (0.175 cm) to reduce exit pressure losses.

Design of the regeneratively cooled nozzle coolant circuit involves a tradeoff between weight, pressure drop, stress, and fabrication ease. A parametric study was undertaken to determine the effects of channel

PC = 500 MR = 5.25, Start of Convergence



ANALYSIS CONDITIONS

$T_{AW} = 7078 \text{ F}$

$h_g = 0.001387 \frac{\text{Btu}}{\text{in}^2 \text{ sec F}}$

$(Q/A = 8.2 \frac{\text{Btu}}{\text{in}^2 \text{ sec}})$

$T_B = 472 \text{ F}$

$h_c = 0.0133 \frac{\text{Btu}}{\text{in}^2 \text{ sec F}}$

Figure 39 . Temperature Distribution in Nickel Thrust Chamber Wall

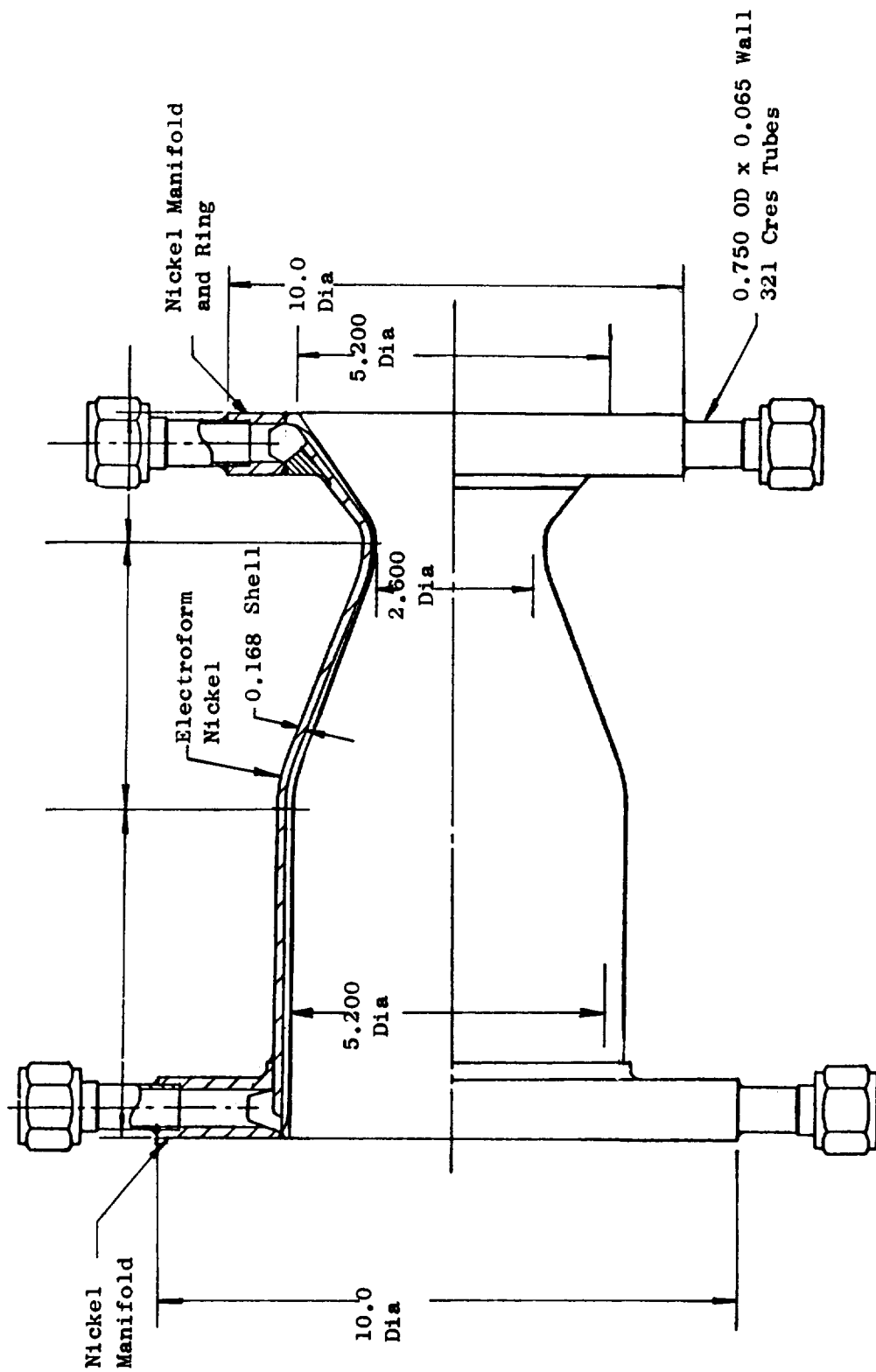


Figure 40. . Electroformed Thrust Chamber

geometry and numbers. The heat flux profile in the nozzle was analytically determined, based on solution of boundary layer equations and was subsequently verified by testing with the solid wall nozzle. A combustion-side wall thickness of 0.040 inches (0.10 cm) was used for all cases. The results are summarized in Table 9. The design with 180 doubly tapered channels had the lowest pressure drop and an acceptable wall temperature at the attached point at $\epsilon = 4$. These temperatures were kept low because the heat flux profile had not yet been experimentally verified at this time. Doubling the analytical heat flux profile resulted in wall temperatures which were still acceptable as shown in Fig. 41. The pressure drop increased from 30 to 50 psi (21 to 35 N/cm²) when the channel height taper was eliminated and to 90 psi (62 N/cm²) when the number of channels was reduced from 180 to 115 and a constant cross section channel used. By keeping the channel width constant at 0.093 inches (0.236 cm) (a standard cutter width) and investigating various channel heights, the effects on wall temperatures and pressure drops were determined. The pressure drop could be reduced from 90 to 38 psi (62 to 26 N/cm²) by increasing the channel height from 0.050 to 0.070 inches (0.127 to 0.178 cm). However, the increased fabrication time for electroforming and machining did not appear to favor a 50 psi (35 N/cm²) saving in pressure drop compared to an approximately 650 psi (450 N/cm²) total system drop.

Therefore, 115 channels which were 0.093 inches (0.236 cm) wide by 0.050 inches (0.127 cm) high were selected for the nozzle design. An outer wall thickness of 0.250 inches (0.63 cm) was required because of the conditions imposed by testing with atmospheric pressure on the outside of the nozzle.

A two-dimensional heat transfer analysis of the constant width channel configuration at the exit plane indicated that wall temperatures were within 100F (56K) of the one-dimensional values. This result is due to the very low heat fluxes involved ($Q/A \approx 0.6$ Btu/in²-sec) combined with the high conductivity of the nickel. Furthermore, wall temperatures are very low and non-critical at this point.

TABLE 8

SUMMARY OF RESULTS OF CHANNEL GEOMETRY VARIATION STUDY

Channel Width		Channel Height		Pressure Drop		*Max. Wall Temperature		Number of Channels
inches	(cm)	inches	(cm)	psia	(N/cm ²)	F	(K)	
Tapered 0.040-0.120 (0.10-0.30)		Tapered 0.080-0.20 (0.20-0.51)		30	(20.7)	1085	(858)	180
Tapered 0.040-0.120 (0.10-0.30)		0.080	(0.20)	50	(34.5)	1085	(858)	180
0.093	(0.24)	0.050	(0.13)	90	(62.1)	986	(803)	115
0.093	(0.24)	0.055	(0.14)	70	(48.3)	1037	(831)	115
0.093	(0.24)	0.060	(0.15)	55	(37.9)	1088	(860)	115
0.093	(0.24)	0.070	(0.18)	38	(26.2)	1129	(883)	115

*Hot-gas wall thickness = 0.040 inches (0.10 cm). The temperature can be reduced by 110 F (61K) for a 0.025 inch (0.063 cm) wall thickness.

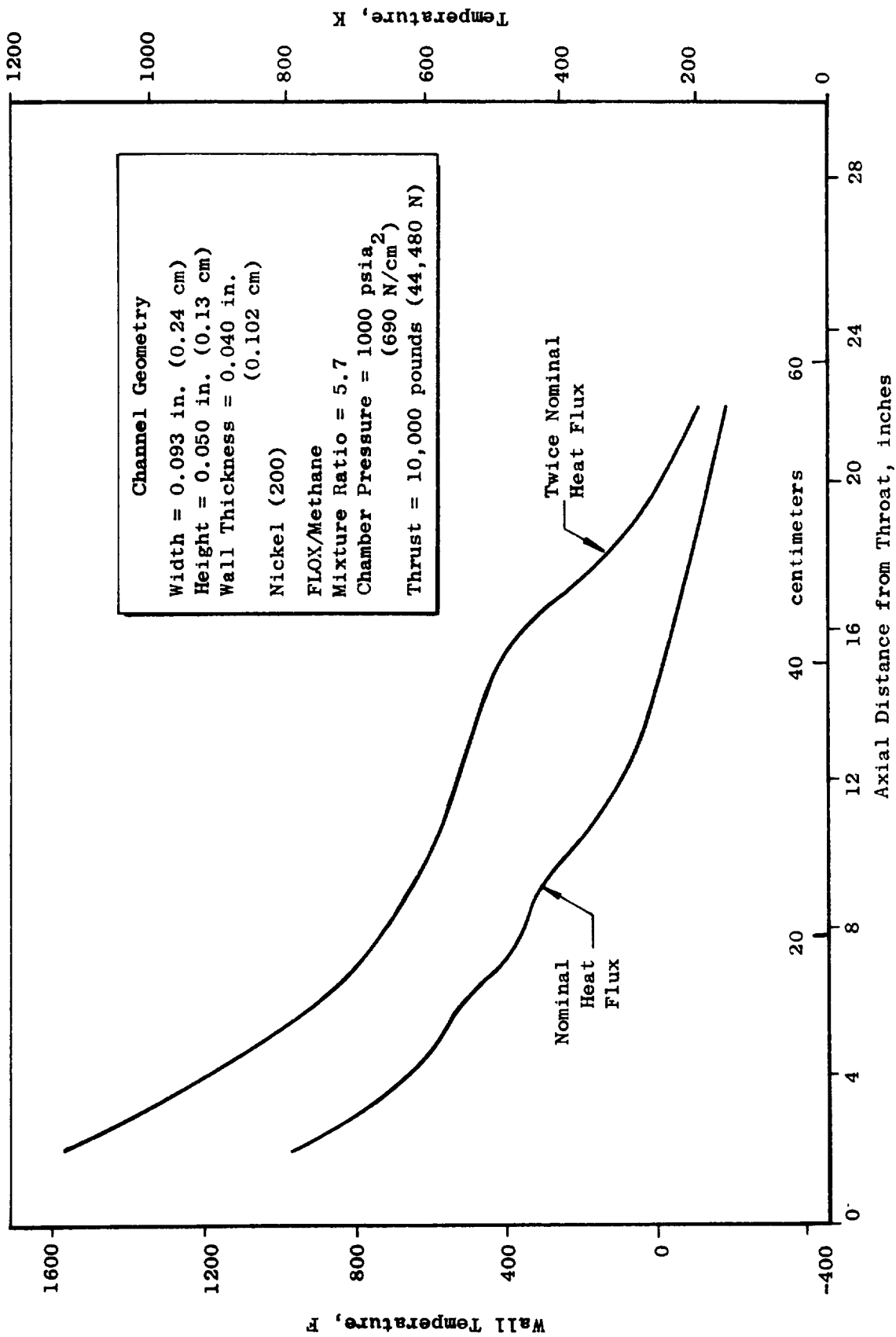


Figure 41. Effect of Heat Flux Level on the Regeneratively Cooled Nozzle, Hot-Gas Wall Temperature Profile

The combustion-side wall temperature profile calculated by a one-dimensional analysis based on the final heat transfer rate measurements is shown in Fig. 42 for operation at 500 psia (345 N/cm^2) with a mixture ratio of 5.25. The methane bulk temperature is shown in Fig. 43. The pressure profiles in the chamber for the same operating conditions are shown in Fig. 44. The exit pressure of 1000 psia (690 N/cm^2) reflects discharge conditions for an engine using an expander power cycle. By comparing Figs. 43 and 44 it can be seen that the methane is above either the critical pressure or the critical temperature at all points. Thus, bulk boiling does not occur during mainstage operation. The heat flux profile for these operating conditions is shown in Fig. 45. Predicted temperatures and pressure drops for various operating conditions are shown in Table 10.

The fabrication sequence for the regeneratively cooled thrust chamber is shown in Fig. 37. The initial fabrication steps are similar to those used to fabricate the water-cooled and solid nozzles. Nickel was electroformed on the combustion chamber and nozzle mandrels. The electroformed nickel was then contoured and grooved to form the coolant channels as shown in Fig. 46. The channels were then filled with wax and the outer wall of nickel deposited over the channels. This was the final electroform for the combustion chamber. Circumferential manifolds were machined into either end of the chamber and the electroforming wax removed (Fig. 47). Individual flow checks of the channels with water indicated low and erratic flowrates. A dimensional check of the channel widths prior to electroforming the outer wall indicated good tolerance control. The channel heights after electroforming were checked with wire gages and did not corroborate the flow discrepancies. The nickel 200 manifolds were electron beam welded to the chamber. A subsequent test indicated that the flowrate of the chamber was in good agreement with the predicted flow and was confirmed by subsequent methane blowdown and hot firing data. The assembled combustion chamber is shown in Fig. 48.

The nozzle design was such that at the low-area-ratio end additional strength was needed on the outside of the circumferential manifold groove. This was accomplished by electroforming additional nickel over the groove

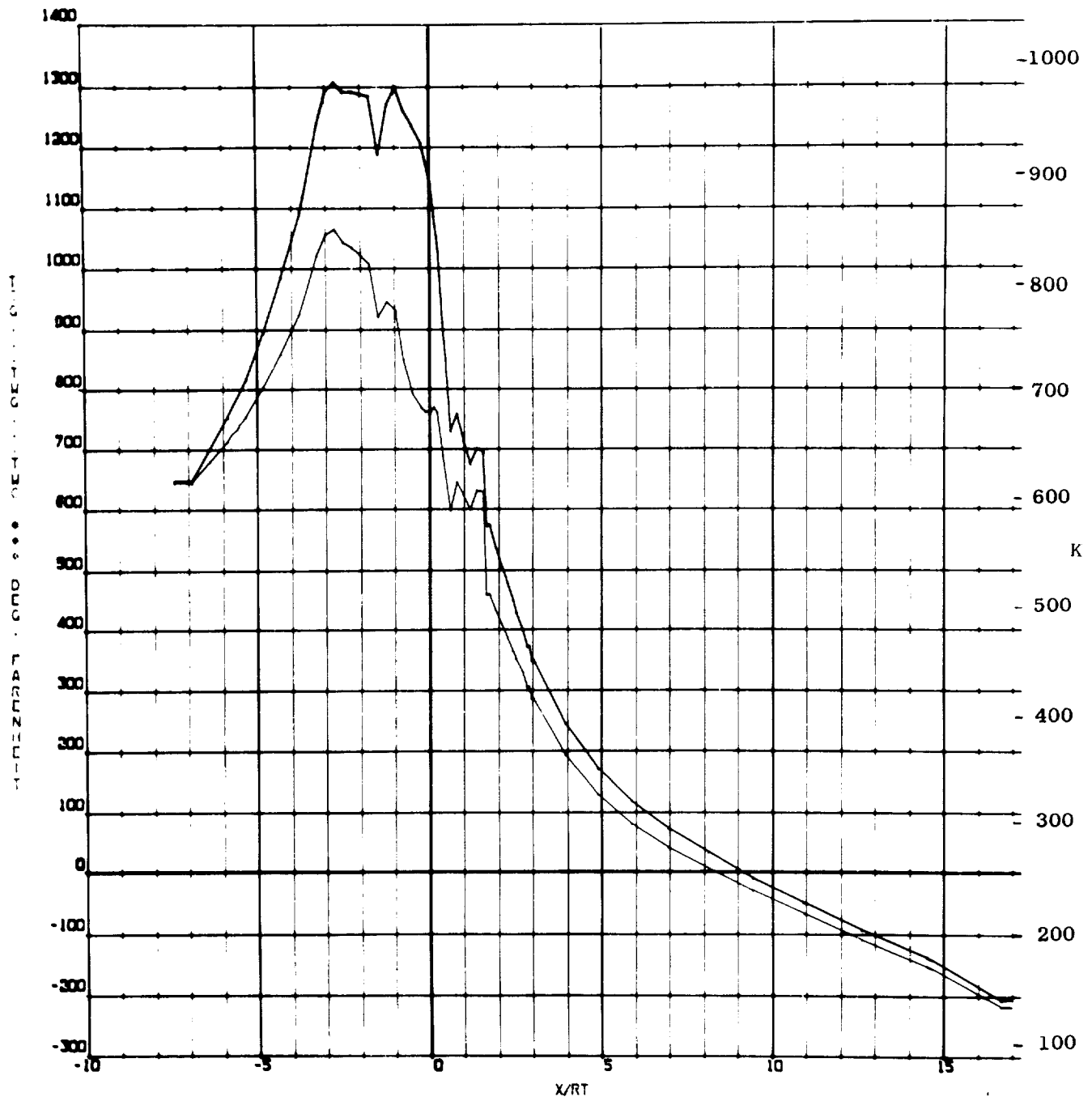


Figure 42. Hot Wall Temperature Profiles; Combustion and Coolant Sides

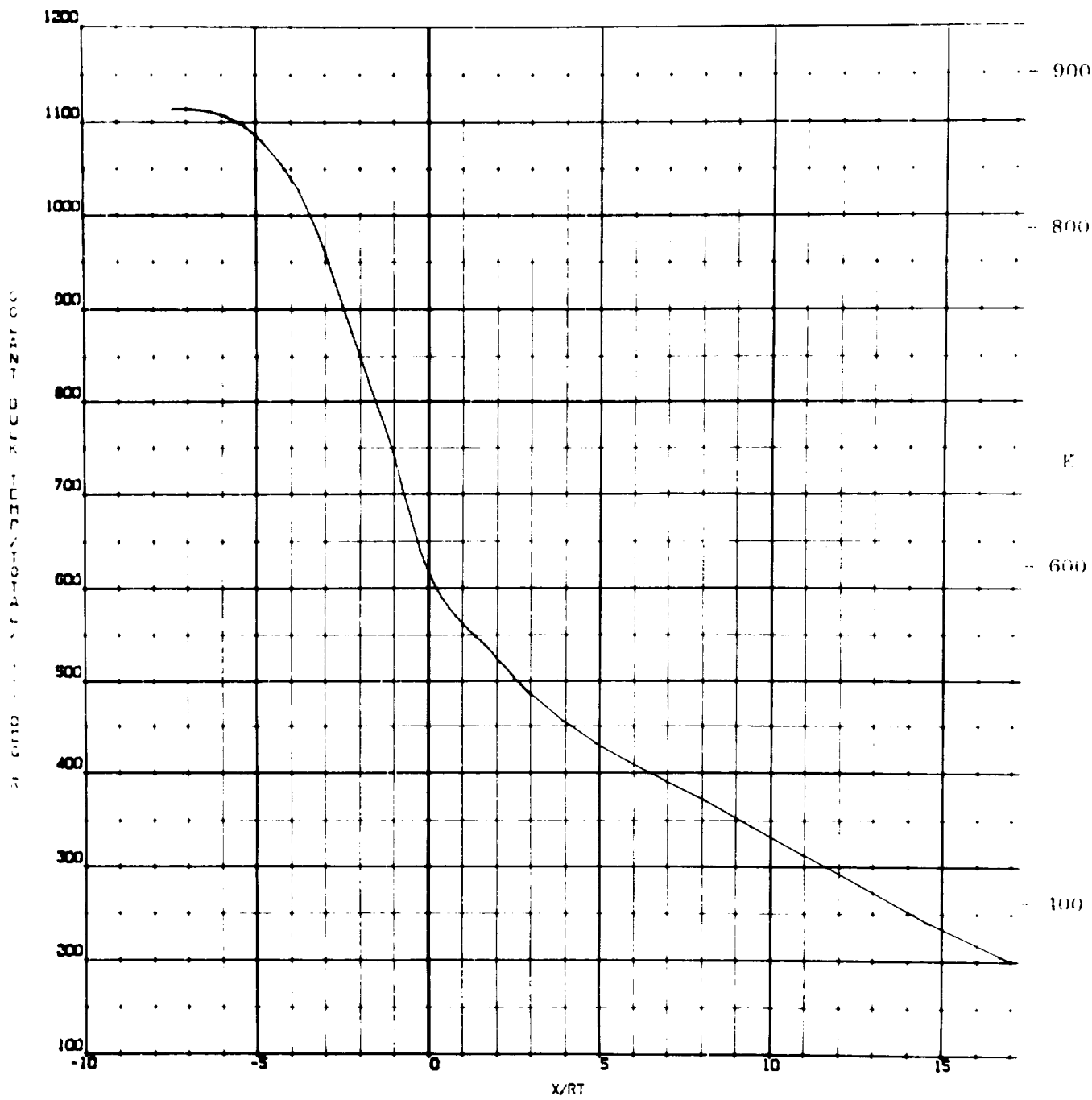


Figure 43. Coolant Temperature Profile

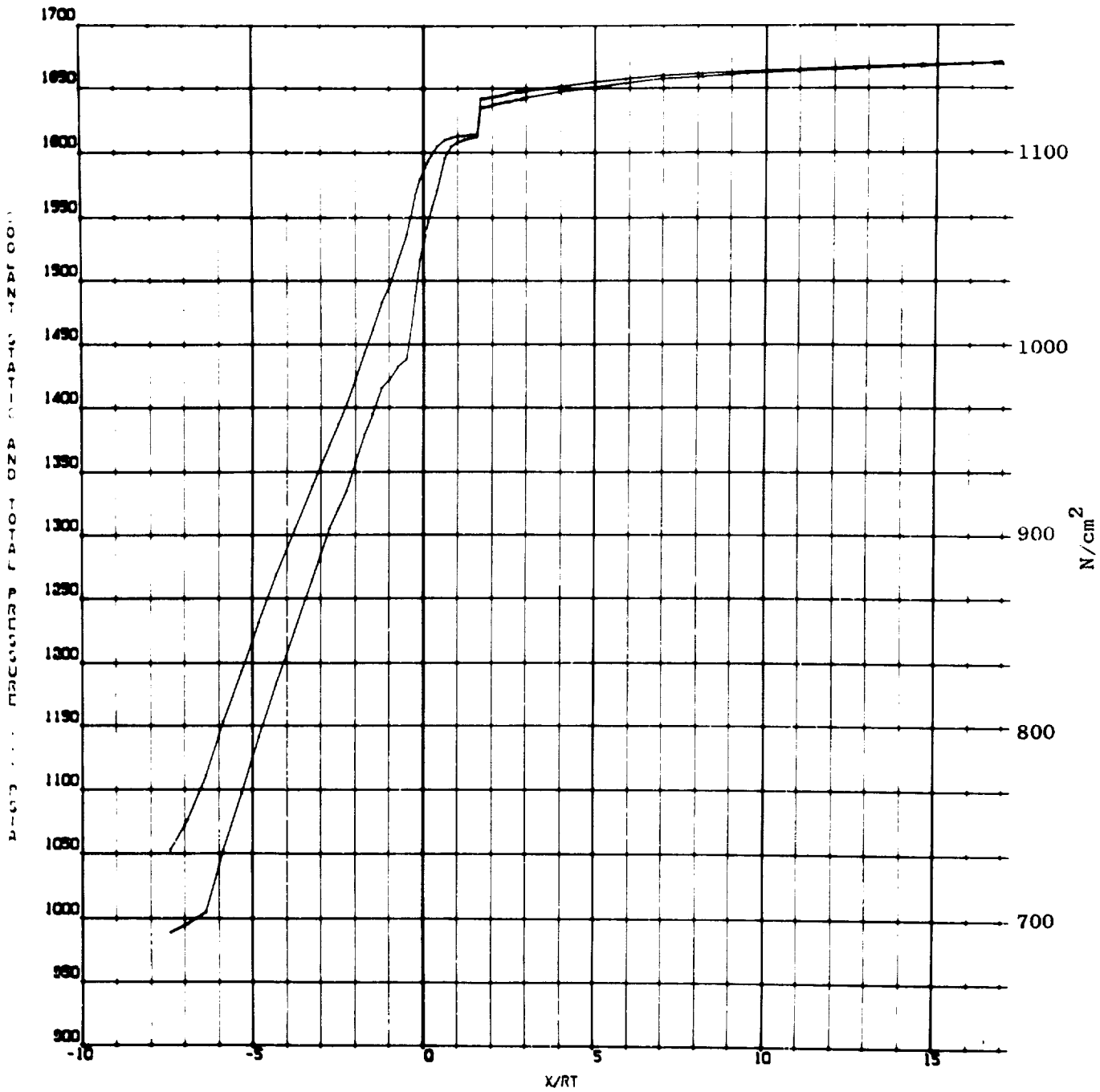


Figure 44. Coolant Pressure Profiles

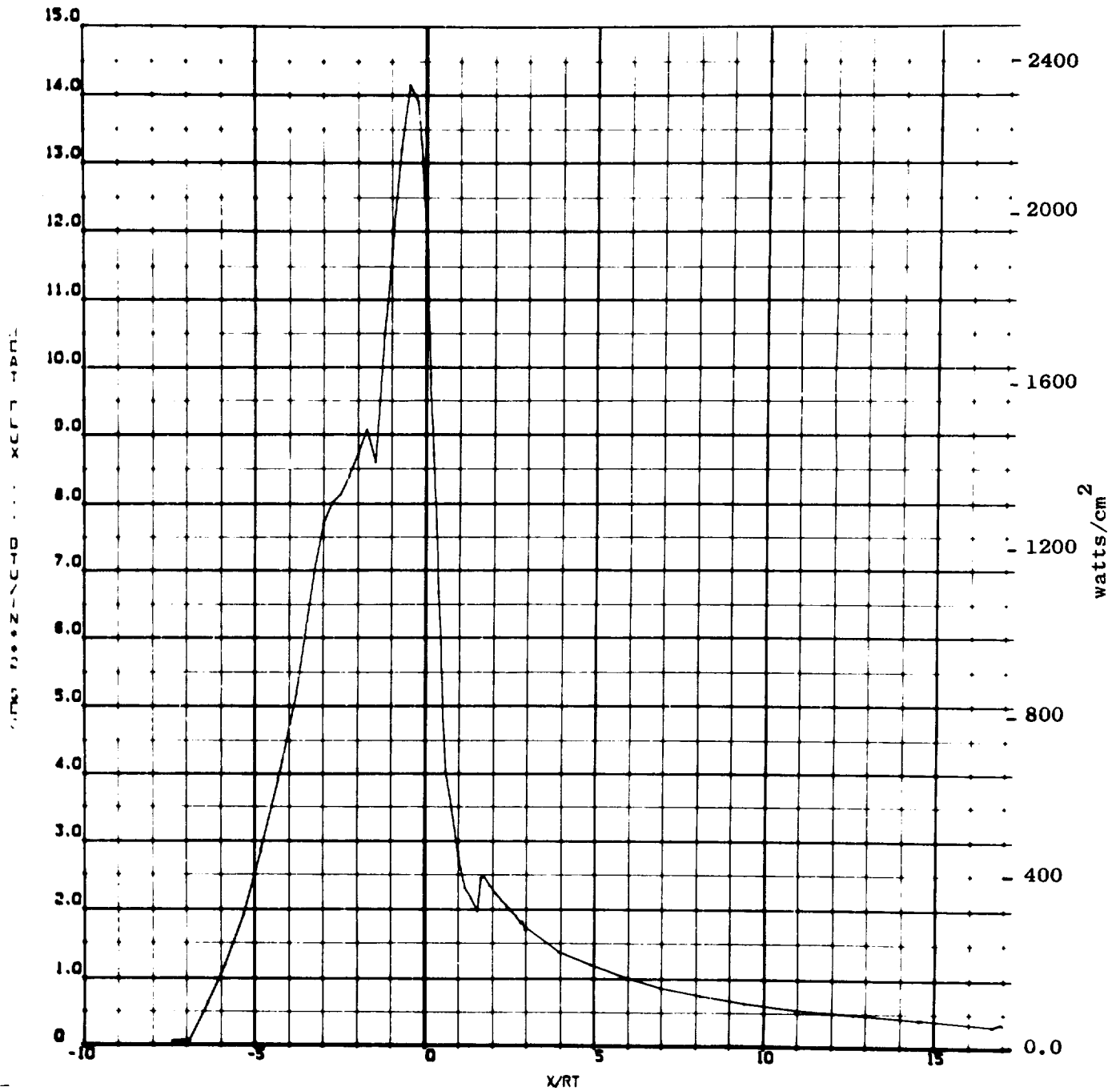
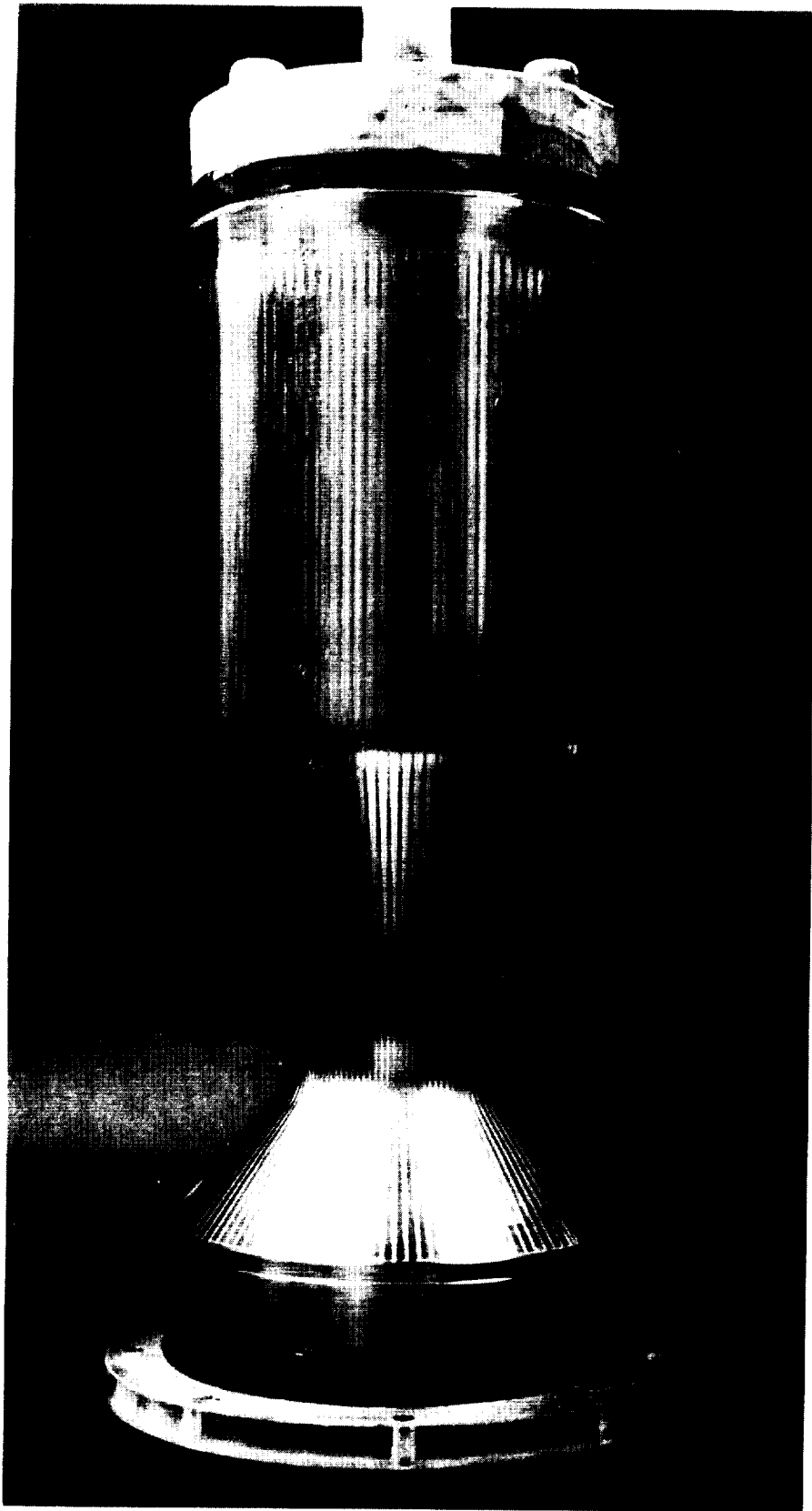


Figure 45. Heat Flux Profile

TABLE 9
 REGENERATIVELY COOLED COMBUSTION CHAMBER
 OPERATING CHARACTERISTICS

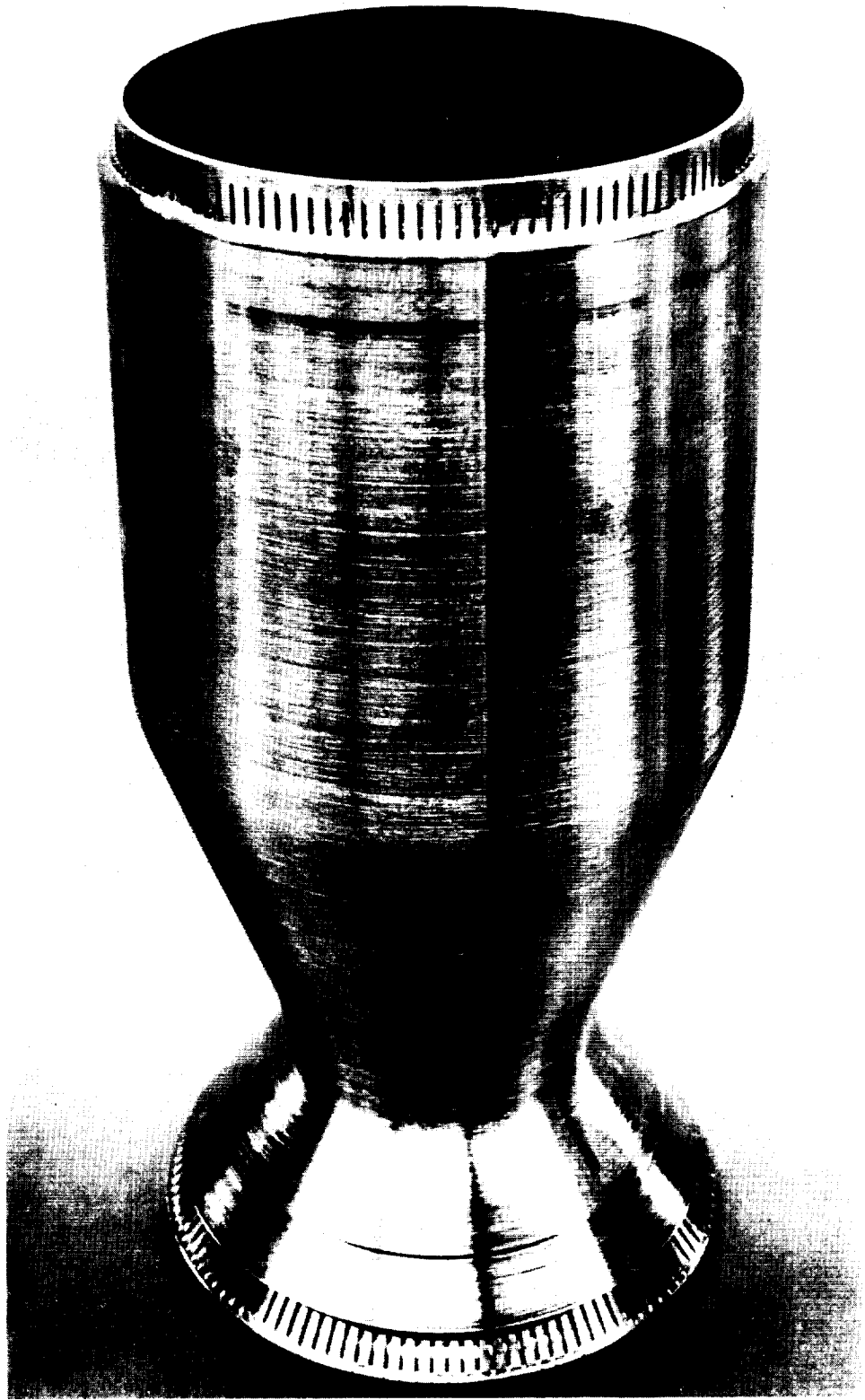
CHAMBER PRESSURE		MIXTURE RATIO					
psia	N/cm ²	4.0		5.25		5.7	
Maximum Wall Temperature at Start of Convergence							
		F	K	F	K	F	K
500	342	1065	848	1415	1043	1520	1100
700	483	1135	887	1615	1154	1675	1187
800	552	1200	923	1800	1257		
Pressure Drop							
		psi	N/cm ²	psi	N/cm ²	psi	N/cm ²
500	345	750	517	670	462	650	448
700	483	1275	789	1160	800	1125	776
800	552	1525	1052	1300	896		
Methane Temperature at Jacket Exit							
		F	K	F	K	F	K
500	345	400	478	655	619	735	664
700	483	385	469	645	614	725	658
800	552	375	464	640	611		

For 1000 psia (690 N/cm²) jacket discharge pressure and 200 R (111K) jacket inlet temperature.



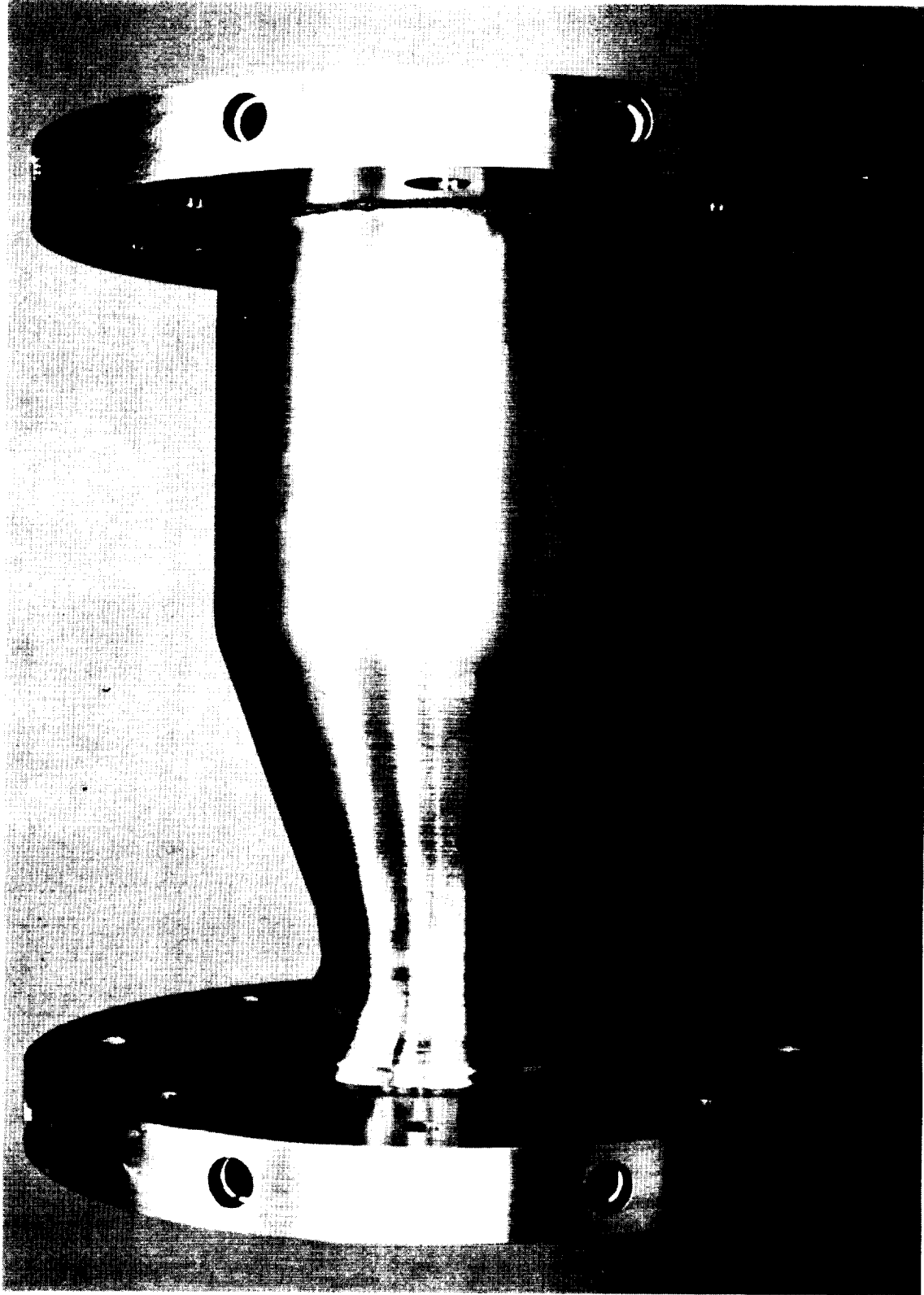
1XW32-2/10/69-C2B

Figure 46. Regeneratively Cooled Combustion Chamber



1XW32-3/13/69-C1B

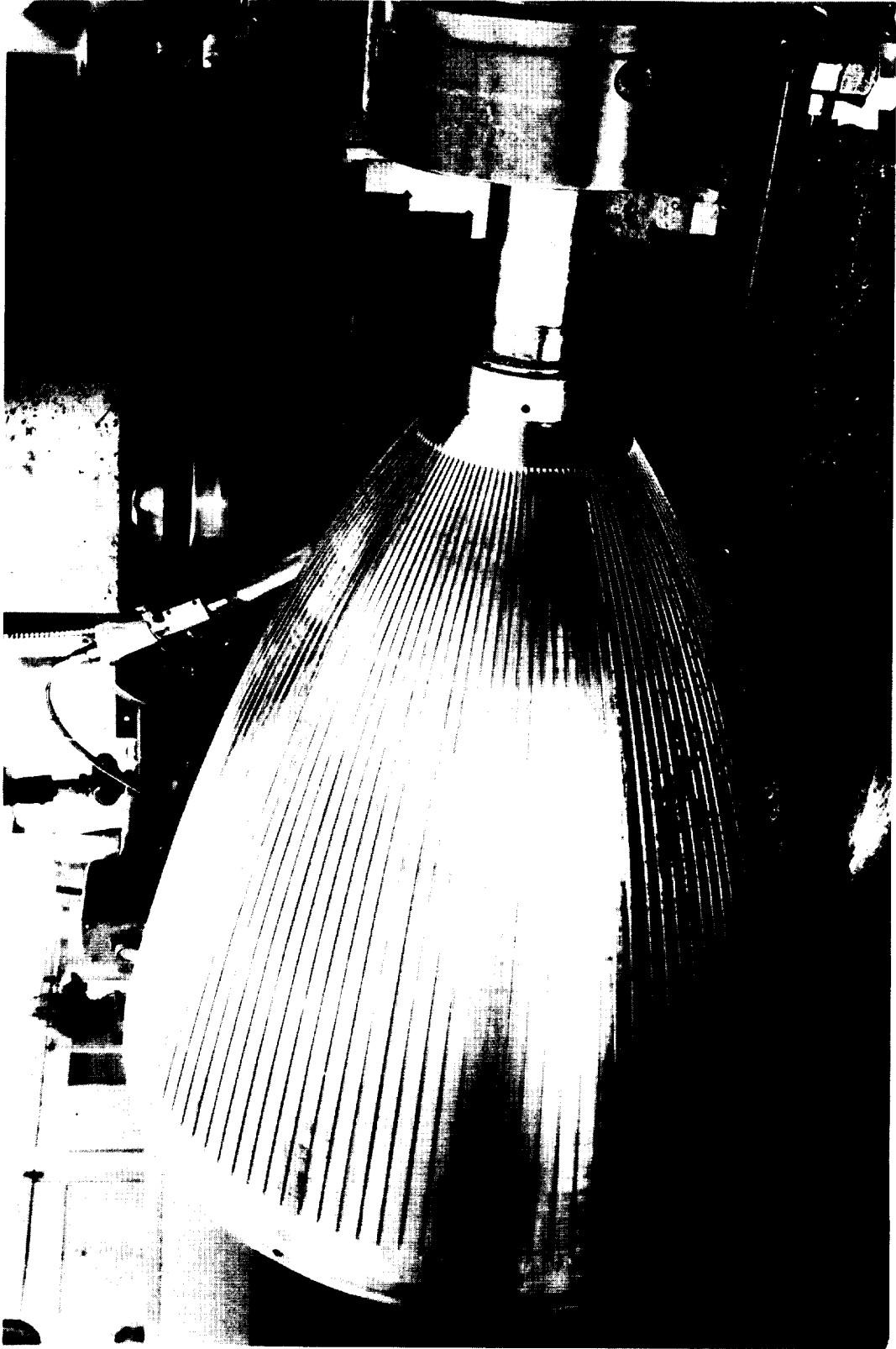
Figure 47. Regeneratively Cooled Thrust Chamber After
Electroforming and Machining



1XW32-4/29-69-C1C

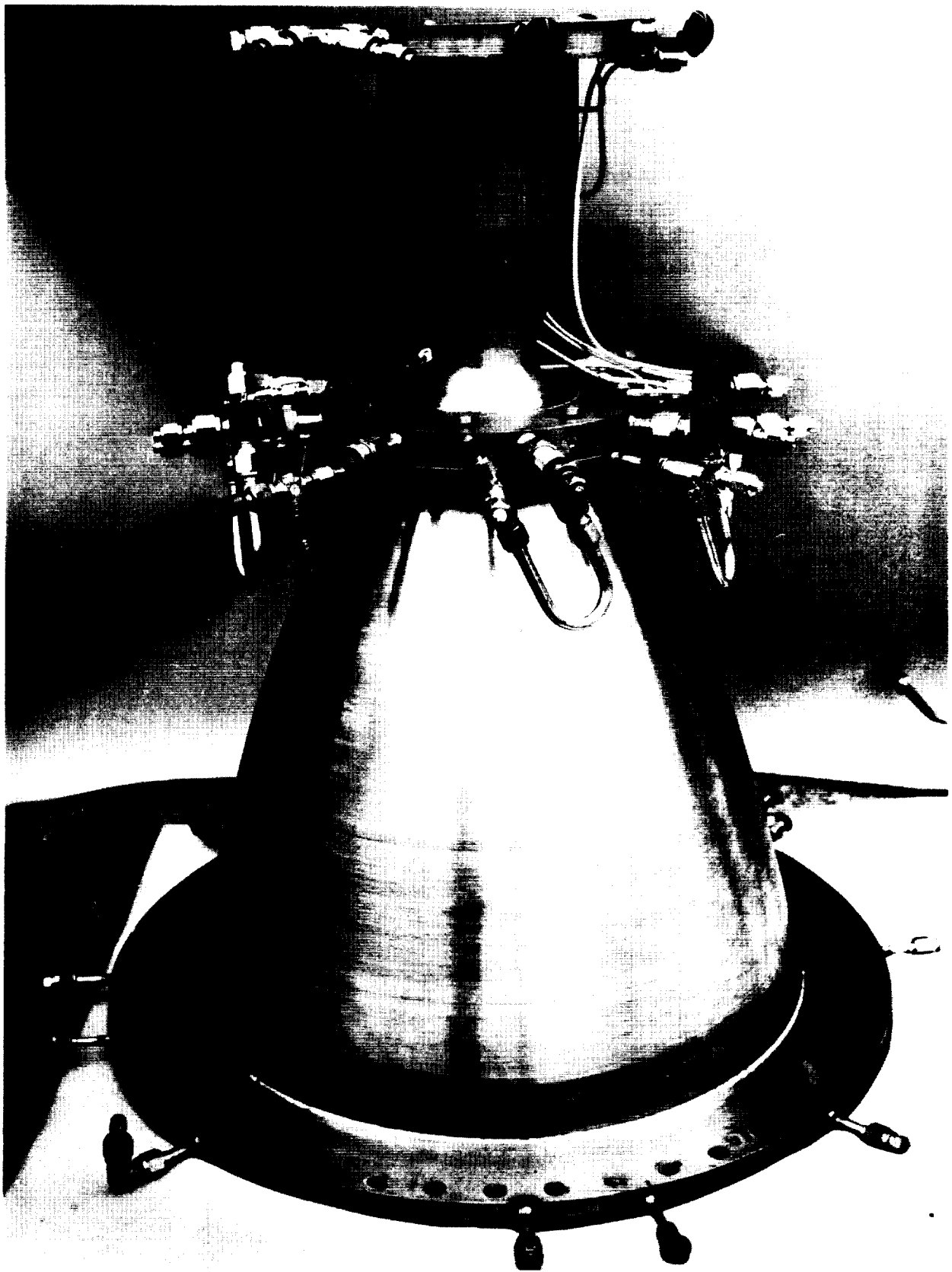
Figure 48. Assembled Regeneratively Cooled Combustion Chamber

and drilling 120 holes into the manifold. The channel configuration in the as-fabricated condition consisted of a 0.050 inch (0.127 cm) combustion-side wall and a channel width and height of 0.053 and 0.040 inches (0.134 and 0.10 cm) respectively. Figure 49 is a photograph of the nozzle after the channels were cut. The completed combustion chamber and nozzle assembly is shown in Fig. 50.



1XW32-1/10/69-CIA

Figure 49. Cutting Channels on the Regeneratively Cooled Nozzle



5AJ36-6/4/69-S1C

Figure 50. Regeneratively Cooled Thrust Chamber

SECTION III

INJECTOR CHARACTERIZATION AND ALTITUDE TESTS

Cold flow and hot firing tests were accomplished under Tasks III, IV, and VII of the contract. Cold flow tests were conducted on single elements and complete injectors. These tests were followed by hot firings with solid and water-cooled hardware at sea level and altitude conditions. Injector and thrust chamber performance and heat transfer characteristics were demonstrated together with injector integrity and combustion stability. This section contains descriptions of the test facilities, test conditions and results.

COLD FLOW TESTS

Tests were conducted on single impinging elements, hydraulic and mechanical swirlers for concentric element injectors and complete injectors.

Impinging Element Tests

Single element cold flow tests were conducted with triplet, impinging fan, and pentad elements to obtain qualitative data on oxidizer atomization and quantitative data on distribution. Fastax and Schlieren systems were used to obtain photographic data. A 100 tube liquid collection matrix was used to establish the distribution characteristics of each element. The collector was located 1.5 inches (3.8cm) from the element, a point where development of the fan was essentially complete. The oxidizer was simulated by water, the fuel by helium.

For impinging gas/liquid stream injectors, maximum exposure of the liquid surface area to the high velocity gas is necessary for aerodynamic atomization. Most effective use of the available gas momentum for atomization of the liquid occurs when the liquid streams are able to sufficiently penetrate the gas jet. In addition, the degree of penetration of the liquid streams into the gas stream also affects the

mixing level attained by the propellants. Without full penetration, a gas-rich condition will exist within the core, and if penetration exceeds full penetration, then high liquid concentration will occur at the core. The equations governing the penetration capability of the liquid streams into the gas stream are derived in Appendix E. The final equation is given below.

$$\frac{x_p}{D_L} = 2.5 \left[\frac{\rho_L v_L^2}{\rho_g v_g^2} \right]^{1/2} \cos \theta$$

Note that the relative liquid to gas momentum ratio is the significant variable, affecting liquid penetration and, consequently, the distribution and atomization. Cold flow modeling for penetration, therefore, requires that the gas-to-liquid momentum ratio of the cold flow match that for the hot firing. Therefore:

$$\frac{M_g}{M_L} \Big|_{\text{cold}} = \frac{M_g}{M_L} \Big|_{\text{hot}}$$

where M_g = gas momentum

M_L = liquid momentum

Calculation of the penetration distance for nominal operating conditions indicated that maximum fuel injection velocity and minimum oxidizer pressure drop limits could result in excessive penetration for the triplet element (two oxidizer streams impinging on a central fuel stream). These calculations indicated that matching of the available gas and liquid momentums for full penetration at the nominal hot firing conditions could be better attained by using four liquid jets. Two injector element designs consisting of four liquid jets and one gas jet were selected: (1) a pentad element, four liquid (oxidizer) jets impinging directly onto the gas (fuel) jet, and (2) an impinging

fan element where two fans, each formed from the impingement of two liquid jets, then impinge on a centrally located gas jet.

The triplet, pentad, and fan elements in the following configurations were used during the cold flow program:

1. Triplet with one fuel orifice ($D_g = 0.25$ inches, 0.63 cm) and two oxidizer orifices ($D_L = 0.037$ inches, 0.93 cm).
2. Pentad with one fuel orifice ($D_g = 0.25$ inches, 0.63 cm) and four oxidizer orifices ($D_L = 0.026$ inches, 0.65 cm).
3. Impinging fan with one fuel orifice ($D_g = 0.25$ inches, 0.63 cm) and two pairs of impinging oxidizer orifices ($D_L = 0.026$ inches, 0.65 cm).
4. The pentad element with the fuel orifice enlarged to 0.358 inches (0.900 cm).
5. Impinging fan element with the fuel orifice enlarged to 0.358 inches (0.900 cm)

Test Results. A total of 20 mass distribution and 18 photographic cold flow tests were conducted during the cold flow characterization studies with the elements described in the previous paragraph. A summary of the cold flow tests is given in Table 10. The fuel orifice diameter (D_g) was varied as indicated above. For each value of D_g the flow parameters (gas velocity and relative liquid/gas momentum) were varied to provide differing degrees of penetration of the gas by the liquid stream as shown in the table.

High speed movies were taken at several conditions of penetration employing all three element types. The overall objective of this effort was to obtain a qualitative indication as to the relative degree of atomization accomplished between the injector types. In general, at all conditions evaluated, no noticeable difference in the quality of

TABLE 10
Cold Flow Impinging Element Configurations

Test	Element (1)	(X_p/D_g) calc	Test Data	
			Collection	Photographic
1	T-100	1.00	X	
2		.69	X	
3		.50	X	
4		.45	X	
5	F-100	1.00	X	
6		.69	X	
7		.50	X	
8		.45	X	
9	T-100	1.00		X
10		.69		X
11		.50		X
12		.45		X
13	F-100	1.00		X
14		.69		X
15		.50		X
16		.45		X
17	F-100A	1.00	X	
18		.69	X	
19		.50	X	
20		.45	X	
21	T-101	1.00	X	
22		.69	X	
23		.50	X	
24		.55	X	
25		.60	X	
26	F-100A	Gas Only		X
27		1.00		X
28		.69		X
29		.50		X
30	T-101	1.00		X
31		.69		X
32		.50		X
33	T-101A	1.00	X	
34		.60	X	
35		.50	X	
36	T-101A	1.00		X
37		.60		X
38		.50		X

(1)

Model	Type	D_g		D_L	
		inches	cm	inches	cm
T-100	Triplet	0.257	0.652	0.037	0.091
T-101	4-on-1	0.257	0.652	0.026	0.066
T-101A	4-on-1	0.358	0.909	0.026	0.066
F-100	Fan	0.257	0.652	0.037	0.091
F-100A	Fan	0.358	0.909	0.037	0.091

atomization was observed between the triplet, pentad, or impinging fan injector types. The photographs indicated that in every instance the resulting sprays contain extremely small droplets which appear as dense fogs. In fact, even at the edges of the spray the droplets were too small to be measured from the photographs. As a result, the specific sizes of the droplets were not ascertained. These results support the calculations of the expected dropsizes, which indicated that dropsizes of less than $80\ \mu$ would be obtained. Therefore, the limiting combustion process for FLOX/methane at the operating conditions and for the chamber geometry employed in this program was mixing.

Mass distribution data for the three element types at a calculated penetration value (X_p/D_g) of 0.5 are shown in Figures 51 thru 53. This value of X/D_g represents penetration of the oxidizer jets to the center of the fuel jet and results in most uniform distribution for each configuration. The row and column number refer to the centerline of each 1/4 inch diameter tube in the collection device. In Fig. 51 it can be seen that even for the optimum distribution condition for the triplet, a significant gas-rich area occurs in the center of the element. The liquid distribution appears quite even for the fan element, as shown in Fig. 52. However, the large amounts of liquid well beyond the area of the gas orifice (0.257 in. diameter) could result in oxidizer rich zones. The liquid distribution for the pentad, shown in Fig. 53 indicates the presence of a gas rich core which is much less significant than that of the triplet.

Since only the liquid was collected, calculations of E_m would require an assumption as to the gas distribution. The simplest assumption would be to assume that the gas was uniformly distributed across the element.

However, assuming that pressure gradients across the gas jet cannot be sustained, then areas of high liquid mass concentration would require low gas concentrations in these areas and vice-versa. These

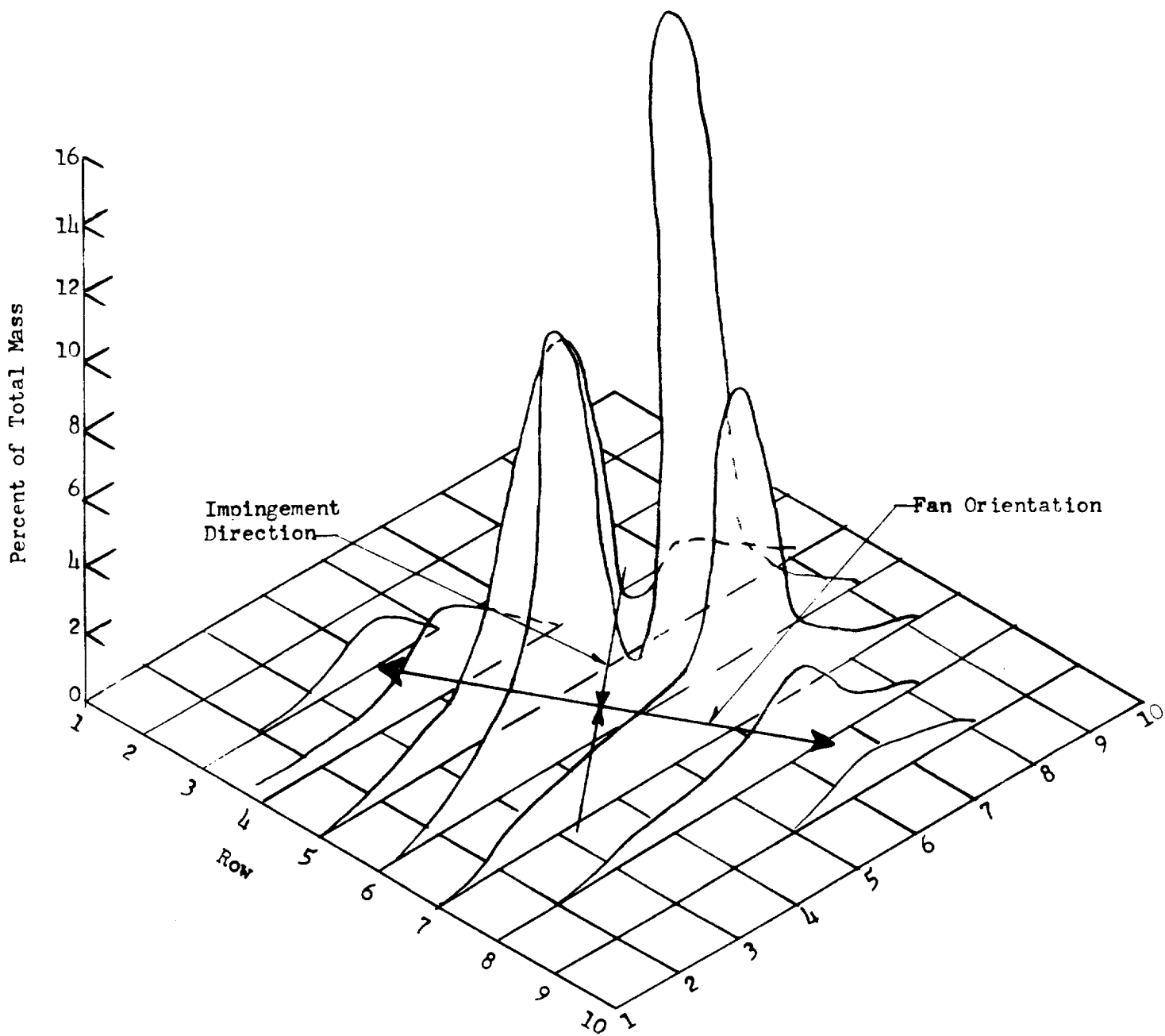


Figure 51. Liquid Mass Distribution for the Triplet Element.

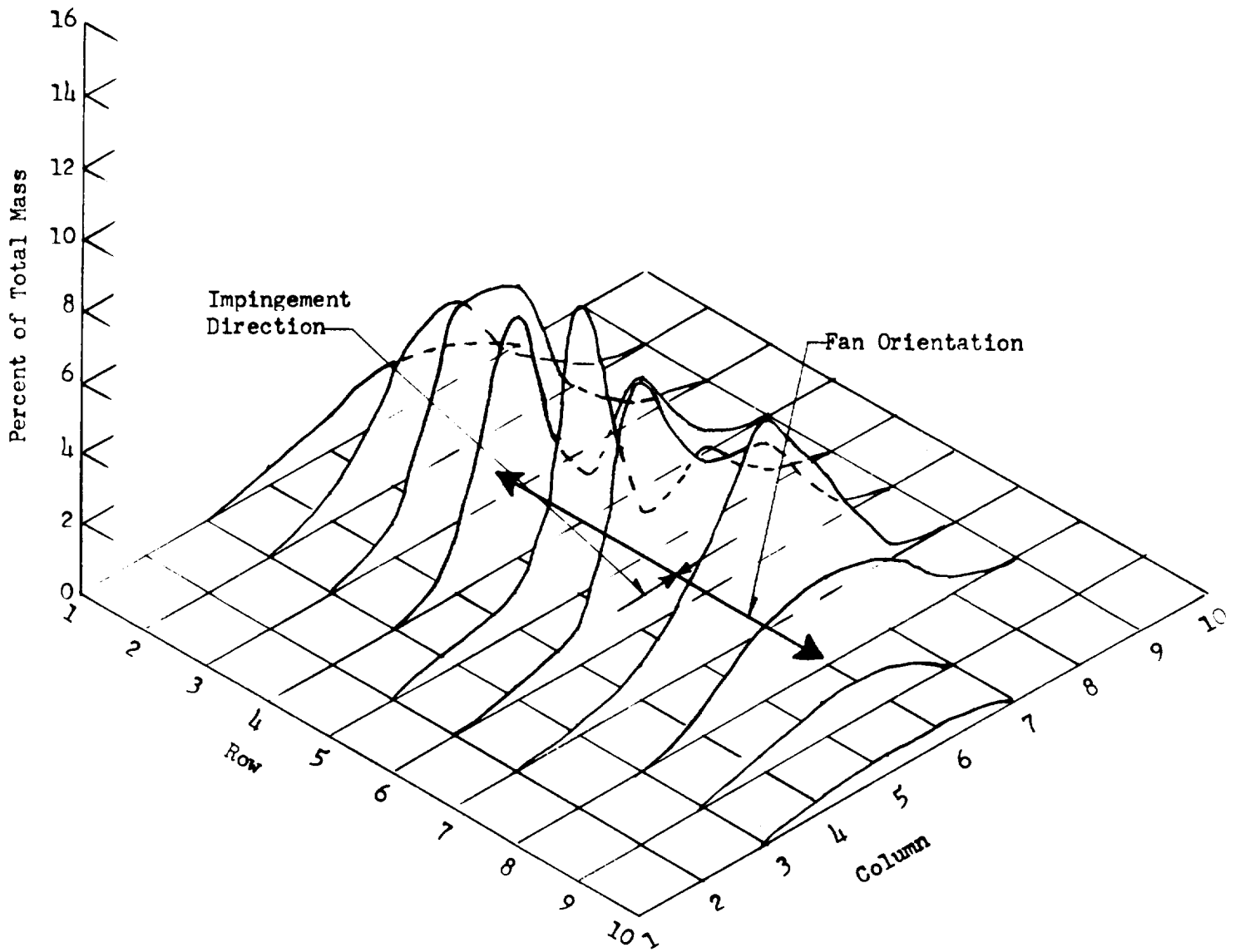


Figure 52. Liquid Mass Distribution for the Fan Injector Element.

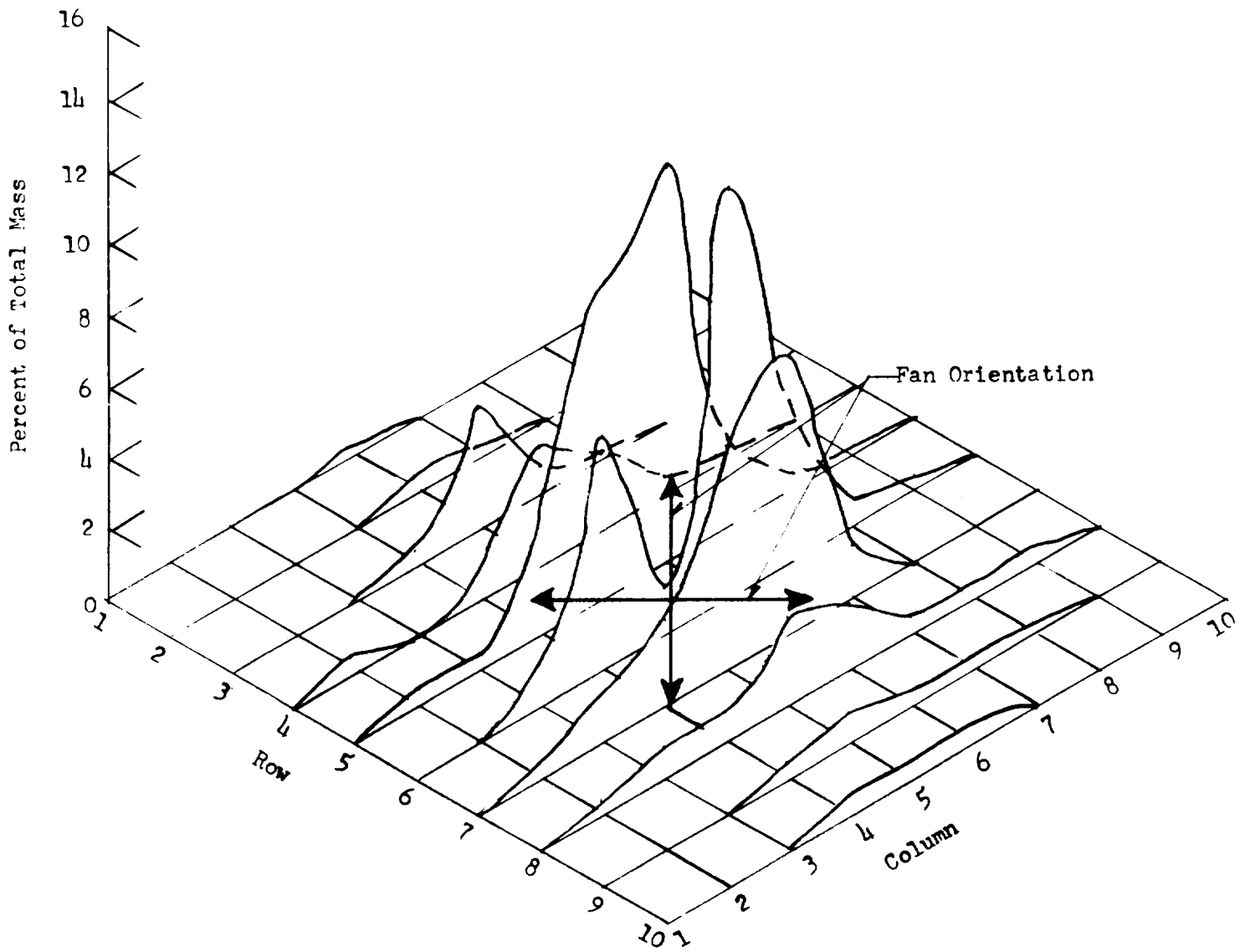


Figure 53. Liquid Mass Distribution for the Pentad Injector Element.

conclusions suggest that an assumption of equal gas distribution across the spray field is not realistic. An alternate and more realistic assumption is that uniform liquid mass distribution will result in the most uniform mixture ratio distribution. Consequently, the liquid mass uniformity can be used to characterize each of the injector element designs and the conditions resulting in uniform liquid mass distribution will imply uniform mixture ratio distribution. Studies of liquid and gas distributions are being conducted under Contracts NAS 3-12001 and NAS 3-11199 for impinging and concentric elements. These studies have shown that increasing the penetration parameter tends to spread the gas distribution.

The liquid mass distribution index utilized represents the deviation from the uniform liquid mass distribution. This relationship is given by the following equation:

$$1 - \sigma = 1 - \left[\sum_{i=1}^n \left(\frac{M_i - M_a}{M_t} \right)^2 \right]^{1/2} (n-1)^{1/2}$$

- where
- σ = standard mass deviation
 - M_i = mass in i^{th} tube
 - M_t = total collected mass
 - n = number of sampling stations containing liquid
 - M_a = average mass per tube (M_t/n)

The mass deviation index is plotted in Fig. 54, for the triplet, pentad, and fan as a function of the penetration distance $(X_p/D)_g$ calc. These data show that the penetration distance has a significant influence on the liquid mass distribution. Liquid mass distribution is most uniform (noted by high values of $1 - \sigma$) with full penetration of the liquid stream into the gas stream. A distribution index of about 98 percent was obtained for both the fan and the pentad while a value of 97 percent was obtained for the triplet.

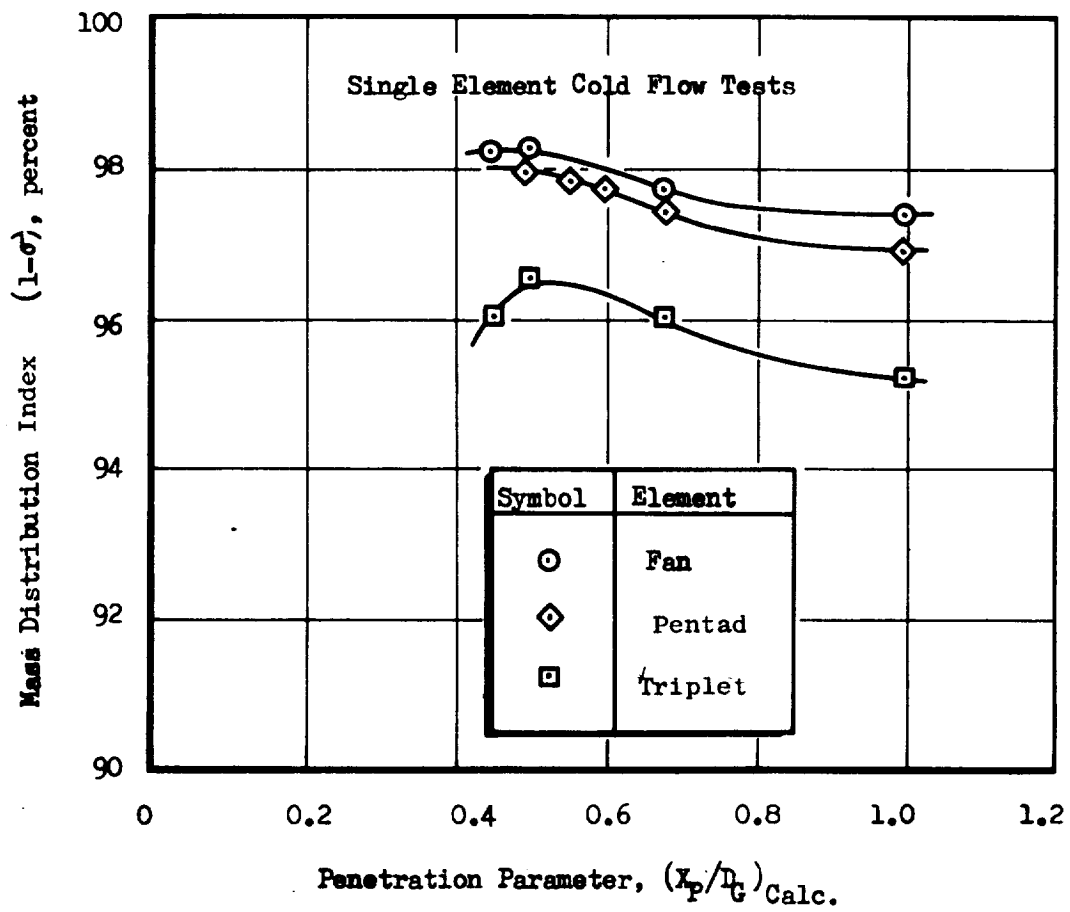


Figure 54. Mass Distribution as a Function of Jet Penetration

The effect of penetration distance on η_{c*} is shown in Fig. 55 where performance data from contract NAS8-19 are plotted as a function of $(X_p/D_g)_{calc}$. Note that the correspondence between the cold flow results presented in Fig. 54 and the hot fire data of Fig. 55 indicate injector mixing (distribution) and c^* performance optimized at or near the full penetration point $(X_p/D_g = 0.5)$.

Concentric Element Tests

A plexiglass model of the FLOX element of the concentric element injector was fabricated to test various hydraulic swirler configurations with respect to pressure drop, flow divergence angle and stability, and vortex propagation. Two-, three-, and four-port tangential entry swirlers of various port diameters were tested. Some configurations exhibited bistable flow characteristics and incomplete unstable cones. The vortex propagated through the entire length of the FLOX tube in most cases and the divergence angle of the cone was generally close to the divergence angle of the FLOX tube. The effect of swirler inlet area on FLOX pressure drop is shown in Fig. 56 for flowrates corresponding to 500 and 1000 psia (345 and 690 N/cm²) chamber pressure.

A two-port hydraulic swirler with 0.055 inch (0.140 cm) diameter ports was selected on the basis of stable flow and suitable pressure drop characteristics.

Photographs of the water spray pattern with the selected swirler configuration are shown in Figs. 57 and 58 for flowrates corresponding to 500 and 1000 psia (345 and 690 N/cm²) chamber pressure operation respectively. Swirl patterns can be seen in the transparent plastic block which simulates the FLOX tube. Flow was uniform and stable with pressure drops corresponding to 120 and 400 psi (83 and 276 N/cm²) for FLOX flowrates at 500 and 1000 psia (345 and 690 N/cm²) chamber pressure respectively at the design area ratio.

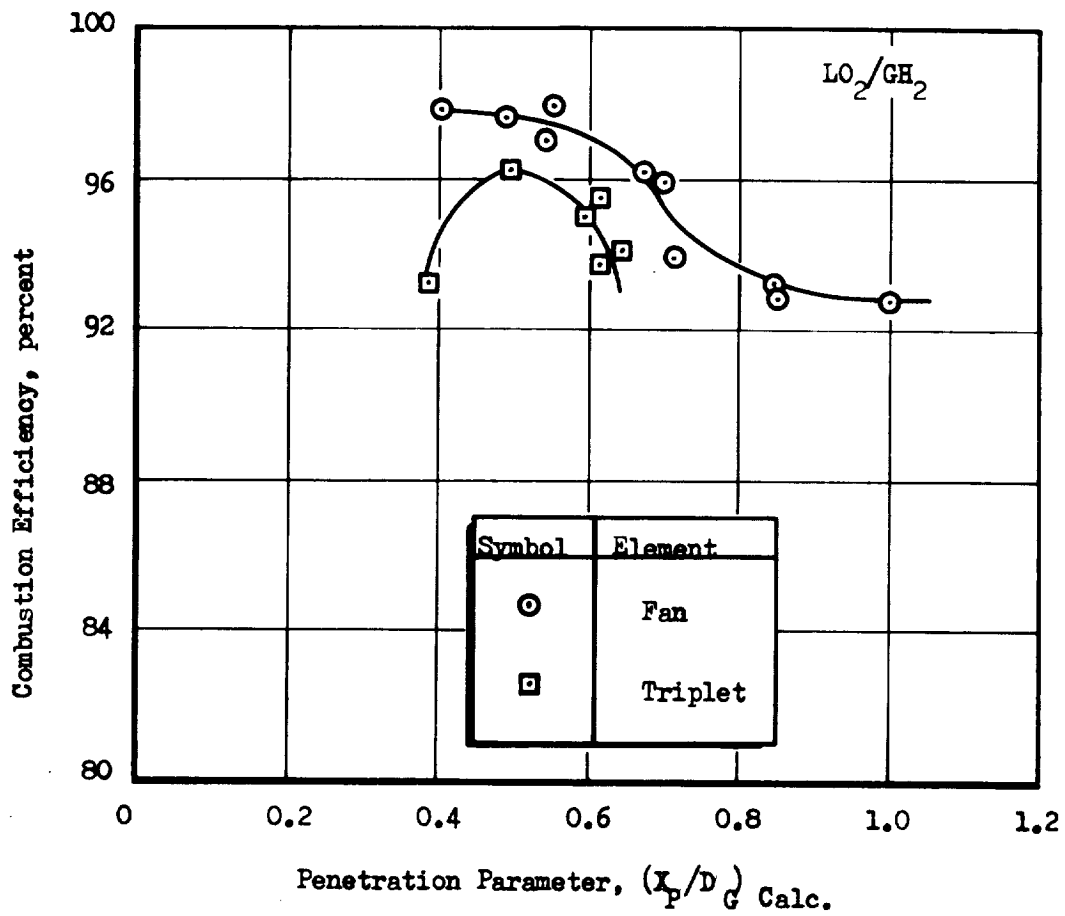


Figure 55. Combustion Efficiency as a Function of Jet Penetration

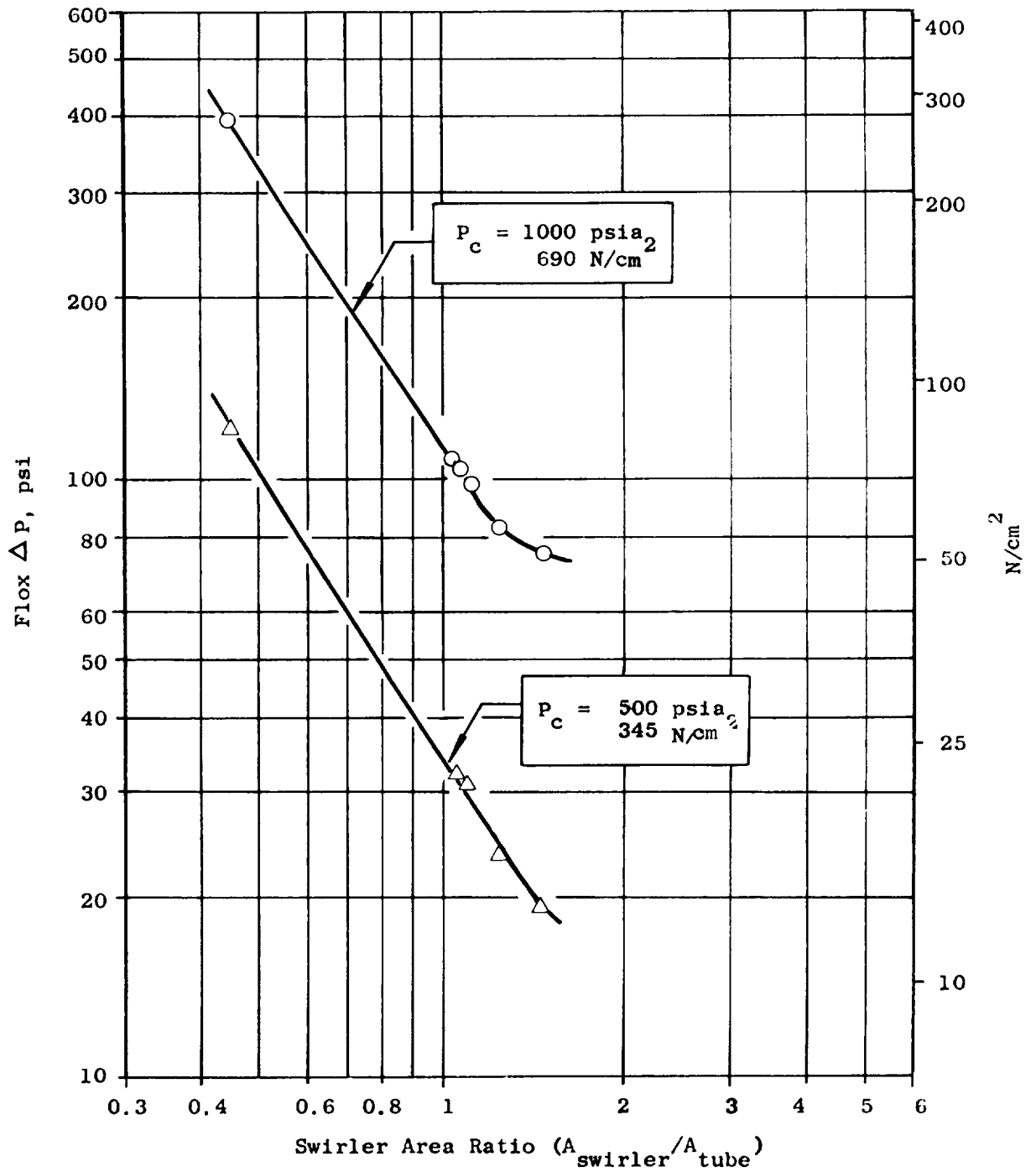
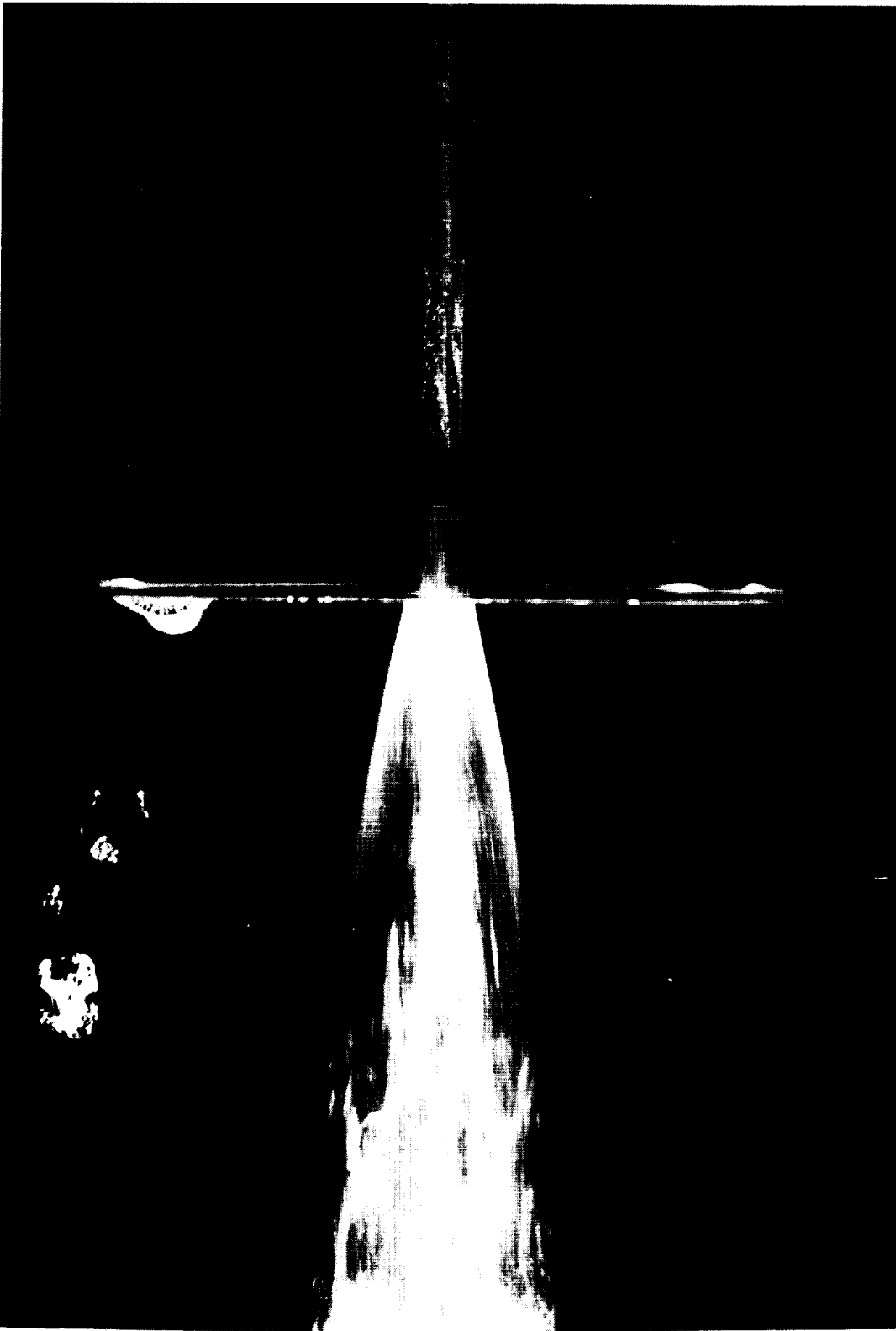
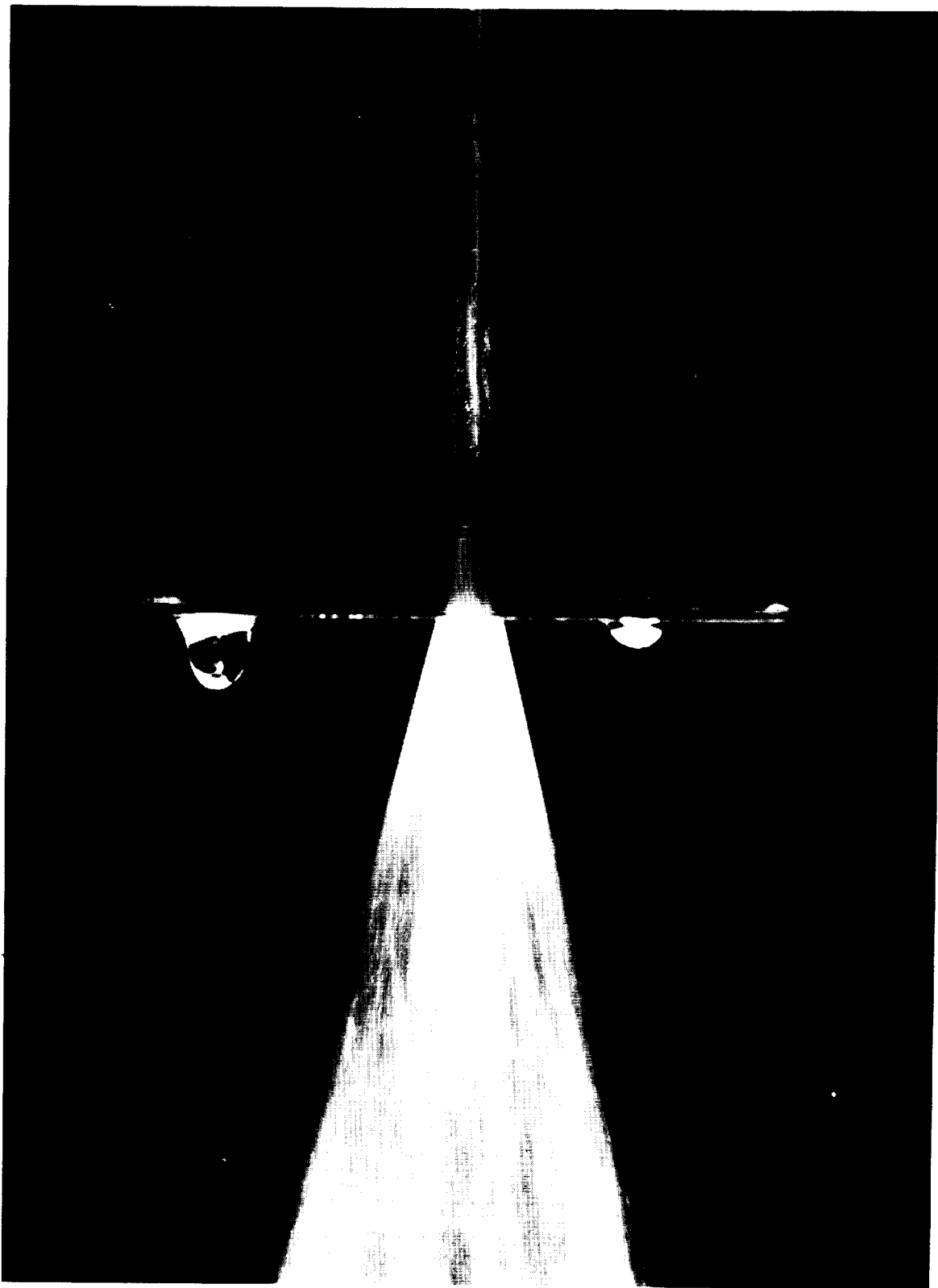


Figure 56 . Concentric Injector Flux ΔP vs Swirler Area Ratio



1XW34-9/11/68-CLB

Figure 57. FLOX Tube Simulation Corresponding to 500 psia Chamber Pressure



1XW34-9/11/68-C1A

Figure 58. FLOX Tube Simulation Corresponding to 1000 psia Chamber Pressure

A concentric element injector with mechanical swirler was made and tested under an IR&D program. The injector had good performance but indicated high heat fluxes near the injector end of the thrust chamber. The apparent reason for the high heat fluxes in this region was an oxidizer-rich condition near the injector.

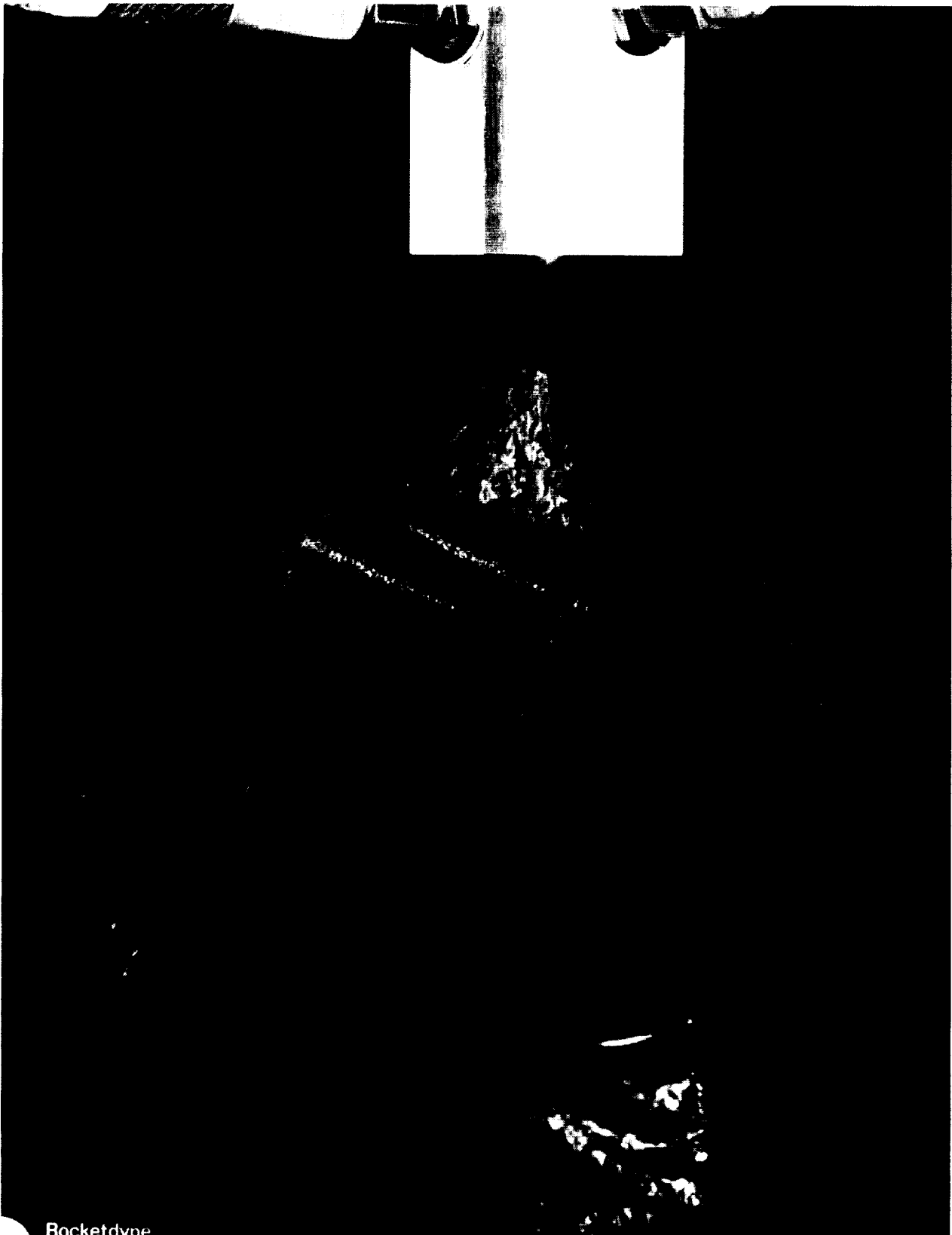
A series of cold flow tests was conducted with a single element using water and GN_2 to simulate the propellants. The purpose of these tests was to determine the effects of recess and propellant flowrates on the injector pressure drops and spray characteristics. Tests were conducted with recess depths of 0 to 0.5 inches (1.27 cm) and flowrate combinations described in Table 12. The combined effects of fuel flowrate and recess on the oxidizer injection pressure drop (at constant oxidizer flowrate) were less than ± 3 percent. The fuel injection pressure drop increased by 4 percent as the recess was varied from 0 to 0.5 inches (1.27 cm).

The effects of recess on the flow pattern are shown in Figs. 59 thru 63. The water flowrate in all cases was 1.0 gpm (0.063 liter/sec). A rather wide angle spray (80 degrees total included angle) resulted for conditions of zero recess and no gas flow (Fig. 59). Increasing the recess to 0.107 inches (0.265 cm) caused the cone to narrow to approximately 55 degrees as shown in Fig. 60. Further increases in recess with no gas flow did not appreciably reduce the cone angle further. The cone consisted of a continuous sheet, near the element, which subsequently broke up into fairly coarse droplets. Tangential flow was clearly visible in the cone. The dramatic effect of gas flow on the spray pattern can be seen in Figs. 61 thru 63. The finely atomized spray fanned out close to the injector face in the zero recess configuration shown in Fig. 61. The fan became progressively narrow as the recess was increased as shown in Figs. 62 and 63 for recesses of 0.107 and 0.500 inches (0.265 and 1.27 cm).

TABLE 12

HEAT EXCHANGER ELEMENT FLOW TESTS

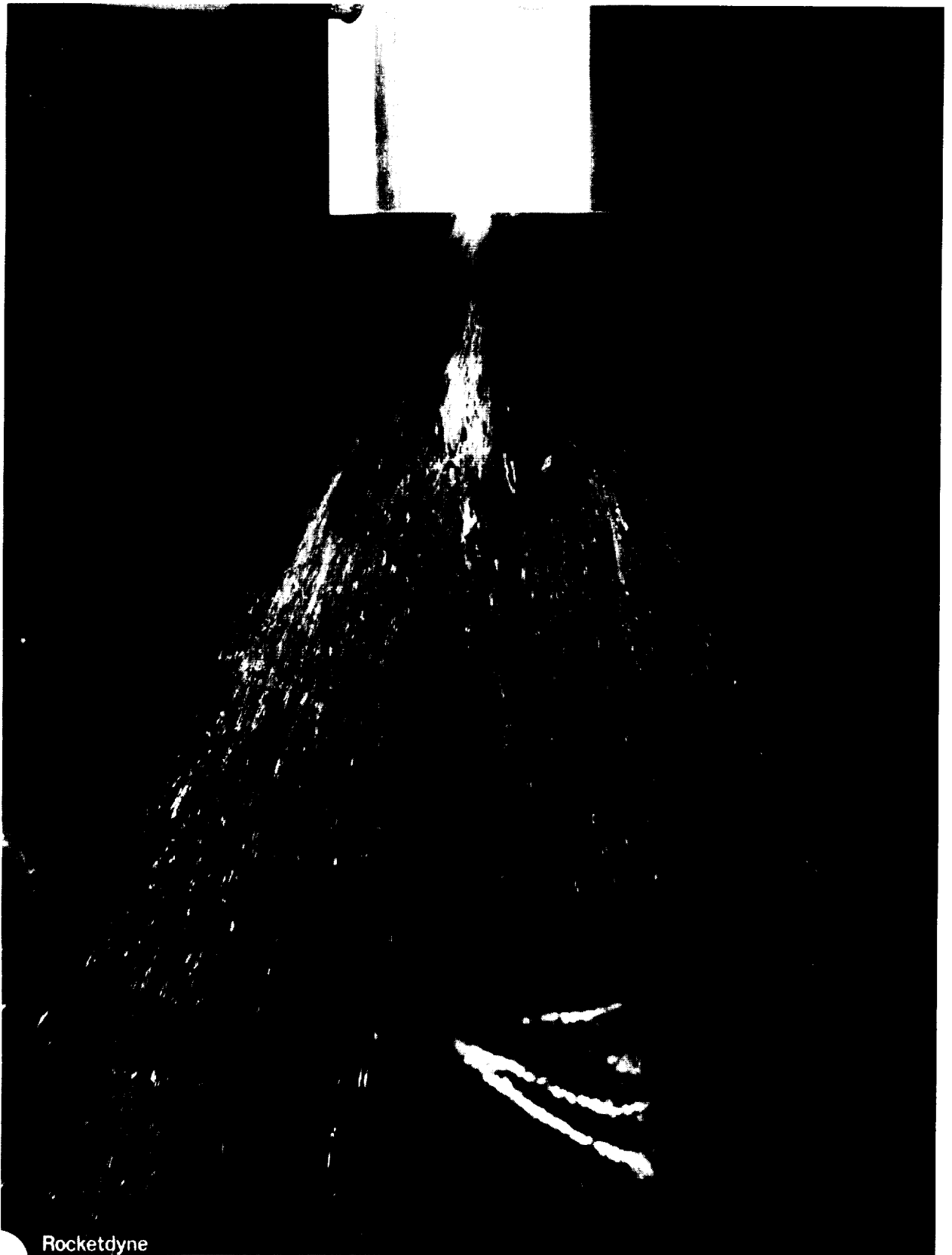
Recess inches (cm)		Oxidizer Side				Fuel Side			
		ΔP psi (N/cm ²)		Flow gpm (liter/sec)		ΔP psi (N/cm ²)		Flow lb/sec (g/sec)	
0	0	28	(19)	0.5	(0.03)	0	(0)	0	(0)
0	0	106	(73)	1.0	(0.06)	0	(0)	0	(0)
0	0	106	(73)	1.0	(0.06)	50	(35)	0.0139	(63)
0	0	109	(75)	1.0	(0.06)	70	(48)	0.0221	(100)
0	0	109	(75)	1.0	(0.06)	85	(59)	0.0294	(133)
0.107	(0.272)	0	(0)	0	(0)	50	(35)	0.0141	(64)
0.107	(0.272)	0	(0)	0	(0)	70	(48)	0.0216	(98)
0.107	(0.272)	0	(0)	0	(0)	80	(55)	0.0265	(120)
0.107	(0.272)	105	(72)	1.0	(0.06)	50	(35)	0.0145	(65)
0.107	(0.272)	105	(72)	1.0	(0.06)	70	(48)	0.0223	(101)
0.107	(0.272)	105	(72)	1.0	(0.06)	85	(59)	0.0298	(135)
0.242	(0.615)	105	(72)	1.0	(0.06)	50	(35)	0.0136	(62)
0.242	(0.615)	109	(75)	1.0	(0.06)	70	(48)	0.0222	(100)
0.242	(0.615)	110	(76)	1.0	(0.06)	85	(59)	0.0292	(132)
0.300	(0.762)	108	(75)	1.0	(0.06)	70	(48)	0.0223	(101)
0.367	(0.932)	109	(75)	1.0	(0.06)	70	(48)	0.0228	(103)
0.500	(1.27)	108	(75)	1.0	(0.06)	70	(48)	0.0229	(104)
0.500	(1.27)	104	(72)	1.0	(0.06)	0	(0)	0	(0)



Rocketdyne

1XX44-10/2/69-C1F

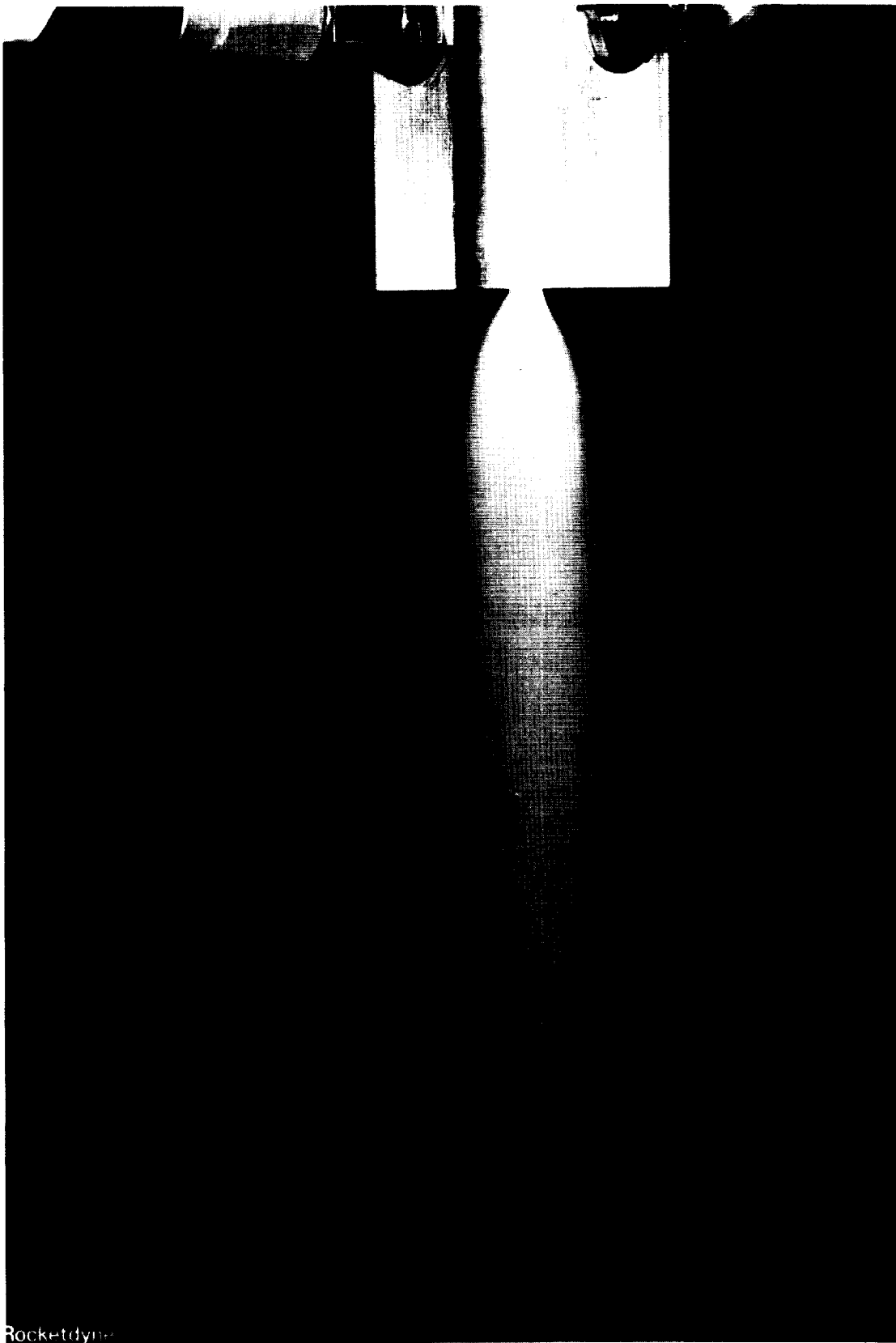
Figure 59. Heat Exchanger Element Cold Flow, Recess = 0, $\dot{w}_f = 0$



Rocketdyne

1XX44-10/2/69-C1B

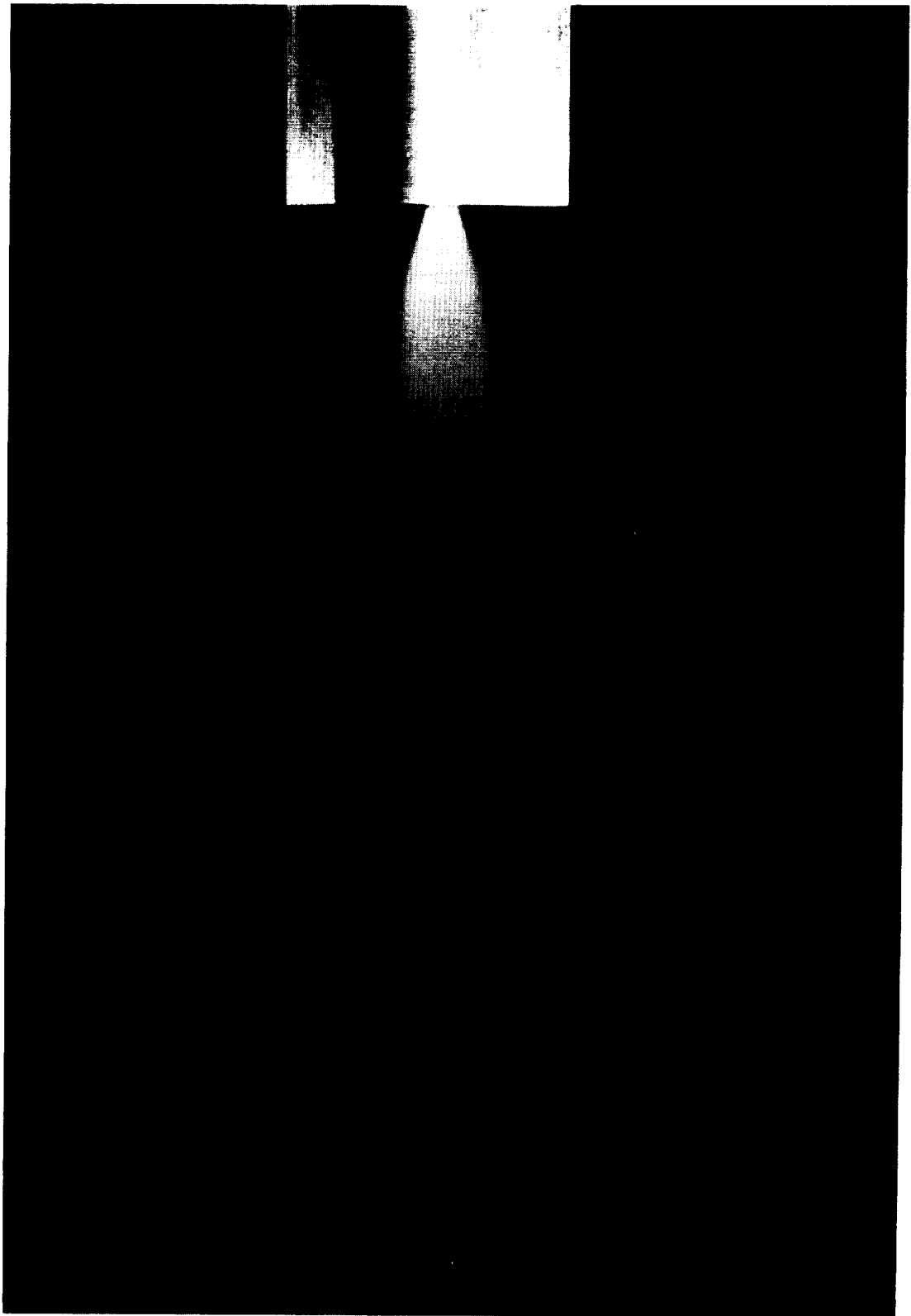
Figure 60. Heat Exchanger Element Cold Flow Recess = 0.107 in., $\dot{w}_f - 0$



Rocketdyne

1XX44-10/2/69-C1G

Figure 61. Heat Exchanger Element Cold Flow Recess = 0, $w_f = 0.022$ lb/sec



1XX44-10/2/69-C1A

Figure 62. Heat Exchanger Element Cold Flow, Recess = 0.107 inches
 $\dot{w}_f = 0.022$ lb/sec



Rocketdyne

1XX44-10/2/69-C1J

Figure 63. Heat Exchanger Element Cold Flow Recess = 0.500 inches,
 $\dot{w}_f = 0.022$ lb/sec

Injector Cold Flow Tests

Complete injectors using pentad and triplet elements were cold flowed to determine impingement, atomization, distribution, and pressure drop characteristics. The concentric element injector was cold flowed to obtain atomization and pressure drop characteristics. The distribution tests were conducted using a 29 by 29 tube collection matrix with water and helium simulating the FLOX and methane respectively. The liquid distribution for test conditions was calculated to yield a penetration factor, X_p/D_g , of 0.5 indicate a mass distribution index $(1-\sigma)$ of approximately 99.85 percent for both injectors.

Pressure drop data for the three triplet injectors, the pentad injector, and the concentric injector are shown in Fig. 64 for water flow calibrations. Pressure drops with FLOX were calculated to be approximately 72 percent of the pressure drops with water at the same flowrate. The different pressure drop curves for the triplet injector reflect variations in the oxidizer orifice diameters. Photographs of the three injector types flowing water and low-pressure air (photography at the distribution test facility was not practical) are shown in Figs. 65, 66, and 67.

The mixture ratio variation from element to element was estimated by flowing air through the fuel and oxidizer sides of each element of the heat exchanger and recessed post injectors. The mixture ratio distributions are shown in Figs. 68 and 69 for both injectors, based on an overall mixture ratio of 5.25. The average mixture ratio in the outer row of the heat exchanger injector was 4.90.

The effect of the mixture ratio variation was calculated on the basis of uniform mixing in each element and no mixing of the flows between elements. The overall injector performance is

$$C^* = \frac{1}{\dot{w}_t} \sum_{i=1}^{61} \dot{w}_i C^*_i$$

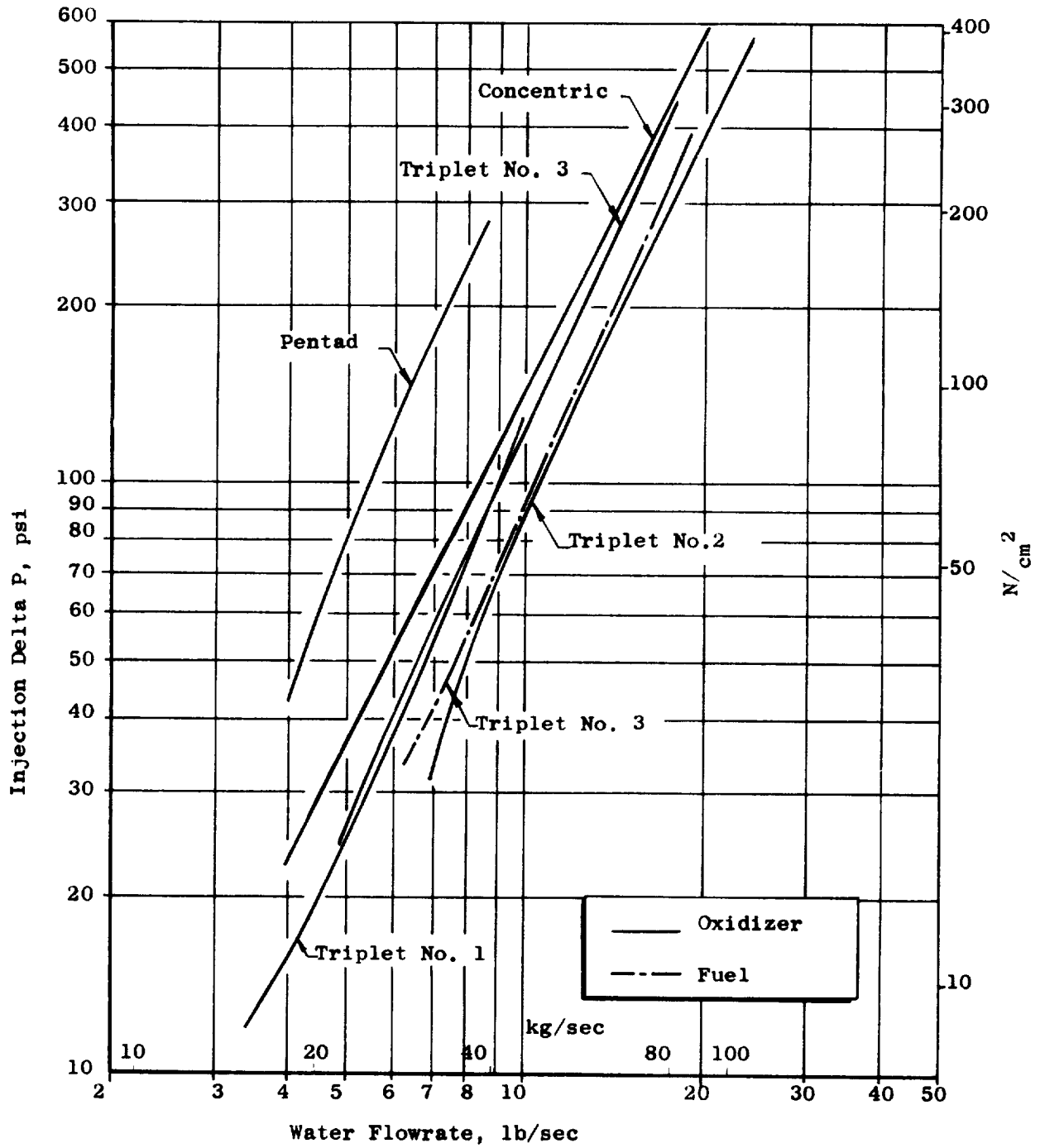
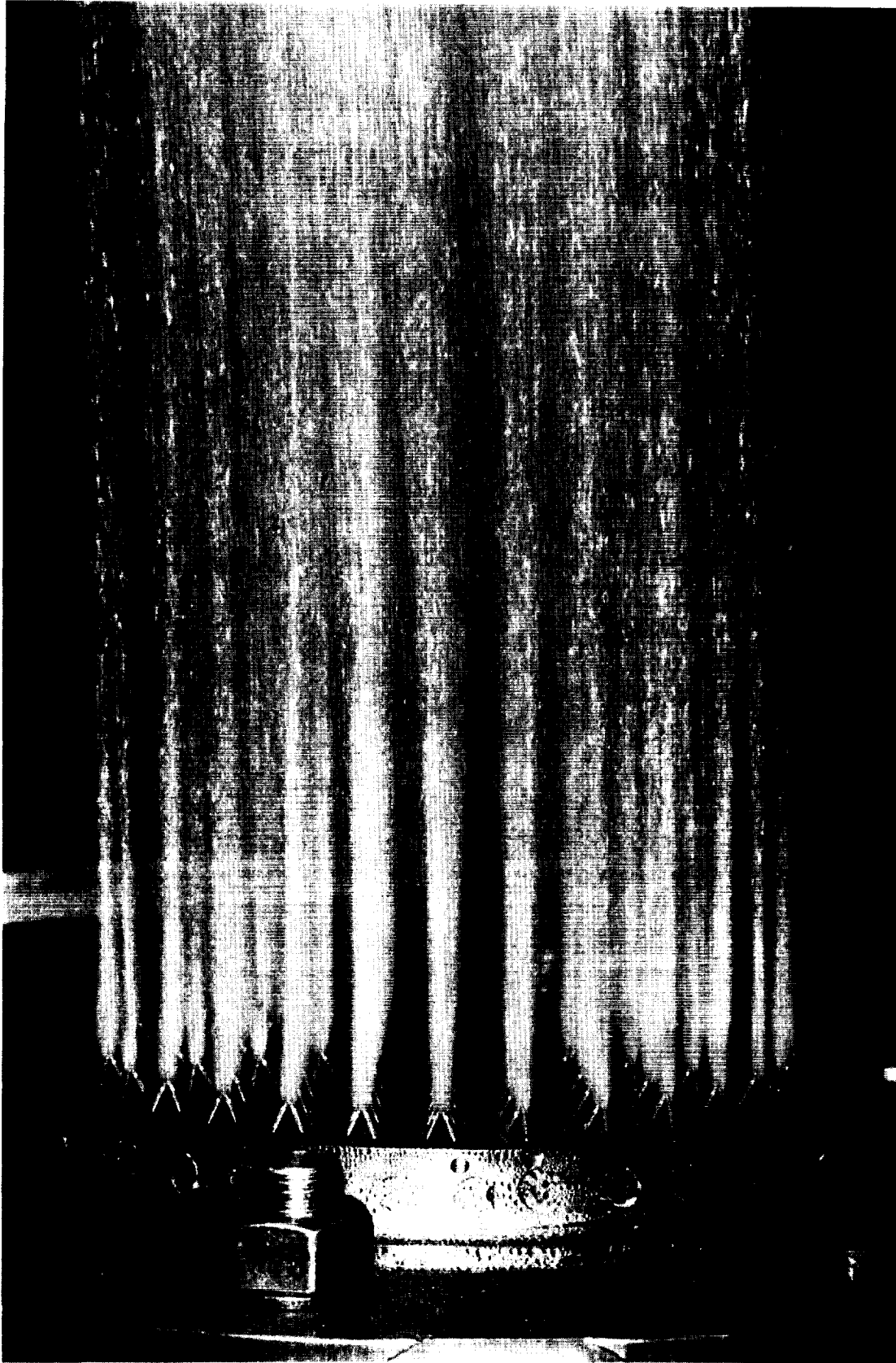


Figure 64 . Injector Water Calibration Data



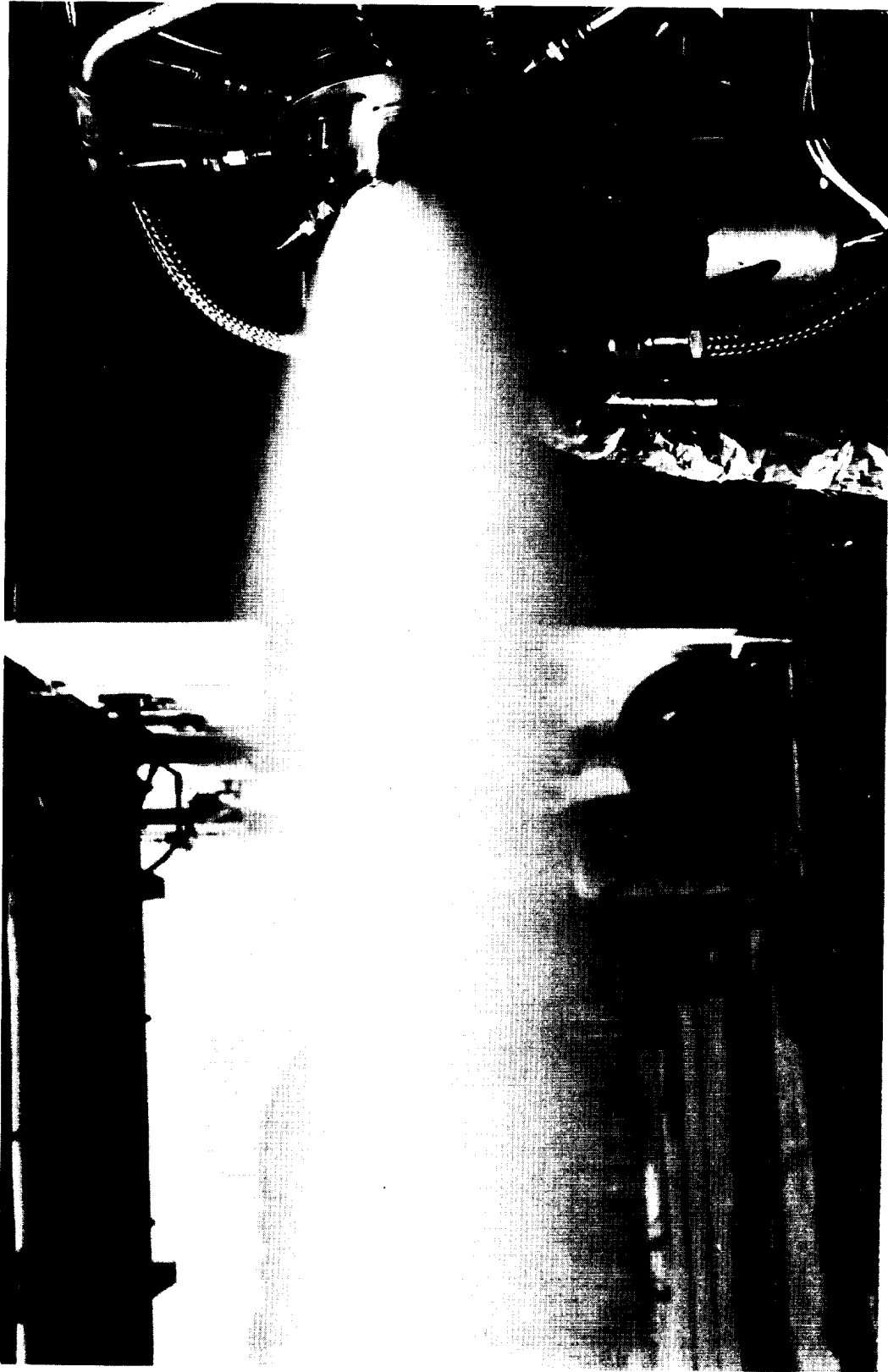
5AA34-5/22/68-S1B

Figure 65 . Water Flow of Triplet Injector



1XX44-6/5/68-S1B

Figure 66 . Water Flow of Pentad Injector



5AJ34-10/2/68-S1A

Figure 67. Concentric Element Injector Cold Flow Test

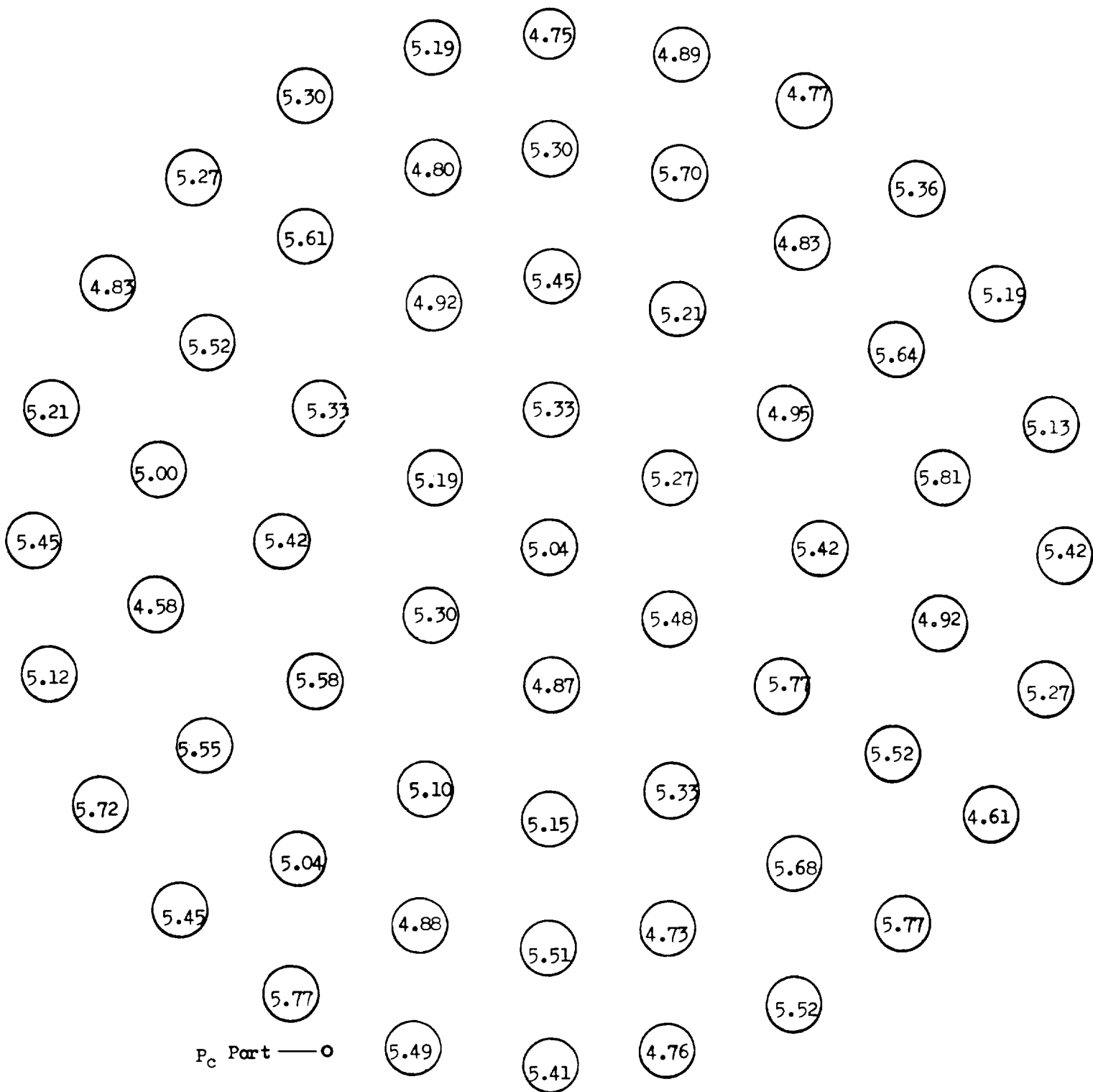


Figure 68. Mixture Ratio Distribution in Recessed Post Injector

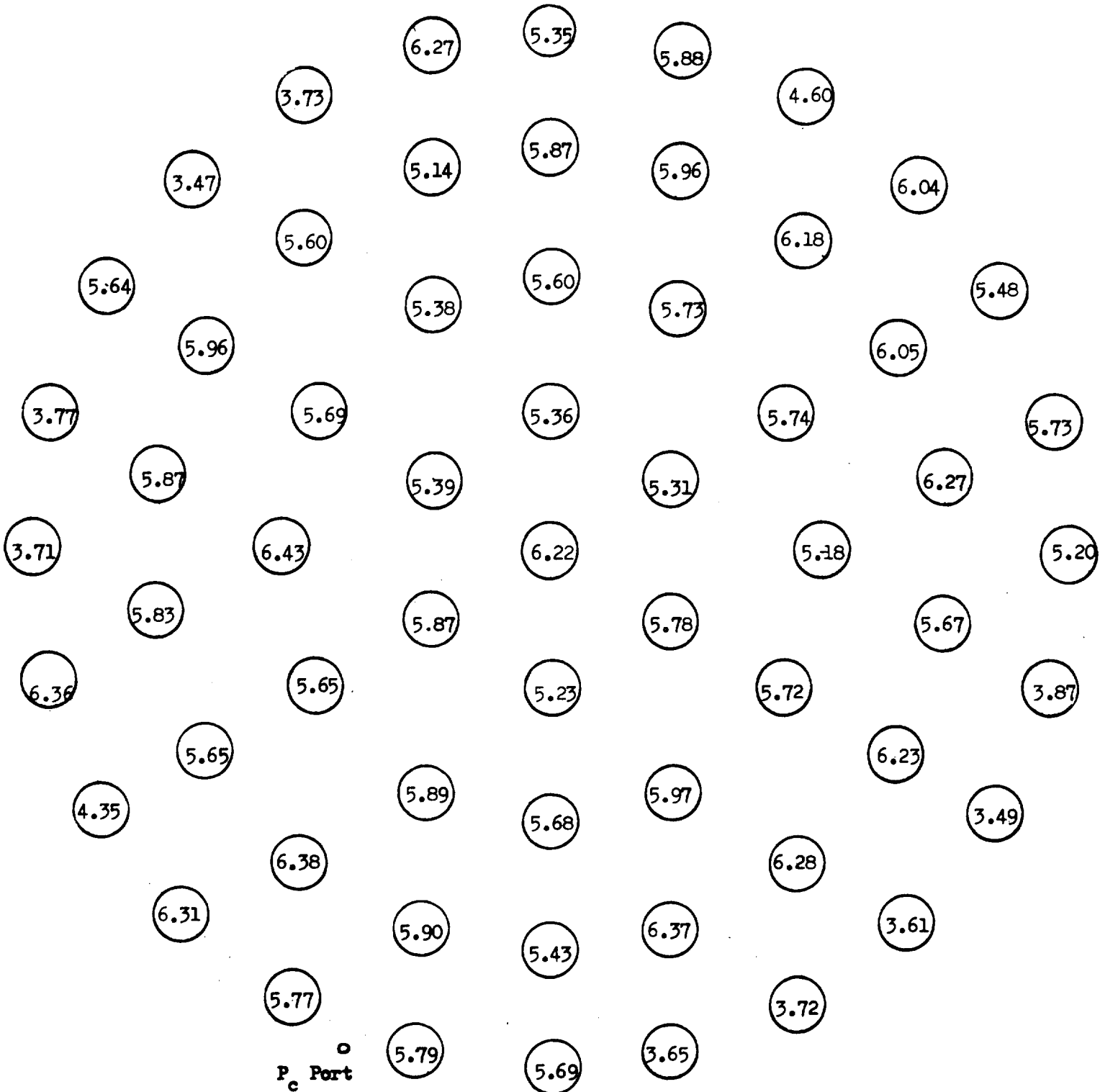


Figure 69. Mixture Ratio Distribution in Modified Heat Exchanger Injector

where \dot{w}_t is the total injector flowrate, \dot{w}_i is the flow in the i^{th} element, and C^*_i is the performance of the i^{th} element. The overall performance of the heat exchanger injector was calculated to be 98.5 percent of the performance of an injector having a uniform mixture ratio of 5.25. The mixture ratio distribution of the recessed post injector is seen to be much more uniform than that of the heat exchanger injector. The performance loss resulting from mixture ratio variations was calculated to be 0.5 percent for the recessed post injector.

HOT FIRING TESTS

The purpose of these tests was to determine and compare the performance, heat transfer, and stability characteristics of various types of injectors over a range of operating conditions. Triplet, pentad, and concentric element injectors were tested in solid and water-cooled chambers at sea level and altitude conditions. All three injectors were tested at sea level and the concentric element injector was also tested at simulated altitude conditions. A total of 32 tests were conducted at chamber pressures ranging from approximately 500 to 900 psia (345 to 623 N/cm²) and mixture ratios ranging from 3.5 to 6.8.

Experimental Equipment

The chambers and injectors tested are described in Section II. In addition to this hardware a solid-wall thrust chamber fabricated for an IR&D program was available for testing. This chamber was fabricated in two sections, the throat section and the cylindrical combustion zone. Both sections had cylindrical steel outer cases (structural). The throat contour was formed by a graphite insert. A copper liner provided heat sink capability in the combustion zone. High speed and normal instrumentation taps were provided for chamber pressure measurement. Operating durations were limited to 1-3 seconds depending upon chamber pressure. The solid-wall chamber was used for the initial facility and injector checkout tests.

Test Facility

The test facilities are located in the Propulsion Research Area (PRA) (Fig. 70). The PRA is comprised of five multi-position firing pits with a centrally located blockhouse which permits direct observation of the engine firings. Test Stand Uncle was employed for the hot-firing tests.

FLOX (Oxidizer) System. The system schematic is shown in Fig. 71. The oxidizer was stored in a 5000 pound (2270 kg) storage trailer (subsequently replaced with a 120 gallon (454 liter) triple wall storage tank) and loaded into a run tank during each test day through 1 inch (2.54 cm) LN₂ jacketed lines. Procedures for the storage, transfer and handling have been established on previous Rocketdyne programs. FLOX (82% F₂ - 18% O₂) was supplied to the engine from the 2000 psi (1380 N/cm²) 43-gallon (163 liter) capacity run tank through 1-1/2 inch (4 cm) lines. The run tank was pressurized with filtered helium from a 6000 psi supply. The oxidizer flowrate was determined from two turbine flowmeters in series. Annin valves were used for the tank "pre" valve and the oxidizer main valve.

The oxidizer feed system was chilled by jacketing with LN₂ from the run tank to the engine. Pre-run chilldown of the manifold and injector was accomplished by a liquid nitrogen bleed directly through the injector into the thrust chamber, thus preventing the oxidizer from flashing in the initial portion of the firing, and thus minimizing flow transients. The chill and purge line was connected downstream of a two way main oxidizer valve for the first two tests. The final configuration using a three way valve provided positive shutoff of the purge when the FLOX valve opened.

Prior to assembly, FLOX feed system components were carefully and thoroughly cleaned in accordance with prescribed procedures (Ref. 3).

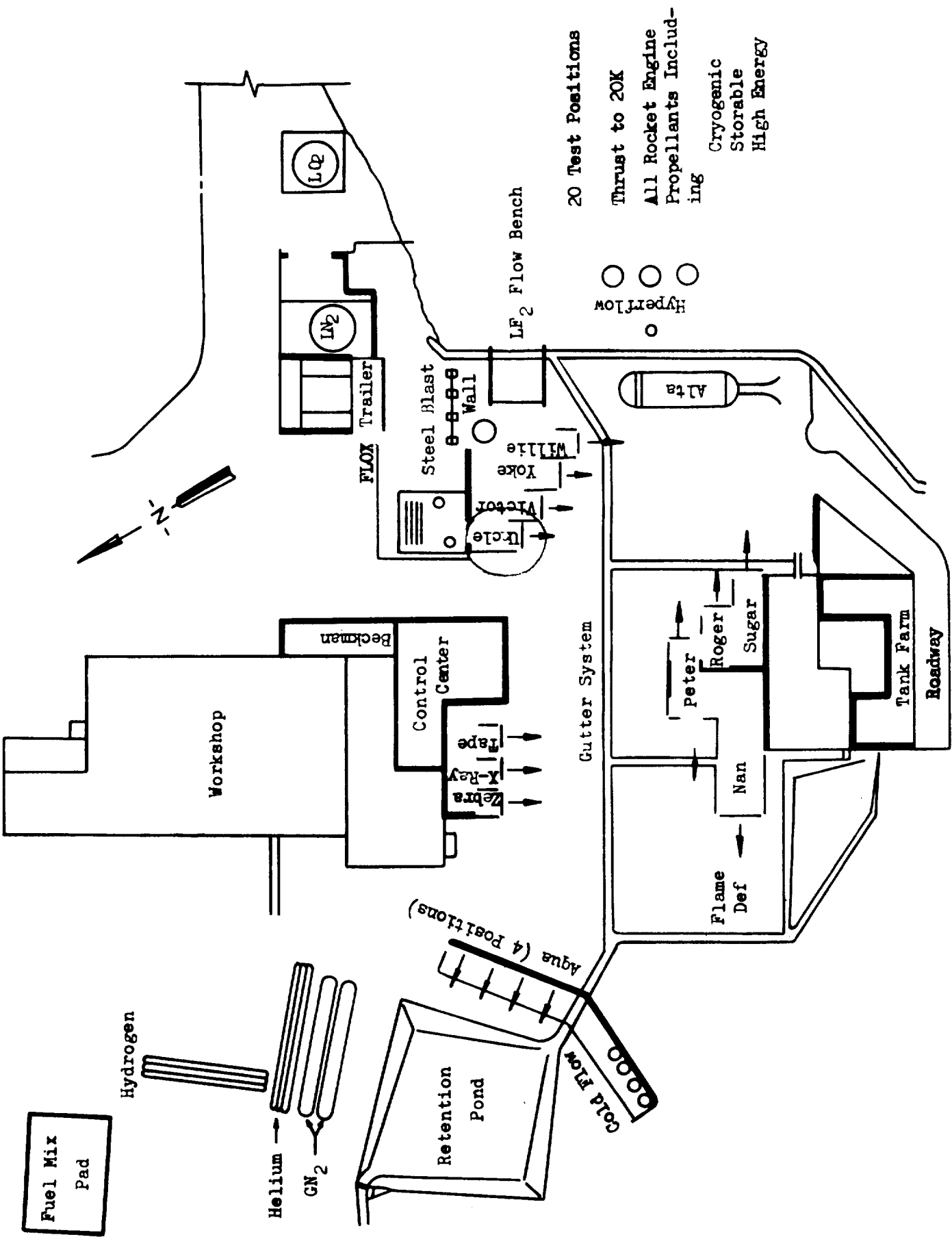


Figure 70. Propulsion Research Area

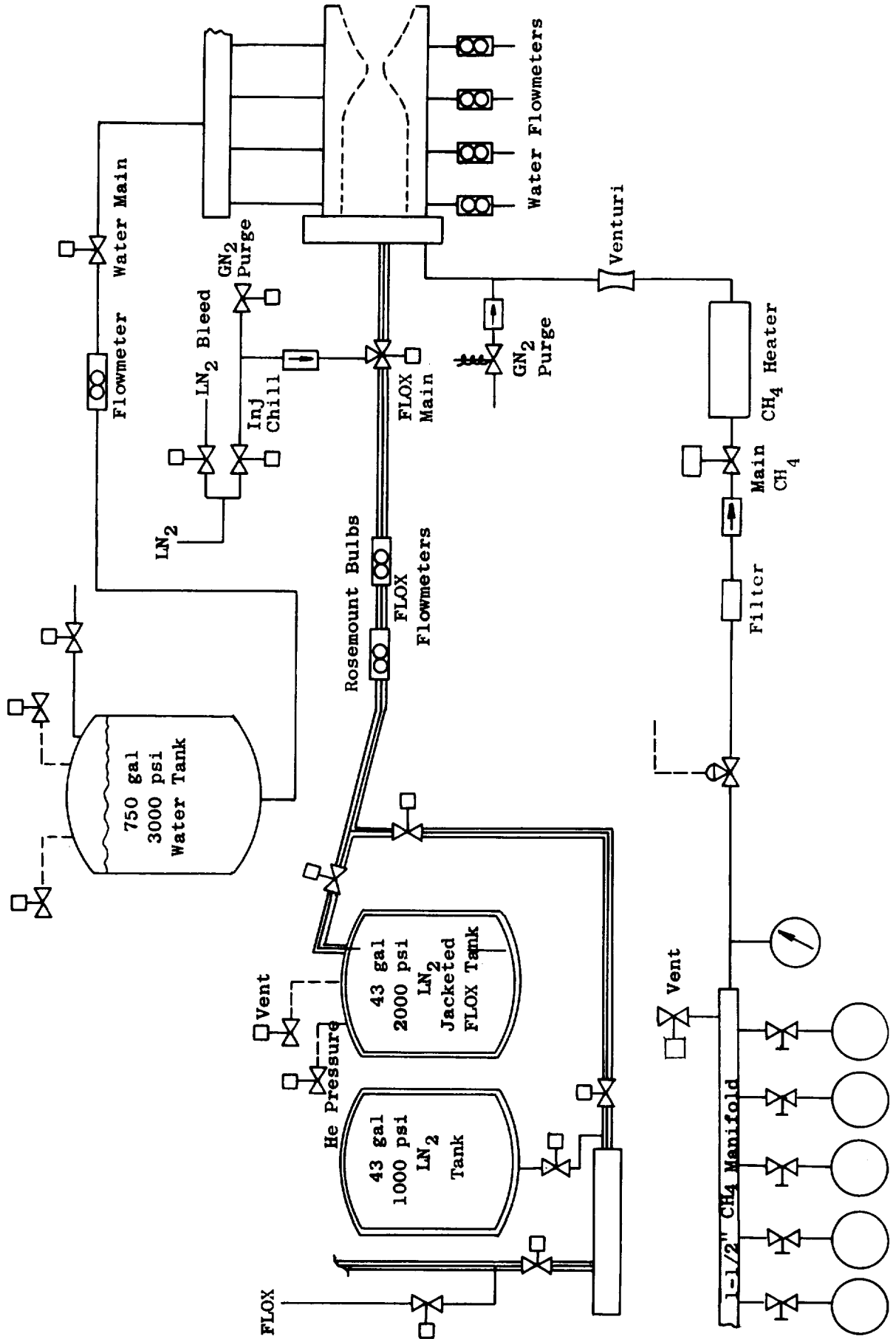


Figure 71. Facility Schematic

Passivation of the assembled system (to the main oxidizer valve), by provision of protective fluoride films on exposed surfaces, was carried out as follows: low-pressure gaseous fluorine was introduced into the system and maintained for successive 15-minute periods at 5, 10, and 15 psig; finally, 20 psig was maintained for several hours. The feed line and thrust chamber system downstream of the main valve was passivated immediately before each set of firings by flowing gaseous, then liquid FLOX through the system for short intervals of time.

Methane (Fuel) System. High purity (99 percent) methane was stored as a gas at 2400 psia (2000 N/cm^2) in twenty-six 16 pound (net weight) cylinders which were manifolded to the feed line. Methane was supplied to the engine through a 1-1/2 inch (4 cm) line to a pressure regulator and then through a 1 inch (2.5 cm) line from the regulator. A sonic venturi meter was used to measure and control the fuel flowrate. Methane was passed through a pebble-bed heat exchanger and heated to approximately 650 F (620 K) to simulate regenerative coolant jacket exit conditions. Electrically heated GN_2 was used to heat the bed prior to testing. The methane heater was designed to operate for 20 seconds with no significant temperature decay.

Propellant Vent Systems. Vent systems were provided which allow safe venting of the fuel and oxidizer. The methane manifold was vented through the facility burn stack. The oxidizer tank was vented, depending on wind conditions, through either a stack vent above the oxidizer tank or through a GH_2 afterburner.

Coolant Water System. Deionized water for the water cooled hardware was supplied to the engine from the 750-gallon (2850 liter), 3000 psig (2000 N/cm^2) tank. The water was distributed by a manifold upstream of the engine to the different engine coolant passages. Turbine flowmeters downstream of the engine were used to measure the individual passage flowrates. The coolant passages were connected in series where possible, to minimize the number of flowmeters required. The total water flow was measured upstream of the water main valve.

Purge Systems. GN₂ purges were provided to purge the transfer line, injector, and run lines. The GN₂ purge systems were supplied from a 3000 psi (2000 N/cm²) bottle bank. Individual purge pressures were set by hand loaders in the stand area. The oxidizer purge system had both a check valve and a positive closing valve to prevent contamination of the GN₂ system by the high pressure oxidizer during engine operation. The fuel purge system was protected by a check valve.

Propellant Sampling. The FLOX composition was determined at intervals during the test program. Due to safety considerations, a gas sample, rather than a liquid sample was analyzed. The gas sample was obtained remotely by complete vaporization of a liquid sample. Therefore, the gas sample was the same composition as the liquid. The methane was sampled and analyzed periodically to assure constant purity.

Altitude Diffuser. A self-pumping diffuser with the dimensions shown in Fig. 72 was fabricated from 3/8 inch (.95 cm) mild steel for the altitude simulation tests. The diffuser was designed to operate uncooled for durations consistent with solid-wall nozzle operation. The exit of the nozzle was connected to the diffuser by a steel bellows which had a very low axial spring constant (180 lb/in) to avoid significant thrust interactions, and a high lateral spring constant (16,800 lb/in) to resist side loads during start and shutdown transients. The diffuser installation is shown in Fig. 73. Inspection of the injector and forward end of the thrust chamber without disassembling the diffuser was accomplished between tests with the aid of a camera and lighting system uniquely designed for the purpose. Use of Polaroid film permitted immediate evaluation of internal hardware condition after each test.

Start Sequence. Before each firing, liquid nitrogen was bled through the main oxidizer valve to chill the FLOX inlet line.

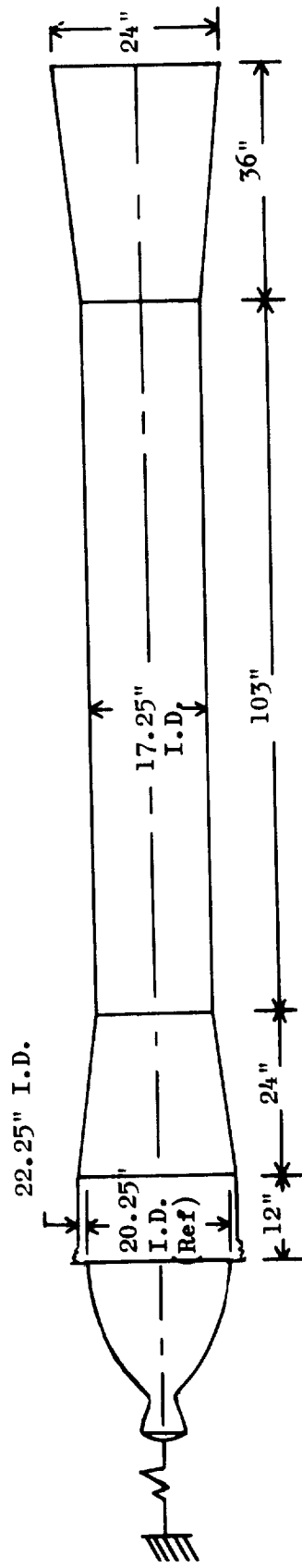


Figure 72. Diffuser Schematic



5AC36-1/22/69-SIA

Figure 73. Self-Pumping Diffuser with High Area Ratio Thrust Chamber

The firing itself was sequenced through an automatic timer which controls operation of propellant main valves, chart drives, and cameras. Coolant water and injector purges were initiated prior to test start. The purge pressures were lower than the corresponding injection pressures and were, therefore, suppressed as the injection pressures built up in addition to the positive shutoff valve on the FLOX purge system. Both fuel and oxidizer leads were utilized during the test program to determine an optimum start sequence.

Instrumentation

Facility and engine instrumentation locations are shown in Fig.74. Additional information is given in Table 13. Redundant measurements were made on the important experimental parameters to increase data reliability. The particular transducers used for the various types of measurements are described below.

The thrust chamber mount was supported on flexures, which allow free movement parallel to the engine axis (horizontally), restrained in the thrust direction by a load cell.

Pressures were measured with Taber "Teledyne" Series 206 or equivalent transducers for low frequency response and with Photocon and Kistler transducers (propellant injection and chamber pressures) for high frequency response. Chamber pressures were measured at several circumferential positions near and at the injector face and at the start of nozzle convergence. Pressures were measured at the exit and base of the high area ratio nozzle to verify full flow in the nozzle for the altitude simulation tests.

The oxidizer flowrates were measured by means of Fischer-Porter turbine flowmeters of a type proved suitable for service in FLOX. The oxidizer line had two flowmeters in series to measure the volumetric flowrate. The fuel flowrate was measured by calibrated sonic venturis.

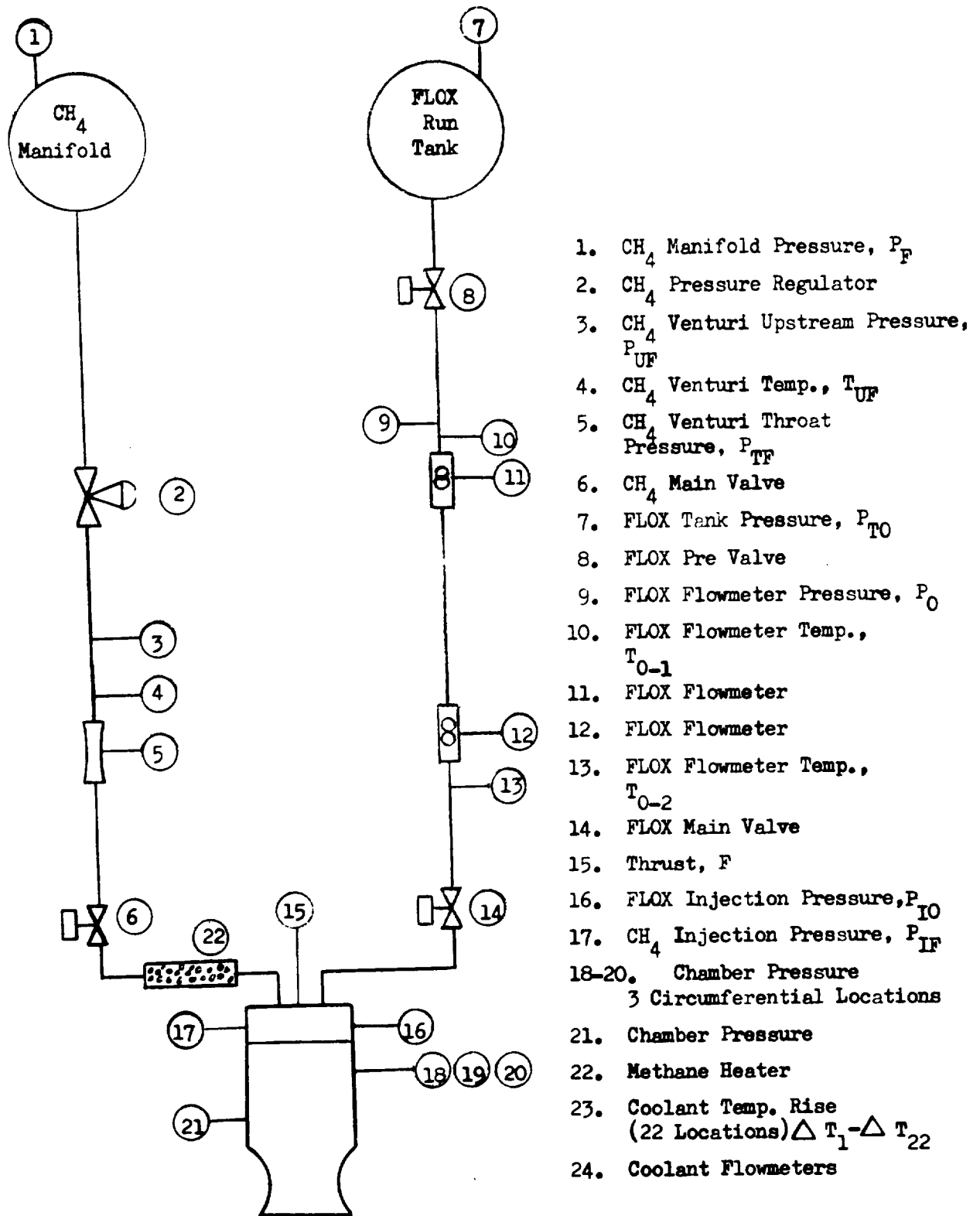


Figure 74. . Instrumentation Location

TABLE 13

INSTRUMENTATION LIST FOR TASKS III-IV TESTS

Nomenclature	Parameter Measured	Measurement and Range	Recorder	
			Beckman Oscillograph	Digital
P _{TO}	Oxidizer Tank Pressure, psig (N/cm ²)	Taber 0-2000 (0-1379)		X
P _F	Fuel Manifold Pressure	Taber 0-3000 (0-2068)		X
P _{WT}	Water Tank Pressure	Taber 0-3000 (0.2068)		X
P _{IO*}	Oxidizer Injection Pressure	Taber 0-2000 (0-1379)	X	
		Photocon 0-2000 (0-1379)	X	
P _{IF*}	Fuel Injection Pressure	Taber 0-2000 (0-1379)	X	
		Photocon 0-2000 (0-1379)	X	
P _{C-1}	Chamber Pressure	Taber 0-1000 (0-689)	X	
P _{C-2}	Chamber Pressure	Taber 0-1000	X	
P _{C-3}	Chamber Pressure	Taber 0-1000 (0-689)	X	
P _{C-4*}	Chamber Pressure	Photocon 0-1000 (0-689)	X	
P _{NE}	Nozzle Exit Pressure	Taber 0-50 (0-34)	X	
P _{NB}	Nozzle Base Pressure	Taber 0-50 (0-34)	X	
P _{UF}	Fuel Venturi Upstream Pressure	Taber 0-3000 (0-2068)	X	
P _{TF}	Fuel Venturi Throat Pressure	Taber 0-3000 (0-2068)	X	
P _O	Oxidizer Flowmeter Pressure	Taber 0-2000 (0-1379)	X	
P _{W2}	Water Manifold Pressure	Taber 0-2500 (0-1723)		X
P _{NF}	Fuel-GN ₂ Purge Pressure	Gage 0-2000 (0-1379)		
P _{NO}	Oxidizer GN ₂ Purge Pressure	Gage 0-2000 (0-1379)		
F	Thrust, pounds (Newtons)	Baldwin 0-10,000 (0-44,500)	X	
T _{IO}	Oxidizer Injection Temp., F (K)	I/C, -240 to -305 (86 to 122)	X	
TO-1	Oxidizer Temperature at Flowmeter	R.B.** -290 to -310 (83 to 95)	X	
TO-2	Oxidizer Temperature at Flowmeter	R.B. -290 to -310 (83 to 95)	X	

TABLE 13 (Continued)

<u>Nomenclature</u>	<u>Parameter Measured</u>	<u>Measurement and Range</u>	<u>Recorder</u>	
			<u>Beckman</u>	<u>Oscillograph Digital</u>
T _{IF}	Fuel Injection Temperature, F (K)	I/C 60 to 1000 (289 to 812)	X	X
T _{UF}	Fuel Upstream Venturi Temp., F (K)	I/C 60 to 1000 (289 to 812)	X	
T _{WL}	Water Manifold Temperature, F (K)	I/C 60 to 1000 (289 to 812)	X	
TW-1 to TW-22	Water Temp Rise thru Engine, F (K)	C.A. 10 to 70 Rise (5.6 to 39)	X	X
TC-1 to TC-9	Chamber Wall Temperature, F (K)	C.A. 60 to 1500 (289 to 1090)	X	
TN-1 to TN-11	Nozzle Wall Temperature, F (K)	C.A. 60 to 1500 (289 to 1090)	X	
WO-1	Oxidizer Flow, gpm (l/sec)			
WO-2	Oxidizer Flow, gpm (l/sec)	F.P.***36 to 120 (2.27 to 7.57)	X	X
WW-1 to WW-9	Water Flowrate, gpm (l/sec)	F.P. 5 to 20 (0.32 to 1.26)	X	X

* Also recorded on high speed tape

** Rosemount Bulb

*** Fisher-Porter

Reliable measurement of cryogenic propellant flowrates requires accurate determination of liquid density as well as of volumetric flowrate. Density of cryogenic propellants is a sensitive function of temperature; therefore, it is important to make accurate measurements of propellant temperature as close to the flowmeters as practical. This was done by use of shielded platinum resistance bulbs (Rosemount Model 176) immersed in the liquid stream. These instruments are very sensitive to temperature changes in the cryogenic region and are the preferred method of measurement.

The temperature rise of the water in each of 22 coolant passages was measured with 3-element iron-constantan thermopiles to provide a finely incremented heat flux profile. Temperature measurements at several circumferential locations in a land near the injector were made to provide circumferential heat flux data. Temperature measurements in eleven copper plugs and eight back wall locations in the solid wall nozzle were made to obtain data for determining the axial and circumferential heat flux profiles in the nozzle.

Data Recording

All pressure, temperature, and flow measurements were recorded on tape during each firing by means of a Beckman Model 210 Data Acquisition and Recording System. This system acquired analog data from the transducers, which it converted to digital form in binary-coded decimal format. The latter were recorded on tapes which are then used for computer processing.

The Beckman Data Acquisition Unit sequentially sampled the input channel at a rate of 5625 samples per second. Programmed computer output consists of tables of time versus the average parameter value (in engineering units), over an approximately 200 ms time slice printed out at approximately 200-millisecond intervals during the firing, together with calibration factors, prerun and postrun zero readings, and related data. The instantaneous

parameter values were machine-plotted and displayed on appropriately scaled and labeled grids for simple determination of gradients, establishment of steady state, etc.

Primary data recording for these firings used the Beckman 210 System. In addition, the following auxiliary recording systems were employed:

1. An 8-channel, Brush, Mark 200 recorder was employed in conjunction with the Beckman unit, primarily to establish time intervals for computer data reduction and, additionally, for "quick look" information on the most important parameters. This is a direct-inking system, with display on high-gloss, graduated paper moving at 20 mm/sec.
2. A CEC, 36-channel, direct reading oscillograph was used as backup for the Beckman 210 System and for indication of any oscillatory combustion.
3. Direct-inking graphic recorders (DIGR's), either Dynalog rotary chart or Esterline-Angus strip chart, were used to set prerun propellant supply pressures, for recording of propellant manifold pressures, to provide quick-look information, and as secondary backup to the Beckman and oscillograph recorders.
4. An Esterline-Angus, 20-channel event recorder was used for direct-inking recording of main propellant valve signal and travel, as well as for chart drive and camera actuations.
5. An Ampex, Model FR-100, 54 khz tape recorder was used to record the output from the high frequency transducers.

Test Summary

The tests conducted in Tasks III and IV are summarized in Tables 14 thru 16. A total of 32 tests was conducted, 22 at sea level and 10 under simulated altitude conditions. One test was conducted with the pentad element injector, 19 with triplet element injectors, and 12 with concentric element injectors. The solid-wall chamber was used for 14 tests and the water-cooled chamber for 18 tests. The experimental hardware is described in Section II. The first series of tests was conducted at sea level in the solid wall chamber ($\epsilon = 4$) to check out the facility and injectors.

One test was conducted with the pentad injector. A detonation in the FLOX system (probably in the injector manifolds) during propellant priming damaged some of the FLOX manifold plugs. As a result of the FLOX leakage, the injector face was burned around the circumference. The injector was damaged beyond repair. The copper liner in the combustion chamber was also damaged and was replaced.

Seven tests were conducted with the first triplet injector in the solid-wall chamber to determine a satisfactory start sequence. Various oxidizer and fuel leads were sequenced. A short FLOX lead was found to produce the smoothest start transient. The first test conducted with the triplet injector resulted in high frequency combustion instability but no hardware damage. The instability was ascribed to unusually warm FLOX ($\sim 260R$). No cases of high frequency instability occurred with colder (160R) FLOX except on Test 9. Examination of the injector after Test 9 disclosed an interpropellant leak resulting from a mechanical defect in the copper injector body.

Slight erosion of the copper chamber was observed after the fourth test with the triplet injector (Test 5). The injector was then modified to the TIA configuration by adding 12 methane showerhead

TABLE 14
SEA LEVEL TESTS IN SOLID WALL CHAMBER

Test	Injector	Duration, sec	Chamber Pressure		Mixture Ratio	Pro- pellant Lead	Comments
			psia	N/cm ²			
SL1	Triplet #1	0.3	500	345		Fuel	Unstable. Warm FLOX.
SL2	Pentad	0.3	500	345		Fuel	Extended chill. Injector damaged during start.
SL3	Triplet #1	0.2	500	345		Fuel	Replumbed FLOX system. Stable
SL4	Triplet #1	0.2	500	345		Oxidizer	Stable. Smooth start.
SL5	Triplet #1	0.5	493	340	6.5	Oxidizer	Stable. Smooth start.
SL6	Triplet #1A	0.2	500	345		Fuel	LN ₂ used during fuel lead. Hard start. Stable.
SL7	Triplet #1A	0.2	500	345		Fuel	LN ₂ and GN ₂ sequence. Smooth start. Stable.
SL8	Triplet #1A	1.0	487	336	6.66	Fuel	Smooth start. Stable.
SL9	Triplet #1A	0.3	500	345		Fuel	Unstable. Interpropellant leak.
SL10	Concentric	0.2	520	359		Fuel	Hard start. Hardware OK.
SL11	Concentric	1.1	525	362	5.07	Fuel	Hard start. Fuel sleeves burned. Face damage. High performance.
SL12	Triplet #2	0.1	500	345		Oxidizer	Smooth start. Stable.
SL13	Triplet #2	1.1	514	354	6.61	Oxidizer	Smooth start. Stable.
SL14	Triplet #2	2.2	519	358	6.26	Oxidizer	Smooth. Stable. Injector OK T/C eroded locally. High performance.

TABLE 14 (Cont'd)
SEA LEVEL TESTS IN WATER COOLED CHAMBER WITH INJECTOR T2A

<u>Test</u>	<u>Duration</u>	<u>Chamber Pressure</u>		<u>O/F</u>	<u>Comments</u>
		<u>psia</u>	<u>N/cm²</u>		
SL15	0.5	500	345		Smooth start. Stable.
SL16	1.0	495	341	6.8	Smooth start. Stable.
SL17	2.0	515	355	3.6	125 psi 500 cps buzz. T/C and injector OK.
SL18	3.0	550	379	5.0	Smooth start. Stable.
SL19	6.0	500	345	4.5,4.9	40, 25 psia buzz. T/C and inj. OK.
SL20	4.0	505	348	4.8	Stable.
SL21	4.0	500	345	6.5	Stable.
SL22	3.7	500	345	5.7	Most data good. Low water flow in channels 1, 2, and 3. T/C and injector burned.

TABLE 15
 ALTITUDE TESTS - WATER-COOLED CHAMBER AND SOLID NOZZLE - CONCENTRIC INJECTOR

<u>Test</u>	<u>Duration</u>	<u>Chamber Pressure</u>		<u>O/F</u>	<u>Comments</u>
		<u>psia</u>	<u>N/cm²</u>		
ALT1	0.5	550	379		Checkout. Shortened (22 in. L*) chamber. Concentric injector. Good start.
ALT2	2.0	580	400	3.94	Good start. Stable.
ALT3	3.5	524	361	3.46	1 FLOX post burned and repaired.
ALT4	3.0	512	353	4.67	Good start. Stable.
ALT5	3.0	512	353	5.70	Good start. Stable.
ALT6	3.0	707	488	4.75	Good start. Stable.
ALT7	3.0	500	345	5.71	Diffuser did not pump down.
ALT8	3.0	715	493	4.08	Good start. Stable.
ALT9	3.0	713	492	5.70	Good start. Stable.
ALT10	2.0	888	612	4.76	Chamber eroded locally by injector streak.

orifices (0.031 inch diameter) around the perimeter of the face. None of the tests on this injector were of sufficient duration to obtain a very accurate value of C^* . However, the performance indicated on Test 8 was encouraging and data obtained on Contract NASw-1229 with a very similar injector at 100 psia chamber pressure also indicated high C^* efficiency. Therefore, an identical triplet injector, T2, was fabricated and tested.

Eleven tests were conducted with the second triplet injector. The first three tests were conducted in the solid-wall chamber. Local erosion of the copper chamber near the injector was noted after the third test which was conducted at a mixture ratio of 6.26. FLOX orifices in 8 of the elements near the perimeter were plugged to provide a more uniform mixture ratio distribution. This configuration, T2A, was tested in the water-cooled chamber at chamber pressures of 495 to 553 psia (340 to 382 N/cm^2) and propellant mixture ratios of 3.64 to 7.55. The first two tests were of 0.5 and 1.0 seconds duration. Smooth starts and stable operation were obtained. C^* efficiency based on chamber pressure was approximately 98 percent. Carbon streaks along the wall at the location where the oxidizer orifices were removed verified that the previous FLOX-rich condition had, indeed been over-corrected. Schedule limitations, however, did not permit optimization of the performance vs heat transfer characteristics of the injector.

The next test, Test 17, demonstrated that steady state performance and throat heat transfer data could be achieved in tests of 2 seconds duration. The low mixture ratio resulted in fairly severe (± 120 psi) oscillations in chamber pressure at 500 cps because of the low oxidizer injection pressure drop.

The oxidizer injection pressure was increased on Test 18 and smooth operation resulted. Steady state heat transfer data was achieved on all 23 coolant passage water temperatures

except the passage located at $\epsilon = 6$ which nearly reached the equilibrium value by the end of the three second test. The injector/dome seal is effected by a pair of concentric hollow steel rings with pressurized GN_2 between them. GN_2 leakage into the chamber was noted after the test and the inner ring was replaced.

Test 19 was run for 6.0 seconds with a programmed step variation in the fuel flowrate during the test. A 500 cps chamber pressure oscillation occurred of ± 70 psi during the first (lower mixture ratio) half of the test which decreased to ± 50 psi during the latter half. The duration of this test allowed all components to reach equilibrium temperature. The hardware was in good condition indicating that no thermal problems exist in the 500 psia (345 N/cm^2) chamber pressure operating region.

Test 20 was 4.0 seconds duration and was stable. Thus, it appears that injector/facility interactions occur only in the low chamber pressure and low mixture ratio corner of the operating envelope. This condition could be relieved by decreasing the oxidizer orifice diameter slightly on subsequent triplet injectors.

A facility modification was made prior to Test 21 to reduce the fuel feed system pressure drop. Propellant mixture ratio was high but the test was otherwise normal and the hardware was in good condition after the test.

Test 22 was terminated because of a fire. Test data indicated that the water in the coolant passages near the injector was frozen by the injector purges. The purges had been left on and the water turned off after the previous test. The injector was destroyed and the forward end of the chamber was eroded. The chamber was repaired by removing the forward end and welding on another flange. The L^* of the chamber was thus reduced from 30 inches to 24 inches (76 to 60 cm). Corrective operating

procedures included allowing the water to run under tank head pressure between tests and verification of operation of all water flowmeters immediately prior to test start.

Two tests were conducted with the first concentric element injector in the solid-wall chamber. This injector had a Rigimesh face and steel fuel tubes which were flared against the Rigimesh. A fuel lead was used on both of these tests (Tests 10 and 11) and hard starts resulted in each case. No damage occurred on the first test. After the second test the Rigimesh face was deformed and the steel tubes were eroded. The injector dome, FLOX body, and the thrust chamber were in good condition. A high C^* efficiency was indicated.

Another fuel body for the concentric element injector was fabricated of solid copper for improved thermal and mechanical durability. This injector was tested 10 times with the shortened water-cooled combustion chamber and the solid high-area-ratio (60:1) nozzle. Chamber pressure and propellant mixture ratio ranges during this test series were approximately 500 to 900 psia (345 to 620 N/cm^2) and 3.46 to 5.7 respectively. One FLOX post in the outer row was slightly burned during the third altitude test and was repaired. The damage was caused by a metal chip blocking the methane flow in the annulus. No other injector damage was sustained during the test series. The diffuser did not start on Test ALT 7 and resulting recirculation flow burned the bellows.

Tests ALT 8 & 9 were conducted at approximately 700 psia (480 N/cm^2) to cover the range of propellant mixture ratios from 4.0 to 5.7. Inspection of hardware internally between tests was accomplished photographically by means of a special camera and lighting system which is inserted from the exit end of the diffuser to the throat of the thrust chamber. The camera was primarily designed to show the condition of the injector and has served this purpose excellently. No injector damage was apparent after these tests. The combustion chamber wall generally had a very thin hard carbon coating after operation although the characteristics of the deposition varied around each element in

the outer row of the injector. These variations appeared particularly prominent at two locations after these tests. However, no indication of copper erosion was seen.

Test ALT 10 was, fortunately, terminated prematurely at 2.6 seconds (3.0 seconds intended) for a small fire in the engine area. The fire was, apparently, either imaginary or a small fire caused by one of the electric heaters on the fuel line. Post test inspection revealed a carbon-free streak extending from the injector to the end of the nozzle. At various locations along this streak: 1) erosion occurred in the converging section of the thrust chamber and at the thrust chamber/nozzle interface; 2) a small hole was burned in the passage upstream of the throat (passage 17, one of the two passages which record the highest heat flux); 3) a larger hole was burned in the fourth passage upstream of the throat (passage 14). A second streak persisted as far as the throat and resulted in erosion but no leakage. The gasket seal between the nozzle and diffuser bellows leaked after the test but base and nozzle pressures appeared normal during the test. Apparently the gasket was worn.

Test records indicate failure of passage 17 approximately 1.9 seconds after start with failure of passage 14 following 0.2 seconds later. The circumferentially averaged heat flux values at passages 14 and 17 were 20.5 and 30.1 Btu/in²-sec (3.0 and 4.4 KW/cm²) respectively. The burnout heat fluxes calculated for these passages, assuming fully developed water flow, were 31.0 and 48.2 Btu/in²-sec (4.6 and 7.1 KW/cm²) respectively. The respective cooling margins were, therefore, 51 and 60 percent. This would imply a severe excess heat flux. However, the coolant path is such that the water flow enters each channel through an inlet port, splits in half so that each half of the flow cools 180 degrees of the channel, then reconverges at the exit port. Conditions at the channel near the exit port represent some degree of stagnation of the coolant flow. The burned-through area

of passage 14 was located at the exit port. The burned area of passage 17 was approximately one-half inch (1 cm) from the exit port. The average heat flux measured by passage 16, which had no ports near the streak and was not damaged, was $31.2 \text{ Btu/in}^2\text{-sec}$ (4.6 KW/cm^2) and the predicted burnout value was $46.6 \text{ Btu/in}^2\text{-sec}$ (6.85 KW/cm^2). The safety margin, 43 percent, was lower for this passage than for either of the burned channels. It, therefore, appears that the failure was caused by a combination of injector streaking and undercooling near the passage outlets.

The annular gaps were measured on each of the 24 outer elements of the concentric injector. There was no gap adjacent to the wall where maximum streaking occurred. The FLOX post of this element had been previously repaired and was 2-1/2 mils (0.03 mm) larger in diameter than the other posts which were all within a $\pm 1/2$ mil (.025 mm) variation band.

The injector was repaired by remachining the larger FLOX post and truing the fuel holes to obtain a gap of 9 mils (0.23 mm). Additionally, since some variation in mixture ratio was evidenced on the chamber wall by each element, a fuel showerhead orifice was located between each outer element and the chamber wall. These 0.032 inch (0.080 cm) diameter orifices flow 4 percent of the total fuel flow or 0.6 percent of the total propellant flow at a mixture ratio of 5.7. If it is assumed that the showerhead flow reacts with half the flow from the outer elements the effect on C^* efficiency was calculated to be less than 1 percent. This assumption leads to a calculated mixture ratio reduction of 20 percent near the wall, e.g., a wall mixture ratio of 4.7 at an overall mixture ratio of 5.7. Experimental data indicates a reduction of 15 percent would be expected to result in the peak heat flux because of the lower mixture ratio near the wall. The injector, thus modified, was used for the regeneratively cooled tests described in Section IV.

Test Results

Two basic types of data were generated during these tests: performance and heat transfer. The performance data is expressed in terms of characteristic velocity, C^* , vacuum specific impulse, $I_{s\text{vac}}$, and their related efficiencies. Heat transfer data is presented as heat flux profiles and total heat input values. Data reduction procedures are described in Appendix F.

Performance. Characteristic velocity values were calculated for the triplet injector based on chamber pressure and thrust data. Thrust data could be used to calculate C^* because this test series was conducted with a short ($\epsilon = 6$) nozzle which had very small kinetic and boundary layer losses. Data from tests of 2 seconds or longer duration were used. The C^* efficiencies are presented in Table 17 and plotted in Fig. 75 to show the good agreement between the efficiencies calculated both ways.

A comparison of the C^* efficiencies of the triplet and concentric injectors is shown in Fig. 76. The concentric injector achieved higher performance at lower propellant mixture ratio while the triplet injector performed best at higher mixture ratios. However, the triplet injector buzzed at the lowest mixture ratios and it was felt that elimination of this buzz would improve performance significantly in this operating region. Both the triplet and the concentric element injectors achieved approximately 98 percent C^* efficiency at the design point of 500 psia (345 N/cm^2) chamber pressure and 5.25 propellant mixture ratio. The efficiencies were calculated using theoretical values of C^* based on the injection temperature of the methane. C^* efficiencies would be approximately 0.5 to 1.0 percent higher if the theoretical values of C^* were based on the ambient boiling temperature of methane. The triplet element injector achieved this efficiency in a chamber with an effective L^* of approximately 29.5 inches (75 cm). (The L^* of the chamber was 30 inches (76 cm) but the injector was

TABLE 17
WATER-COOLED TEST PERFORMANCE SUMMARY

Test	Chamber Pressure		\dot{w}_o		\dot{w}_f		O/F	C^*P_{Exper}		C^*_{Theo}		C^*P	$\eta_{C^*}^{\text{injP}}$	F_{Site}		F_{vac}		$\eta_{C^*}^{\text{injF}}$
	psia	N/cm^2	lb/sec	kg/sec	lb/sec	kg/sec		ft/sec	m/sec	ft/sec	m/sec			lb	kg	lb	kg	
SL17	516.1	356.2	10.43	4.73	2.86	1.297	3.65	6616	2017	6986	2129	94.2	94.7	3556	15,830	3993	17,780	94.5
SL18	552.6	381.4	11.08	5.02	2.20	0.998	5.03	7080	2158	7155	2181	98.4	98.9	3822	17,020	4258	18,940	98.1
SL19	499.6	344.8	10.14	4.60	2.07	0.939	4.89	6963	2122	7143	2177	96.9	97.4	3407	15,150	3843	17,110	96.5
SL20	507.5	350.0	10.11	4.59	2.11	0.957	4.78	7066	2154	7142	2176	98.4	98.9	3495	15,560	3931	17,500	98.6
SL21	481.3	332.3	10.73	4.87	1.42	0.644	7.56	6740	2054	6651	2027	100.8	101.2	3312	14,740	3748	16,680	101.5
SL22	499.2	344.6	10.40	4.72	1.63	0.739	6.37	7056	2150	6925	2111	101.3	101.7	3464	15,410	3900	17,350	101.9
A2	579.7	400.0	11.28	5.12	2.86	1.297	3.94	6976	2126	6976	2126	99.4	99.6					
A3	524.6	364.2	9.95	4.51	2.87	1.302	3.46	6964	2123	6873	2095	100.8	101.0					
A4	511.8	353.2	10.28	4.66	2.20	0.998	4.67	6965	2124	7113	2168	97.4	97.6					
A5	512.2	353.7	10.59	4.80	1.86	0.844	5.70	6986	2129	7143	2177	97.2	97.5					
A6	707.3	488.1	14.21	6.45	2.99	1.356	4.75	6986	2129	7138	2176	97.3	97.4					
A7	499.9	344.0	10.43	4.73	1.83	0.830	5.71	6928	2112	7138	2176	96.5	97.6					
A8	715.0	493.5	14.05	6.37	3.44	1.560	4.08	6945	2117	7017	2139	98.4	98.5					
A9	713.4	492.3	15.00	6.80	2.63	1.193	5.70	6874	2095	7180	2188	95.2	95.3					
A10	887.8	612.4	18.18	8.25	3.82	1.733	4.76	6853	2089	7155	2181	95.2	95.3					

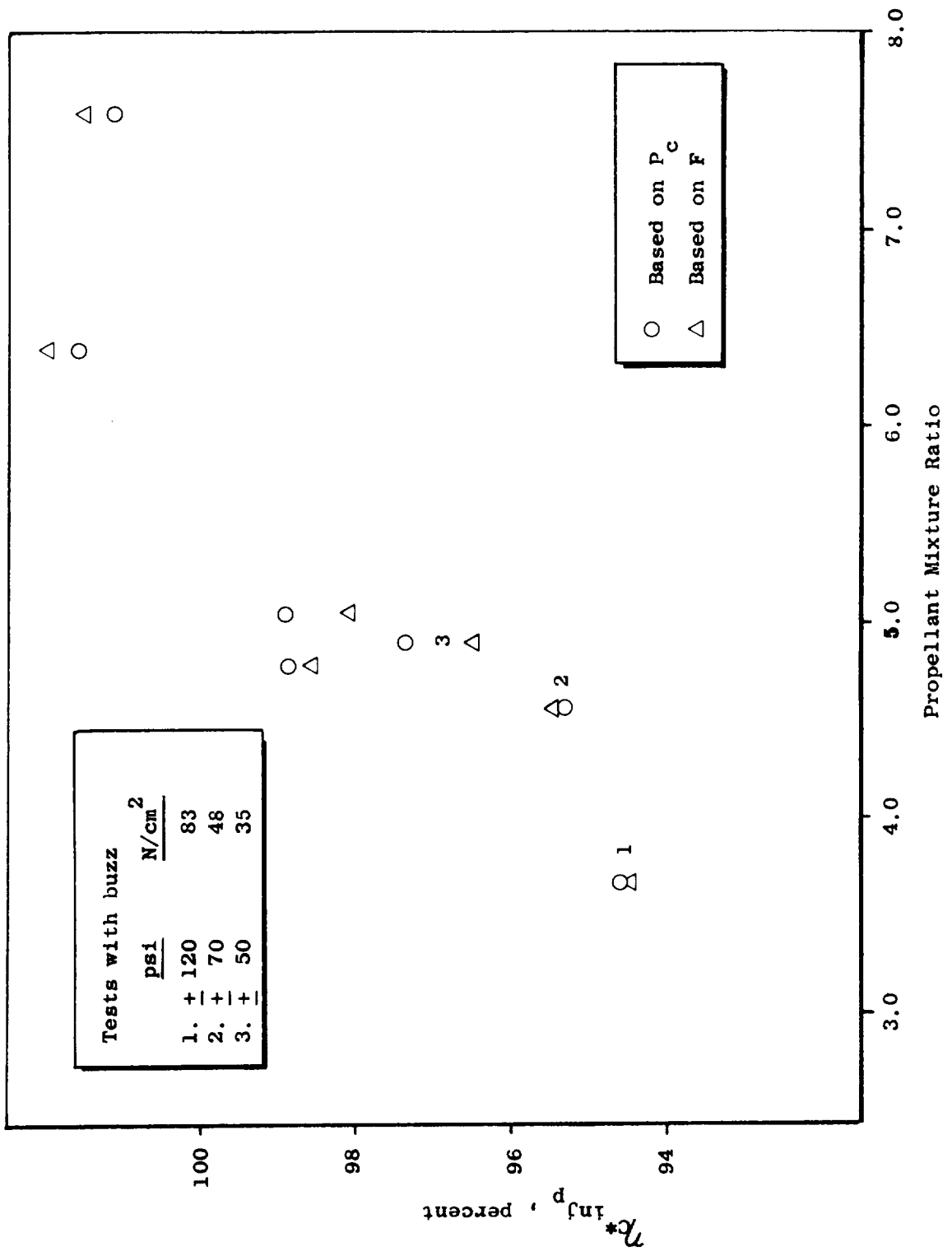


Figure 75. C* Efficiency of Triplet Injector at 500 psia (345 N/cm²) Chamber Pressure

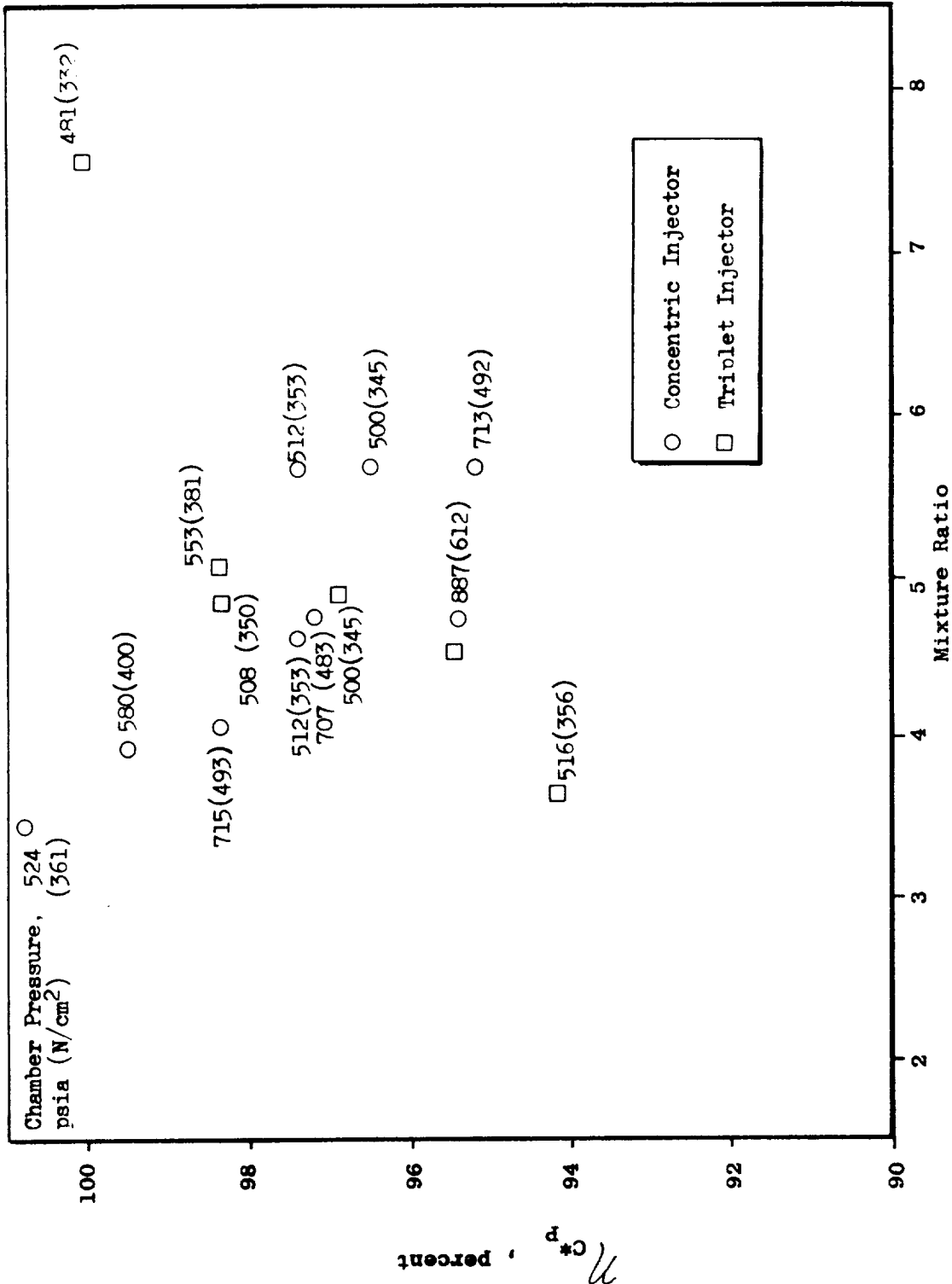


Figure 76 . Comparison of Triplet and Concentric Injector Performance

inserted 0.1 inches (0.25 cm) into the chamber). The efficiencies shown in Fig. 58 were obtained with the concentric element injector in a chamber with an effective L^* of less than 22 inches (55 cm).

The correlation of C^* efficiency with propellant injection momentum ratio for the concentric injector is quite good as shown in Fig 77 . All except one data point fall within one percent of the correlation curve. The performance correlation with the difference between the fuel and oxidizer injection velocities, $V_f - V_o$, is shown in Fig. 78 . The correlation with momentum ratio is better for this injector because the swirl and divergent exit of the FLOX post tend to give the element the characteristics of an impinging stream injector. Both the momentum ratios and velocity differences should be considered as relative rather than absolute values because injection temperatures were measured in the propellant manifolds and the swirl effects on the FLOX velocity were ignored. The fuel velocity was based on the area of the annular gap between the outside diameter of the FLOX post and the fuel body. Actually the fuel velocity decreases as the fuel diffuses around the tip of the FLOX post. The FLOX stream is diverging because of swirl and the exit geometry of the FLOX tube so that the propellants meet and interact at some diameter (and corresponding fuel velocity) between the inside and outside diameters of the FLOX post. The point of interaction is to some extent affected by chamber pressure and mixture ratio. Fuel injection temperatures on these tests were in the order of 800R (450K). Higher fuel temperatures increase the fuel velocity and, therefore, increase the momentum ratio.

Thrust measurements were taken during the altitude test series with the solid-wall nozzle. However, accurate data were not obtained until the regeneratively cooled test series because of various interactions between the thrust chamber and diffuser.

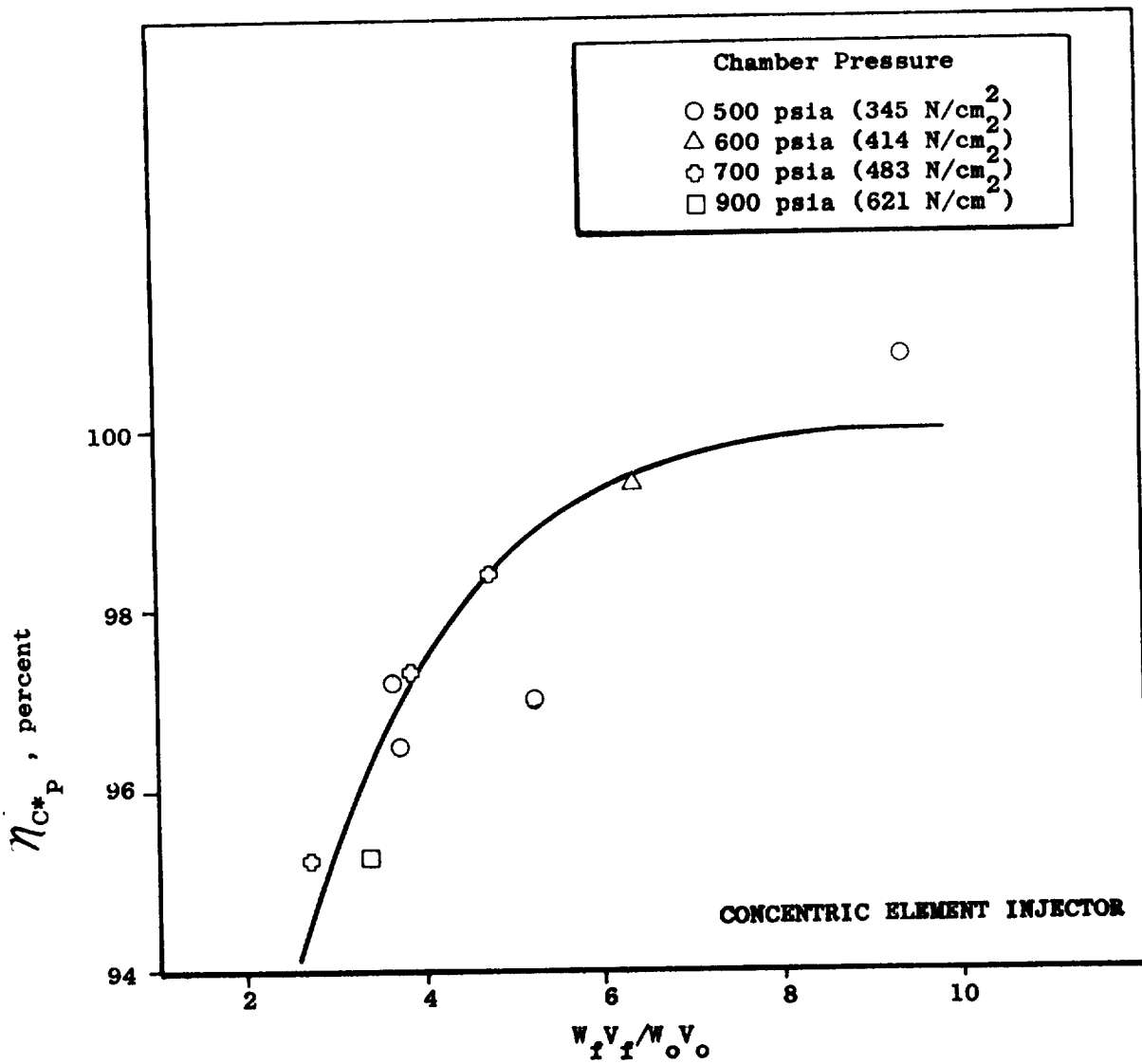


Figure 77. Propellant Injection Momentum Ratio

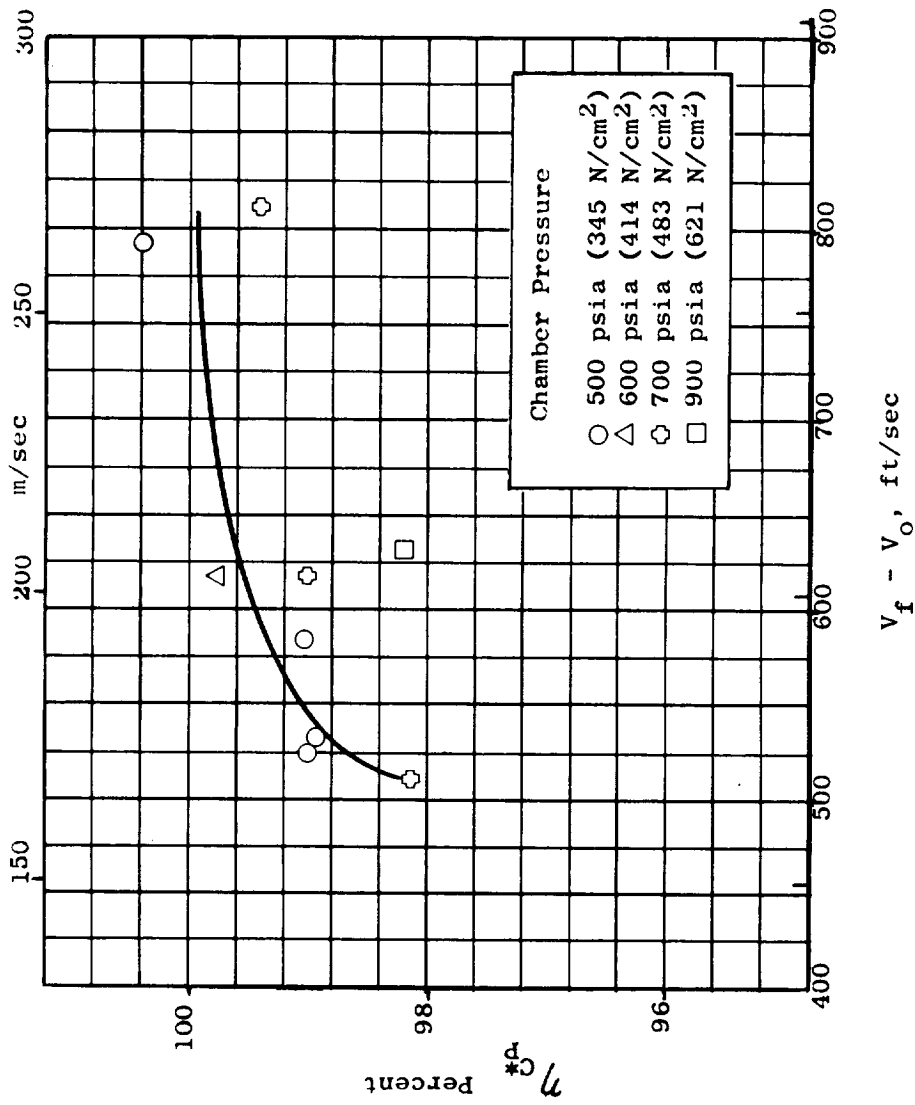


Figure 78. Concentric Element Injector Performance vs Injection Velocity Difference

Combustion stability was monitored by an accelerometer mounted on the combustion chamber and by high-response transducers measuring fuel and oxidizer injection pressures and chamber pressure. Two cases of high frequency instability which were encountered with the triplet element injector occurred under abnormal conditions: one time when the FLOX temperature was approximately 100F (55K) higher than nominal and once when an interpropellant leak occurred in the injector. No cases of high frequency instability were encountered with the concentric element injector. Intermediate frequency "buzz" (\sim 500 cps) occurred with the No. 2 triplet injector at low mixture ratio conditions (O/F < 4.9). This injector had enlarged oxidizer orifices to avoid facility pressure limits when operating at high thrust levels.

Heat Transfer. Very good heat flux profiles were obtained with the calorimeter chamber ($\epsilon = 4$) for both triplet and concentric element injectors. The good reproducibility of the data is illustrated in Fig. 79 which presents heat flux profiles for the triplet injector under conditions of similar chamber pressure and mixture ratio.

A comparison of analytical and experimental heat transfer coefficient profiles is shown in Fig. 80. The Bartz equation predicted values lower than the experimental data in the combustion region, close to the data in the throat region, and higher than the data in the nozzle region. Analytical predictions utilizing the Rocketdyne boundary layer equations and based on starting the boundary layer near the injector (as was done for the Task I analyses) were found to also predict lower than measured coefficients in the combustion region. However, using the boundary layer equations with the boundary layer starting near the start of convergence resulted in good agreement with the data in the converging, throat, and diverging regions, and fair agreement near the nozzle exit. The sharp increase in heat flux measured at the start of convergence implies that the boundary layer was attaching at this point. A

Symbol	Chamber Pressure		O/F
	psia	N/cm ²	
○	553	381	5.03
□	500	345	4.89
△	508	350	4.78

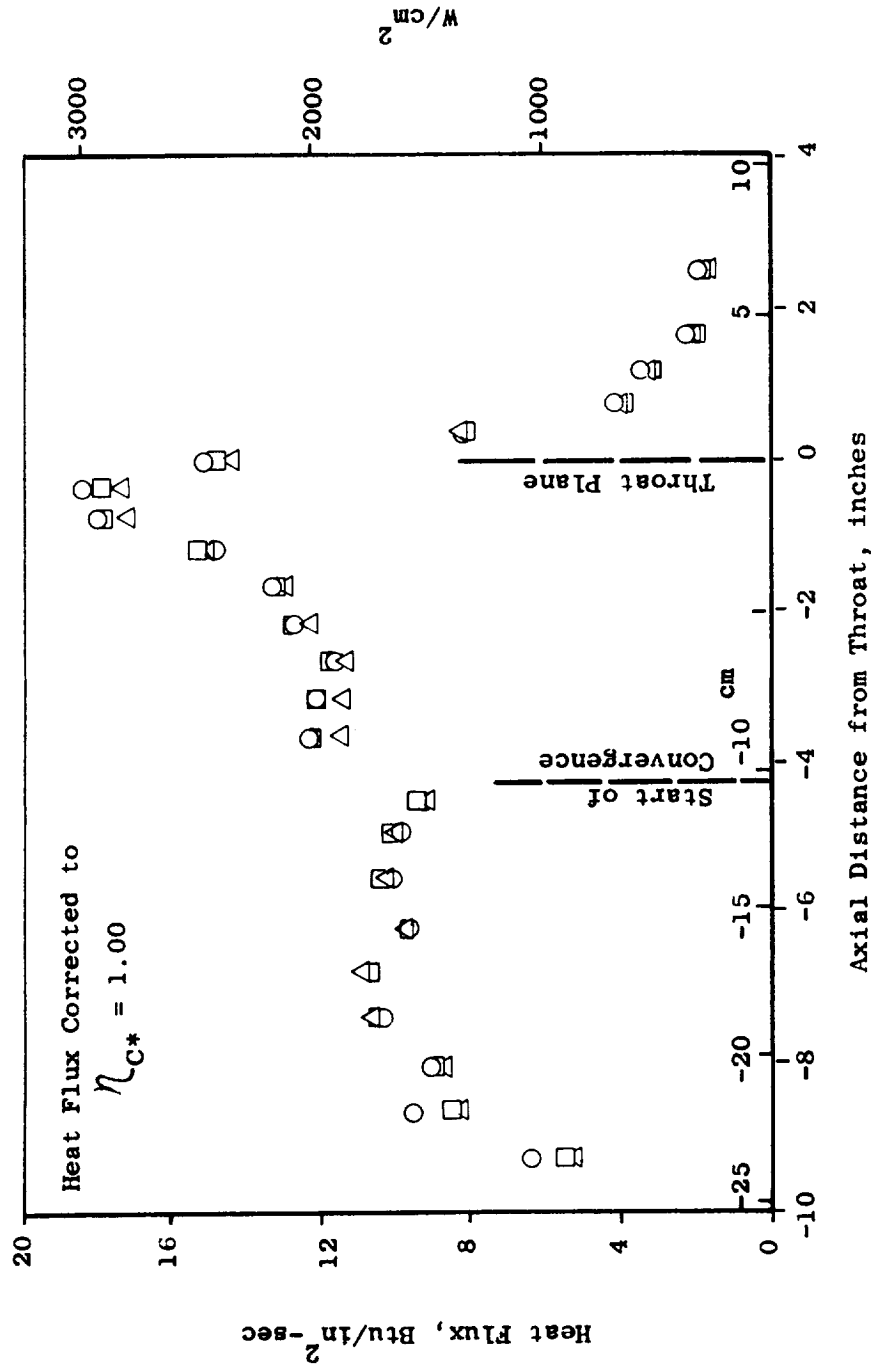


Figure 79. Experimental Heat Flux Profiles with Triplet Injector

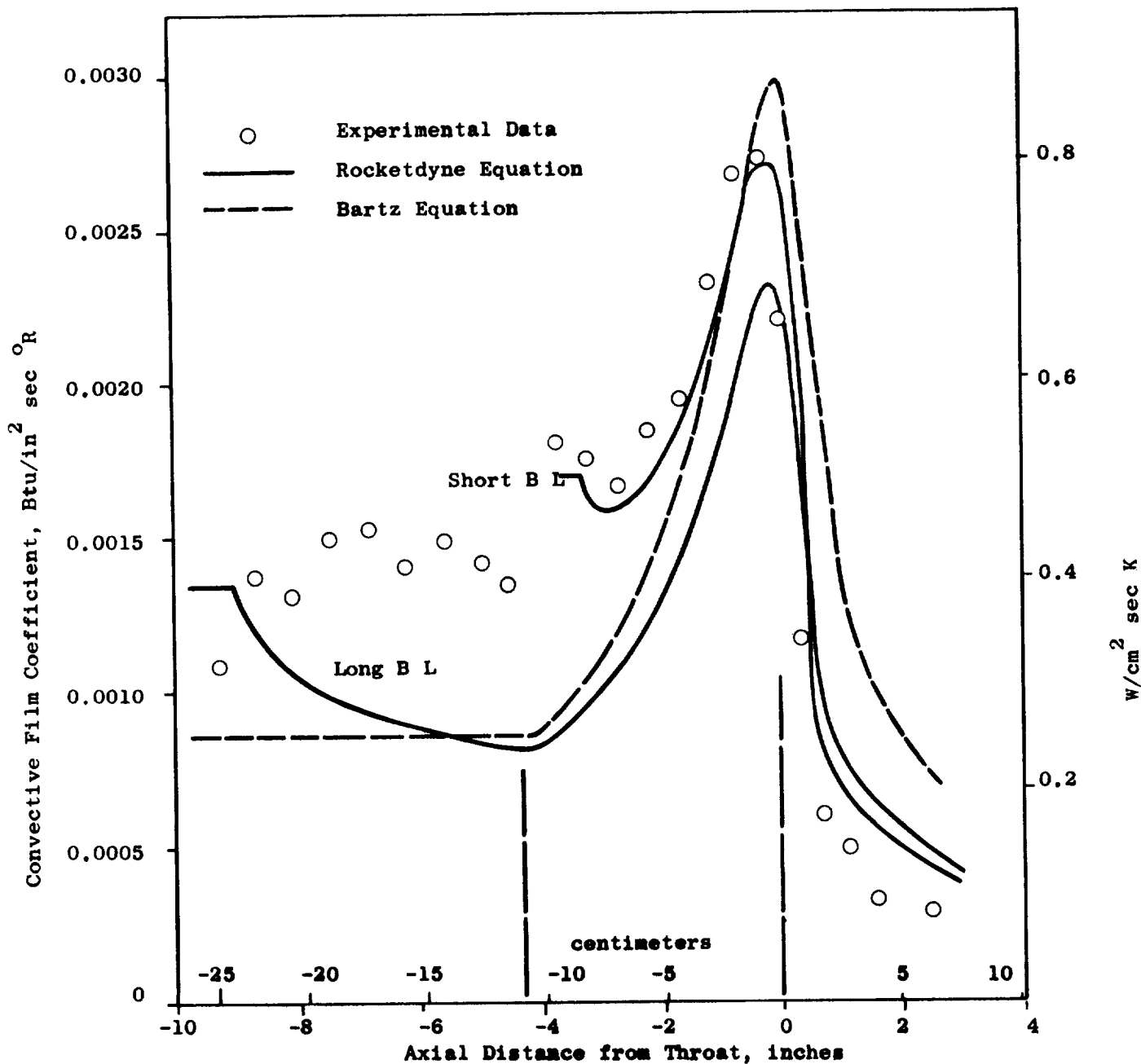


Figure 80 . Comparison of Experimental and Theoretical Heat Transfer Coefficient Profiles

continuously converging combustion chamber contour would probably result in earlier attachment of the boundary layer, a longer boundary layer development length, and lower throat heat flux values.

The effect of propellant mixture ratio on the heat flux profile is shown in Fig. 81 for the triplet injector. The data indicates that high mixture ratios result in high heat fluxes at the injector face and in the throat and divergent regions. The lower heat flux in the combustion zone at the highest mixture ratio implies the possibility of a cool, high mixture ratio layer in this region which mixes and combusts by the time the throat region is reached. The effect of chamber pressure on heat flux with the triplet element injector could not be determined accurately because of the narrow range of pressures tested.

Although the peak heat flux measured with the triplet element injector was 18 percent higher than the value predicted in Task I, the high heat fluxes measured in the combustion and converging zones were more significant in affecting the design pressure drop for a regeneratively cooled thrust chamber. Heat transfer rates in the combustion zone would probably have been reduced by modifying the elements to produce a radial mixture ratio gradient. However, the results of the tests with the concentric element injector showed markedly reduced heat fluxes in this region as indicated in Fig. 82. The thrust chamber in which the concentric element injector was tested was approximately two inches shorter than that in which the triplet was tested. Performance was similar for the two injectors as previously indicated. The heat fluxes in the throat and diverging regions were nearly equal for the two injectors as shown in Fig. 82. Peak heat fluxes are plotted against mixture ratio and chamber pressure in Fig. 83 for both injectors.

The peak fluxes were approximately the same for both injectors at nominal and higher mixture ratios while at lower mixture ratios the concentric element injector produced slightly lower peak flux values.

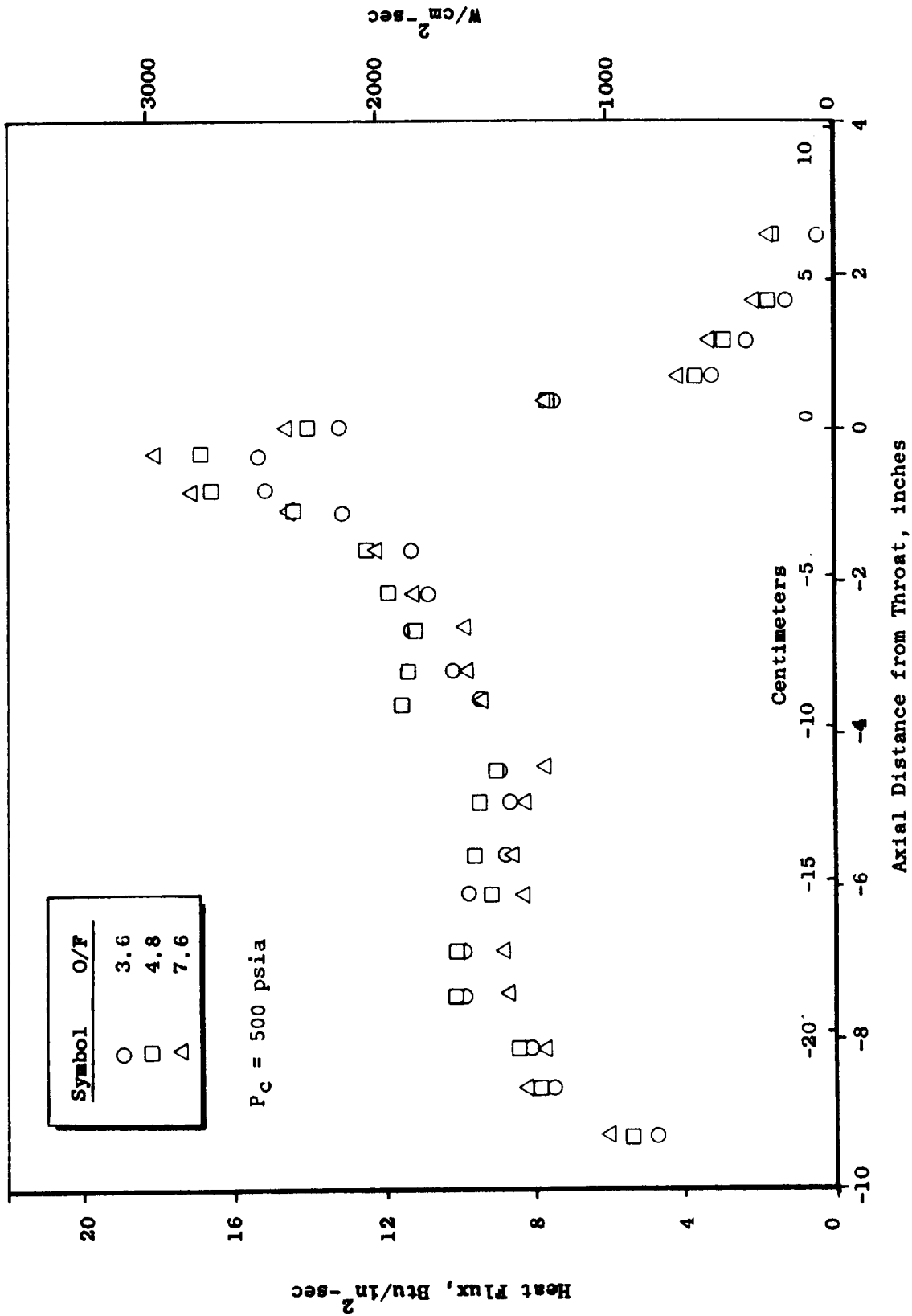


Figure 81 . Heat Flux Profiles for Various Mixture Ratios with Triplet Injector

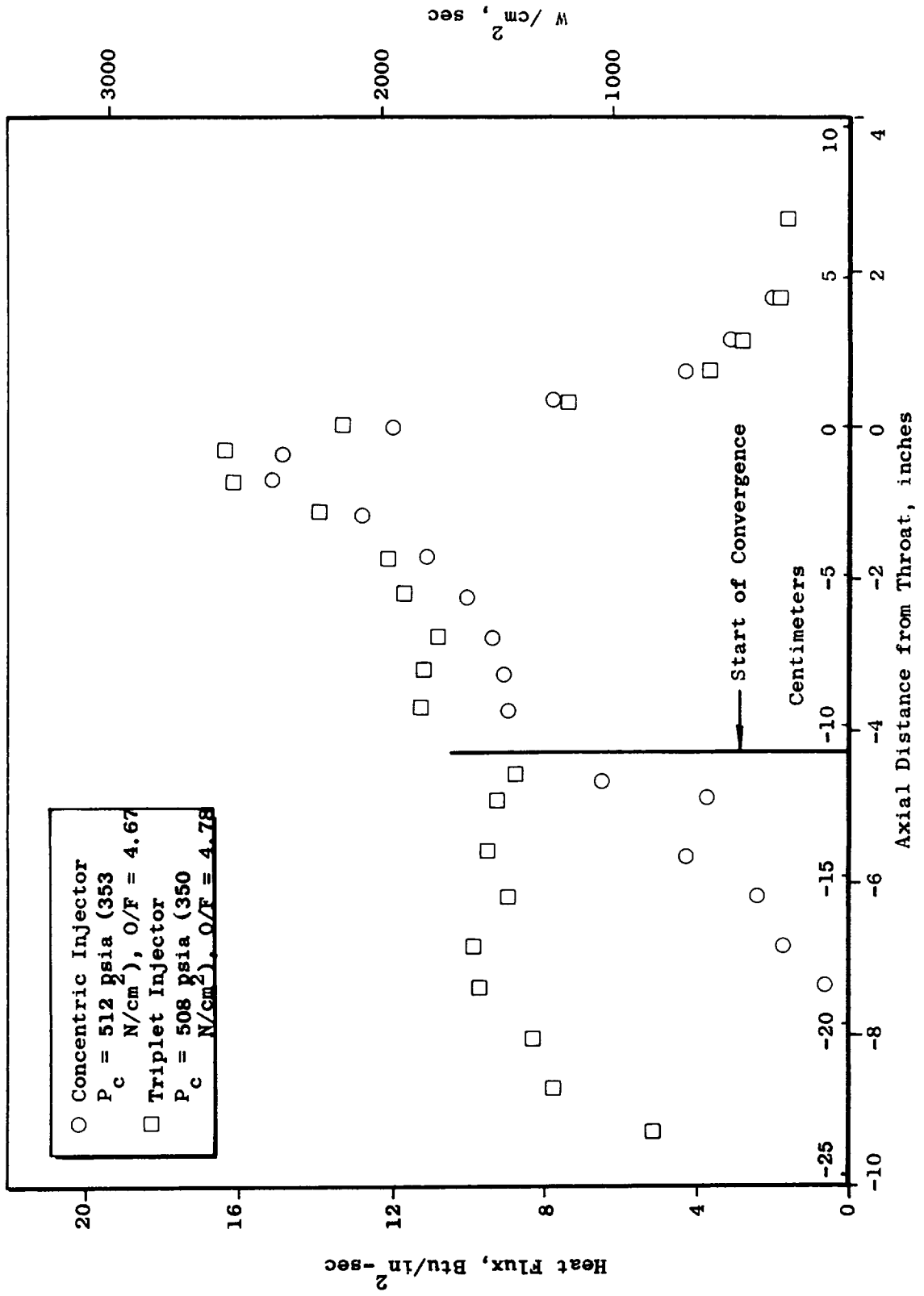


Figure 82. Experimental Heat Flux Profiles

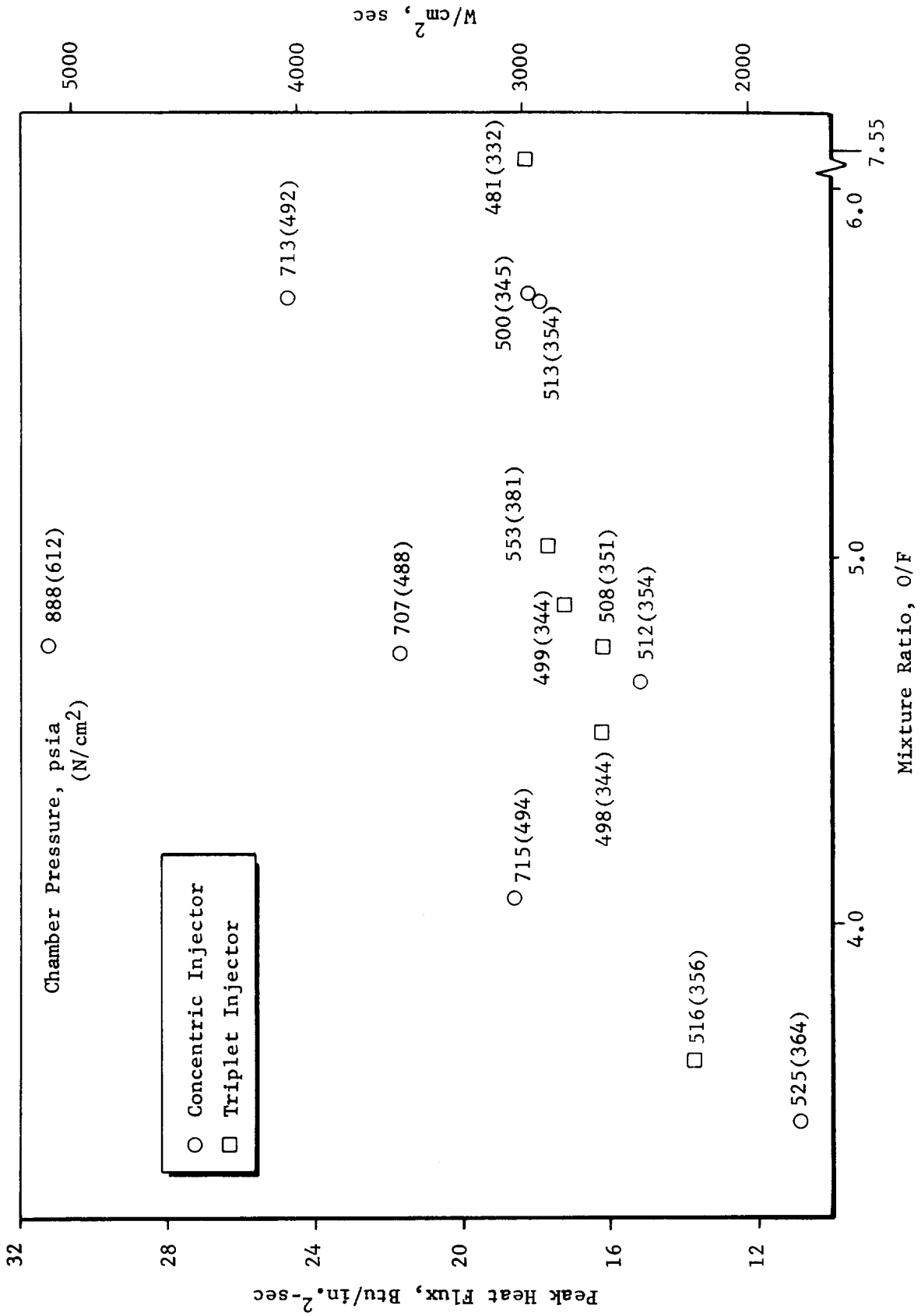


Figure 83. Experimental Peak Heat Fluxes

The effect of chamber pressure on the heat flux profiles with the concentric element injector is shown in Fig. 84 . The abrupt increase in heat flux at the start of convergence is apparent at all pressures. The area immediately downstream of the injector does not appear to be as much affected as the remainder of the chamber. The dramatic difference between the integrated heat fluxes from injector to $\epsilon = 6$ with the two injectors is shown in Fig. 85 . The heat input with the concentric element injector was only 65 percent of that with the triplet at a mixture ratio of 5.7 and 50 percent at a mixture ratio of 4.0. Shortening the chamber (at $9 \text{ Btu/in}^2\text{-sec}$) by 2 inches (to the effective length in which the concentric element injector was tested) would reduce the triplet total heat input by approximately 18 percent. The heat input with the concentric element injector at nearly 900 psia chamber pressure was close to that measured with the triplet element injector at 500 psia (345 N/cm^2). The marked effect of propellant mixture ratio on the integrated heat inputs is evident in Fig. 85 . In fact, a good empirical correlation of the heat input with the parameter $P_c \times (O/F)$ was possible as shown in Fig. 86 .

Eleven temperature measurements were made on the solid nozzle; eight measurements in one plane and three in a plane 45 degrees from the first. The concentric element injector was used for these tests. Copper-sheathed thermocouples in copper plugs were used for the tests at 500 psia (345 N/cm^2) chamber pressure and for one test at 700 psia (482 N/cm^2). The data obtained on the 500 psia (345 N/cm^2) tests are shown in Fig. 87 . Although the data are somewhat scattered, probably resulting from deviations in the thermocouple mounting, a definite trend is evident. The measured heat transfer coefficients at area ratios below 20 were approximately 25 percent below the predicted value. The theoretical prediction was closely followed at area ratios between 20 and 50. Measured heat transfer coefficients exceeded the predicted values near the nozzle exit. Coefficients measured in the plane 45 degrees from the first differed by 20 to 30 percent.

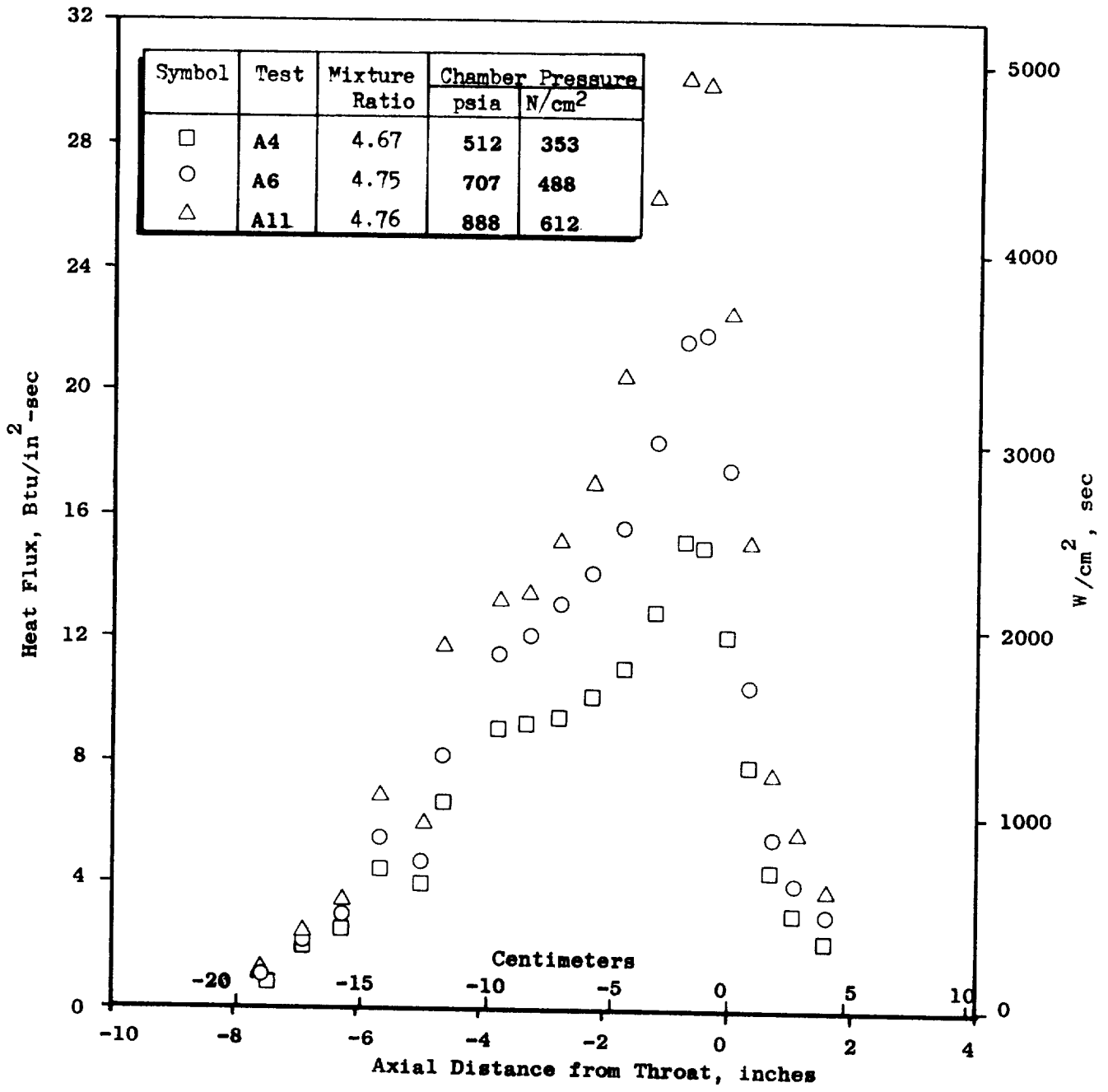


Figure 84. Concentric Injector Axial Heat Flux Profiles

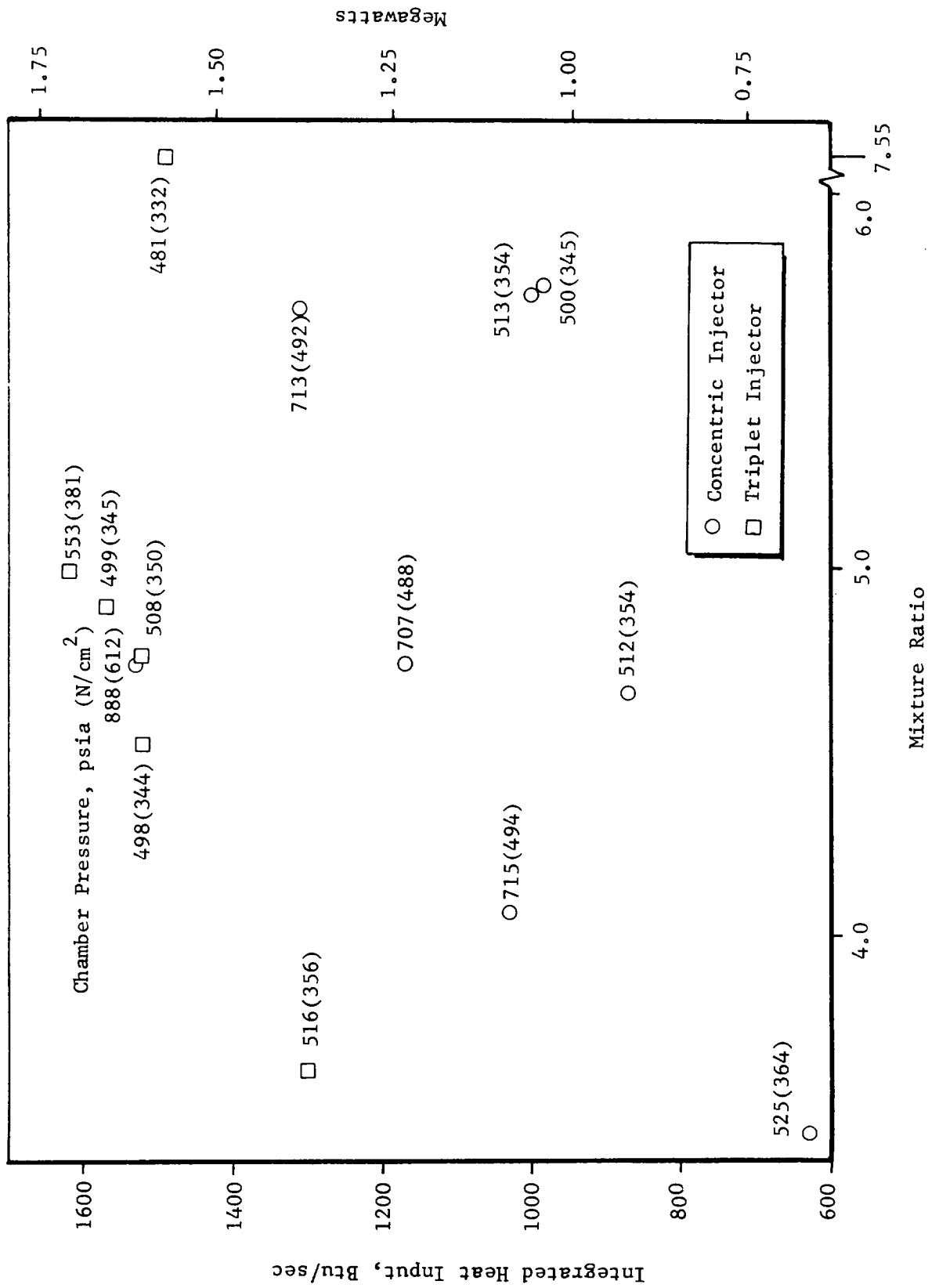


Figure 85. Experimental Heat Inputs

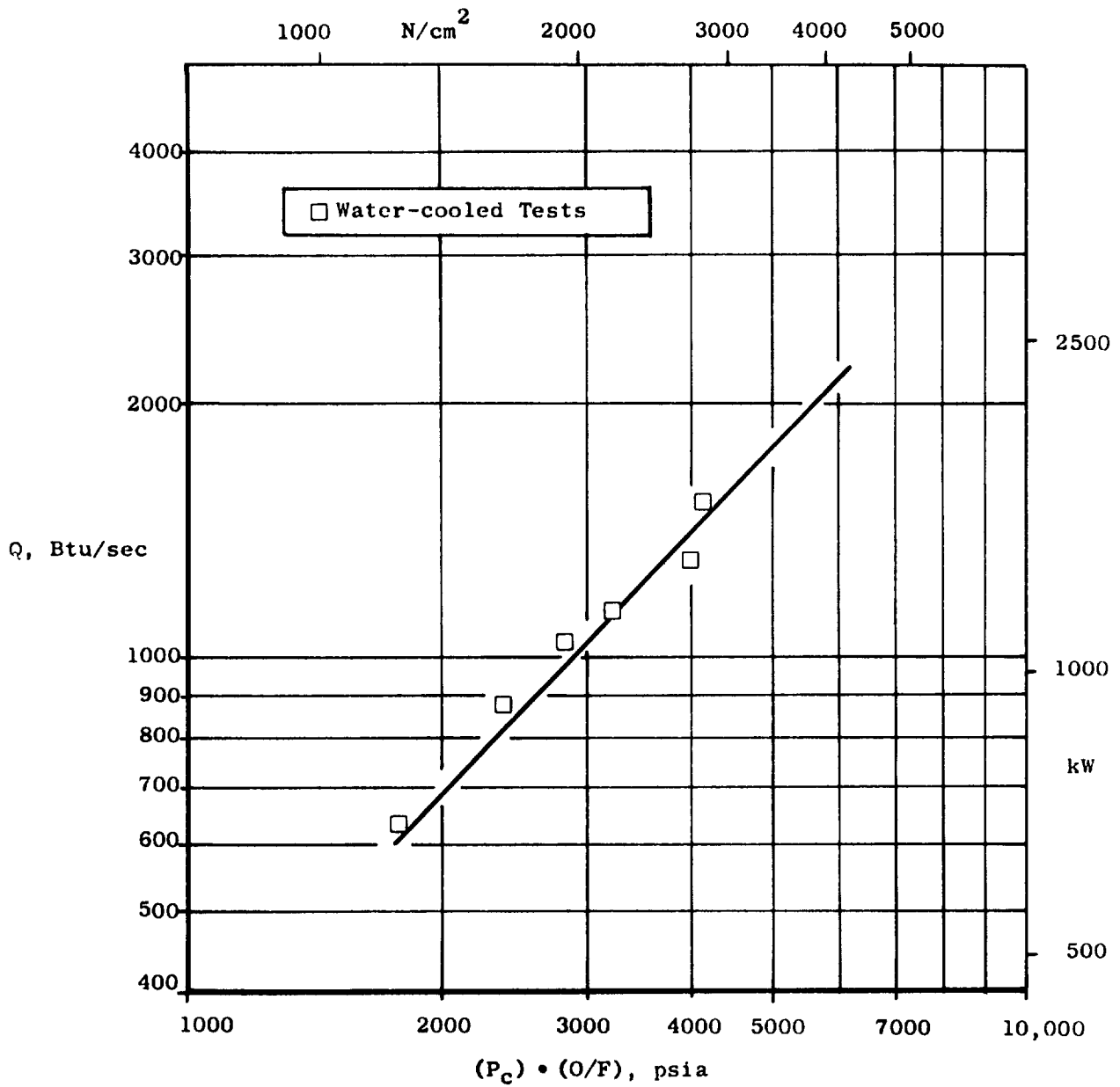


Figure 86. Combustion Chamber Heat Inputs

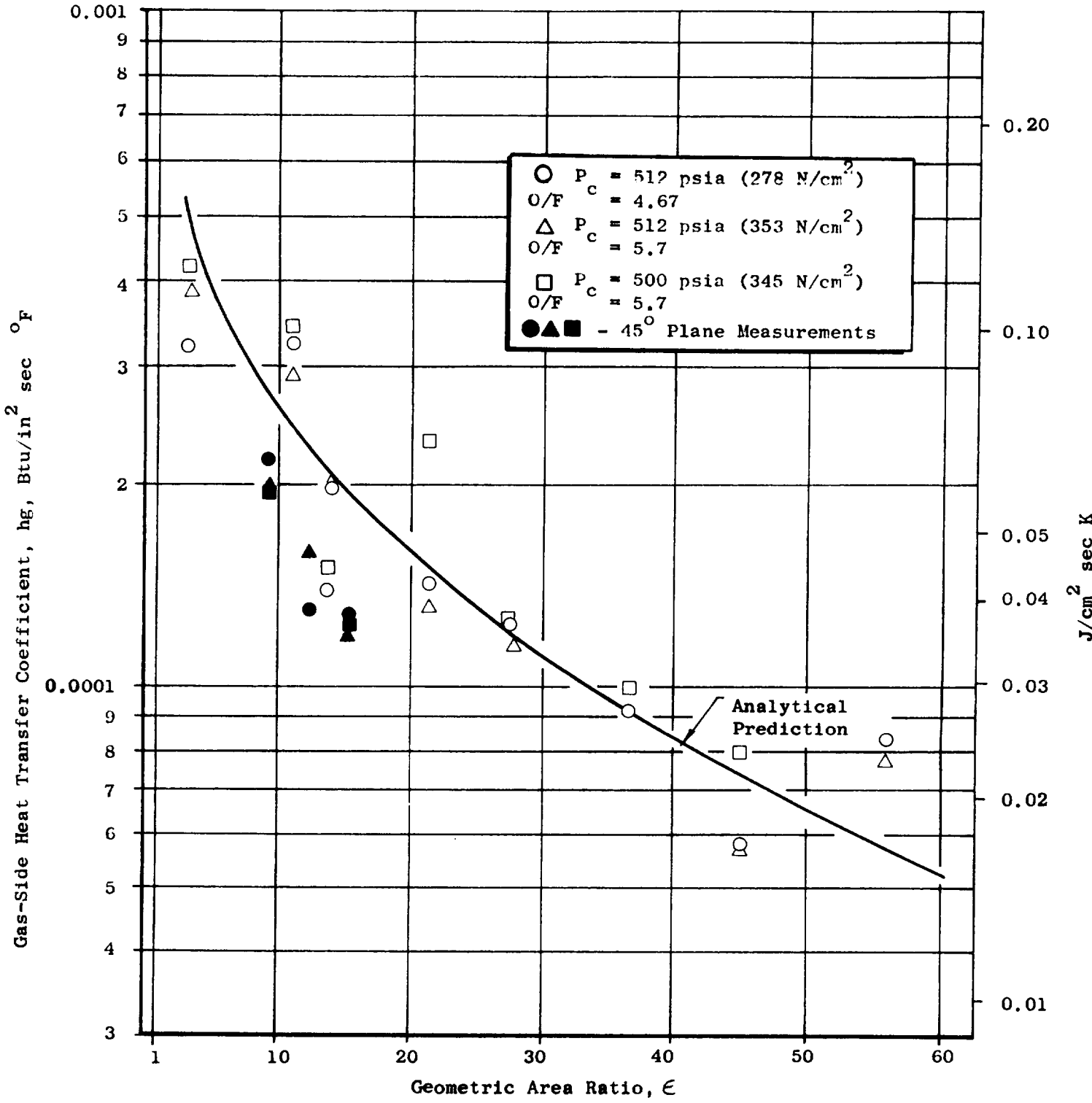


Figure 87. Nozzle Heat Transfer Coefficient Distribution at $P_c \approx 500$ psia (345 N/cm²)

Thermocouple wires were resistance-welded to the outside of the nozzle wall at eight locations after the first 700 psia (482 N/cm^2) test and replaced the eight copper thermocouple measurements at these locations. Much-improved data were obtained with these outside thermocouples. Comparison of one-dimensional and two-dimensional heat transfer analysis results indicated that one-dimensional analysis of the temperature rise transients was entirely satisfactory. Predicted and experimental heat transfer coefficients obtained with the outside wall thermocouples at a chamber pressure of approximately 700 psia (482 N/cm^2) are plotted in Fig. 88 .

Trends were similar to those observed at 500 psia (345 N/cm^2) with the heat transfer coefficients being lower than theoretical in the low area ratio region and equal to, or slightly higher than theoretical near the exit. In the low area ratio region of the nozzle the heat transfer coefficients increased with increasing propellant mixture ratio, which is consistent with trends in the water-cooled thrust chamber data. The effect of mixture ratio on heat transfer coefficients was reversed at the higher area ratios, possibly because of downstream burning. Experimental data and the theoretical predictions for heat transfer coefficients at 900 psia (622 N/cm^2) chamber pressure are shown in Fig. 89 . Experimental heat transfer coefficients were slightly higher in general, relative to the theoretical curve than the 700 psia results.

Thus, it appears that the boundary layer theory may be used to predict heat transfer rates with a reasonably good accuracy in the converging, throat, and nozzle regions. However, the point of initiation of the boundary layer is a function of injector and chamber geometry which must be determined experimentally or based on previous data on similar geometries.

Data from the thermocouples in the land between the third and fourth coolant passages are plotted in Fig. 90. The data imply that significant heat flux variations occur near the injector.

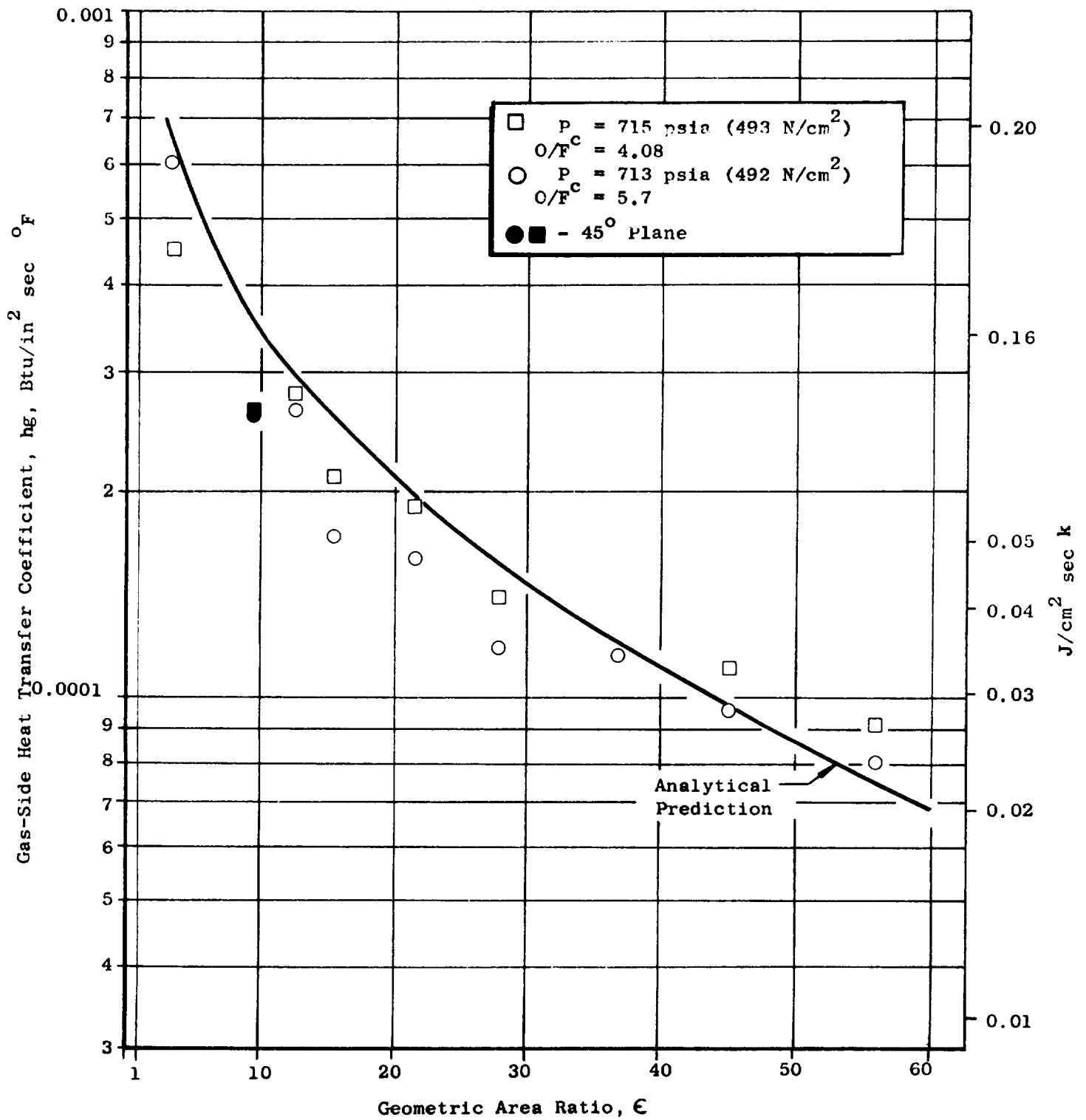


Figure 88. Nozzle Heat Transfer Coefficient Distribution at $P_c \approx 700$ psia (485 N/cm²)

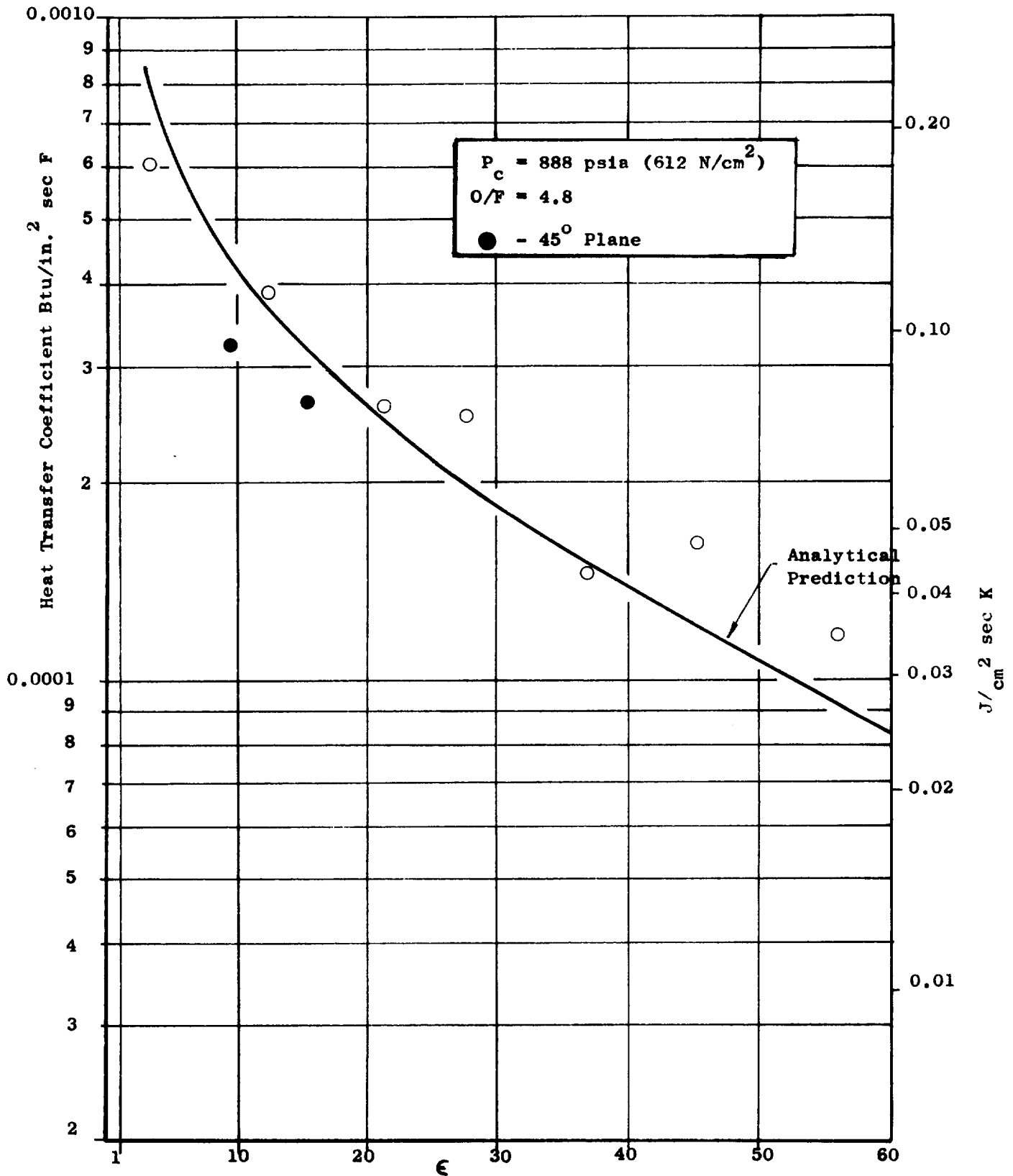


Figure 89 . Nozzle Heat Transfer Coefficient Distribution
 at $P_c \approx 900 \text{ psia (620 N/cm}^2\text{)}$

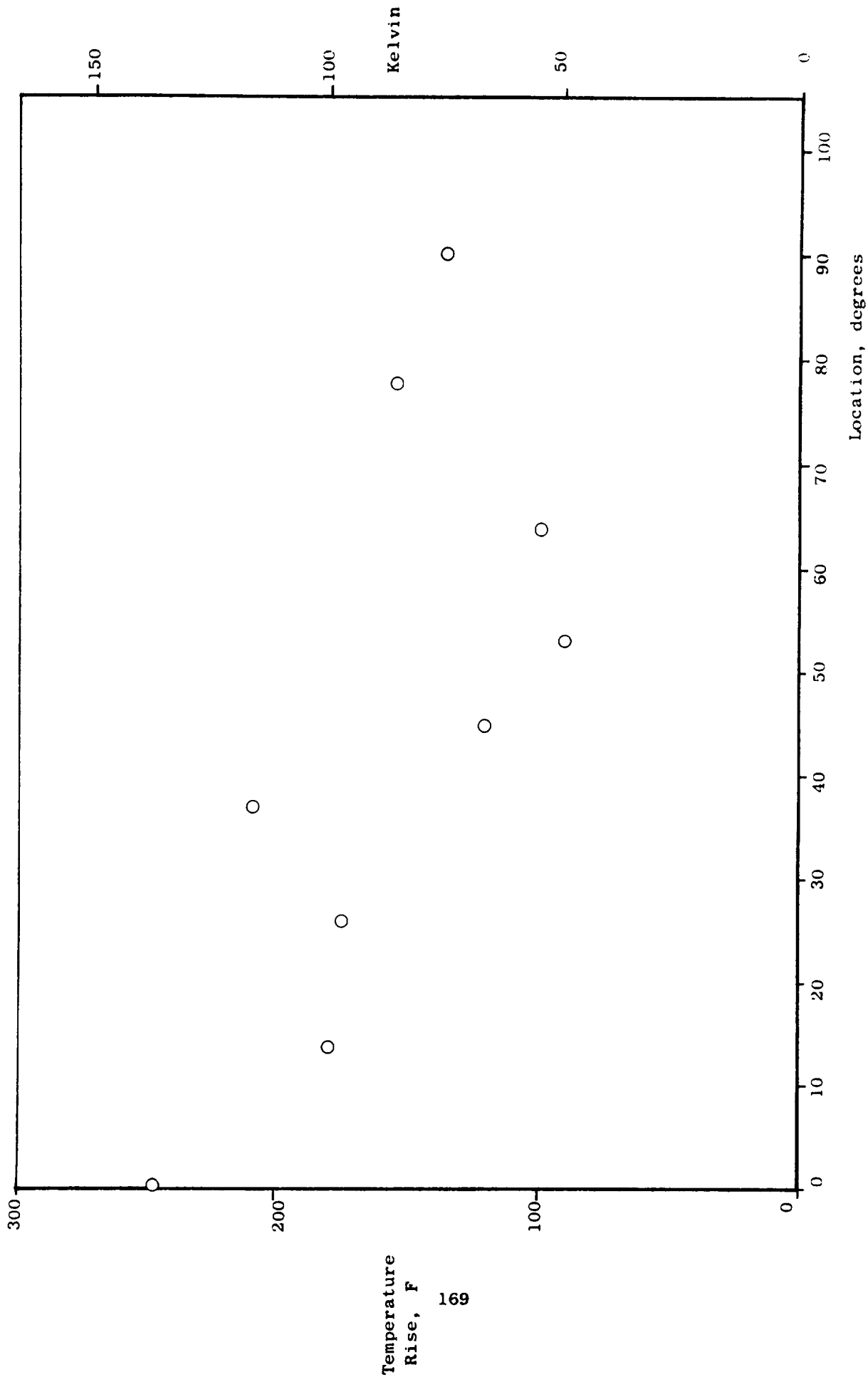


Figure 90. Circumferential Temperature Profile Near Concentric Injector

APPLICATION TO REGENERATIVELY COOLED T/C DESIGN

The heat flux and heat transfer coefficient data obtained in Tasks III and IV may be used in the design of coolant channel geometry for regeneratively cooled thrust chambers with high area ratio bell nozzles. Although the use of other injectors would probably affect the heat flux near the injector, the heat fluxes in the throat and nozzle regions would probably correspond closely to the predicted values.

The design of the regeneratively cooled thrust chamber for the Task V tests in this program was described in Section II. Two significant features of this design bear repeating. First, the combustion chamber contour was identical to that of the water-cooled thrust chamber to assure that a known heat flux profile would be imposed on the chamber. The abrupt rise in heat flux at the start of convergence indicates flow impingement or initiation of the thermal boundary layer at this point. Future designs should avoid this by reduction of the angle of convergence from the present 20 degrees to, at most, 15 degrees. A minimum convergence angle characteristic of a continuously converging chamber (i.e., little or no cylindrical section) would probably be most satisfactory.

The second feature of the present design is that the chamber was designed to operate at 800 psia (550 N/cm^2) chamber pressure with a heat flux profile extrapolated from data from early tests with the triplet injector at moderately low mixture ratios. As a result, the present chamber is thermally conservative in the cylindrical section, slightly optimistic in the converging and throat sections, and has a coolant jacket pressure drop which is higher than necessary for operation at 500 psia (345 N/cm^2) with the concentric injector.

The designs described in the following paragraphs were accomplished in conjunction with the efforts under contract NAS3-12024 and are reported in further detail in Ref. 4.

The following ground rules and assumptions were used in the designs:

1. Heat fluxes were based on boundary layer equations in the converging and diverging regions except that the concentric element injector measured heat flux profile near the injector was faired into the analytical profile.
2. Single-pass counterflow coolant circuits were used.
3. The Dittus-Boelter equation was used to calculate the coolant-side heat transfer coefficients. Transport properties were evaluated at the coolant bulk temperature.
4. Coolant-side heat transfer coefficient enhancements of 1.18 for roughness and a maximum of 1.5 for curvature were used.
5. Combustion-side wall temperatures were limited to 1700 F in the throat region and 1600 F (1140 K) in the combustion zone.
6. A stress safety factor of 2.0 was used.
7. Two constant-width steps were assumed for the channels in the nozzle. The height varied continuously but was limited to a minimum value of 0.050 inches (0.127 cm).
8. Combustion-side wall thickness was 0.025 (0.063 cm) inches from the injector to $\epsilon = 4$ and 0.040 inches (0.10 cm) for $4 \leq \epsilon \leq 60$.
9. The channel width and height and land width were equal at the throat. A minimum value of 0.030 inches (0.076 cm) was assumed for these dimensions.

Two combustor shapes were considered for a preliminary, comparative analysis: a combustor with a 15 degree converging angle, and a continuously converging (7.3 degree angle) combustor. Both combustors had a contraction area ratio of 4 and the same integrated heat input. The actual and characteristic lengths of the combustors were as shown in the following table.

	Length		L*	
	in.	cm	in.	cm
15 Degree	9.8	25.2	30	76
7.3 Degree Combustor	10.25	26.1	24	60

Both chambers had 90 channels and approximately the same coolant jacket pressure drop (230 psi (157 N/cm²) at 500 psia (345 N/cm²) chamber pressure and 5.25 mixture ratio). The continuously tapered combustor had a maximum wall temperature of 1525F (1095K) while the cylindrical/tapered chamber had a maximum wall temperature of 1965F (1345K). Although the heat transfer coefficient profiles differ somewhat for the two combustors, the primary reason for the different peak wall temperatures is that the peak occurs in the tapered chamber at a point where the land width is considerably smaller than the corresponding point on the cylindrical/tapered chamber (0.116 inches vs 0.138 inches). The tapered combustor was selected for further optimization on the basis of these heat transfer analysis results, as well as considerations of performance, weight and fabrication ease.

The number of channels, 90, in the combustor was determined using 2 dimensional analyses to determine the peak wall temperature. An 0.030 inch (0.076 cm) nickel closeout and an 0.090 inch (0.228 cm) Hastelloy C backup structure were assumed for these analyses. The chamber was designed for operation at 10 percent thrust level as well as at full thrust. The heat flux profile at 10 percent thrust was based on $Q/A \propto P_c^{0.8}$. The combustion-side wall temperatures at both thrust levels are shown in Table 17. The peak

TABLE 17
Maximum Wall Temperatures, Tapered Chamber

No. Channels	Full Thrust			10:1 Throttled		
	72	90	120	72	90	120
Throat T _{WG} , F(K)	1350(1005)	1310(985)	1260(955)	1070(845)	1050(838)	970(790)
Combustor T _{WG} , (X = 7.5-inch) (19.1 cm)	1630(1155)	1525(1095)	1450(1060)	1740(1220)	1650(1170)	1550(1115)

wall temperature at the 10 percent thrust level dictated that 90 channels be used. A non-throttling chamber could use a design featuring approximately 70 channels. A final design, based on actual throttled test results, is presented in Section IV.

For ease of manufacturing the channel width was kept constant from the injector to an expansion area ratio of 4. Likewise, the channel height was kept constant in the immediate area of the throat and increased in two linear tapers to the injector in order to minimize pressure drop while limiting the wall temperature to 1600F (1140K). The channel height was tapered linearly in the divergent section. A maximum value of 0.100 inches (0.254 cm) was selected to reduce weight.

Nozzle channel dimensions were determined by weight, stress, and fabrication considerations because pressure drops and wall temperatures were generally low in this region. The channel height at the nozzle exit was designed to a minimum value (0.050 inches) based on fabrication ease and the channel width was maximized (0.218 inches) to reduce weight subject to stress limits. This combination of width and height was maintained back to an area ratio of 16 where the reduced land width became the limiting factor. Channel width was decreased to 0.143 inches (0.360 cm) while the channel height was increased to 0.073 inches (0.185 cm) to maintain a constant mass velocity. This channel geometry was maintained back to an area ratio of 4.

The profiles of wall temperature (one-dimensional) propellant bulk temperature, and pressure drop are shown in Figs. 91, 92, and 93 respectively. The results of two-dimensional analysis indicate throat temperatures approximately 100F (0.55K) lower than the one-dimensional values. Two-dimensional temperatures in the combustion zone are approximately 100F (55K) higher than the one-dimensional values.

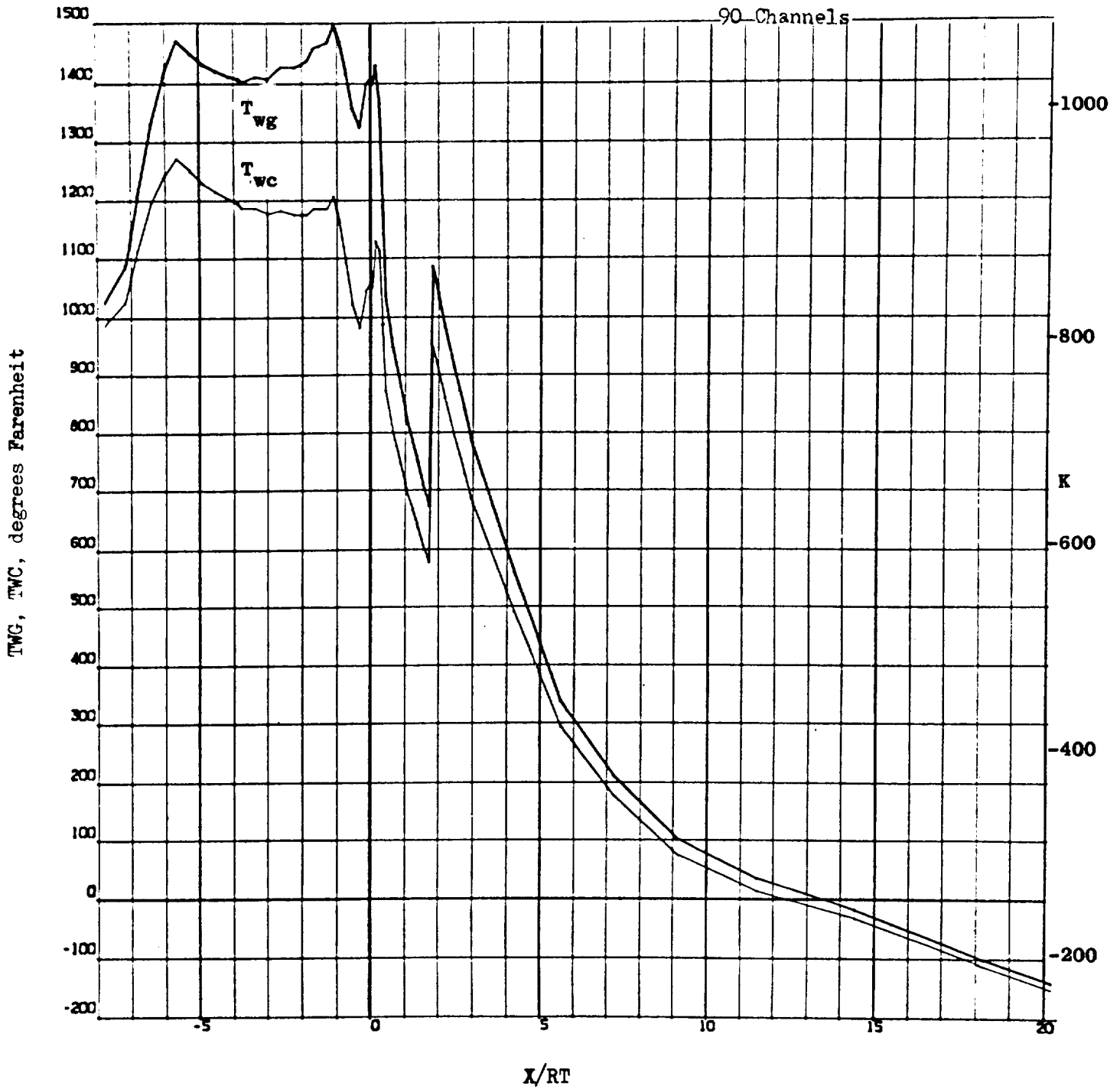


Figure 91 . Wall Temperature Profile

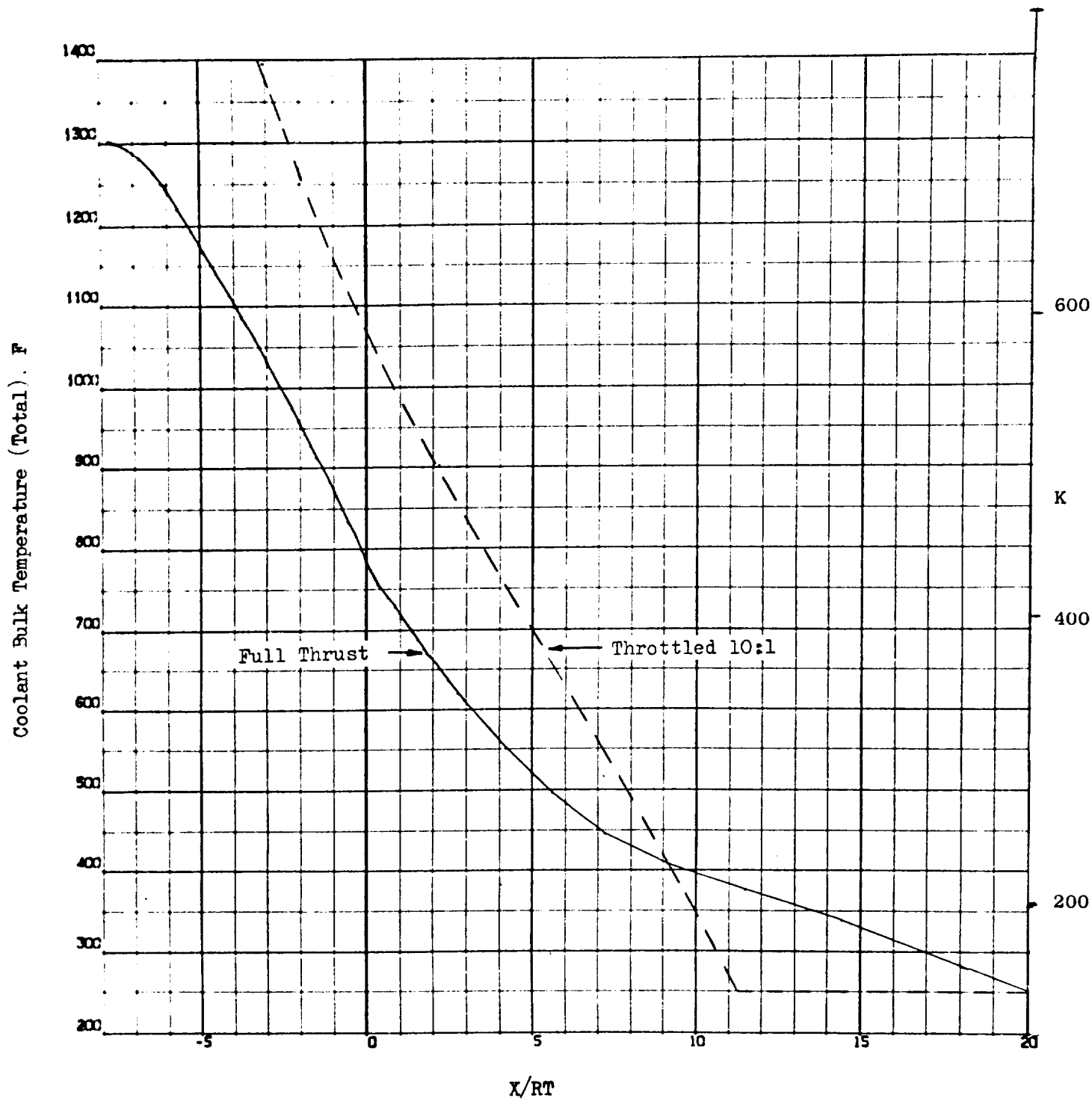


Figure 92 . Coolant Bulk Temperature Profiles

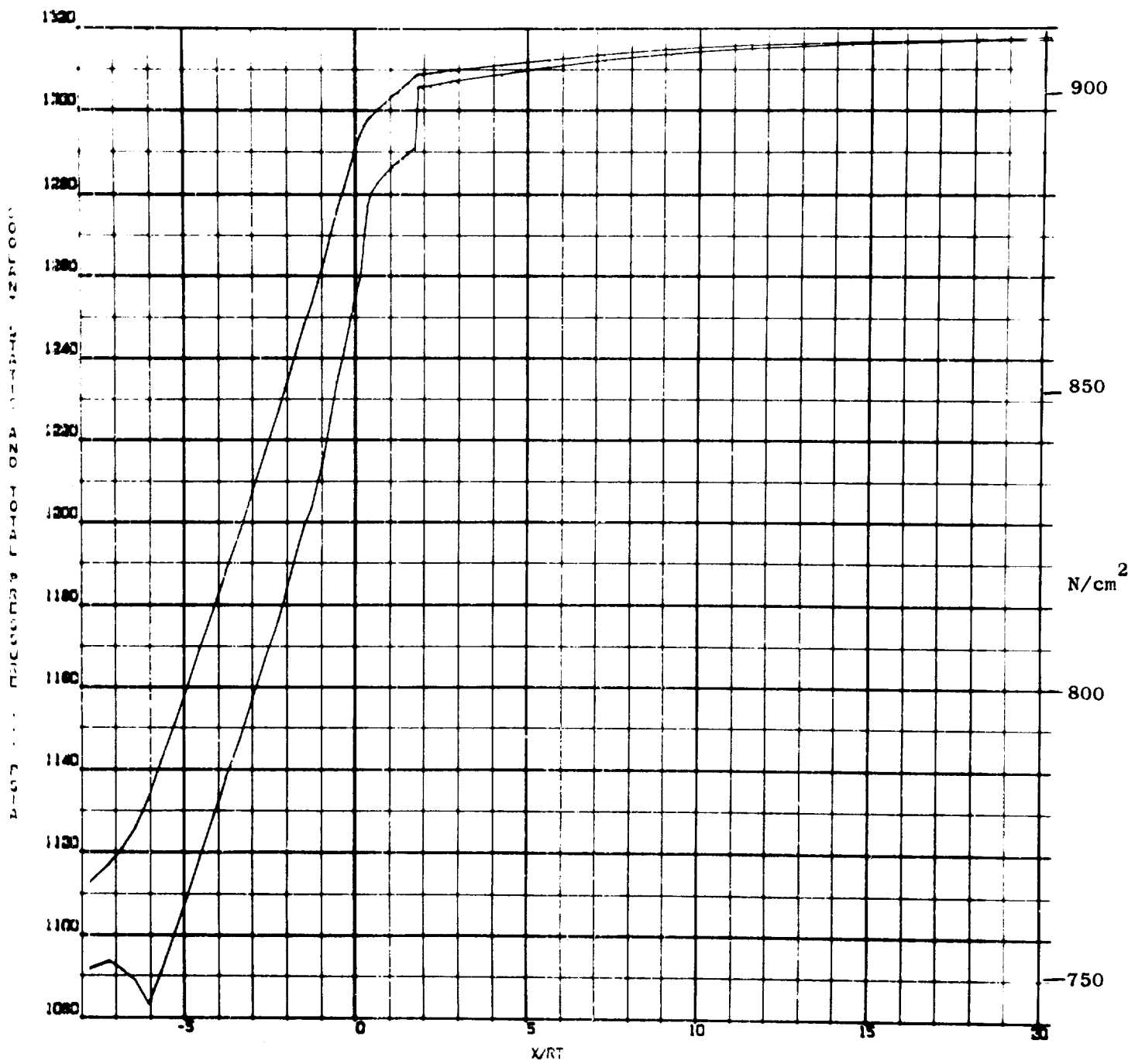


Figure 93. Coolant Pressure Profiles

A thrust chamber with the channel dimensions specified above could be operated at 800 psia (500 N/cm^2) chamber pressure with reduced margin of safety. The peak wall temperature in the combustion zone would increase to 1645F (1165K) from 1525F (1100K). The stress safety factor in the nozzle would be reduced from 2.0 to approximately 1.5. In order to maintain the safety factor of 2.0 the channel width would have to be reduced from 0.143 to 0.094 inches (0.360 to 0.240 cm) in the $4 \leq \epsilon \leq 16$ region and from 0.218 to 0.156 inches (0.545 to 0.390 cm) in the $\epsilon > 16$ region. These channel modifications in the nozzle would increase the pressure drop by approximately 10 psi (3.5 N/cm^2).

CONCLUSIONS

Analysis of the data from the tests conducted under Tasks III and IV lead to the following conclusions.

1. High injector performance (C^*) can be achieved with the liquid FLOX/gaseous methane propellant combination using either triplet or concentric element injectors.
2. High performance can be achieved in a combustion chamber with a characteristic length of 22 inches (55 cm) and an absolute length (injector-to-throat) of 7.5 inches (19 cm).
3. Injector performance is limited by non-uniform mixing rather than by vaporization and combustion because of the rapidity of the latter two processes, for liquid FLOX/gaseous methane.
4. The concentric element injector produces significantly lower heat fluxes in the cylindrical and converging regions of the combustion chamber than the triplet element injector.
5. The integrated heat load from the injector to an expansion area ratio of 4 with the concentric element injector is 50 to 75 percent of the load with the triplet element injector.

6. The heat flux at the injector face is sufficiently low that a solid copper face may be used.

7. Combustion is stable in the high frequency mode for both injectors under nominal operating conditions. (Dynamic stability was not tested).

SECTION IV

REGENERATIVE COOLING TESTS

The electroformed thrust chamber described in Section II was tested in the dump cooled and regeneratively cooled modes with methane as the coolant. Heat inputs consistent with Task IV results were obtained and thrust chamber durability was demonstrated. The facilities, test conditions, and test results are described in this section.

TEST FACILITY AND EQUIPMENT

The tests were conducted in the same facility as the Task III and IV tests. The facility is the same as described in Section III with exceptions described in the following paragraphs. The modifications were made primarily in the fuel system to provide liquid methane inlet conditions.

Propellant Storage and Feed Systems

The feed system is shown in Fig. 94 . A low-flow oxidizer bypass valve was plumbed in parallel with the main oxidizer valve to provide a low-pressure, low mixture ratio step in the start transient.

Two methane fuel systems were used. The dump-cooled tests were conducted using gaseous methane to supply the injector as shown in Fig. 94 which is the identical system used in Tasks III and IV tests. Four thousand gallons of LCH_4 were stored in a vacuum jacketed, low-pressure trailer. Prior to testing, LCH_4 was transferred to the 25 gallon (95 liter) LN_2 vacuum jacketed high pressure (2500 psig) run tank. The LCH_4 flowed through a turbine flowmeter and through the main fuel valve and bypass valve to the engine. The lines and valves were jacketed with LN_2 . The methane flowed through a pair of parallel dump lines after exiting the chamber at the injector end. One of the dump lines was orificed to control the flow during mainstage. The other line contained a valve which could be opened during the start transition and closed during mainstage.

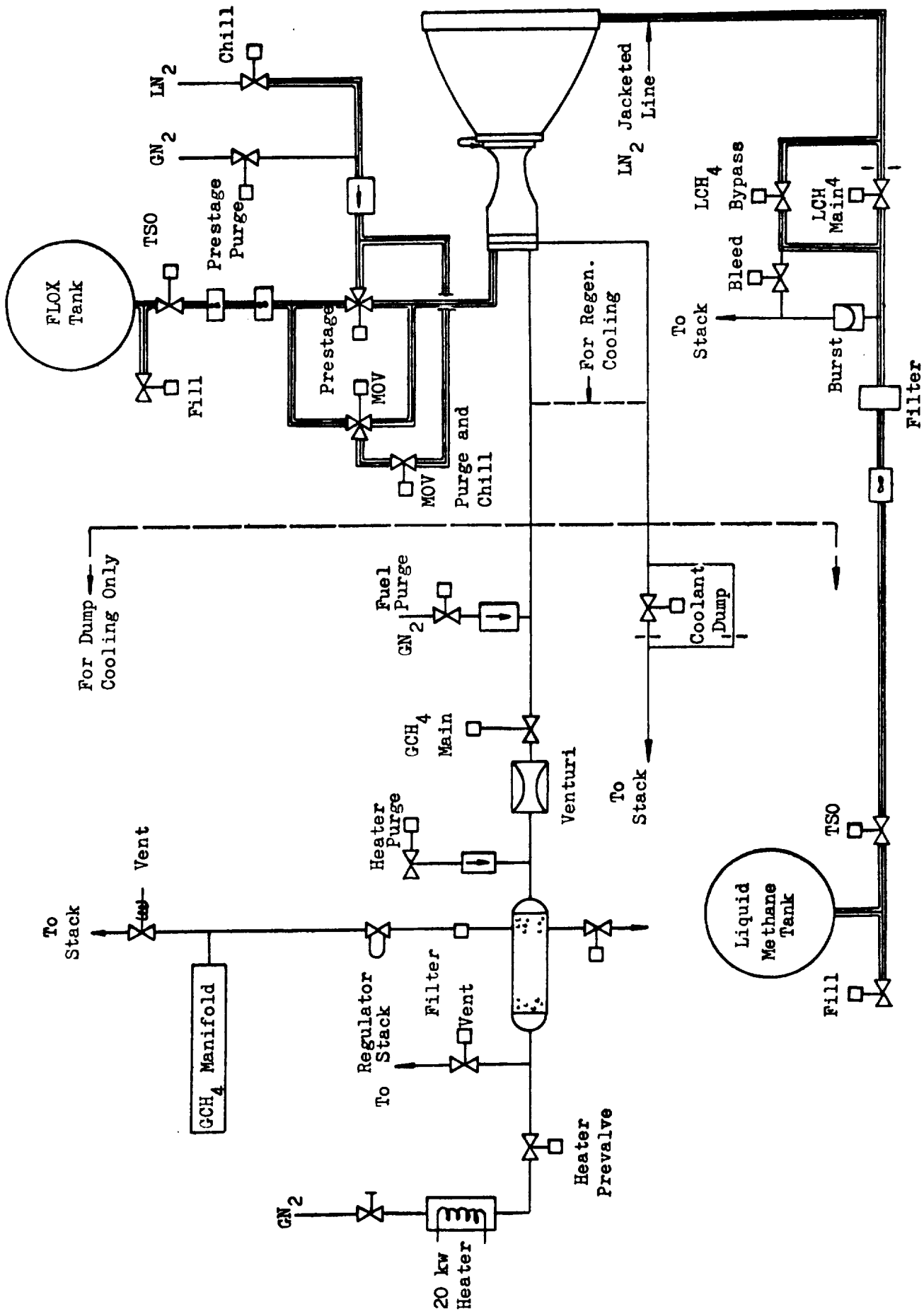


Figure 94 . Facility Schematic

Test Procedures

Inasmuch as stable mainstage, rather than transient, data were desired the run procedures were established to minimize the hazards encountered during transition with liquid light hydrocarbons on earlier test programs.

Dump Cooled Tests. Two separate fuel systems were used for the dump cooled tests. Liquid methane was supplied to the coolant jacket and dumped overboard after leaving the jacket. Heated gaseous methane was supplied to the injector under simulated turbine discharge conditions typical of an expander cycle engine. The start sequence for the dump cooled tests used the same 0.6 second gaseous methane lead (insofar as the injected propellants are concerned) as that used successfully during IR&D tests with a regeneratively cooled chamber.

The coolant jacket flow characteristics are particularly important to assure a successful start. The coolant flow was initiated prior to injector flow. Initially the coolant flashes in the inlet lines and the jacket. As these components are cooled, the temperature of the fuel decreases, the density increases, the flow-rate increases, and the mass of the coolant stored in the jacket increases. At some point, the mass of the coolant stored in the jacket equals, and then later exceeds, that stored during mainstage.

If the engine is started before that point (i.e., when there is less CH_4 in the jacket than during mainstage), mass accumulation continues so that jacket outlet flow may be less than mainstage flow. The downstream (from the coolant flow standpoint) portion of the chamber may then be undercooled. If the engine is started after that point, the excess mass of coolant in the jacket must be removed. This is accomplished by an increase in the jacket outlet flow and a decrease in the jacket inlet flow. Undercooling of the inlet occurs under these conditions. This simplified description of events is modified by such factors as coolant inertia, heat flux profile, and heat flux transients. A coolant lead of 2.2 seconds was used for the dump-cooled tests.

By use of an excess dump valve at the exit of the jacket during transition, together with allowing the coolant to achieve a slightly greater average density than the mainstage values, the following beneficial conditions exist: 1) excessive accumulation during transition is prevented; 2) the steady-state flowrate represents an overcooled condition; 3) the high flowrate of the coolant presents a favorable inertial condition; 4) the low pressure on the downstream side of the jacket permits rapid exit of the excess mass. As soon as steady state is approached, the excess dump valve is closed and the coolant flows only through the orificed parallel mainstage dump line. High flowrate and back pressure could be achieved by the use of the coolant bypass valve during the start transient. A low-flow oxidizer bypass valve (pre-stage valve) was also provided to obtain a low chamber pressure, low mixture ratio (i.e., low heat flux) step in the start transient. This would further reduce the tendency towards a coolant flow undershoot.

Computer model simulations indicated that a satisfactory start could be achieved without the use of the CH₄ bypass and dump valves. This was subsequently verified by the actual dump cooled tests which did not use the bypass and fuel dump valves for starting.

The start sequence used was as follows:

1. Fuel Purge ON
2. Injector LN₂ Chill ON
3. Injector LN₂ Chill OFF
4. Oxidizer Purge ON
5. Main Fuel Valve OPEN
6. Main Oxidizer Valve OPEN

The fuel purge was automatically checked off as the injection pressure built up. The oxidizer purge flowed through one side of the three way oxidizer valve and was shut off as the valve opened.

Regeneratively Cooled Tests. A liquid fuel lead (0.5 seconds) was used for the regeneratively cooled tests in order to assure priming and chilling of the jacket based on computer model simulations. These simulations indicated that no overshoot would occur in the injector oxidizer flowrate although the flowmeter would

experience an overshoot while the feed line was priming. A comparison of flows from an actual test and the predicted transients is shown in Fig. 95.

The start sequence for the regeneratively cooled tests was:

1. Injector LN₂ Chill ON
2. Injector LN₂ Chill OFF
3. Injector Purges ON
4. Fuel Main Valve OPEN
5. Oxidizer Main Valve OPEN

The fuel purge was automatically checked off as the injection pressure built up. The oxidizer purge was shut off when the oxidizer valve opened.

Equipment

The experimental hardware used for these tests consisted of the two-piece electroformed thrust chamber and the concentric element injector with a solid copper face described in Section III. The injector was modified after the previous (water-cooled chamber) test series by adding a fuel showerhead orifice between each element in the outer circle and the thrust chamber wall.

INSTRUMENTATION AND DATA RECORDING

Facility and engine instrumentation is described in Table 18. Transducers and data recording equipment were described in Section III.

TEST SUMMARY

A total of seven dump cooled and regenerative cooled tests were conducted under this task. The accumulated duration was 41.4 seconds. The test conditions are summarized in Table 19 and described in the following paragraphs. Prior to conducting these tests a series of tests was accomplished under IR&D funding with a thrust chamber of similar design but with a low area ratio nozzle. The data from these tests was used to update the engine computer model developed under Contract NAS 3-12024. Simulations made with the updated model indicated that a very simple

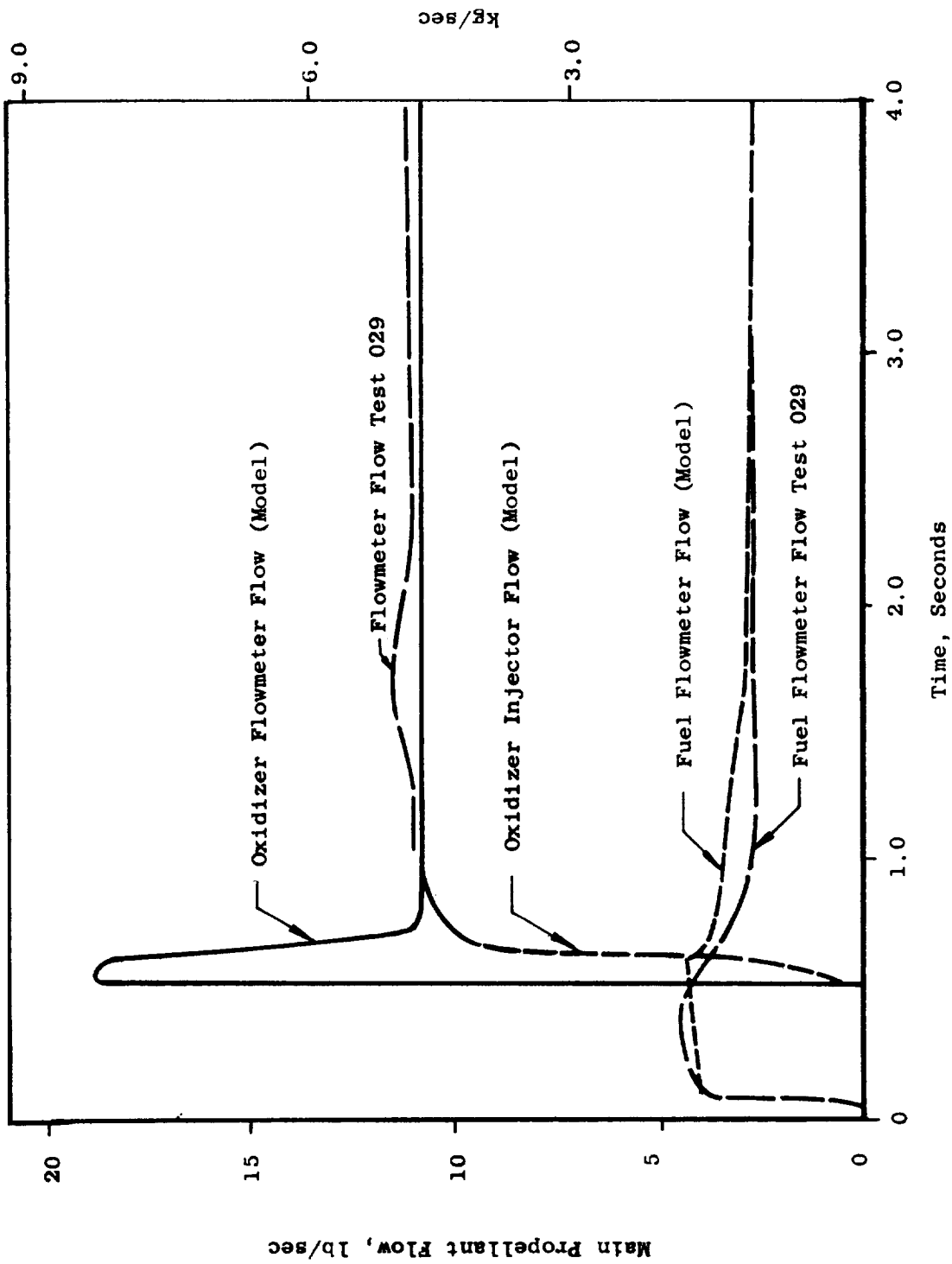


Figure 95. Comparison of Start Model and Actual Start

TABLE 18
INSTRUMENTATION FOR TASK V TESTS

PARAMETER	RANGE		TRANSDUCER	RECORDING*
	psig	N/cm ²		
PRESSURE				
GCH ₄ Manifold	0-3000	0-2068	Taber	G, B
GCH ₄ Regulator Inlet	0-3000	0-2068	Taber	B
GCH ₄ Venturi Inlet	0-3000	0-2068	Taber	G, B
GCH ₄ Venturi Throat	0-3000	0-2068	Taber	G, B
LCH ₄ Tank	0-3000	0-2068	Taber	G
Coolant Jacket Inlet	0-3000	0-2068	Taber	G, B
Coolant Jacket ε = 4	0-3000	0-2068	Taber	B
Coolant Jacket Discharge	0-2000	0-1379	Taber	G, B
Fuel Injection	0-2000	0-1379	Taber	G, B, O
Fuel Injection	0-2000	0-1379	Photocon	T, O
Oxidizer Tank	0-2000	0-1379	Taber	G
Oxidizer Injection	0-2000	0-1379	Taber	G, B, O
Oxidizer Injection	0-2000	0-1379	Photocon	T, O
Chamber Pressure (2)	0-1000	0-690	Taber	G, B, O
Chamber Pressure	0-1000	0-690	Photocon	T, O
Nozzle Wall	0-15	0-10	Data Sensor	B
Nozzle Base (2)	0-15	0-10	Taber	G, B
TEMPERATURE				
	F	K		
Heater Inlet	60-100	289 to 311	I/C	G, B
Heater Bed (2)	60-1000	289 to 812	I/C	B
Venturi Inlet	60-1000	289 to 812	I/C	G, B
LCH ₄ Flowmeter Inlet	-200 to -320	145 to 78	Bulb	B
Coolant Jacket Inlet	-200 to -320	145 to 78	Bulb	B

TABLE 18 (Continued)

INSTRUMENTATION FOR TASK V TESTS

PARAMETER	RANGE		TRANSDUCER	RECORDING*
	F	K		
TEMPERATURE				
Nozzle Coolant, $\epsilon = 4$ (8)	60 to 2000	289 to 1430	C/A	G, B
Chamber Outlet (8)	60 to 2000	289 to 1430	C/A	G, B
Fuel Injection	60 to 2000	289 to 1430	C/A	B
FLOX Flowmeter (2)	-290 to -310	83 to 95	Rosemount Bulb	G, B
FLOX Injection	-240 to -305	86 to 122	I/C	G, B
Coolant Jacket Wall (11)	60 to 1500	289 to 1090	I/C	B
FLOWRATES				
	gpm	l/sec		
LCH ₄	8 to 110	0.50 to 6.9	Fisher- Porter	B, O
FLOX (2)	36 to 120	2.27 to 7.57	Fisher- Porter	B, O

* G - Graphic, B - Beckman, O - Oscillograph, T - Tape

TABLE 19
 ALTITUDE TESTS IN REGENERATIVELY COOLED CHAMBER
 CONCENTRIC ELEMENT INJECTOR

TEST NO.	DURATION SEC	P _C PSIA (N/cm ²)	MIXTURE RATIO	COOLING
26	0.5	519 (358)		Dump
27	5.5	526 (363)	5.0	Dump
28	8.0	553 (381)	1.7	Regenerative
29	5.1	510 (352)	4.8	Regenerative
30	7.0	518 (357)	5.1	Regenerative
31	7.8	645 (445)	3.5-2.8	Regenerative
32	8.0	516 (356)	5.7	Regenerative

start sequence could be used for both the dump cooled and regeneratively cooled tests with no problems of temperature overshoot. A series of liquid methane blowdowns were made to verify the thermal capacitances used in the computer model. The actual blowdown transients were slightly slower than the predicted transients. The coolant jacket pressure drops agreed well with water calibration data.

On the basis of these results the dump cooled tests were started by simply opening the coolant valve 2.2 seconds before the main FLOX valve and opening the main gaseous methane injection valve 0.5 seconds before the FLOX valve. The duration of the first test was 0.5 seconds. This test successfully checked out the thrust chamber and injector, the facility (particularly the LCH_4 feed system) and instrumentation, and the start sequence. A leaking fitting was found and sealed. The start transient was satisfactory with no indication of overshoot on the bulk temperature or skin temperature measurements. The duration of the second test was 5.5 seconds which was long enough to obtain valid performance and heat transfer data. The chamber pressure on this test was 525 psia (362 N/cm^2). The injector mixture ratio was 5.0 and the coolant flow corresponded to a mixture ratio of 4.5. The thrust chamber and injector were in good condition after these tests.

In view of the good results obtained on the analog model and the smooth starts observed with the dump cooled tests, it was decided to proceed directly to the fully regeneratively cooled tests. A low mixture ratio test was scheduled (test 28) as a safety feature for the first regeneratively cooled test. No orifice was used in the facility LCH_4 feed system. The actual mixture ratio, 1.7, was even lower than targeted because the coolant jacket ΔP constituted a large portion of the total CH_4 system resistance and because of the relationships between mixture ratio, heat flux, and methane density at the particular operating conditions. The test duration was approximately 8 seconds. During the latter part of the test 500-900 psi (345 to 620 N/cm^2) 'pops' occurred in chamber pressure. These disturbances damped out quickly with no indication of combustion instability and did provide an unintentional demonstration of system dynamic stability.

The fuel system was orificed for test 29 and a 0.5 second fuel lead substituted for the previous 2.0 second fuel lead. The engine started well (a 10 percent overshoot in chamber pressure occurred) and operated stably at 510 psia (352 N/cm^2) chamber pressure for 5 seconds. At this point low amplitude ($\pm 25 \text{ psi}$) oscillations developed in oxidizer injection pressure which had an average value of 628 psia (433 N/cm^2). The Combustion Stability Monitoring System senses this parameter and initiated cutoff at this value. No instabilities were indicated on the high speed chamber pressure, fuel injection pressure, or accelerometer data. The thrust chamber was in good condition after the test. One oxidizer post tip was burned slightly. The annular fuel gap was closed at one point on this element apparently as a result of the installation procedure which permitted the injector face to expand against the chamber during hot firing. The injector post was repaired and the installation procedure revised. The chamber and the rest of the injector were in good condition.

The mixture ratio was increased to 5.0 on the next test (test 30). The test was terminated after 6.7 seconds by an observer because of a fire caused by a slight leak in a chamber pressure transducer fitting. No hardware damage resulted from the fire. Post-test inspection revealed a very slight erosion of the tip of one FLOX post which was repaired by welding and remachining. The circumference of the injector face, which extends 0.5 inches (1.3 cm) into the thrust chamber, was machined to provide a 0.025 inch (0.063 cm) gap between the injector and the chamber. This was done so that thermal expansion of the copper injector face could not result in distortion of the outer ring of elements by pressure against the chamber.

The facility LCH_4 orifice was removed before the next test because of the high fuel flowrate and pressure requirements of the test which was targeted for higher chamber pressure at low (4.0) mixture ratio. A short fuel lead was used as on the two previous tests. The thrust chamber reached a quasi-equilibrium condition of approximately 620 psia (430 N/cm^2) chamber pressure and 3.5 propellant mixture ratio. The methane flowrate continued to increase slowly during the test while the jacket discharge temperature decreased. At cutoff the chamber pressure was 640 psia (440 N/cm^2) and the mixture ratio was 2.8. The relationships between coolant flowrate, jacket pressure drop, heat input, and propellant mixture ratio are analyzed in Appendix H.

This analysis indicated that the coolant jacket pressure drop cannot be reliably used to control the fuel flowrate. In a pump fed engine system other flow-controlling devices are present so that the conditions experienced on this test would not occur. The injector and chamber were in good condition after this test.

The facility orifice was replaced and a test was conducted at approximately 510 psia (350 N/cm^2) chamber pressure and a mixture ratio of 5.6. Test parameters appeared normal but a post-test inspection of the injector revealed erosion of a FLOX post and adjacent copper face. This post had been eroded and repaired twice previously indicating the probability that the failure was due to improper flow characteristics in the element. The injector was removed and inspected more closely. The post was burned back more than two inches (5 cm) and the adjacent portion of the copper face was eroded into a conical shape with a maximum diameter of approximately one-half inch (1 cm) at the injector face. The thrust chamber and all other elements of the injector were in good condition.

TEST RESULTS

Data taken during the regeneratively cooled thrust chamber tests yielded information about injector and nozzle performance, heat input to the thrust chamber, and pressure drop characteristics of the injector and thrust chamber.

Performance

Concentric element injector performance data for the regeneratively cooled test series is presented in Table 20. Performance was calculated in the same manner as for the water-cooled tests except that the maximum correction for throat area thermal enlargement was 0.5 percent for the regeneratively cooled test data instead of 0.2 percent. The maximum heat transfer correction was 0.2 percent. This correction was based on the measured coolant enthalpy rise from $\epsilon = 4$ to the injector and a distribution of heat flux assumed to be equal to that of the water-cooled tests.

TABLE 20

REGENERATIVELY COOLED TEST PERFORMANCE SUMMARY

Test	Chamber Pressure psia	Oxidizer Flowrate lb/sec	Fuel Flowrate lb/sec	Mixture Ratio	Fuel Inlet Temp R	C* meas ft/sec	C* Theo ft/sec	C* _p percent	C* _{inj} P percent	
										kg/sec
27	526	10.85	2.16	5.02	1021	6982	7081	2158	98.0	98.2
28	553	10.22	6.04	1.69	343	5847	6207	1892	94.5	94.6
29	510	10.57	2.22	4.76	1020	6842	7108	2166	96.8	96.9
30	518	10.82	2.14	5.06	1031	6851	7146	2178	96.5	96.6
31	645	12.32	4.41	2.79	445	6633	6668	2032	100.0	100.0
32	516	10.83	1.92	5.65	1116	6935	7180	2188	97.1	97.2

The average performance for the tests at near-nominal mixture ratio (tests 27, 29, 30, 32) was 97.2 percent. This agrees with the performance data obtained in the water-cooled thrust chamber. Differences in test conditions between the two series affected performance in opposite manners. The showerhead fuel orifices added before the regeneratively cooled tests and deviations from element concentricity caused by flute wear could be expected to reduce performance slightly by affecting the propellant mixture ratio distribution. Conversely, the higher methane injection temperature and longer chamber length were expected to improve performance slightly. These two effects apparently cancelled each other since the injector performance did not change significantly.

Thrust measurements were taken during this test series. However, facility interactions invalidated most of the data. Only on Test 30 did the pre- and post-test calibrations indicate that the interactions were at an insignificant level. The method of analyzing the thrust data taken with the self pumping diffuser is presented in Appendix G. The measured thrust level on Test 30 was -1290 pounds which was equivalent to 5225 pounds of thrust at vacuum. This yielded a specific impulse of 403 seconds (3960 N sec/kg) which corresponds to a specific impulse efficiency of 94.2 percent. The C* efficiency on this test was 96.6 percent. These efficiencies imply a nozzle efficiency of 97.5 percent.

Heat Transfer

The basic heat transfer results for the regeneratively cooled thrust chamber are summarized in Table 21. The measured temperature rises were slightly low compared to the predicted value of 860F (480K) at $P_c = 500$ psia (345 N/cm^2), $O/F = 5.0$. (The temperature rise was 792 F (440K) on Test 30). The heat inputs into the combustion chamber, from the injector to $\epsilon = 4$, were found to be proportional to the product of chamber pressure and mixture ratio as observed during the water-cooled tests. The correlation is shown in Fig. 96 and includes the tests with the water-cooled copper chamber as well as the dump and regeneratively cooled tests on the nickel chamber. The correlation is empirical but is quite good and includes a broad range of chamber pressures (~ 500 to 900 psia) and propellant mixture ratios (1.7 to 5.7). The relatively strong

TABLE 21

HEAT TRANSFER RESULTS FOR REGENERATIVELY COOLED THRUST CHAMBER

Test Number	Chamber Pressure		Mixture Ratio	Fuel Flowrate		Inlet Temp		Avg Exit Temp		Total Heat Input**		Q/ψ Total	Inlet Pressure		Outlet Pressure		
	psia	N/cm ²		lb/sec	kg/sec	F	K	F	K	Btu/sec	kw		Btu/lb	J/gr	psig	N/cm ²	psia
27	526	362	5.02	2.16	0.98	-242	121	561	567	1612	1702	125	290	1998	1377	1197	825
				2.37*	1.08*												
28	553	381	1.69	6.05	2.74	-250	116	-117	190	835	882	51	119	1762	1215	586	404
29	510	352	4.76	2.22	1.01	-225	130	560	566	1554	1641	120	279	1744	1202	641	442
30	518	357	5.06	2.20	1.00	-221	132	571	572	1485	1568	113	263	1677	1156	577	398
32	516	356	5.65	1.96	0.89	-218	134	656	619	1450	1531	113	263	1653	1139	569	392

* Dump Coolant Flowrate

** Nozzle and Combustion Chamber

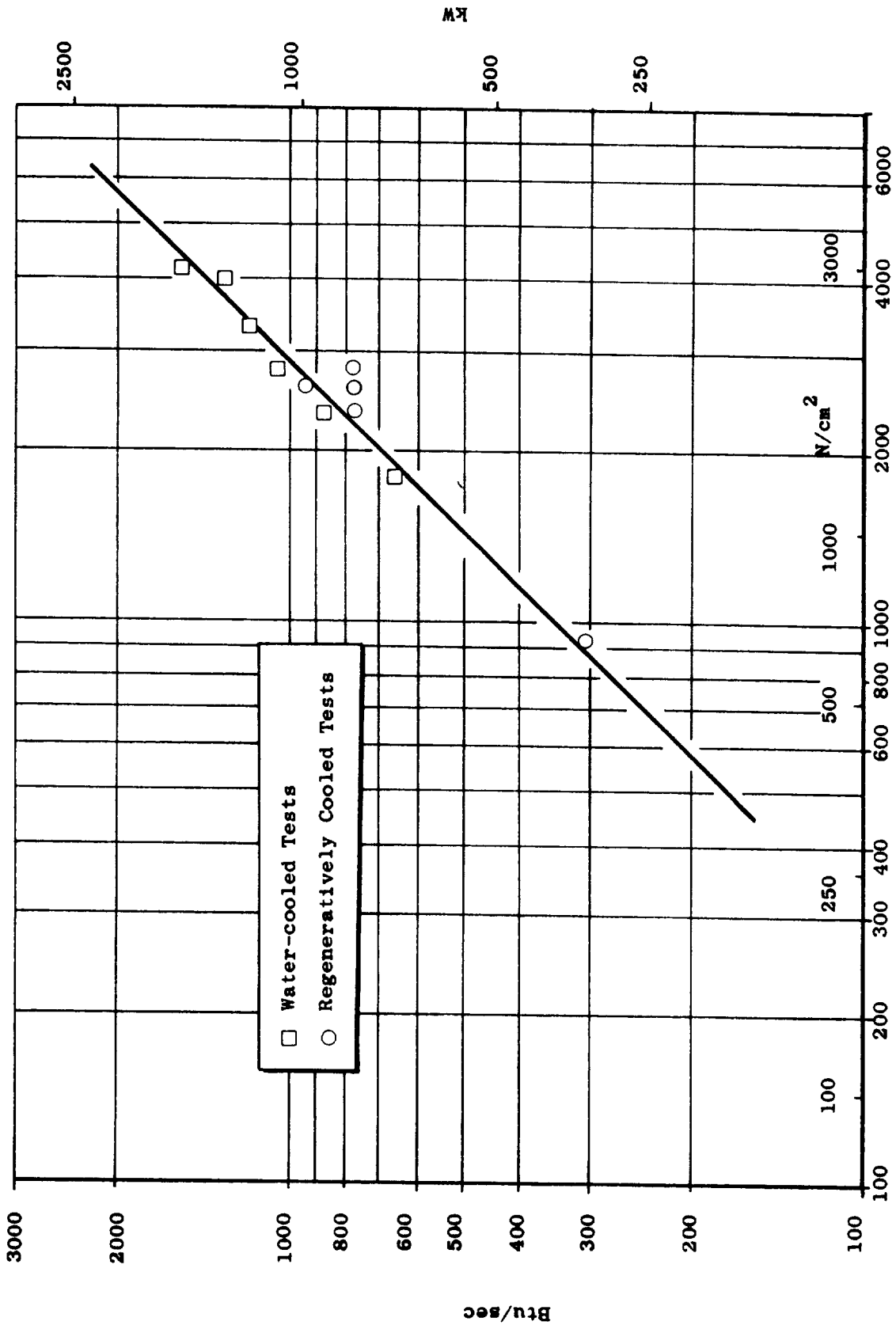


Figure 96 . Combustion Chamber Heat Inputs
 $(P_c) \cdot (o/F), \text{ psia}$

effect of mixture ratio on combustion chamber heat flux is interesting because the theoretical effect is quite small between mixture ratios of 2.0 and 5.7. A carbon deposition effect at lower mixture ratios may be responsible for this trend.

Thermocouples were welded to the outside of the combustion chamber at several locations. Several holes were drilled from the outside of the nozzle to the tops of the lands at the midpoint of the lands. The location of these thermocouples and the temperatures achieved at cutoff on the longest duration test (Test 32) are shown in Table 22. These temperatures, in some instances, had not quite stabilized even though the bulk temperatures had stabilized on this test. These data indicate that the structural wall of the thrust chamber is fairly cool and should possess good strength characteristics. It is interesting to note that the hottest part of the outer wall of the combustion chamber was near the injector. The condition of the chamber after the regeneratively cooled tests was excellent.

TABLE 22

REGENERATIVELY COOLED CHAMBER WALL TEMPERATURES

Thermocouple	T _{CH1}	T _{CH2}	T _{CH3}	T _{CH4}	T _{CH5}	T _{N1}	T _{N2}	T _{N3}	T _{N4}	T _{N5}	T _{N6}
Approximate Location (€)	Inj. End	Start of Convergence	Throat	2	3.5	10	15	20	30	40	50
Temperature F On Test 32, (K)	560 (570)	460 (510)	440 (500)	370 (460)	160 (340)	190 (360)	-	130 (330)	100 (310)	50 (280)	0 (260)

Pressure Drops

Figure 97 is of correlation of the $(\bar{\rho}) (\Delta P)$ product for the coolant jacket of the combustion chamber with flowrate for the water and liquid methane flow calibrations as well as for the firing tests. Methane density, $\bar{\rho}$, is the average of the densities at the inlet and outlet of the chamber. The data are all in good agreement but appear to follow a slightly lower slope than the expected 2:1 slope, probably because of the simple method used to obtain an average density of the coolant.

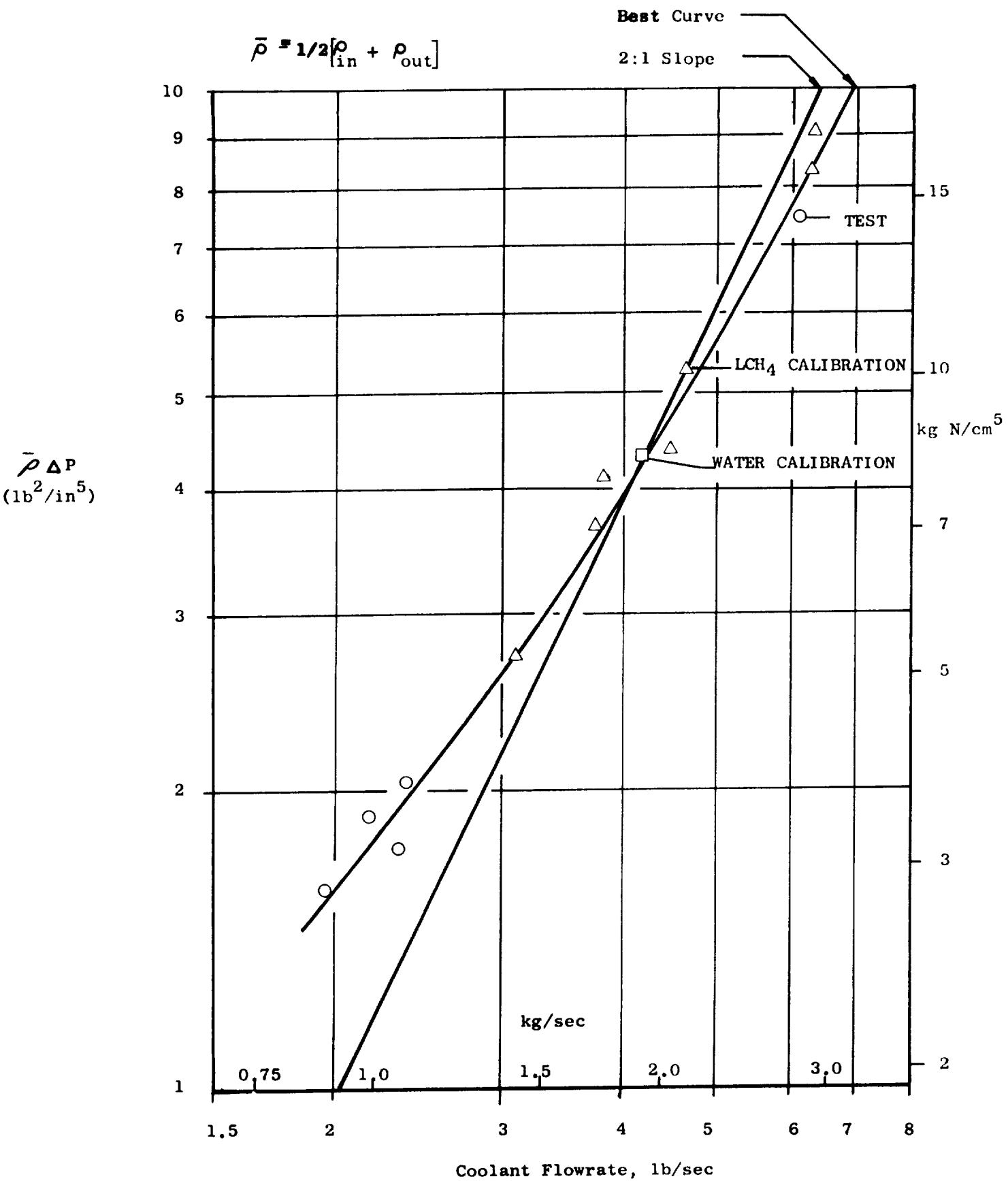


Figure 97 . Combustion Chamber Pressure Drop Relations

The pressure drops are seen to be rather high, e.g., 1084 psi (740 N/cm^2) on Test 32. A number of factors contribute to this, The methane inlet temperature was 42 degrees warmer than the nominal (260R) value. The density of the methane is very sensitive to temperature. Reducing the inlet temperature to the nominal value would increase the average density, and therefore reduce the ΔP , by approximately 25 percent. The back pressure also affects the density and pressure drop considerably which can be seen by comparing the results of Test 32 with those of the dump cooled Test 27. On the dump cooled test the back pressure was maintained at approximately 1200 psia (720 N/cm^2) by a facility orifice. Although the coolant flowrate was 20 percent higher on this test the pressure drop was 75 percent of that on Test 32. A back pressure of approximately 1000 psia (690 N/cm^2) is typical for a system using an expander power cycle. With the temperature and back pressure corrections the pressure drop would be nearly 600 psi (413 N/cm^2) on Test 32, which is fairly close to the predicted value for this chamber. As previously mentioned the channel design was based on early heat flux profile data taken with the triplet element injector which indicated high heat fluxes in the cylindrical section of the chamber compared to the values obtained with the concentric element injector. The combustion zone is, therefore, conservatively designed which results in a high pressure drop which is enhanced by the low density of the hot methane in this region.

The pressure drops for the concentric element injector are summarized in Tables 23 and 24 and plotted in Fig. 98. The $\rho \Delta P$ products are again plotted to account for propellant density variations. Data for the water cooled altitude tests with this injector are included with the regeneratively cooled test data. The FLOX injection pressure drop data shown in Fig. 98 are consistent for each of the two test series and follow the theoretical 2:1 slope quite well. The 10 percent reduction in oxidizer flowrate (at constant ΔP) between the two test series is not easily explainable. The fuel side of the injector was modified slightly between test series but the oxidizer side was unchanged. Possible reasons for the shift are: 1) A consistent error in the FLOX injection pressure measurement on one of the series, or: 2) a deposition of approximately 0.001 inches (0.003 cm) foreign material in the orifices of the hydraulic swirlers between test series. The pressure drop at 500 psia (345 N/cm^2) chamber pressure and 5.25 mixture ratio is 110 psi (70 N/cm^2) based on the higher ΔP curve.

CONCENTRIC INJECTOR OXIDIZER DELTA P

Test Number	ΔP_o		T_{I_o}		K	ρ	lb/ft ³	kg/m ³	lb ² /in. ⁵	kg N/cm ⁵	$\rho \Delta P_o$	lb/sec	kg/sec
	psi	N/cm ²	F										
Alt 2	104	72	-266		108	81	1294		4.86	0.93		11.3	5.1
3	86	59	-284		98	85	1356		4.22	0.80		10.0	4.5
4	89	61	-277		102	83	1331		4.28	0.81		10.3	4.7
5	96	66	-281		100	84	1347		4.67	0.89		10.6	4.8
6	174	120	-287		96	86	1376		8.66	1.65		14.2	6.4
7	92	63	-287		96	86	1369		4.55	0.86		10.4	4.7
8	171	118	-281		99	85	1353		8.36	1.59		14.0	6.4
9	193	133	-288		95	86	1379		9.62	1.83		15.0	6.8
10	288	198	-310		83	91	1462		15.21	2.89		18.2	8.3
27	116	80	-308		84	90	1448		6.07	1.16		10.9	4.9
28	101	70	-302		88	89	1425		5.20	0.99		10.2	4.6
29	118	81	-289		95	86	1375		5.87	1.12		10.6	4.8
30	116	80	-303		87	89	1428		5.98	1.14		10.8	4.9
31	154	106	-316		80	92	1478		8.22	1.56		12.3	5.6
32	122	84	-315		80	92	1475		6.50	1.24		10.8	4.9

TABLE 24
 CONCENTRIC ELEMENT INJECTOR FUEL DELTA P

Test Number	Fuel Flowrate		Injection Temperature		PIF psia	P_f		ΔP_f		$(P\Delta P)_f$		
	lb/sec	kg/sec	F	K		$\frac{lb}{in.} \times 10^4$	$\frac{kg}{m^3}$	psi	N/cm^2	$\frac{lb^2}{in.} \times 10^3$	$\frac{kg}{N/cm^2}$	
Alt 2	2.87	1.30	320	433	666	459	7.40	20.5	85	59	63	1200
3	2.87	1.30	355	453	637	439	6.78	18.8	110	76	75	1420
4	2.20	1.00	303	424	568	392	6.46	17.9	50	35	32	616
5	1.86	0.85	302	423	556	383	6.34	17.5	38	26	24	461
6	2.99	1.36	304	435	798	550	8.84	24.5	84	58	74	1410
7	1.83	0.83	278	410	542	374	6.37	17.6	36	25	23	440
8	3.44	1.56	313	429	836	576	9.40	26.0	110	76	103	1963
9	2.63	1.19	315	430	779	537	8.72	24.1	54	37	47	895
10	3.82	1.73	367	459	1005	693	10.55	29.2	107	74	113	2153
27	2.37	1.08	383	468	591	407	6.1	16.9	59	41	36	686
28	6.04	2.74			600	414			46	32		
29	2.22	1.01	560	567	656	452	5.4	14.9	146	101	79	1506
30	2.14	0.97	570	572	591	408	4.9	13.4	73	50	35	675
31	3.65	1.66	117	320	717	494	11.8	32.6	89	61	105	2001
	4.41	2.00	-15	247	740	510	17.5	78.4	94	65	165	3145
32	1.92	0.87	656	620	583	402	4.5	12.5	67	46	23	442

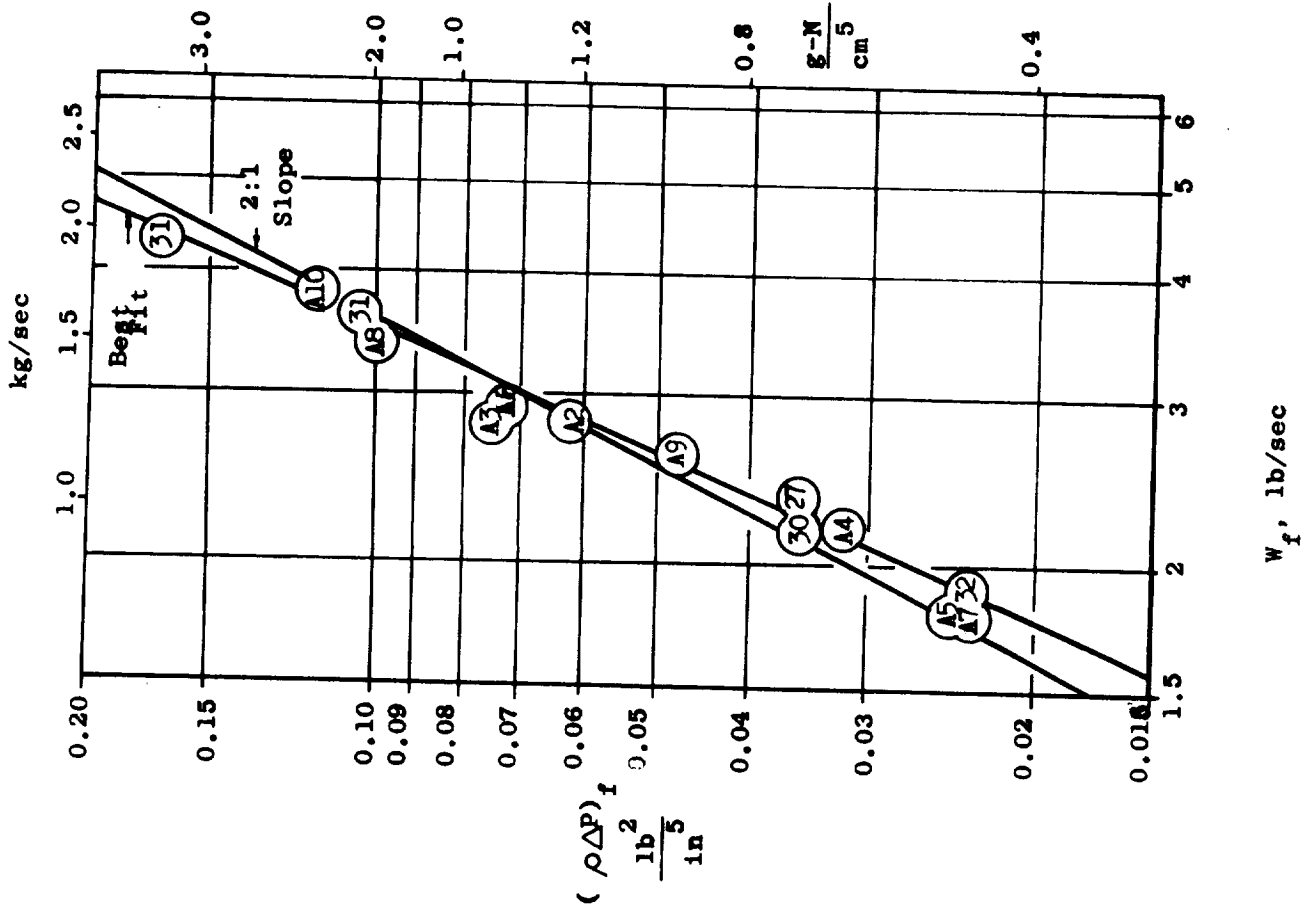
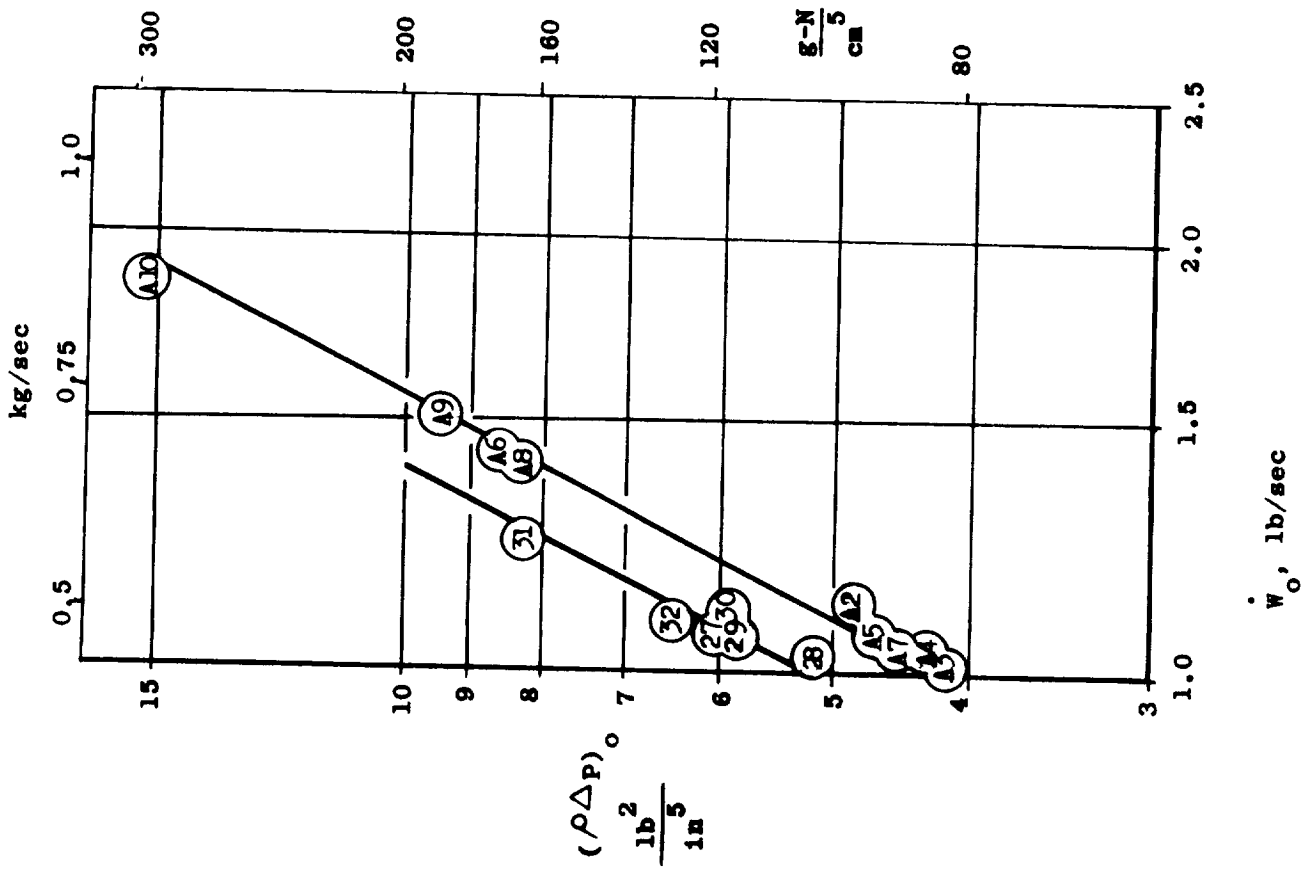


Figure 98. Concentric Element Injector Pressure Drops

The fuel injection pressure drop data are linear on log-log coordinates. The data fit well on a line having a slope of 2.3:1. The difference between the experimental slope and the theoretical slope of 2:1 probably results from the method of calculating \bar{p} . The temperature and pressure in the injector manifold were used to calculate \bar{p} which, in fact is determined by the values of these parameters at the exit of the element also. The fuel injection pressure drop at the nominal conditions is approximately 55 psia (38 N/cm²).

CONCLUSIONS

From the results of the regeneratively cooled thrust chamber fabrication and test program the following may be concluded:

1. Regenerative cooling with methane is feasible in a thrust chamber using FLOX/methane propellants.
2. Electroformed thrust chambers can be fabricated economically and operate well under design conditions.
3. Start transient thermal problems are reduced by the channel wall construction technique. A simple start technique can be used with the regeneratively cooled chamber.
4. Heat transfer and injector performance results concur with those obtained on the water cooled test program.

SECTION V

THROTTLING INJECTOR TESTS

These tests were conducted to demonstrate performance, stability, and heat transfer characteristics over a 10:1 throttling range. Tests were conducted at ambient pressure conditions using water-cooled and regeneratively cooled thrust chambers with low area ratio nozzles. The recessed post and heat exchanger element injectors were tested.

TEST FACILITY AND EQUIPMENT

The facilities built up during the water-cooled and regeneratively cooled test programs were used with slight modifications as described below.

Propellant Feed Systems

Gaseous methane and liquid FLOX feed systems were used. Figure 99 is a schematic of the propellant feed and purge systems. The principal modifications of the feed system were made to provide higher temperature methane and to permit stepping the propellant flowrates to obtain two thrust levels on each test. The latter modification was made in order to double the number of data points per test and to provide capability to demonstrate dynamic throttling.

Higher methane temperatures were obtained by adding a second heater to the system. The second heater consisted of a pipe containing steel balls. The pipe and balls were heated by a hydrogen fire while flowing GN_2 . The GN_2 discharge temperature was monitored to determine the proper degree of preheating of the bed. Temperatures in excess of 1000F (800K) were obtained with this heater. It was used with the water-cooled thrust chamber to simulate the outlet temperature of the regeneratively cooled thrust chamber. A GN_2 purge downstream of the second heater provided the normal ambient temperature fuel injection purge.

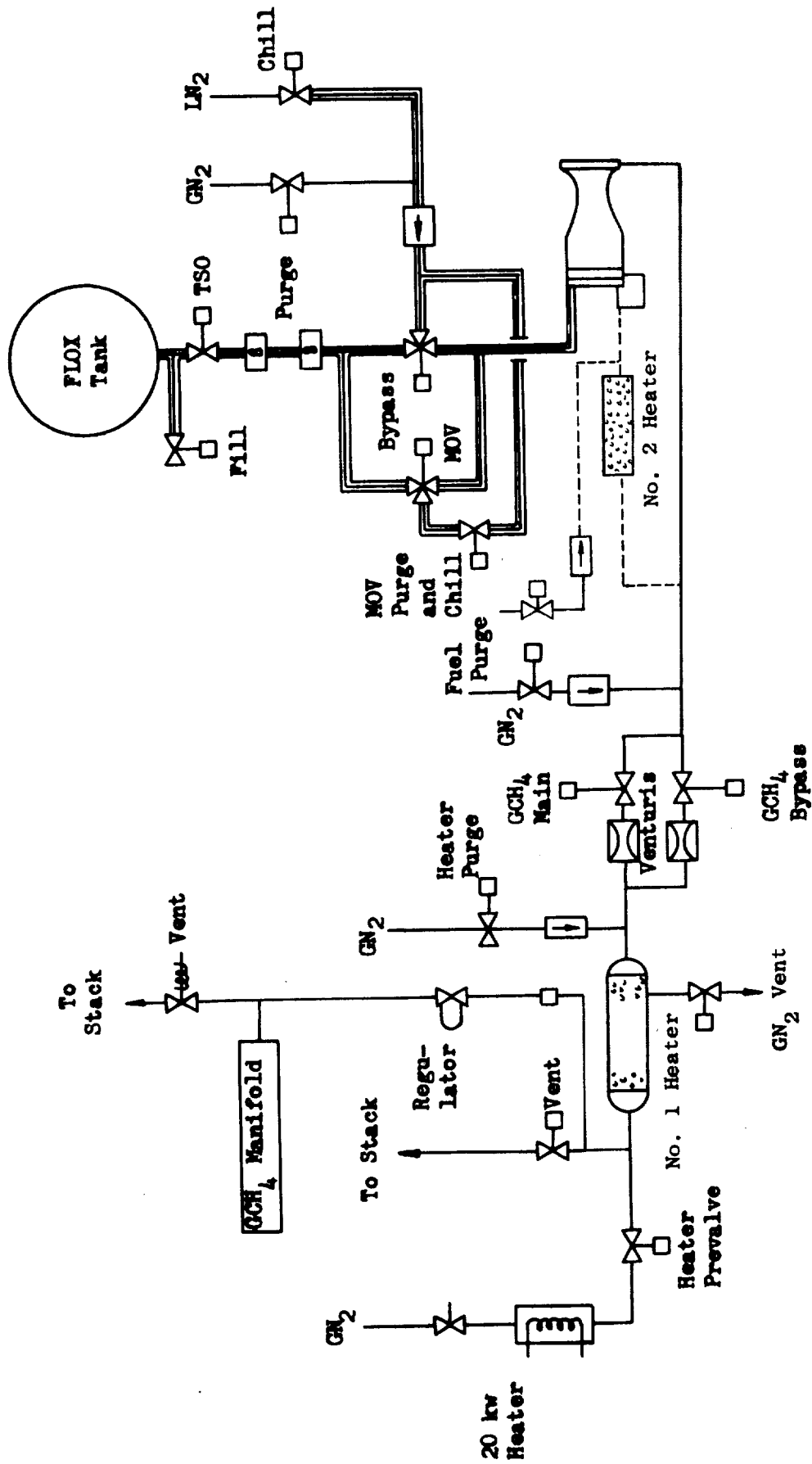


Figure 99. Facility Schematic

Stepped thrust levels were obtained by using bypass valves in the propellant lines. The oxidizer bypass valve had already been installed for the regenerative cooling test program. A bypass valve was installed in the gaseous methane feed system.

Flow through the oxidizer valves was controlled by orifices in the common line and in the bypass line. Flow through the fuel valves was controlled by venturis in the main and bypass lines.

Test Procedures

It was particularly important to chill the injector prior to the start of the throttling tests because the FLOX enters the injector under conditions close to the boiling point on tests at the lowest chamber pressures. The procedure finally adapted was to chill the injector with LN₂ through the FLOX feed system, while purging the fuel side, until the injector face temperature was less than 200R (110K). A short fuel lead (~ 0.5 seconds) was used to avoid heating the injector with the preheated methane. The methane heaters were brought up to temperature prior to chilling the injector. The temperature to which the methane was heated was determined by the chamber pressure and the chamber configuration (water - or regeneratively cooled).

Both fuel valves were opened and both oxidizer valves were opened to provide high flowrates for the initial, high thrust portion of the tests. The oxidizer main valve was subsequently closed followed by the main fuel valve to meter propellants through the prevalues, at the same mixture ratio as the high thrust portion of the test, for the low thrust portions of the tests. Durations were scheduled to assure attainment of steady state conditions. The scheduled duration increased as the targeted chamber pressure decreased.

Instrumentation

The instrumentation was generally the same as that described previously (Tables 13 and 18) for the water-cooled and regeneratively cooled thrust chambers. The FLOX flowmeters were replaced with a pair calibrated to a lower flowrate. A methane temperature measurement was added downstream of the second heater. Two injector face temperature measurements were made: one close to an element and one at a point furthest from all adjacent elements. Twenty four outer wall temperatures were measured on the regeneratively cooled chamber. These measurements were all in the same plane, approximately 1.5 inches downstream from the injector face plane. The thermocouples were aligned with each of the elements in the outer row of the injector. These measurements were made to provide an indication of unsafe operating conditions and of the circumferential distribution of heat flux near the injector end of the chamber.

Equipment

The recessed post and heat exchanger element injectors were tested. Three different recesses were tested on the recessed post injector and two on the heat exchanger injector. The regeneratively cooled and water-cooled thrust chambers were tested. The water coolant passages were numbered consecutively starting at the injector end. The first passage was behind the face of the injector; no flow or temperature measurements were made on this passage. The remaining passages were grouped into several series flow circuits as follows:

Circuit:	1	2	3	4	5	6	7	8
Channels:	1	2,3	4,5,6	7,8,9	12,11,10	15,14,13	16,17,22	18,19,20,22

Water flowrates were measured by a flowmeter in each of the above circuits. The total water flowrate was also measured. The water temperature rise across each channel was measured.

TEST SUMMARY

A total of 41 throttling tests were conducted (each throttling step is counted as a test); 12 in the regeneratively cooled thrust chamber and 29 in the water-cooled chamber. The heat exchanger injector was tested 11 times; the recessed post injector 30 times. A total of 545 seconds test time was accumulated during the throttling test program. The test conditions are summarized in Table 25.

The first test series was conducted with the regeneratively cooled thrust chamber and the heat exchanger injector. The first test, 33, was a 0.5 second test to verify proper start and shutdown sequences. A fuel lead of 2 seconds was used.

Test 34 was then conducted for 2.5 seconds at 251 psia (174 N/cm^2) chamber pressure to calibrate engine and system pressure drops. Most instrumentation functioned properly except the FLOX flowmeters which indicated flows almost an order of magnitude lower than that targeted and indicated by chamber pressure and system pressure drops. The flowmeters were subsequently flow checked in LN_2 and again indicated low flows but indicated the correct flow in water and GN_2 . The problem was resolved to be improper adaptation of RF coils to DC flowmeter bodies. Low range DC flowmeters were procured and calibrated.

A 5.5 second test, 35, was conducted for calibration purposes. Control center preliminary data indicated a mixture ratio of 5.4 so a longer duration test was scheduled to obtain steady-state heat transfer data. This test, 36, was terminated when a high value was indicated for the thrust chamber outer wall temperature being monitored. It was subsequently determined that one of the two fuel flow control venturis had been isolated from the system resulting in a very low fuel flow and high propellant mixture ratio. In spite of operating for 16 seconds at a mixture ratio of 15 and an estimated combustion-side wall temperature reaching a maximum of 1750F (1230K), the chamber and injector were in excellent condition. Oscillations of ± 15 psi (10N/cm^2) at approximately 500 cps occurred in chamber pressure for the first two seconds of operation on tests 35 and 36. The

TABLE 25

THROTTLING TEST SUMMARY

TEST	DURATION		CHAMBER PRESSURE		MIXTURE RATIO O/F	THRUST* CHAMBER	INJECTOR **	COMMENTS
	sec		psia	N/cm ²				
33	0.5		250	172		R	HE-230	Checkout test.
34	2.5		251	173		R	HE-230	Flowmeters inaccurate, changed. Stable.
35	5.5		124	86	13.6	R	HE-230	CH ₄ system malfunction, Stable.
36	10.5		123	85	15.2	R	HE-230	CH ₄ system malfunction. Stable. Hardware OK.
37	5.5		232	160	7.5	R	HE-230	FLOX orifice oversize. Injector and T/C erosion; repaired.
38	5.0		193/91	133/63	3.8/3.7	R	RP-0	Stable until warm FLOX reached engine.
39	10.2		282/172	195/119	5.0/4.8	R	RP-0	Stable until warm FLOX reached engine.
40	5.3		333	230	5.8-6.2	R	RP-110	Stable. CH ₄ pressure decayed. T/C erosion, repaired.
41	10.0		164/77	113/53	4.9-4.7	R	RP-110	Stable until warm FLOX reached engine. T/C erosion.
1	0.4		210	145		W	RP-110 A	Checkout. New FLOX post restrictions.
2	2.9		216	149	4.2	W	RP-110 A	Stable.
3	10.6		206	142	5.0	W	RP-110 A	Stable.
4	9.8		105	72	5.8	W	RP-110 A	Stable.
5	17.0		57	39	4.9	W	RP-110 A	Chugging.
6	40.0		110/61	76/42	5.0/4.5	W	RP-110 A	Stable at high P _c and during most of low P _c .
7	15.0		279	193	4.9	W	RP-110 A	Stable. Fuel fire.
8	16.0		134	92	5.7	W	RP-110 A	Stable. FLOX depletion.
9	39.0		209/106	144/74	5.0/5.2	W	RP-150	Stable. Instrumentation damage.
10	17.0		97	67	6.2	W	HE-230 A	Stable. Slight erosion at injector face, repaired.
11	9.9		413	285	6.6-7.1	W	RP-110 A	High facility CH ₄ Δ P.
12	9.5		439	303	10.2-10.8	W	RP-110 A	High facility CH ₄ Δ P.

* R - Regenerative, W - Water-Cooled

** HE - Heat Exchanger, RP - Recessed Post

TABLE 25 (Continued)
THROTTLING TEST SUMMARY

TEST	DURATION sec	CHAMBER PRESSURE		MIXTURE RATIO O/F	THRUST* CHAMBER	INJECTOR **	COMMENTS
		psia	N/cm ²				
13	3.5	321	221	2.8	W	RP-110A	Facility FLOX orifice error.
14	5.7	513	354	5.7	W	RP-110A	Seven FLOX posts burned. Evidence of fuel maldistribution.
15	3.7	518	357	4.3	W	HE-110	Successful test.
16	3.8	507	350	5.0	W	HE-110	Successful test.
17	18/9	91/55	63/38	5.7/5.6	W	HE-110	Chugging on first step.
18	97	62	43	4.7	W	HE-110	Stable. Much carbon in chamber after test.
19	3.0	522	360	4.7	W	RP-110B	Seven FLOX posts replaced with nickel posts. Eight inlets used. Additional distribution holes drilled in fuel body
20	3.0	522	360	5.3	W	RP-110B	Successful test.
21	38/21	78/46	54/32	4.5/4.8	W	RP-110B	Chugged T _{fuel} = 280 F.
22	38/21	72/46	50/32	4.6/4.8	W	RP-110B	Chugged T _{fuel} = 70 F.
23	29/9	229/135	158/93	5.2/5.4	W	RP-110B	Stable.

oscillations damped out completely as the injector fuel temperature rose.

Test 37 was scheduled as a stepped chamber pressure test. At 5.5 seconds cutoff was initiated when one of the chamber outer wall temperatures reached 1500F (1080K). The chamber pressure and propellant mixture ratio were 232 psia (160 N/cm²) and 7.5 respectively. The high value of these parameters was the result of improper orificing of a new facility FLOX feed system. A larger FLOX tank (120 gallons) was being used to prepare for future long duration tests. Thrust chamber erosion was localized to an area within 1/2 inch (1 cm) of the injector face and in the regions of three of the four methane coolant outlet tubes. Approximately 20 channels were eroded through the combustion-side wall; the openings being 0.2 inches (0.5 cm) long or less. A blister was observed at the start of convergence extending over approximately three channels and of approximately one inch length.

The damage to the heat exchanger injector consisted of erosion of the copper fuel body at the edge of the injector near four of the elements (2 pairs of elements approximately 180 degrees apart). The repair was effected by building up the eroded areas with OFHC weld copper and reboring the four affected holes. In order to reduce the possibility of a FLOX-rich condition on the chamber wall, a 0.041 inch (0.10 cm) diameter hole was added between each outer element and the wall. These holes were electrodischarge machined 1.1 inches (2.8 cm) into the fuel body at which point a connecting hole was drilled into the main fuel orifice to provide a relatively high fuel driving pressure.

Test 38 was the first test with the recessed post injector and the first test on which chamber pressure was stepped. The duration was 5.0 seconds and the mixture ratio was intentionally

programmed to be lower than nominal. Operation was stable for the first two seconds at a chamber pressure of 193 psia (135 N/cm²). The FLOX injection temperature then increased as a slug of warm FLOX entered the engine. Chamber pressure dropped to 168 psia (115 N/cm²) and oscillations developed. Chamber pressure was then stepped to 91 psia (63 N/cm²) and the oscillations continued at a lower amplitude.

The propellant mixture ratio, chamber pressure, and duration were increased on the next test (39). The chamber operated stably for approximately 1.5 seconds at a chamber pressure of 282 psia (155 N/cm²). As the FLOX injection temperature rose, chamber pressure oscillations developed at a frequency of 90 cps. After 4.5 seconds chamber pressure was stepped to 172 psia (119 N/cm²) and the oscillations continued.

The injector FLOX posts were recessed 0.110 inches (0.280 cm) beneath the face for test 40. The chamber pressure was 333 psia (230 N/cm²) and the initial mixture ratio was 5.8. Methane supply pressure decreased during the test below the regulator setting with the result that the mixture ratio gradually increased to 6.2. Operation was stable during the 5.3 second duration test. After the test it was observed that the blister which had developed in the converging section of the thrust chamber during test 37 had enlarged and cracked along one side. A leak check revealed five small pin hole leaks at a previously welded portion of the chamber and near the throat. The leaks were so small that they could be sealed to contain 350 psig (240 N/cm²) pressure by rubbing the surface with a blunt rod.

The crack was sealed with a light weld and the blister pressed down; the intent being to conduct tests at low pressure prior to attempting a more radical repair of the blister. LN₂ jets were directed on unjacketed sections of the FLOX line but a warm FLOX slug again entered the engine approximately 2 seconds after

the start of test 41. At this point chamber pressure dropped as the FLOX injection temperature rose and oscillations developed in chamber pressure. After 4.9 seconds the chamber pressure was stepped down to 77 psia (53 N/cm^2) and the oscillations continued. The blister in the converging section of the chamber enlarged slightly and was eroded on the highest surface.

Test 01 was a 0.4 second checkout test of the No. 2 water cooled thrust chamber and the modified recessed post injector. The modification consisted of reducing the diameters of the orifices at the entrances to the FLOX tubes. This was done because the pressure drop was lower than the design value. The diameter of the restrictors was changed from 0.070 to 0.047 inches (0.178 to 0.119 cm) and the entrances were tapered.

Test 02 was a 3 second checkout and calibration test at a chamber pressure of 216 psia (149 N/cm^2) and propellant mixture ratio of 4.2. The mixture ratio was increased to 5.0 and the duration to 10.6 seconds on test 03. The chamber pressure was 206 psia (142 N/cm^2). Test 04 was of 9.8 seconds duration at a chamber pressure of 105 psia (72 N/cm^2) and mixture ratio of 5.8. All four tests were stable. The restrictors helped to uncouple the injector FLOX dome from the thrust chamber and a modification of the start sequence eliminated the slug of hot FLOX which entered the engine approximately two seconds after start on previous tests (operation was stable until this hot slug entered the injector). Near-ambient temperature methane was injected for these tests, which reduced the interpropellant heat transfer.

During tests 05 and 06 the relationship between FLOX temperature and chugging was again demonstrated with chugging eliminated when the FLOX inlet temperature was kept within specific limits. Test 05 was a 17 second test at 57 psia (39 N/cm^2) and mixture ratio of 4.9. Chugging occurred during the test. The temperature of the FLOX at the start of the test was quite warm (190R).

On the next test (06) chamber pressure was stepped so that the low pressure portion of the test would be run after the FLOX had cooled down. On the first step the chamber pressure and mixture ratio were 110 psia (76 N/cm^2) and 5.0 respectively and the pressures were stable. Chamber pressure and mixture ratio on the second step were approximately 60 psia (42 N/cm^2) and 4.5 respectively. During the initial portion of the second step chamber pressure undershot to 47 psia (32 N/cm^2) and FLOX injection temperature surged from 172 to 181R (96 to 101K). This surge lasted approximately five seconds during which chugging occurred. After the surge, operation was stable for 15 seconds. The FLOX injection temperature then rose gradually and, as the temperature rose above 176R (98K) an occasional burst of chugging occurred. The boiling point of FLOX at 60 psia (42 N/cm^2) is 185R (103K). It appears that a FLOX temperature of approximately nine degrees below the boiling point (based on chamber pressure) should be maintained. This corresponds to approximately 172R (96K) at 50 psia (35 N/cm^2) chamber pressure.

Test 07 was conducted at a chamber pressure of 279 psia (193 N/cm^2) and mixture ratio of 4.9. The test was stable for a duration of 14 seconds and was terminated because of a fire caused by a fuel feed system leak. Test 08 was terminated for FLOX depletion after 16 seconds. Chamber pressure and mixture ratio were 134 psia (92 N/cm^2) and 5.7 respectively. The test was stable.

The FLOX post recess was increased from 0.110 to 0.150 inches (0.280 to 0.380 cm) on test 09. Two steps were programmed. Chamber pressures were 208 and 107 psia (144 and 74 N/cm^2) and the corresponding mixture ratios were 5.0 and 5.2. The engine was stable on both steps. There was considerable instrumentation damage caused by blowback of the hydrogen fire used to heat the No. 2 methane heater. The hardware was in good condition after the 39 second test indicating the safety of the 0.150 inch (0.380 cm) recess.

The heat exchanger injector was installed with a recess depth of 0.240 inches (0.61 cm) in the water cooled thrust chamber for test 10. The test was terminated after 17 seconds because of the appearance of the exhaust flame. Slight erosion of the copper face by several of the elements was evident. The chamber pressure was 97 psia (67 N/cm^2) and the mixture ratio was 6.2. There was no thrust chamber damage and the test was stable. The heat exchanger injector was repaired by machining the injector face to provide a recess of 0.110 inches (0.280 cm).

The recessed post injector was re-installed for tests 11 and 12 with a recess depth of 0.110 inches (0.280 cm). Test 11 was targeted at 500 psia (345 N/cm^2) chamber pressure. The actual pressure was 413 psia (285 N/cm^2) because of a restriction in the facility fuel system which also resulted in a mixture ratio of 7.1. The duration of the test was 10 seconds. Some 3600 cps oscillations occurred in oxidizer injection pressure while low amplitude ($\pm 1-3$ percent) oscillations were observed in chamber pressure. An attempt was made on test 12 to increase the chamber pressure and reduce the mixture ratio. The test duration was 9.5 seconds. The chamber pressure was approximately 440 psia (303 N/cm^2) but the mixture ratio was again high. There were no oscillations in chamber pressure and all hardware was in good condition.

Tests 13 and 14 were conducted with the recessed post injector. The No. 2 methane heater was removed to reduce the facility pressure drop at high chamber pressures. Chamber pressure and mixture ratio on test 13 were 317 psia and 2.80 because of an undersize orifice in the FLOX feed system. The orifice was replaced for test 14. Chamber pressure and mixture ratio on this test were 503 psia and 5.7. Six FLOX posts were burned (a seventh very slightly) during this test. The locations of these posts and the flow pattern traced by the hot methane on the back of the fuel body of the injector indicated non-uniformity

of the fuel flow distribution. Six of the eight fuel inlet ports had been used (two were being used for injector face thermocouples).

The heat exchanger injector was installed in the water-cooled thrust chamber for tests 15 - 18. The injector had been modified by machining the face to reduce the recess to 0.110 inch. Only the No. 1 methane heater was used for these tests. Tests 15 and 16 were high Pc tests (518 and 507 psia) to explore mixture ratio effects (O/F = 4.3 and 5.0). Test 17 was a stepped throttling test at chamber pressures of 91 and 55 psia at a mixture ratio of approximately 5.6. Test 18 was a long duration (97-second) test at 62 psia chamber pressure.

The recessed post injector was repaired and modified for tests 19 - 23. The burned steel posts were replaced with nickel posts having four wires welded near the tip to maintain concentricity. Two holes were drilled to intersect each fuel inlet port to diffuse the fuel flow as it entered the fuel injection manifold. All eight inlet ports were used. One FLOX post was sealed on the upstream side because of a leak between this post and the inter-propellant cavity.

Tests 19 and 20 were conducted at high chamber pressure (522 psia) and demonstrated the effect of mixture ratio (4.7 and 5.3) on performance and thrust chamber heat transfer. The remaining three tests (21 through 23) were made at lower chamber pressures to explore the effects of reducing heat transfer to the FLOX in the injector. The methane temperature was reduced and LN₂ was flowed through the interpropellant cavity. Tests 21 and 22 were stepped throttling tests from approximately 75 to 45 psia chamber pressure at a mixture ratio of 4.7. Methane temperature was approximately 300F on test 21 and ambient on tests 22 and 23. Test 23 was a stepped throttling test from 230 to 135 psia at a mixture ratio of 5.3. The injector and chamber were both in good condition after these tests which completed the program.

TEST RESULTS

The data from the throttling tests were analyzed to determine injector performance (based on chamber pressure and thrust measurements), heat transfer rates, and stability characteristics. The methods of analysis are the same as used for the data from Tasks III, IV and V. The results of these analyses are presented in the following paragraphs.

Performance

Injector performance data based on chamber pressure is summarized in Table 26. The data represent three different FLOX post recess depths, a range of mixture ratios (2.8 to 11), and variations in FLOX and methane injection velocities. Thus, the data presented include the effects of several variables.

The first step toward correlating the hot-fire data was to describe the injection conditions of the FLOX and gaseous methane. During the hot-firing tests, the propellant temperatures were measured in the fuel and oxidizer manifolds. Heat transfer analyses for the recessed post injector indicated significant heat exchange between the hot methane gas (e.g. at 600F) and the cold FLOX (-300F) within the FLOX post, which acts as an effective parallel flow heat exchanger. The approximate equation used to calculate the heat transfer was

$$q/\dot{w}_{\text{FLOX}} \approx N_{\text{ST}} \frac{4L}{D} C_p k (T_{\text{CH}_4} - T_{\text{FLOX}}) \left(\frac{10.5}{\dot{w}_{\text{FLOX}}} \right)^{0.2} \frac{\text{BTU}}{\text{lbm FLOX}}$$

where N_{ST} is the Stanton number in the FLOX tube, L and D are the length and inside diameter of the FLOX tube in the region of high heat transfer rates, C_p is the specific heat of the FLOX, k is the fraction of the total temperature drop which occurs across the FLOX film, and \dot{w}_{FLOX} is the FLOX mass flowrate.

TABLE 26
THROTTLING TEST PERFORMANCE SUMMARY

Test	Chamber Pressure		w_o lb/sec	\dot{w}_f lb/sec	kg/sec	kg/sec	O/F	$C^*_{p, Exper.}$		C^*_{Theo} ft/sec	m/sec	C^*_{p} percent	C^*_{inj} percent
	psia	N/cm ²						ft/sec	m/sec				
37	232.1	160.2	5.47	0.72	2.48	0.327	7.46	6410	1963	6750	2057	95.0	95.3
38a	189.8	133.2	3.79	1.01	1.72	0.458	3.75	6945	2117	6855	2089	101.3	102.3
38b	91.0	62.8	2.27	0.63	1.03	0.286	3.63	5410	1642	6802	2073	79.8	81.3
39a	282.1	194.7	5.87	1.19	2.66	0.540	4.93	6902	2104	7013	2138	98.4	99.0
39b	171.7	118.6	3.53	0.74	1.60	0.336	4.78	6945	2117	6957	2120	99.9	100.7
40a	332.2	229.2	6.96	1.21	3.16	0.548	5.75	7023	2141	7087	2160	99.0	99.2
40b	334.6	230.8	7.13	1.16	3.23	0.526	6.14	6971	2125	6999	2133	99.6	99.8
41a	159.7	110.1	3.31	0.68	1.50	0.308	4.89	6904	2097	6963	2122	99.1	99.7
41b	77.1	53.2	1.98	0.42	0.898	0.190	4.71	5549	1691	6915	2108	80.4	81.5
2	213.7	147.5	4.28	1.01	1.94	0.458	4.24	6955	2053	6875	2096	100.8	101.4
3	202.5	139.8	4.31	0.86	1.96	0.390	5.01	6744	2053	6899	2103	97.7	98.1
4	104.1	71.8	2.34	0.40	1.06	0.181	5.80	6543	1994	6816	2078	96.0	96.8
5	57.1	39.4	1.39	0.28	0.631	0.127	4.95	5891	1796	6806	2074	86.6	88.8
6a	110.1	76.0	2.45	0.49	1.11	0.222	5.01	6451	1966	6889	2100	93.6	94.7
6b	61.1	42.2	1.47	0.32	0.667	0.145	4.57	5871	1789	6817	2078	86.3	87.6
7	279.3	192.8	5.97	1.22	2.71	0.553	4.89	6691	2039	6953	2119	96.2	96.8
8	133.6	92.2	3.07	0.54	1.39	0.245	5.71	6375	1943	6899	2103	92.4	93.1
9a	208.7	144.0	4.46	0.89	2.02	0.404	5.04	6634	2022	7002	2134	94.7	95.3
9b	106.5	73.5	2.64	0.50	1.20	0.227	5.24	5844	1781	6926	2111	84.4	85.1
10a	96.9	66.8	2.26	0.36	1.03	0.162	6.22	6327	1928	6968	2124	90.8	91.2
10b	71.8	49.5	2.04	0.35	0.925	0.159	5.82	5106	1556	6967	2124	73.3	73.7
11a	418.1	288.7	9.38	1.42	4.25	0.644	6.60	6622	2018	6977	2127	94.9	95.2
11b	413.6	285.3	9.39	1.32	4.26	0.598	7.11	6606	2014	6957	2120	96.3	96.6
12a	439.6	303.3	11.48	1.12	5.21	0.508	10.25	5969	1819	6200	1890	96.2	96.5
12b	433.9	299.3	11.48	1.06	5.21	0.481	10.83	5920	1804	6100	1860	97.0	97.3

TABLE 26 (Continued)

THROTTLING TEST PERFORMANCE SUMMARY

Test	Chamber Pressure		\dot{W}_o		\dot{W}_f		O/F	C* _p , exper.		C* _{Theo} ft/sec	m/sec	C* _p percent	C* _{inj p} percent
	psia	N/cm ²	lb/sec	kg/sec	lb/sec	kg/sec		ft/sec	m/sec				
13	321.0	221.4	6.05	2.74	2.16	0.980	2.80	6685	2039	6670	2034	100.2	100.5
14	512.5	353.8	10.89	4.93	1.90	0.861	5.73	6855	2090	7115	2170	96.4	96.7
15	517.6	357.0	10.22	4.63	2.38	1.079	4.29	7027	2142	2013	2139	100.2	100.4
16	507.3	350.0	10.41	4.72	2.08	0.943	5.00	6948	2119	7111	2168	97.7	97.9
17a	90.6	62.5	2.09	0.948	0.371	0.168	5.65	6301	1921	6949	2120	90.7	90.9
17b	55.0	38.0	1.30	0.589	0.231	0.101	5.62	6146	1875	6894	2102	89.1	90.4
18	62.1	42.9	1.29	0.584	0.276	0.125	4.67	6784	2069	6893	2101	98.4	98.9
19	521.9	360.0	10.40	4.71	2.231	1.011	4.66	7066	2154	7089	2162	99.7	100.0
20	521.5	359.7	10.68	4.84	2.021	0.916	5.28	7024	2142	7149	2180	98.3	98.6
21a	77.7	53.6	1.725	0.782	0.385	0.174	4.48	6300	1921	6882	2099	91.5	92.4
21b	46.5	32.1	1.135	0.514	0.237	0.107	4.79	5797	1767	6874	2096	84.3	85.2
22a	72.4	50.0	1.633	0.740	0.354	0.160	4.61	6232	1900	6880	2098	90.6	91.6
22b	45.6	31.5	1.079	0.493	0.223	0.101	4.84	5992	1827	6861	2092	87.3	88.1
23a	229.2	158.2	4.824	2.18	0.920	0.417	5.24	6823	2081	7033	2143	97.0	97.5
23b	134.5	92.8	2.845	1.29	0.532	0.241	5.35	6815	2078	6985	2130	97.6	98.1

Application of this equation indicated that FLOX vaporization did occur during the low chamber pressure throttling tests of the recessed post injector. The amount which was vaporized varied between zero and 30% of the total FLOX flowrate. An independent verification of FLOX gasification within the post was obtained by plotting the measured hot firing FLOX injection pressure drop versus flowrate. This is shown in Fig. 100. For chamber pressures less than about 150 psia (100 N/cm^2), the log ΔP versus log flowrate curve breaks away from the straight line, which is indicative of two-phase flow in the FLOX post. The tests for which this is indicated in Fig. 100 generally coincide with those for which the heat transfer analysis predicted partial FLOX vaporization in the post.

Data from the tests of the recessed post injector in which no FLOX vaporization was indicated were analyzed for correlation with data from cold flow tests of a coaxial injector obtained under Contract NAS3-12001. In Fig. 101 a and b data are presented for a large thrust-per-element ($\sim 2\text{K}$) injector which was cold-flowed to determine mass median droplet size, \bar{D} , and the mixing efficiency, η_{mix} . The vaporization-limited combustion efficiency, η_{vap} , varies inversely with the mean droplet size, \bar{D} . $\eta_{\text{C*}}$ is proportional to η_{vap} and η_{mix} . The data are presented as a function of mixture ratio for an injection velocity difference, $\Delta V_1 = V_g - V_L$, of 700 fps (210 m/sec). V_g is the gas (methane) velocity and V_L is the liquid (FLOX) velocity. Data are shown for two post recess depths.

As indicated by the cold-flow data for a given mixture ratio, \bar{D} decreased and η_{mix} increased as the post was recessed. Thus the cold-flow data predict that performance should increase as the post recess depth is increased.

The hot-firing data for the nonvaporizing FLOX tests are shown in Fig. 101c. As shown, $\eta_{\text{C*}}$ increased as the FLOX post was

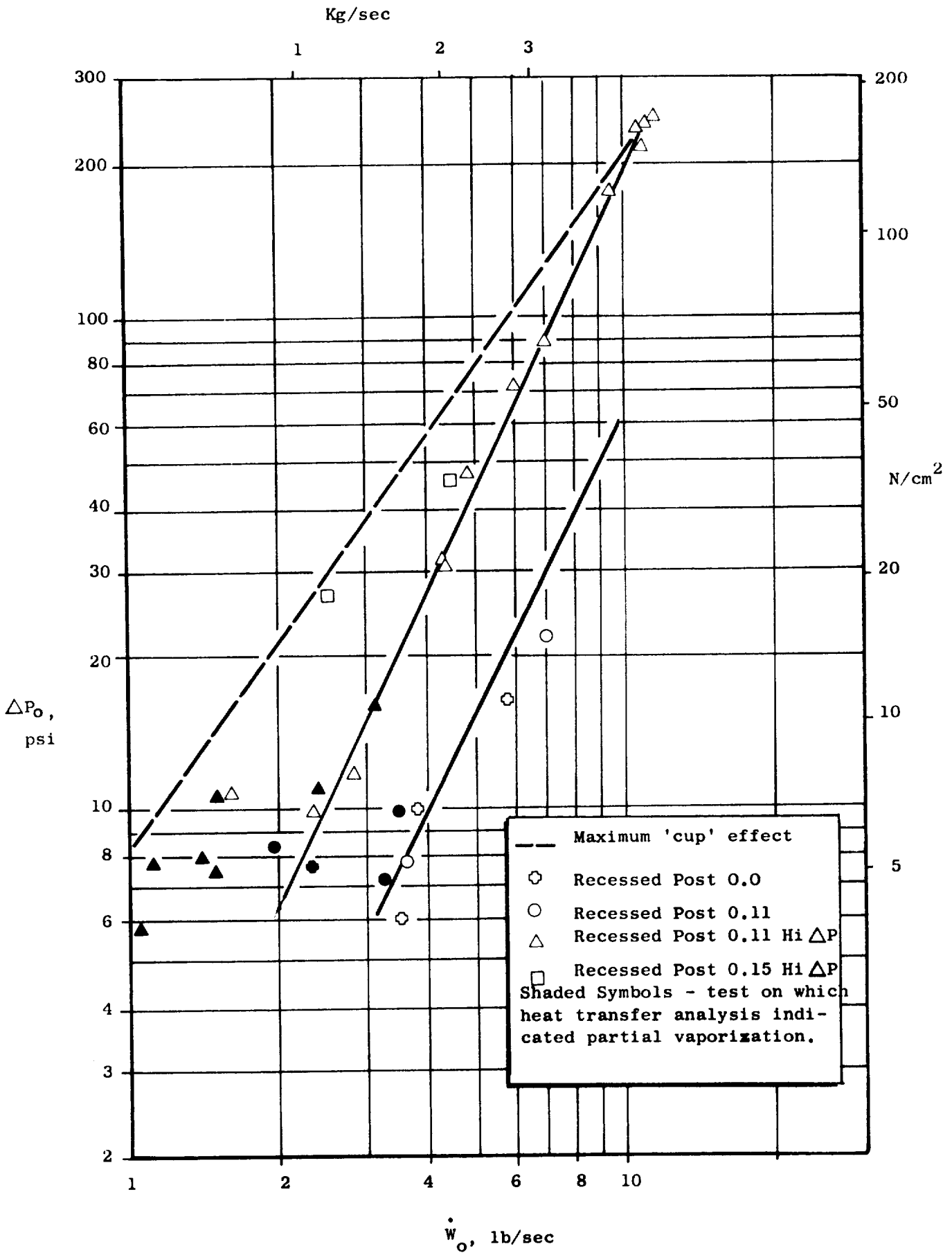
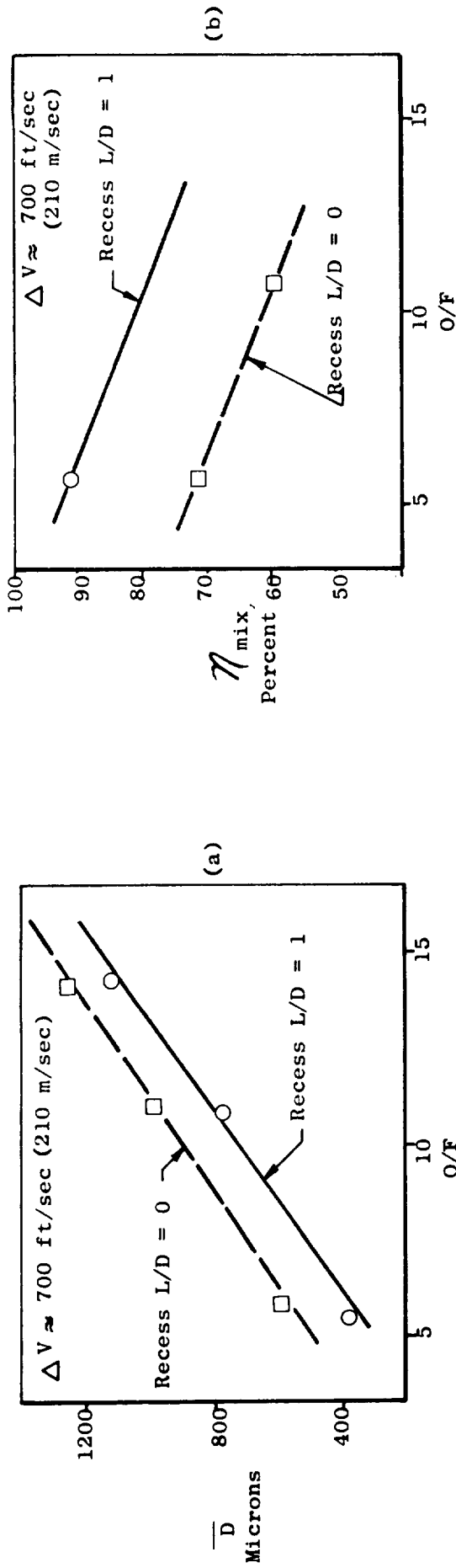


Figure 100. Pressure Drops For FLOX Side of Recess Post Injector.

COLD-FLOW RESULTS



HOT-FIRE RESULTS

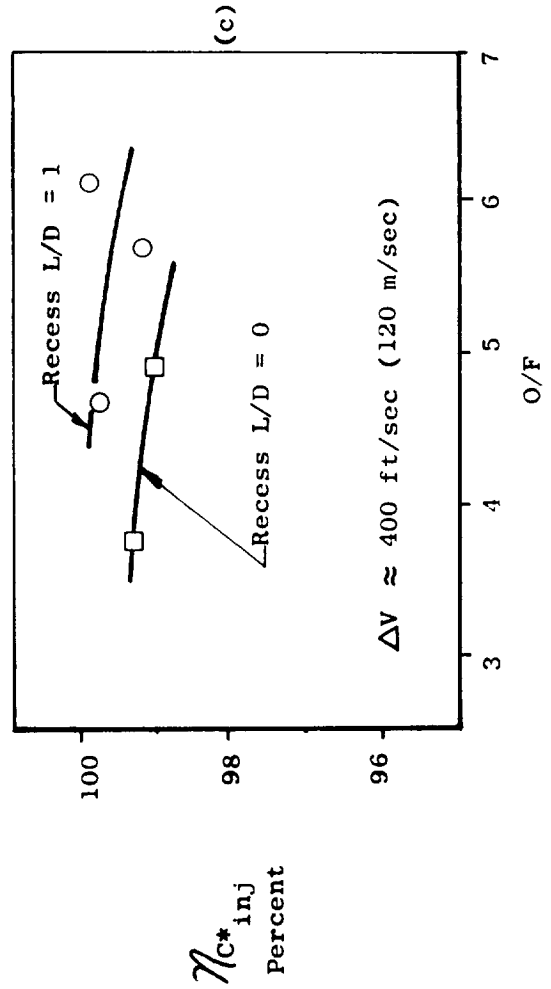


Figure 101. Effects of Recess and Mixture Ratio On Recessed Post Injector Performance

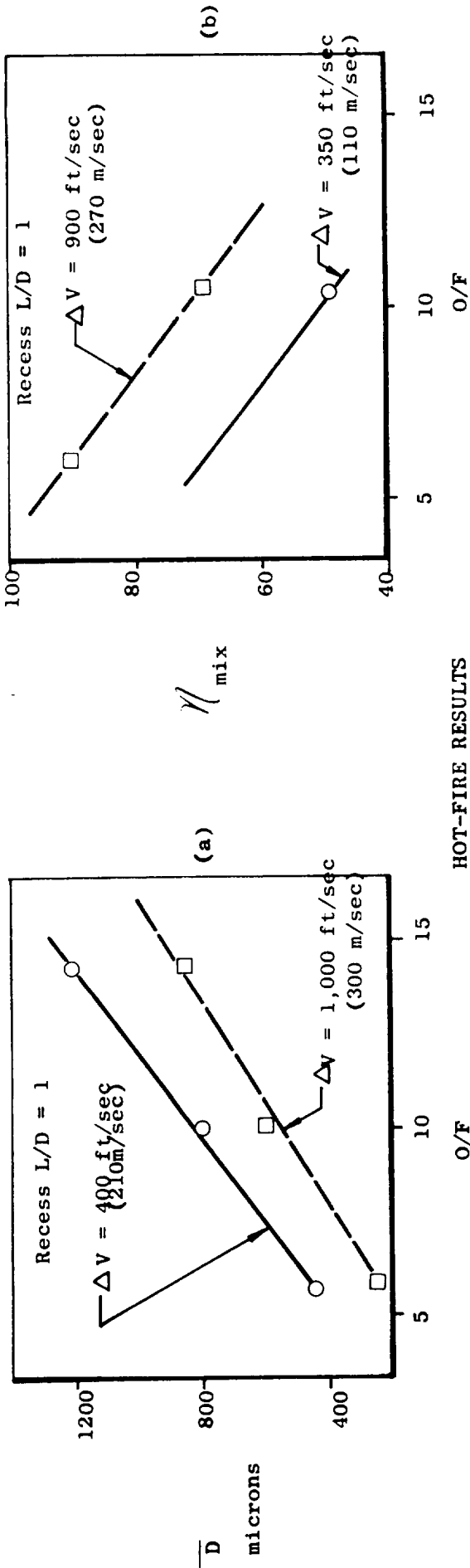
recessed from 0 to approximately 1.0 post diameter which follows the trend predicted by the cold flow data. For each fixed post recess, a similar examination of the trends of cold-flow drop size and cold-flow mixing as a function of mixture ratio likewise predicts a performance trend which agrees well with the hot-firing data. The one test conducted with a recess of 1.4 diameters indicated lower performance. However, there was a fire in the engine area from the methane heater during this test which could have affected instrumentation accuracy.

The effects of ΔV_i on performance are presented in Fig. 102. In Fig. 102 a and b are shown cold-flow \bar{D} and η_{mix} data for a post recess depth of one post diameter. Curves are plotted versus mixture ratio as a function of ΔV_i . The cold-flow data predicts that for a given post recess depth and mixture ratio performance will increase as ΔV_i is increased. Hot-fire data from the present program for a constant FLOX post recess depth and three values of ΔV_i are shown in Fig. 102 c. As predicted by the cold-flow data, performance increased as ΔV_i was increased.

Thus, the hot-fire data are in accord with the cold-flow predictions of NAS3-12001. Absolute levels of performance were not predicted by the cold-flow data since element sizes were considerably different, but the trends with parameter variation are in excellent agreement.

The above data imply that very high performance can be achieved with the recessed post injector at nominal mixture ratio if the propellant injection velocity difference, ΔV_i , is greater than 400 ft/sec (120 m/sec) and the recess L/D is greater than 1. At 500 psia chamber pressure, 5.25 mixture ratio, and fuel injection temperature of 1300R the value of ΔV_i exceeds 450 ft/sec (135 m/sec) so that high performance may be expected. As the chamber is throttled, the fuel injection temperature increases which reduces the density and increases the velocity of the

COLD-FLOW RESULTS



HOT-FIRE RESULTS

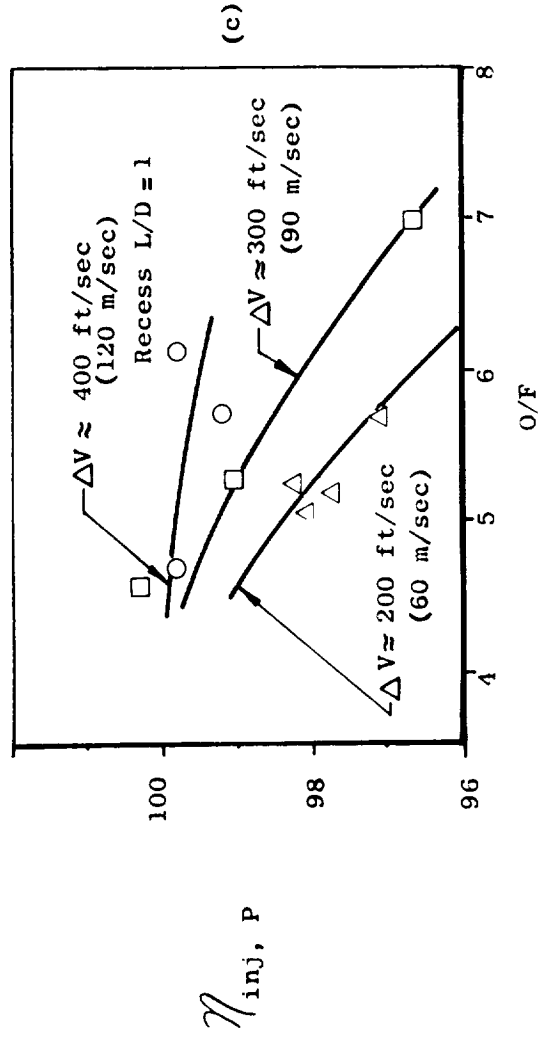


Figure 102. Effects of Injection Velocities and Mixture Ratio on Recessed Post Injector Performance

fuel and ΔV_i . The injector efficiencies of the recessed post injector on stable tests were corrected for mixture ratio and fuel injection temperatures (velocities) and plotted in Fig. 103a.

The mechanical swirlers in the heat exchanger injector elements result in significant divergence of the oxidizer stream as it leaves the posts. As a result, the characteristics of the element are more similar to impinging stream injectors than to true coaxial stream (without swirl) injectors. It was, therefore, anticipated that performance correlations which have been used successfully with impinging stream elements would be more applicable.

The performance data from the heat exchanger injector did not correlate well with the coaxial stream correlating parameter, ΔV_i , but did correlate well with the parameter $V_f \dot{w}_f / \dot{w}_o = M_f / \dot{w}_o$ as shown in Fig. 103b. The product of the fuel velocity, V_f , and flowrate, \dot{w}_f , is the fuel momentum, M_f , which represents an energy available for atomization and penetration (mixing) of the oxidizer stream. At full thrust the FLOX is completely liquid and even at minimum thrust the FLOX is partially liquid. The correlation is shown in Fig. 103b to be quite good although the amount of data is limited. At nominal mixture ratio and fuel temperatures, the values of M_f / \dot{w}_o over the 10:1 throttling range are such that greater than 99 percent injector efficiency are indicated by the correlation for the heat exchanger injector.

Injector performance was calculated on the basis of thrust measurements also for several tests. Only tests at chamber pressures of approximately 250 psia (172 N/cm^2) or higher were applicable because of flow separation in the nozzle at lower pressures. The data for the applicable tests are presented in Table 27. The average difference between injector performance based on chamber pressure and that based on thrust for the tests with the regeneratively cooled thrust chamber, which had a large flange on the exit, was 2.5 percent. The average difference

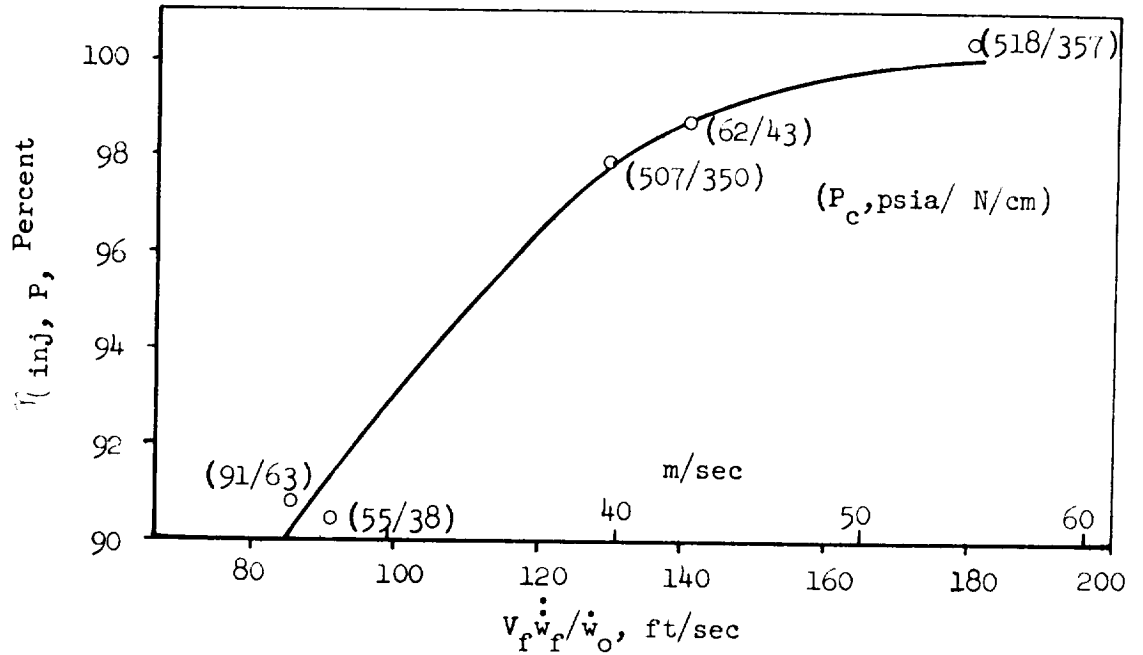


Figure 103b. Performance Correlation for the Heat Exchanger Injector

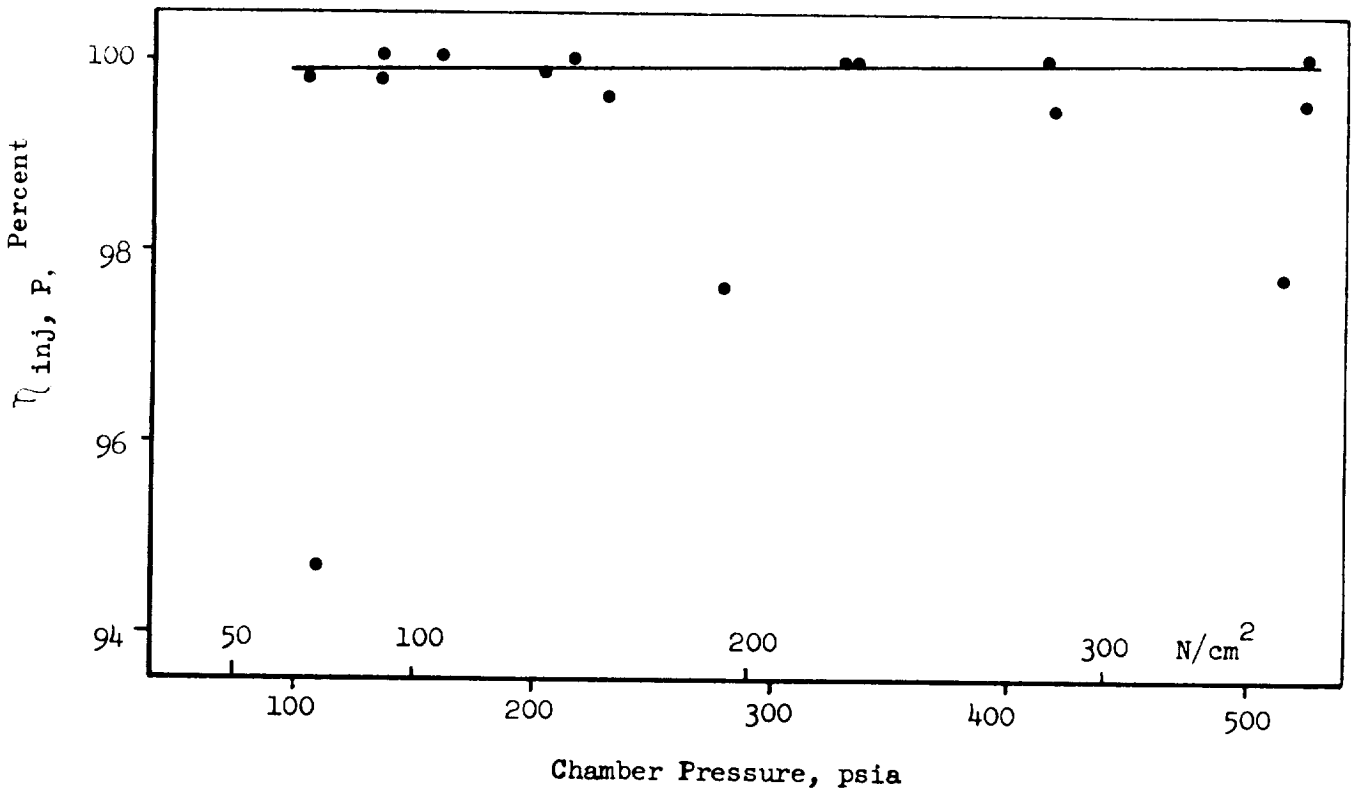


Figure 103a. Performance of Recessed Post Injector Based on Test Data and Correlations

TABLE 27

THRUST-BASED PERFORMANCE: THROTTLING TESTS

Test	F _{site}		F _{vac}		ḡ _T		I _{vac}		T _{IF}	
	lb	N	lb	N	lb/sec	kg/sec	lb _f -sec/lb _m	N-sec/kg	F	K
39	1827	8130	2115	9415	7.08	3.21	298.8	2930	716	654
40	2243	9990	2471	11010	8.20	3.72	301.7	2955	596	587
7	1803	8025	2095	9325	7.16	3.25	292.8	2870	540	556
11	2825	12575	3117	13870	10.71	4.86	291.0	2852	650	617

Test	P _c		O/F	I _{vac,theo}		C _{F,theo} percent	N _{C_F} percent	N _{C_P} percent	C _{P-C_F} percent
	psia	N/cm ²		lb _f -sec/lb _m	N-sec/kg				
39	282.1	194.7	4.93	354.1	3472	88.0	95.8	98.4	2.6
40	332.2	229.2	5.75	355.3	3482	88.1	96.7	99.0	2.3
7	279.3	192.8	4.89	351.7	3446	88.0	94.6	96.2	1.6
11	413.6	285.3	7.11	344.5	3376	88.2	95.7	96.3	0.6

TABLE 27 (Continued)
THRUST-BASED PERFORMANCE: THROTTLING TESTS

Test	F _{site}		F _{vac}		w _T		I _{vac}		T _{IF}	
	lb	N	lb	N	lb/sec	kg/sec	lb _f -sec/lb _m	N-sec/kg	F	K
13	2176	9680	2468	10980	8.25	3.74	299.1	2934	260	402
14	3581	15940	3873	17240	12.89	5.85	300.5	2948	240	390
15	3714	16530	4006	17820	12.60	5.72	318.1	3120	458	511
16	3638	16190	3930	17480	12.49	5.66	314.7	3080	434	498
19	3698	16450	3990	17750	12.63	5.73	316.0	3095	500	534
20	3688	16410	3980	17710	12.70	5.76	313.4	3070	441	500

Test	P _c		O/F	I _{vac} theo		C _F Theo	M _{C_F} *	/C _P *	C _P *-C _F * percent
	psia	N/cm ²		lb _f -sec/lbm	N-sec/kg				
13	321.0	221.4	2.82	328.8	3219	89	102	100.2	-1.7
14	512.5	353.8	5.73	354.0	3468	88.3	96.2	96.4	0.2
15	517.6	357.0	4.29	350.9	3435	88.5	102.5	100.2	-2.3
16	507.3	350.0	5.00	356.8	3495	88.4	99.8	97.7	-2.1
19	521.9	360.0	4.66	351.5	3442	88.5	100.9	99.7	-1.2
20	521.5	359.7	5.28	358.2	3509	88.5	98.8	98.3	-0.5

for tests using the water-cooled chamber, which has no flange, was 0.5 percent. The greater difference on tests with the regeneratively cooled chamber may be due to aspiration of the base flange.

Heat Transfer

Measurements were made during the regeneratively cooled tests to determine the total heat input to the thrust chamber and to indicate the circumferential variation in heat flux near the injector.

Methane temperature was measured at two places in the coolant jacket inlet manifold and averaged. Methane temperature was also measured in the coolant jacket outlet tubes (four tubes for tests 33-37; six tubes on tests 38-41) and averaged. The enthalpy rise of the methane, calculated from these averaged temperatures, and the coolant flowrate were used to compute the heat input to the combustion chamber from the injector end to $\epsilon = 4$. All instrumentation functioned and close to steady state conditions were achieved on tests 39a, 39b and 40. The data from these tests are summarized in Table 28. The heat inputs agree well with data taken with the same injector in the water-cooled thrust chamber as will be shown presently.

Outer wall temperatures at cutoff are plotted in Fig.104 for each of the circumferential thermocouple locations. The hot wall temperature was not more than 150F (83R) hotter than the outer wall under the low heat flux conditions encountered on these tests.

TABLE 28
 THROTTLING REGENERATIVE COOLING DATA
 (Injector to $\epsilon = 4$)

TEST	T _{in}		P _{in}		H _{in}		T _{out}		P _{out}		H _{out}		ΔP _j	
	F	K	psia	N/cm ²	Btu/lb	J/g	F	K	psia	N/cm ²	Btu/lb	J/g	psi	N/cm ²
39a	130	328	1045	720	415	965	1020	823	367	252	1130	2630	678	468
39b	142	335	685	473	440	1025	1090	862	239	165	1200	2790	446	308
40b	162	346	1080	746	440	1025	1090	862	424	293	1200	2790	656	453

TEST	ΔH = Q/Ṁ _f		Ṁ _f		Q	
	Btu/lb	J/g	lb/sec	kg/sec	Btu/sec	kw
39a	715	1660	1.19	0.540	851	899
39b	760	1770	0.74	0.336	562	594
40b	760	1770	1.16	0.526	830	877

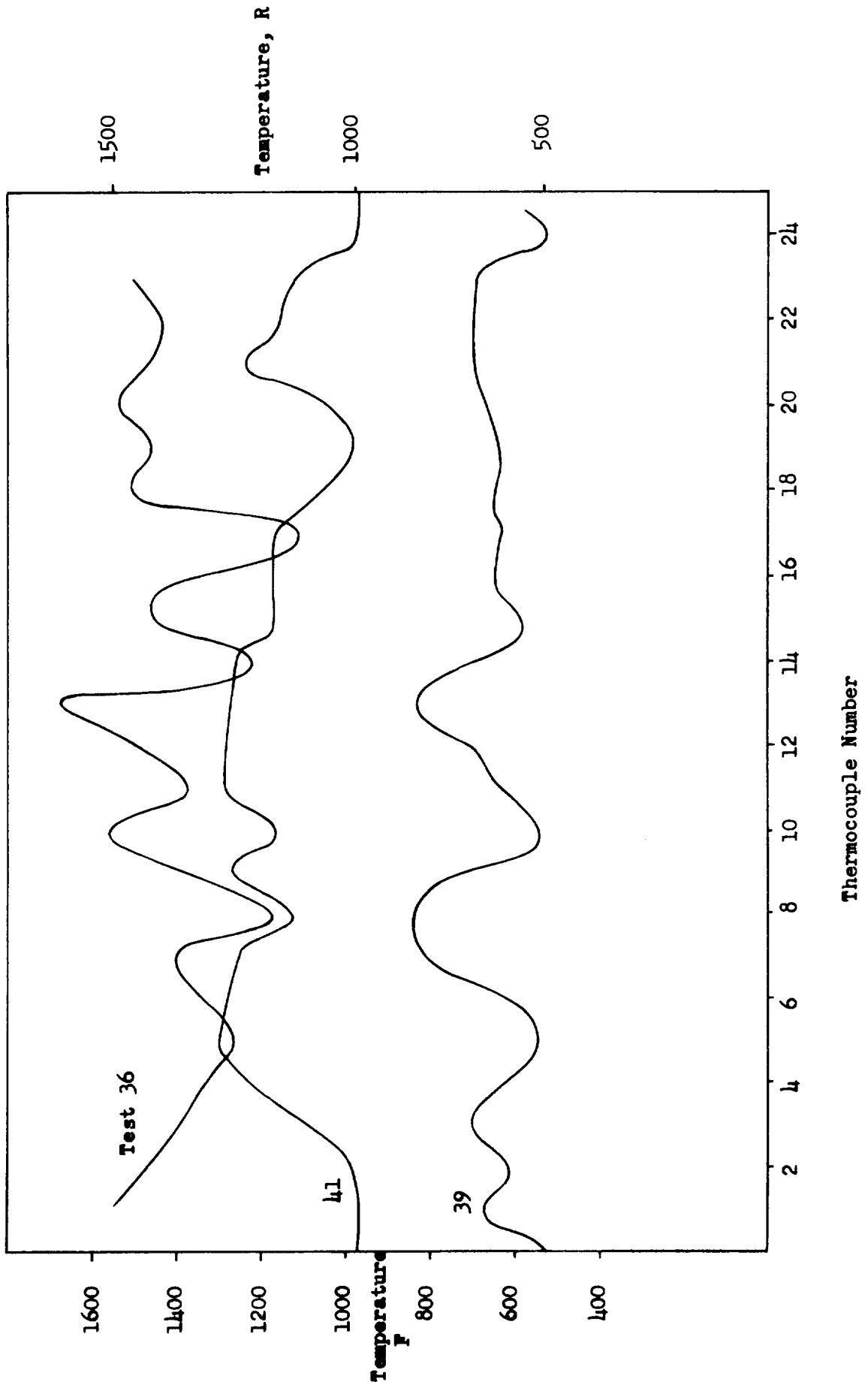


Figure 104. Circumferential Variation of Outer Wall Temperature

A two-dimensional transient conduction analysis was conducted on the section of the chamber where the outside wall thermocouples were located. The purpose of this analysis was to estimate the local heat flux and hot-gas-wall temperature from the outside-wall temperature and coolant flowrate measurements. The analysis was accomplished by varying the combustion-gas convective film coefficient until the analytical outside-wall temperature response matched the experimental data. The resulting hot-gas wall temperature transient was also determined.

The analysis indicated a maximum combustion-side wall temperature of 1750F was achieved during test 36 for which the chamber pressure and mixture ratio were 123 psia (85 N/cm^2) and 15.2 respectively. The combustion gas film coefficient and steady-state heat flux were determined to be $0.0004 \text{ Btu/in}^2\text{-sec-F}$ (0.12 W/cm K) and $1.2 \text{ Btu/in}^2\text{-sec}$ (180 W/cm^2) respectively. The film coefficient and flux at nominal mixture ratio, 5.25, and 125 psia (85 N/cm^2) chamber pressure were analytically calculated to be $0.00006 \text{ Btu/in}^2\text{-sec-F}$ ($0.018 \text{ W/cm}^2\text{K}$) and $0.4 \text{ Btu/in}^2\text{-sec}$ (60 W/cm^2) respectively. The higher heat flux at the high mixture ratio encountered on test 36 resulted primarily from the high combustion-side film coefficient. The thrust chamber was in good condition after the test thus demonstrating that electroformed nickel can be used at high wall temperatures in an oxidizer-rich environment.

A similar analysis was conducted for test 37 during which erosion of the thrust chamber very near the injector face occurred. Compared to test 36 the mixture ratio, 7.5, was lower (although much higher than the 5.25 nominal value) and the chamber pressure, 232 psia (160 N/cm^2), was higher. The analysis indicated that a maximum combustion-side wall temperature of between 1700 - 1800F (1200-1250K) was achieved during test 37 at the axial location of the thermocouple measurements, approximately 1.5 inches

(3.8 cm) downstream from the injector face. The combustion gas film coefficient was determined to be about $0.0004 \text{ Btu/in}^2\text{-sec-F}$ ($0.12 \text{ W/cm}^2\text{K}$). This value results in a heat flux of about $2.4 \text{ Btu/in}^2\text{-sec}$ (310 W/cm^2) at nominal wall temperature of 1500F (1080K).

The experimental wall heat transfer rates were apparently much higher near the injector face plane as evidenced by erosion of the chamber wall in this region. A two-dimensional transient conduction analysis, similar to that discussed previously, was utilized to determine the heat transfer rate necessary to cause melting of the nickel surface. In this case the combustion gas convective film coefficient was increased until the nickel melting temperature ($\sim 2650\text{F}$) was reached. The resulting film coefficient was determined to be approximately $0.002 \text{ Btu/in}^2\text{-sec-F}$ ($0.6 \text{ W/cm}^2\text{K}$). This corresponds to a heat flux level of about $12 \text{ Btu/in}^2\text{-sec}$ (1800 W/cm^2) (for $T_{wg} = 1500\text{F}$).

A streak pattern could be seen in the residual carbon in the chamber after all except the high mixture ratio tests. This pattern agreed qualitatively with the temperature distributions shown in Fig. 104. Element-to-element variations in mixture ratio had been determined by cold flow tests as described in Section III. The correlation between the mixture ratio distribution and outer wall temperature was not very strong--implying that other factors, such as mixture ratio variations within each element and channel-to-channel coolant flow variations, were exerting significant influences.

Heat flux profile data were obtained over a wide range of chamber pressures and mixture ratios with the water-cooled chamber. The water temperature rise data exhibited a peculiar characteristic. In portions of the cylindrical part of the chamber the temperature rise, Δt , rose to a maximum and then decayed to a steady-state value. The most extreme case observed is shown in Fig. 105, which is a test record of voltage of the thermopile across water coolant passage number 6. The transient over-temperature was generally much less than shown in Fig. 105. The magnitude of

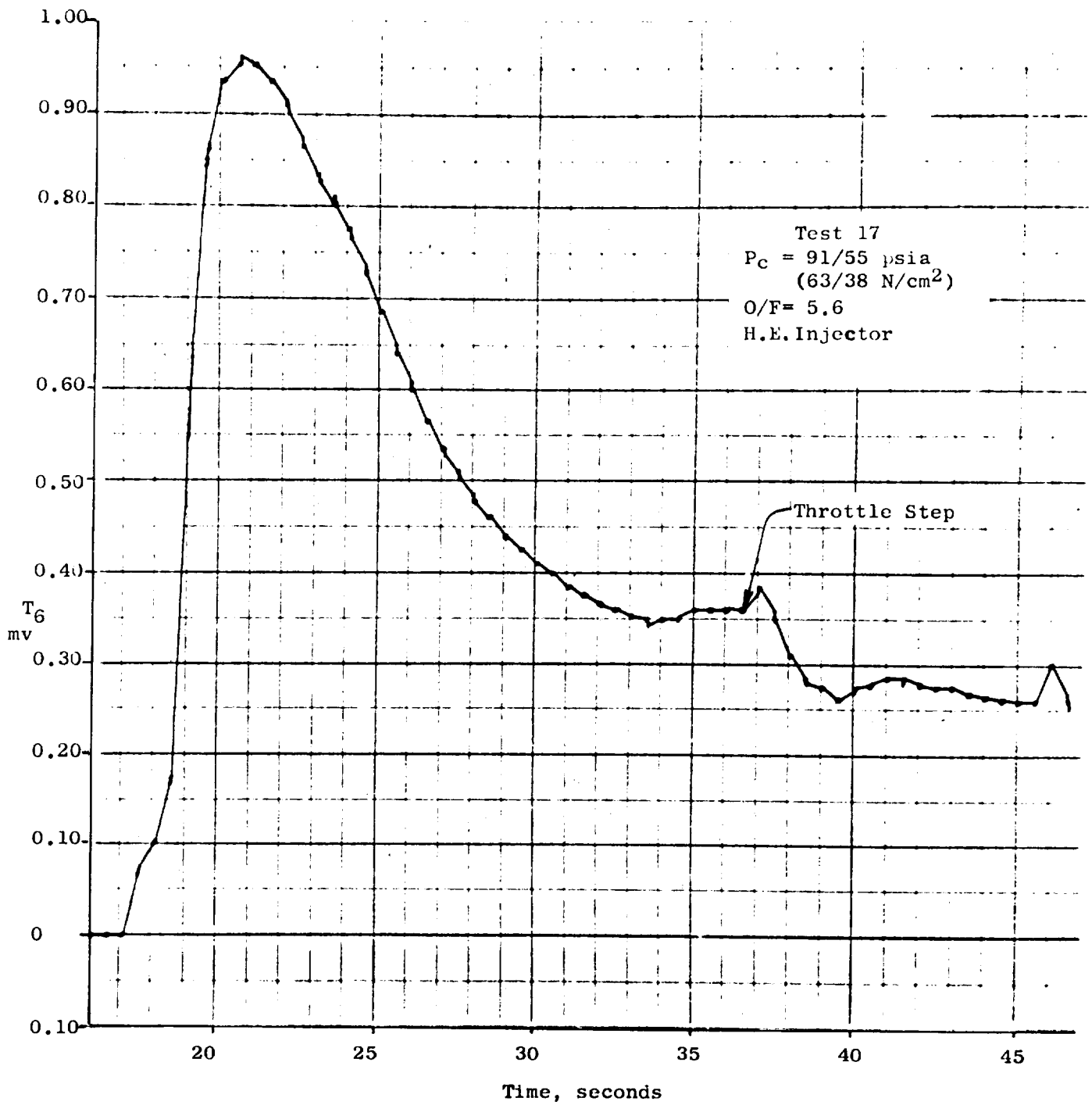


Figure 105. Water Temperature Rise Transient

the effect depended on the location, the injector, and the chamber pressure. The effect was most severe in the forward portion of the chamber for the recessed post injector and near the start-of-convergence for the heat exchanger injector (Fig. 106). The transient was most noticeable with the heat exchanger injector and tended to diminish in magnitude and duration with both injectors at higher chamber pressures. The effect was not observed in the throat region and is most probably due to the formation of an insulating carbon layer. Such a layer would tend to be more effective under conditions of low mass velocity, i.e., in the large cross-sectional area of the chamber at low chamber pressures.

A comparison of the heat flux profiles at approximately 500 psia (350 N/cm^2) chamber pressure is shown in Fig. 107. The concentric and recessed post injectors have similar profiles, while the profile for the heat exchanger injector is much lower except near the injector face. The same qualitative relationship existed between the heat flux profiles at lower pressures for the recessed post and heat exchanger injectors.

The peak (throat) heat flux is shown in Fig. 108 as a function of chamber pressure with propellant mixture ratios indicated by the data points. The heat exchanger injector resulted in a peak heat flux of approximately 50 percent of that of the recessed post injector. The slope of both curves is approximately 0.67, compared to a theoretical value of 0.8. Data taken at high pressures with the concentric (hydraulic swirler) injector indicated definite and strong trends with mixture ratio. The two throttling injectors did not exhibit strong variation of peak heat flux with mixture ratio.

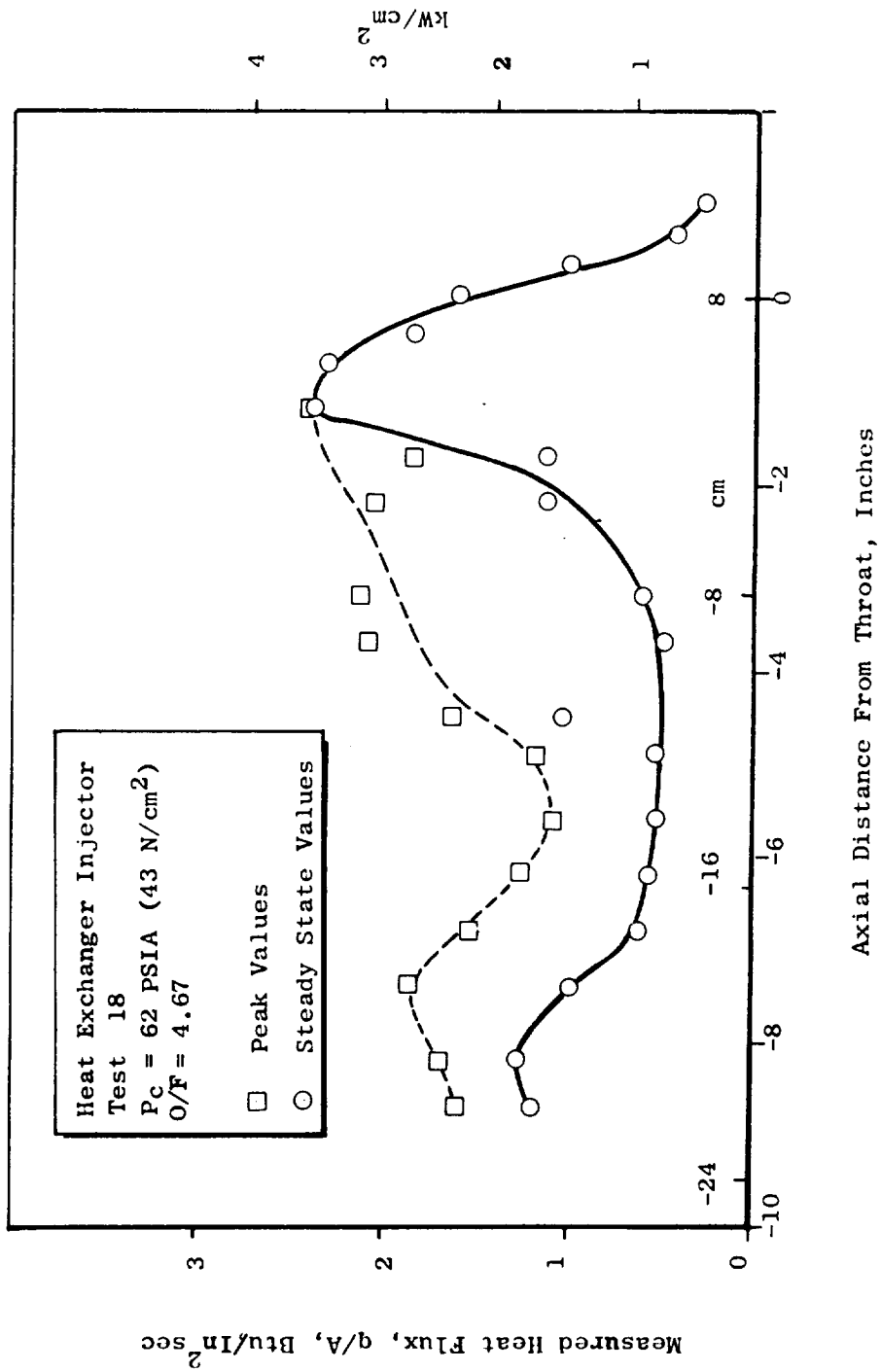


Figure 106. Heat Flux Distribution - Carbon Layer Influence

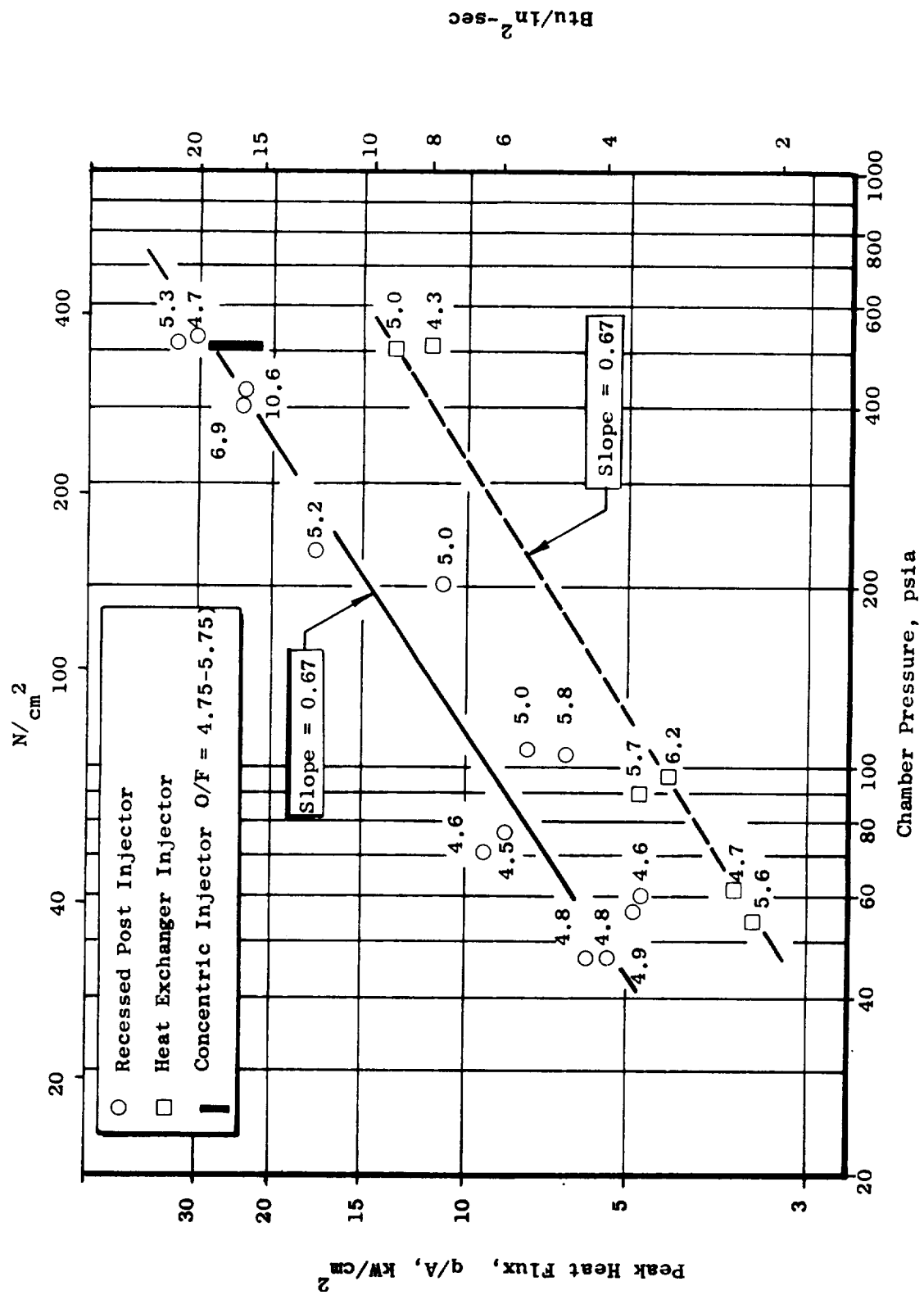


Figure 108. Peak Heat Flux Variation with Chamber Pressure

The integrated heat load in the combustion chamber is plotted in Fig. 109. The data taken with the recessed post injector in the water cooled and regeneratively cooled thrust chambers are in good agreement. The data taken with the heat exchanger injector in the regeneratively cooled chamber were taken before coolant orifices were added to the periphery of the injector. Comparison of the water and regeneratively cooled chamber data implies that a substantial reduction in heat flux resulted from the addition of these orifices. Heat fluxes based on the maximum water coolant temperature rise are shown and indicate that the transient effect is significantly less pronounced at the higher chamber pressures. The copper water-cooled chamber is much more responsive than the nickel regeneratively cooled chamber. Overshoots did not occur in either the methane bulk temperatures or the back wall temperatures in the regeneratively cooled chamber tests.

The slope of the curves in Fig. 109 is approximately 0.5, while the theoretical value of the slope is 0.8. The implication of the low value of the slope of the data is that the temperature of the methane at the exit of the coolant jacket under throttled conditions will be warmer than previously estimated. This is evident from the following equation.

$$\Delta T = T_o - T_i = Q/\dot{w}_f \bar{C}_p \approx k P_c^x / P_c = k P_c^{x-1}$$

where T_o and T_i are the coolant outlet and inlet temperatures, \dot{w}_f is the coolant flowrate, \bar{C}_p is the average specific heat of the coolant between T_i and T_o , and x is the slope of the log-log plot of Q vs P_c . $\Delta T \propto k P_c^{-0.2}$ for the theoretical slope of 0.8 while $\Delta T \propto k P_c^{-0.5}$ for the empirical slope of 0.5.

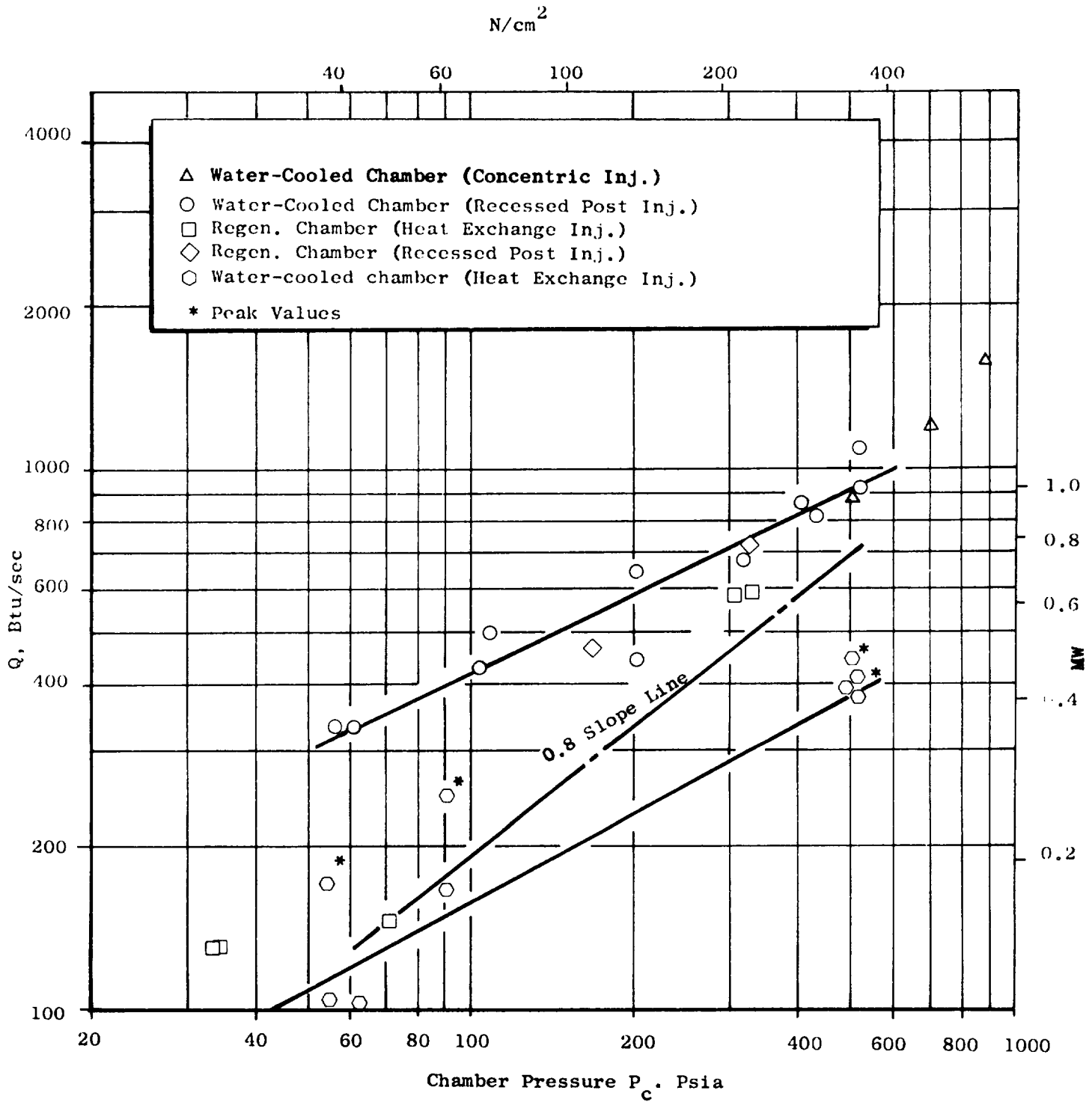


Figure 109. Total Heat Input To Combustion Chamber

Injector face temperature measurements were taken on the recessed post injector. Little difference was indicated between the data from the two thermocouples used (one very close to an element, the other as far as possible from adjacent elements). The difference between the temperature of the injector face and the methane was less than 150 F (85K) when high temperature methane was used. The difference became smaller as chamber pressure increased, which implies that the coolant flowrate increases with chamber pressure more rapidly than the injector face heat flux. The temperature difference became greater, as would be expected, when lower temperature methane was used, (Fig. 110).

The heat flux profile data were used to design a regeneratively cooled chamber for throttling (the existing regeneratively cooled chamber was designed for high thrust operation only). In order to reduce the overall heat input at throttled conditions and to avoid the abrupt rise in heat flux measured at the start-of-contraction, the existing contour was modified as shown in Fig. 111. Previous tests with the hydraulic swirler concentric element injector indicate that shortening the length by the amount shown will not appreciably affect performance. The contraction area ratio and the upstream and downstream radii of curvature at the throat were not changed.

The combustion-side heat transfer coefficients for the combustion zone and throat regions of the modified contour were developed for each injector as follows. The data from the recessed post injector tests agreed well with a heat transfer coefficient, h_g , profile analytically predicted by starting the boundary layer at a point in the converging section having the same diameter as the outer row of injector elements (this has been observed with other injectors also). A few data points in the converging region were higher than predicted, probably because of the abruptness of the turn.

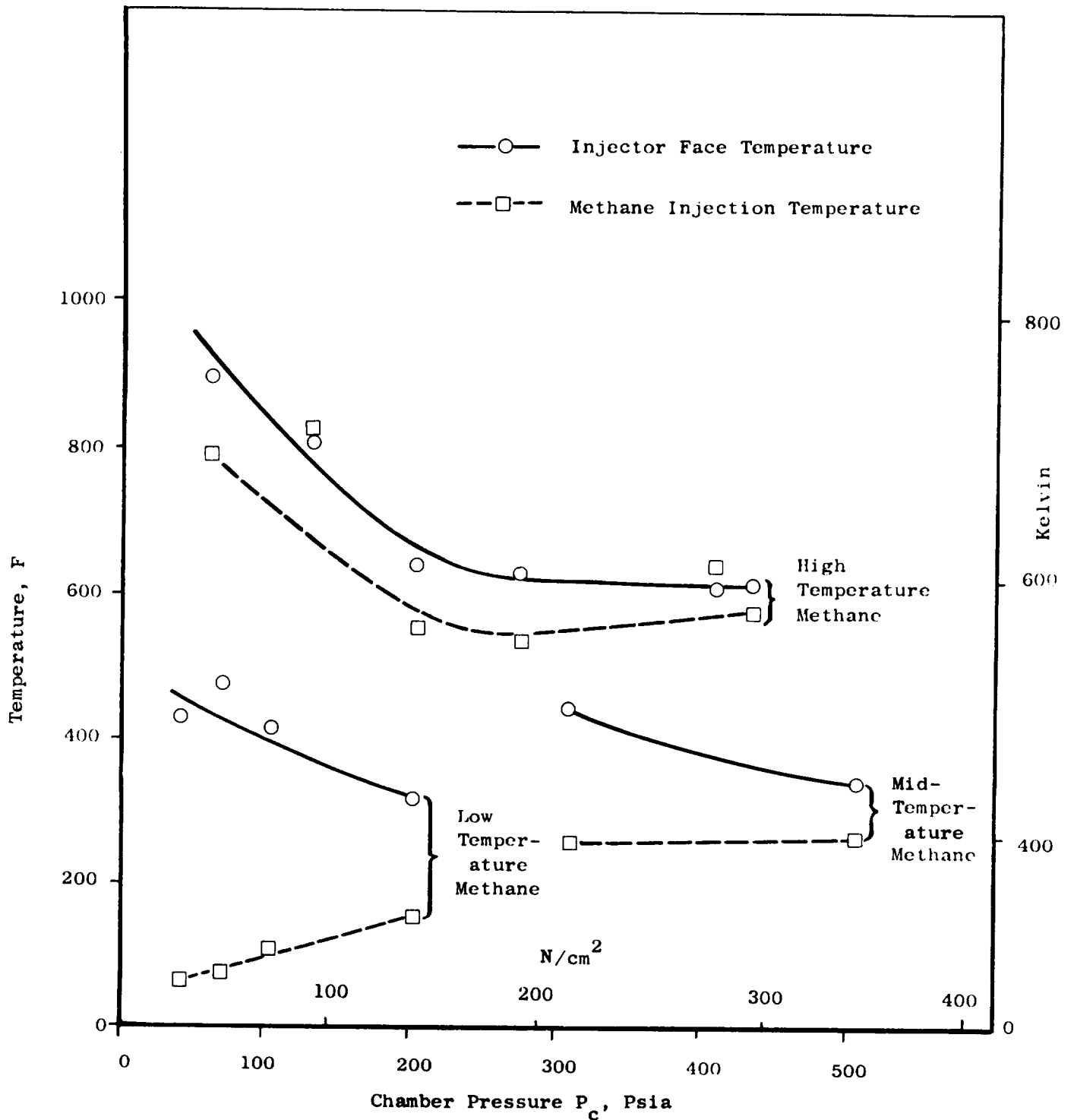


Figure 110. Recessed Post Injector Face Temperatures

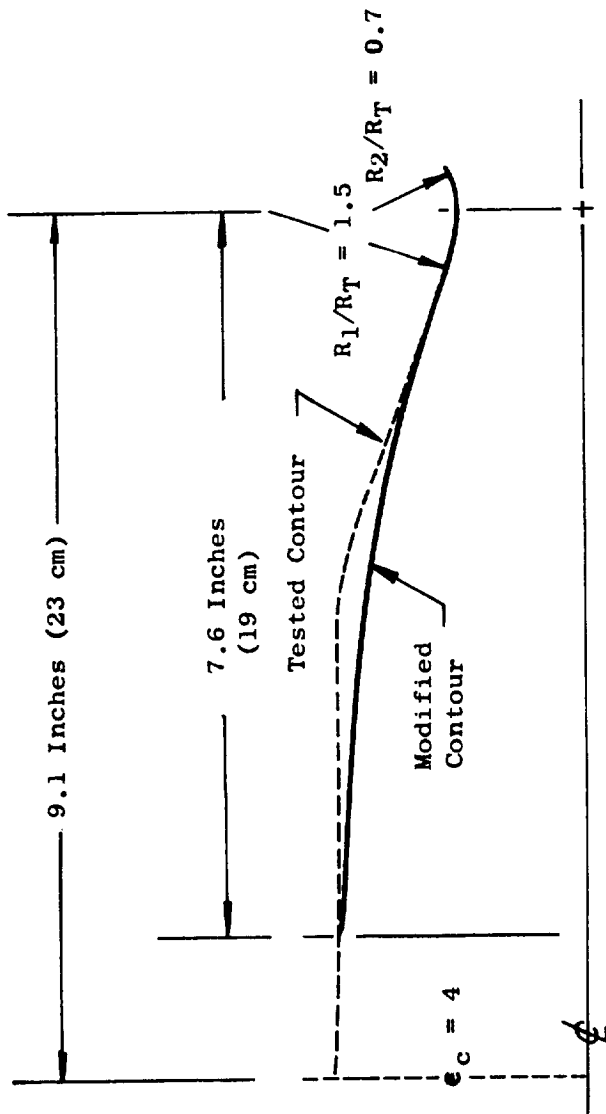


Figure 111 Combustion Chamber Contours

Therefore, the h_g profile was analytically predicted for the modified contour based on a boundary layer being initiated at this same diameter and having a thickness as indicated by experimental data. The h_g profile between the injector and the point where the boundary layer was initiated was not analytically predictable and depends on both the local contraction area ratio and the distance from the injector. Curves of measured h_g vs area ratio and distance were drawn and averaged to obtain the predicted h_g profile near the recessed post injector. This empirical method was used to predict the h_g profile from the injector to the throat for the heat exchanger injector because the measured values of h_g were generally lower than even the most optimistic analytical prediction.

No throttled tests were made with the high area ratio nozzle. The correlations between experimental and analytical h_g profiles in the nozzle were good at high pressures as shown in Section III. The h_g profiles in the nozzle were, therefore, predicted analytically for the 10:1 throttling range.

The nozzle was an 84 percent length bell with an area ratio of 82. The complete h_g profiles are shown in Fig. 112. A 1-1/2-pass coolant circuit was selected, with the coolant entering at $\epsilon = 25$, to provide a lighter weight nozzle, inlet manifold, and inlet duct than a single-pass configuration. A limit of 250 psia (173 N/cm^2) was set for the coolant jacket pressure drop at full thrust level. The pressure drops in the entrance, return, and exit manifolds amounted to a total of 25 psi (9 N/cm^2). Nickel channel wall construction was used. Combustion-side wall thicknesses were 0.024 inch (0.057 cm) in the combustion zone and 0.037 inch (0.094 cm) in the nozzle. Channel dimensions are shown in Fig. 113. The design features a relatively small number (80) of large cross-section channels with a single-step change in width at $\epsilon = 8$ to reduce fabrication costs and hydraulic pressure drop.

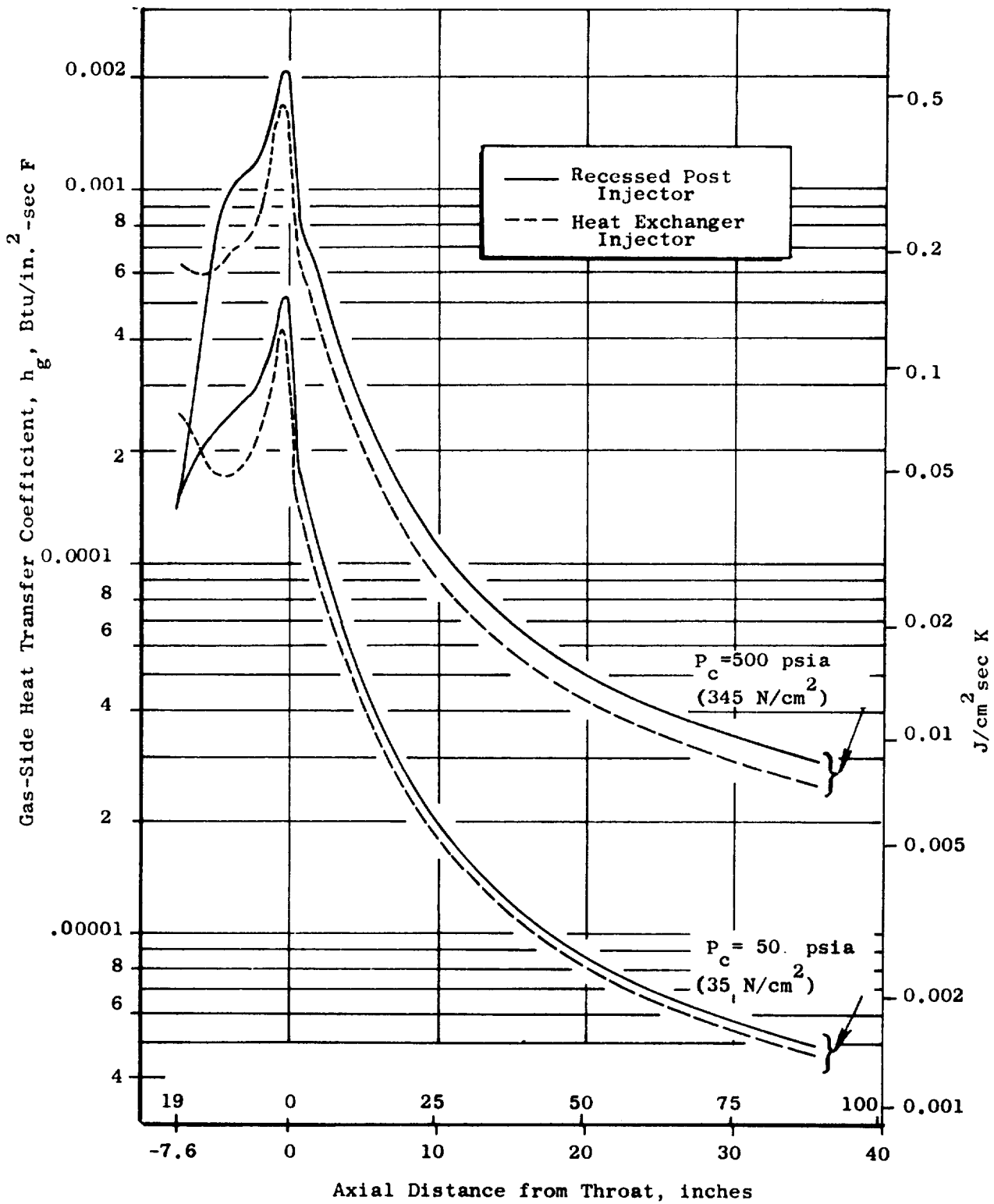


Figure 112. Combustion-Side Heat Transfer Coefficient Distribution

The maximum wall temperatures at full thrust were predicted to be 1350 F and 1200 F for the recessed post and heat exchanger injectors respectively. The static pressure in the coolant jacket was greater than the static pressure in the thrust chamber at all points. The coolant bulk temperatures were 1300 R and 1100 R for the recessed post and heat exchanger injectors respectively at full thrust.

During throttling, phase change initiates in the downpass circuit at $\epsilon = 44-72$ and is completed in the uppass circuit at $\epsilon = 40-60$. In this region the methane velocity is sufficiently high to assure that forced convection prevails over nucleate and film boiling, and the heat flux is less than $0.5 \text{ Btu/in}^2 \text{ sec}$ (70 Watts/cm^2). The combustion-side wall temperatures (including two-dimensional heat transfer effects) at the throat and injector regions are shown in Fig. 114 over the throttling range for both injectors. Throat temperatures increase only slightly as the engine is throttled, but temperatures in the injector region rise more rapidly because of the high bulk temperature of the methane (1200 and 1700 F for the heat exchanger and recessed post injectors respectively at 50 psia (35 N/cm^2 chamber pressure) near the injector. A nickel chamber can probably operate for a limited number of cycles at the 1900 F (1300K) temperature predicted for the 50 psia (35 N/cm^2) chamber pressure. If many cycles of operation are required, a temperature of 1700 F (1200K) should not be exceeded. To achieve this with the present injector configurations would require that the mixture ratio be reduced to approximately 4.5.

The high wall temperatures result from the generally high heat flux/coolant ratio with the recessed post injector and from the locally (injector end) high heat flux/coolant ratio with the heat exchanger injector. The variation of wall

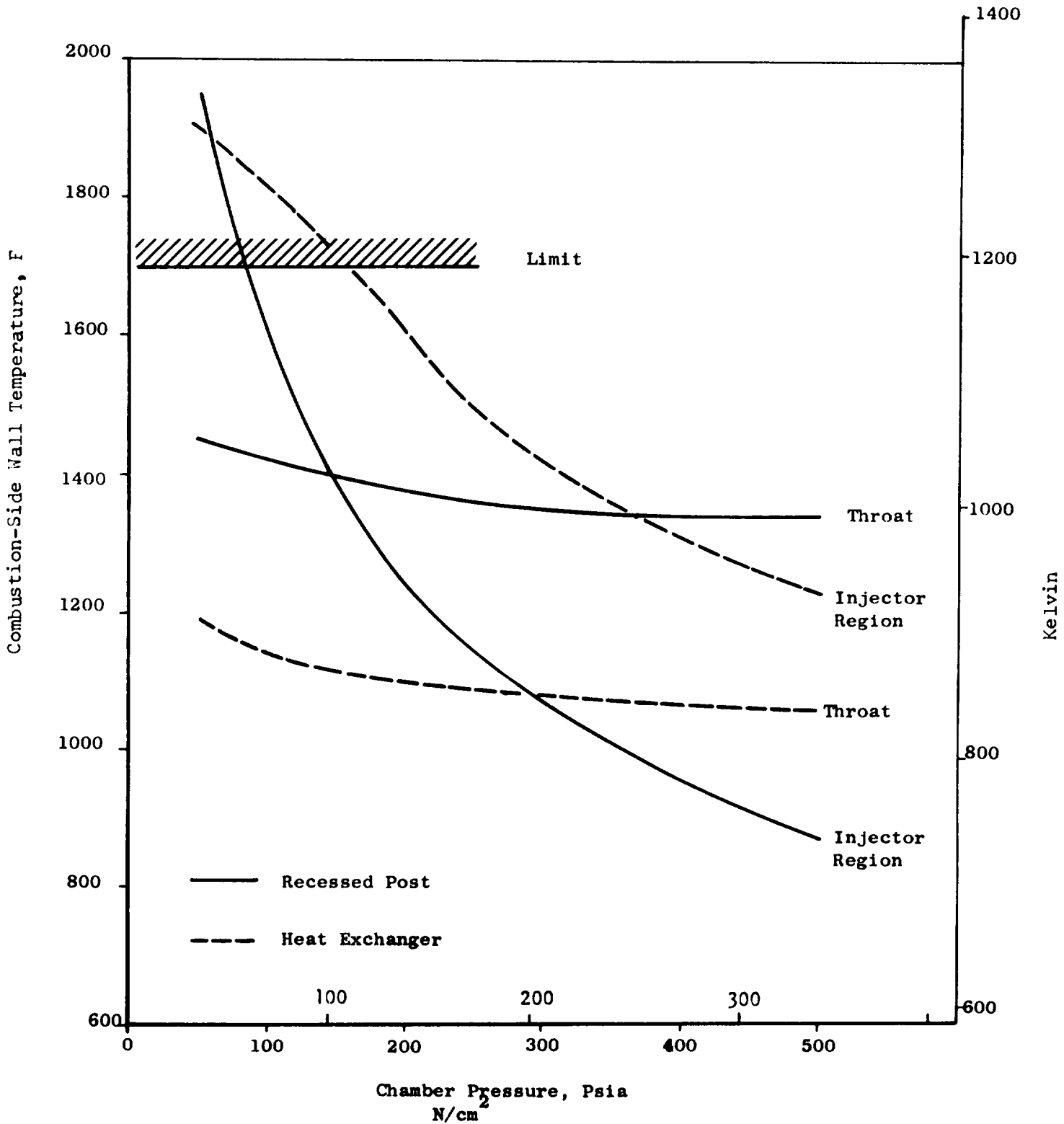


Figure 114. Combustion-side Wall Temperature Variation with Chamber Pressure

temperature with heat flux near the injector is shown in Fig. 115. The heat exchanger injector, therefore, appears to be more amenable to effecting wall temperature control by modification of the peripheral mixture ratio or flow characteristics.

Injector Pressure Drops and Stability

Pressure drop data for the recessed post injector are summarized in Table 29. The pressure drops on the FLOX side were presented in Fig. 100 and were discussed with respect to inferences concerning vaporization in the post. The data for recesses of 0.0 and 0.11 inches (0.28 cm) have too much scatter to indicate the effect of recess on pressure drop except to denote that the maximum cup effect was not being achieved. A significant increase in pressure drop was observed for the test with the FLOX post recessed to 0.15 inches (0.38 cm) although the validity of the data is questionable.

The pressure drop on the fuel side is plotted in Fig. 116 in terms of the $\rho \cdot \Delta P$ product to include pressure and temperature effects. The fuel density, ρ , was calculated based on chamber pressure and injector inlet temperature. Lines which best fit the data for each recess position are shown. An increase of approximately 15 percent occurred in pressure drop when the recess was increased from 0 to 0.11 inches (0.28 cm). The pressure drop increased slightly when the recess was further increased to 0.15 inches (0.38 cm). Additional data with deeper recesses and other element configurations are required to more fully exploit the potential of the recessed post injector.

Pressure drop data for the fuel side of the heat exchanger injector is also shown in Fig. 116. The pressure drop is higher than necessary because of the step in the fuel holes which resulted from the conversion of an existing fuel body.

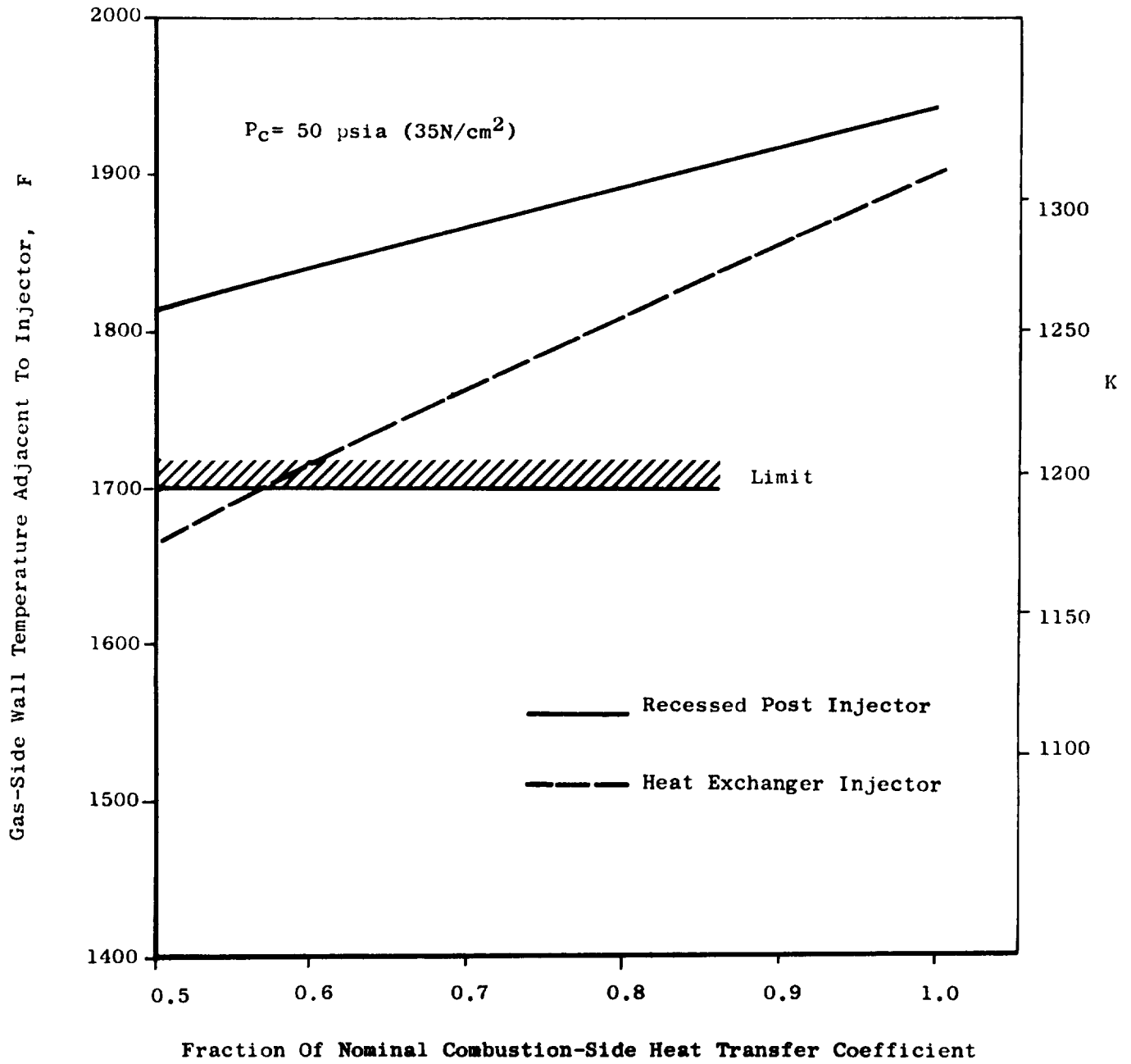


Figure 115 Influence Of Reduced Injector Region Heat Transfer Coefficient.

TABLE 29
THROTTLING INJECTOR PRESSURE DROP SUMMARY

TEST	\dot{W}_o		ΔP_o		\dot{W}_f		ρ_f		ΔP_f		$\rho \Delta P$	
	lb/sec	kg/sec	psi	N/cm ²	lb/sec	kg/sec	lb/ft ³ x 10 ⁶	kg/m ³ x 10 ⁵	psi	N/cm ²	lb ² /in ⁵ x 10 ⁵	N/cm ⁵ x 10 ²
34					0.96	0.435	198	317	161	111	319	610
35	3.86	1.75	36	25	0.28	0.127	88	141	42	29	37	71
36	3.91	1.77	40	28	0.26	0.118	69	111	61	42	42	80
37	5.47	2.48	78	54	0.72	0.327	147	235	130	90	191	365
38a	3.79	1.72	10	6.9	1.01	0.458	188	301	33	23	62	118
38b	2.27	1.03	7.6	5.2	0.63	0.286	74	118	39	27	29	55
39a	5.87	2.66	16	11	1.19	0.540	215	344	44	30	96	183
39b	3.53	1.60	6.0	4.1	0.74	0.336	107	171	39	27	41	78
40a	6.96	3.16	38	26	1.21	0.548	325	520	39	27	127	242
40b	7.13	3.23	22	15	1.16	0.526	212	339	49	34	103	197
41a	3.31	1.50	7.2	5.0	0.68	0.308	127	203	27	19	34	65
41b	1.98	0.898	8.6	5.9	0.42	0.190	46	74	35	24	15	29
2	4.28	1.94	32	22	1.01	0.458	350	560	31	21	107	204
3	4.31	1.96	31	20	0.86	0.390	299	478	25	17	75	143
4	2.34	1.06	9.9	6.8	0.40	0.181	163	261	17	12	28	54
5	1.39	0.631	11	7.6	0.28	0.127	34	54	20	14	6.8	13
6a	2.45	1.11	8	5.5	0.49	0.222	74	118	24	16	18	34
6b	1.47	0.667	7.6	5.2	0.32	0.145	43	69	19	13	8.0	15
7	5.97	2.71	72	70	1.22	0.553	245	392	45	31	111	212
8	3.07	1.39	17	12	0.54	0.245	81	130	24	16	19	36

TABLE 29 (Continued)
 THROTTLING INJECTOR PRESSURE DROP SUMMARY

TEST	\dot{W}_o		ΔP_o		\dot{W}_f		ρ_f		ΔP_f		$\rho \Delta P$	
	lb/sec	kg/sec	psi	N/cm ²	lb/sec	kg/sec	lb/ft ³ x 10 ⁶	kg/m ³ x 10 ⁵	psi	N/cm ²	lb ² /in ⁵ x 10 ⁴	N/cm ⁵ x 10 ²
9a	4.46	2.02	46	32	0.89	0.404	171	274	41	28	69	132
9b	2.64	1.20	27	19	0.50	0.227	98	157	25	17	25	48
10	2.04	0.925	34	23	0.35	0.159	68	109	52	36	35	67
11	9.39	4.26	177	122	1.32	0.598	333	533	44	30	147	281
12	11.48	5.21	248	171	1.06	0.481	350	560	29	20	102	195
13	6.05	2.74	89	62	2.16	0.980	397	1100	98	68	389	745
14	10.89	4.93	218	150	1.90	0.861	650	1800	47	32	306	585
15	10.22	4.63	140	97	2.38	1.079	480	1330				
16	10.41	4.72	138	95	2.08	0.943	485	1350				
17a	2.09	0.948	12	8.3	0.371	0.168	99	275	55	38	54	103
17b	1.30	0.589	9.1	6.3	0.231	0.101	57	158	35	24	20	38
18	1.29	0.584	13	9.0	0.276	0.125	59	164	47	32	28	54
19	10.40	4.71	233	160	2.23	1.011	482	1340	81	56	390	745
20	10.68	4.84	237	163	2.02	0.916	514	1430	61	42	315	600
21a	1.73	0.782	11	7.6	0.385	0.174	94	261	15	10	15	29
21b	1.14	0.514	7.8	5.4	0.237	0.107	56	155	14	9.7	7.7	1.5
22a	1.63	0.740	11	7.6	0.354	0.160	12	33	11	7.6	13	25
22b	1.08	0.493	5.7	3.9	0.223	0.101	7.8	22	9.3	6.4	7.3	1.4
23a	4.82	2.18	48	33	0.920	0.417	40	111	19	13	75	143
23b	2.85	1.29	18	12	0.532	0.241	24	67	15	10	36	69

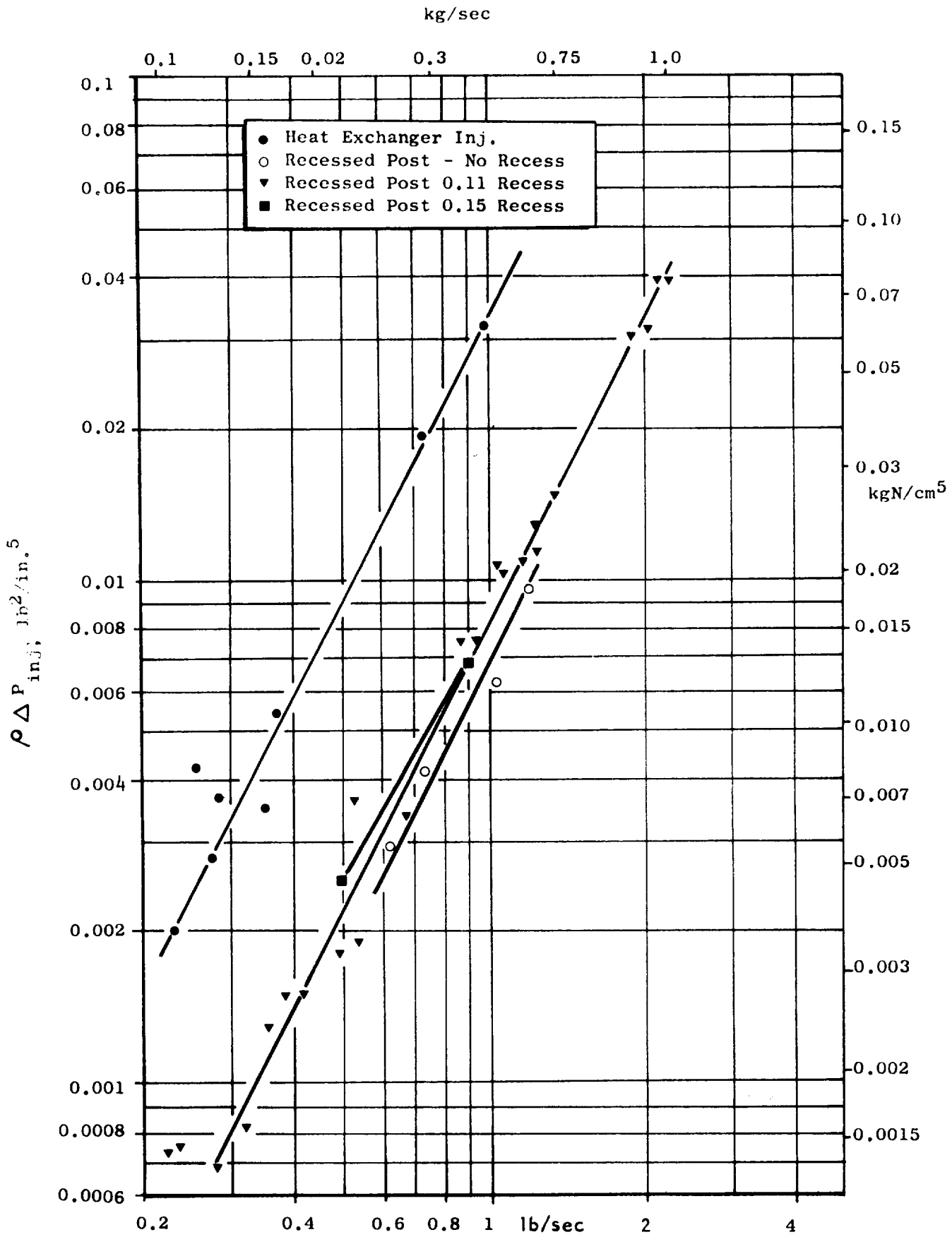


Figure 116. Fuel Side Pressure Drops For Throttling Injectors.

Pressure drops on the oxidizer side of the heat exchanger injector are shown in Fig.117 to depend on the temperature of the methane, T_f , which affects the amount of FLOX vaporized. The IR&D tests were conducted with an injector configuration which promoted heat transfer in addition to having a slightly higher fuel temperature.

The pressure drop data for the regenerative coolant jacket and for the crossover tubes (6) from the jacket to the injector are summarized in Table 30 and plotted in Fig.118 as the $\rho \cdot \Delta P$ product. The crossover tube pressure drops correlate very well which serves to increase confidence in the accuracy of the fuel flowrate and coolant jacket discharge pressure and temperature data. The density could be evaluated based on conditions at the inlet of the tubes because the pressure and temperature drops across the tubes were quite small.

The product of $\rho \cdot \Delta P$ for the coolant jacket correlates well with fuel flowrate at higher chamber pressures but tends to be high at the lower pressures. The reason for this, as well as for the lower than 2:1 slope of the data, is probably the error introduced by the simple arithmetic averaging technique used to obtain ρ .

In addition to the effect on performance previously discussed, partial vaporization of the FLOX in the recessed post injector FLOX tubes also resulted in low frequency chugging in some instances. These incidences occurred mostly during the first part of the throttling test series before a facility modification was made to eliminate a warm FLOX slug which formed in the feed system. The conditions under which chugging occurred were described in the TEST SUMMARY for this section of the report. The amplitude of the chamber pressure oscillations was normalized with respect to chamber pressure, $\Delta P_c/P_c$, and plotted against the enthalpy of

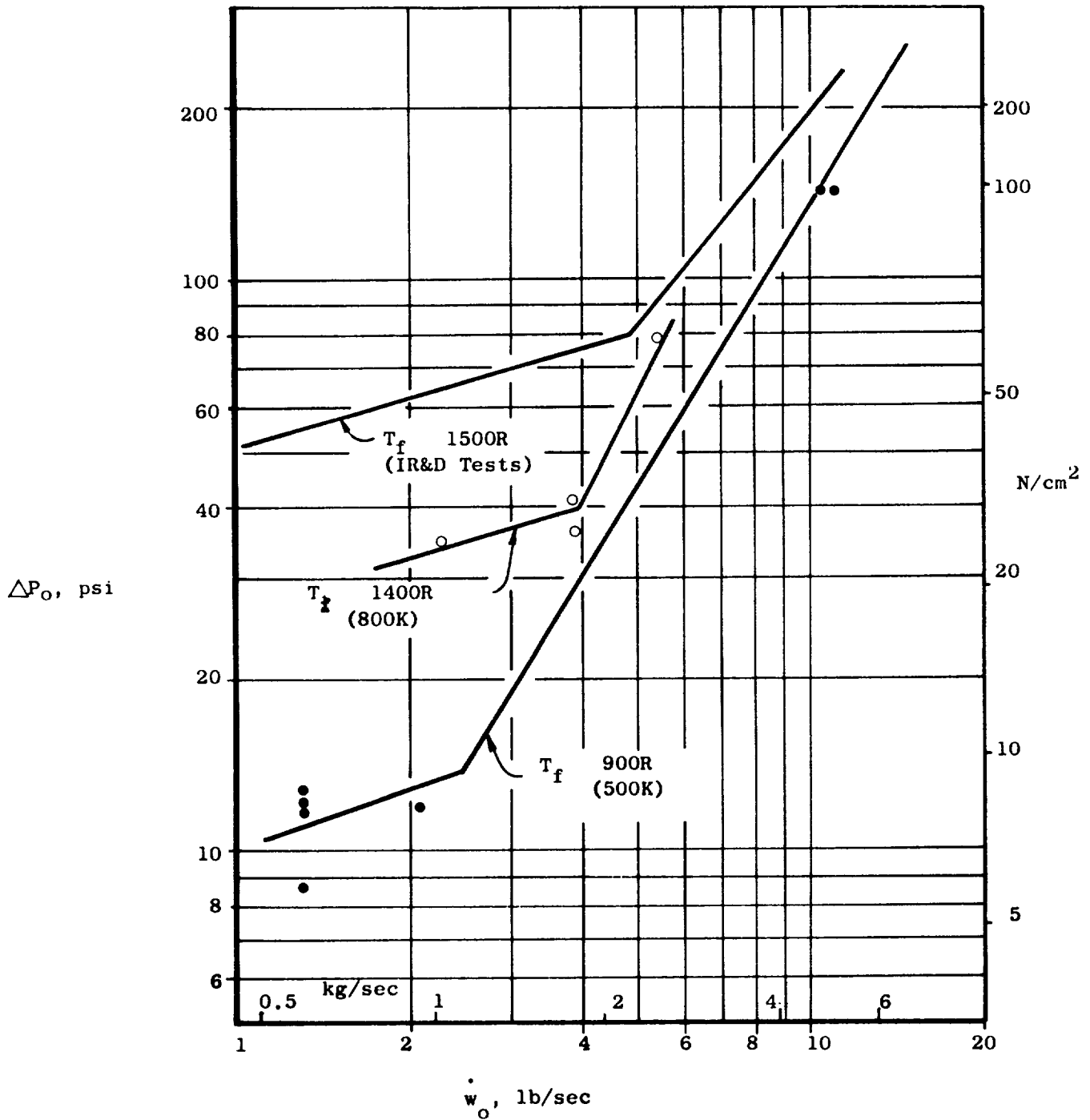


Figure 117. Oxidizer-Side Pressure Drop For Heat Exchanger Injector

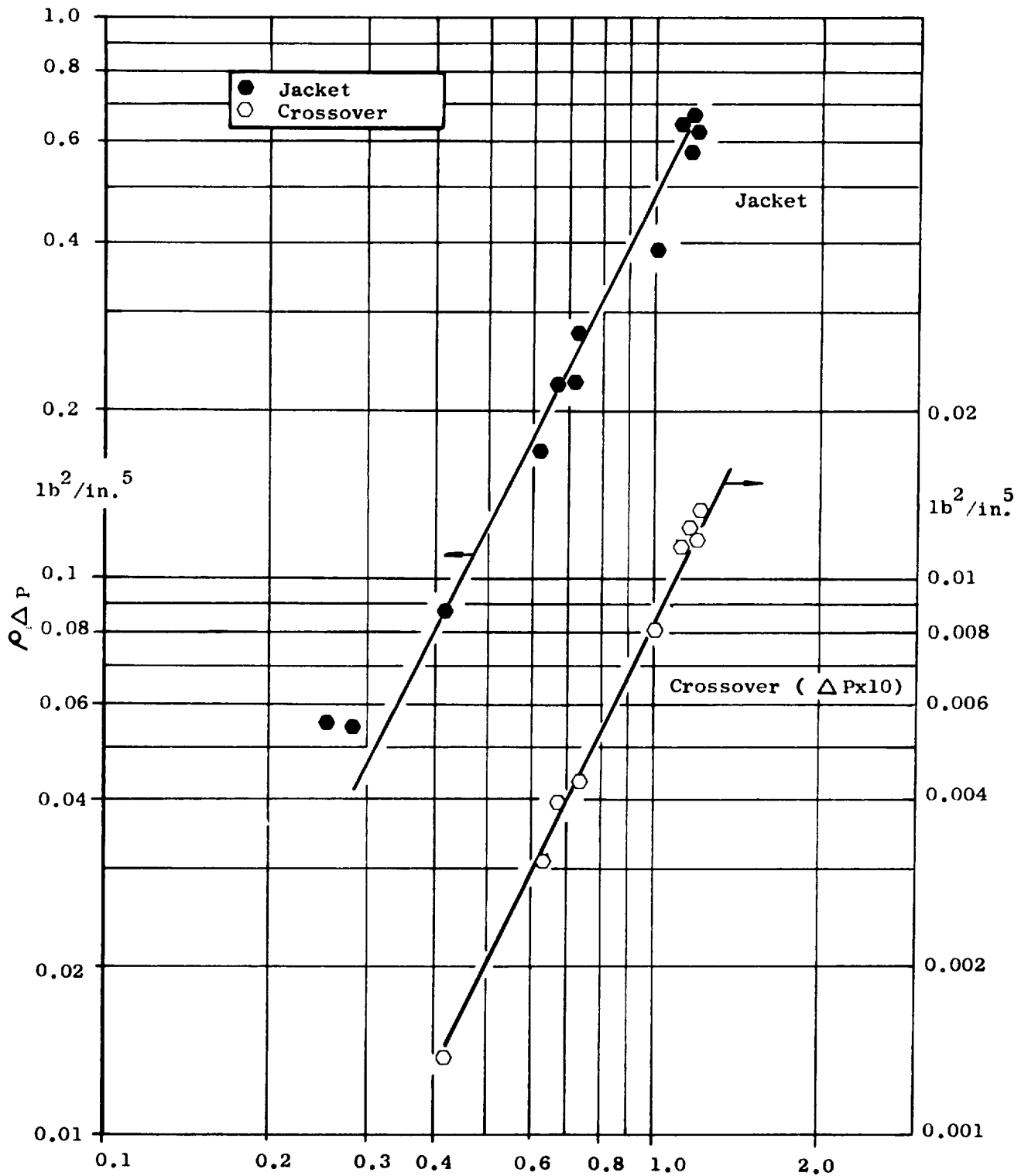


Figure 118. Fuel Jacket and Crossover Duct Pressure Drop Correlations

TABLE 30 REGENERATIVE COOLANT PRESSURE DROPS

Test	\dot{w}_f		TOJ		ΔP_{Cr} psi	$\rho \Delta P_{Cr}$ $lb^2/in^5 \times 10^4$	$\rho \Delta P_{Cr}$ $gN/cm^5 \times 10^2$	TIJ		ΔP_J psi	ΔP_J N/cm ²	$\rho \Delta P_J$ $lb^2/in^5 \times 10^4$	$\rho \Delta P_J$ $gN/cm^5 \times 10^3$
	lb/sec	kg/sec	F	K				F	K				
34	0.96	0.435	680	634	-	-	-	310	428	450	311	540	1032
35	0.284	0.129	800	701	39	49	94	85	303	143	99	550	1051
36	0.257	0.117	1100	867	43	46	88	86	304	144	100	2220	4244
37	0.724	0.328	900	756	86	198	379	162	346	288	199	3900	5541
38a	1.01	0.457	440	500	37	81	155	131	329	523	361	390	554
38b	0.625	0.283	625	603	29	31	59	151	340	364	251	170	32
39a	1.19	0.540	715	653	50	122	233	127	326	667	460	667	128
39b	0.738	0.335	955	787	33	43	82	142	335	446	308	272	52
40a	1.21	0.548	430	495	36	132	252	114	319	606	418	627	120
40b	1.16	0.526	925	770	48	117	223	159	344	659	455	642	123
41a	0.676	0.307	670	628	27	39	75	100	311	377	260	221	424
41b	0.420	0.190	1005	815	20	13.3	25	143	335	257	177	86	16

NOTES: TIJ, TOJ - Coolant Jacket Inlet and Outlet temperatures
 ΔP_J , ΔP_{Cr} - Coolant Jacket and Crossover Line Pressure Drops
 $\rho \Delta P$ - Product of fuel Density and Pressure Drop

subcooling in the FLOX dome, H_{SUB} in Fig. 119. The enthalpy of subcooling signifies the amount of heat that can be added to the FLOX (based on conditions in the FLOX manifold) before it will begin to vaporize. Heat is transferred to the FLOX from the methane primarily in the annular area between the FLOX posts and fuel body because of the high velocity of the methane in this region. Heating rates in the FLOX posts are in the order of 10 Btu per pound of FLOX. Thus, it is apparent that the presence of warm FLOX during deep throttled operation will result in some vaporization in the FLOX posts. A higher injection pressure drop would tend to suppress vaporization and stabilize operation if some vaporization occurs. The correlation between the subcooling enthalpy and the amplitude of the oscillations was reasonably good (Fig. 119) except for the two points at the lowest chamber pressure. The combination of chugging and low pressure drop (< 10 psi) may have resulted in measurement errors on these points. There is a tendency of the data to indicate that recessing contributed to stability because the oscillations were less severe, for a given subcooling, with the recessed configuration.

CONCLUSIONS

The results of the throttling tests led to the following conclusions:

1. High performance is obtainable with both injector types over the complete throttling range.
2. The heat exchanger injector is stable over the 10:1 throttling range. The recessed post injector is stable down to approximately 100 psia (70 N/cm^2) chamber pressure. Additional cup ΔP and/or interpropellant insulation would be required to extend the throttling range.

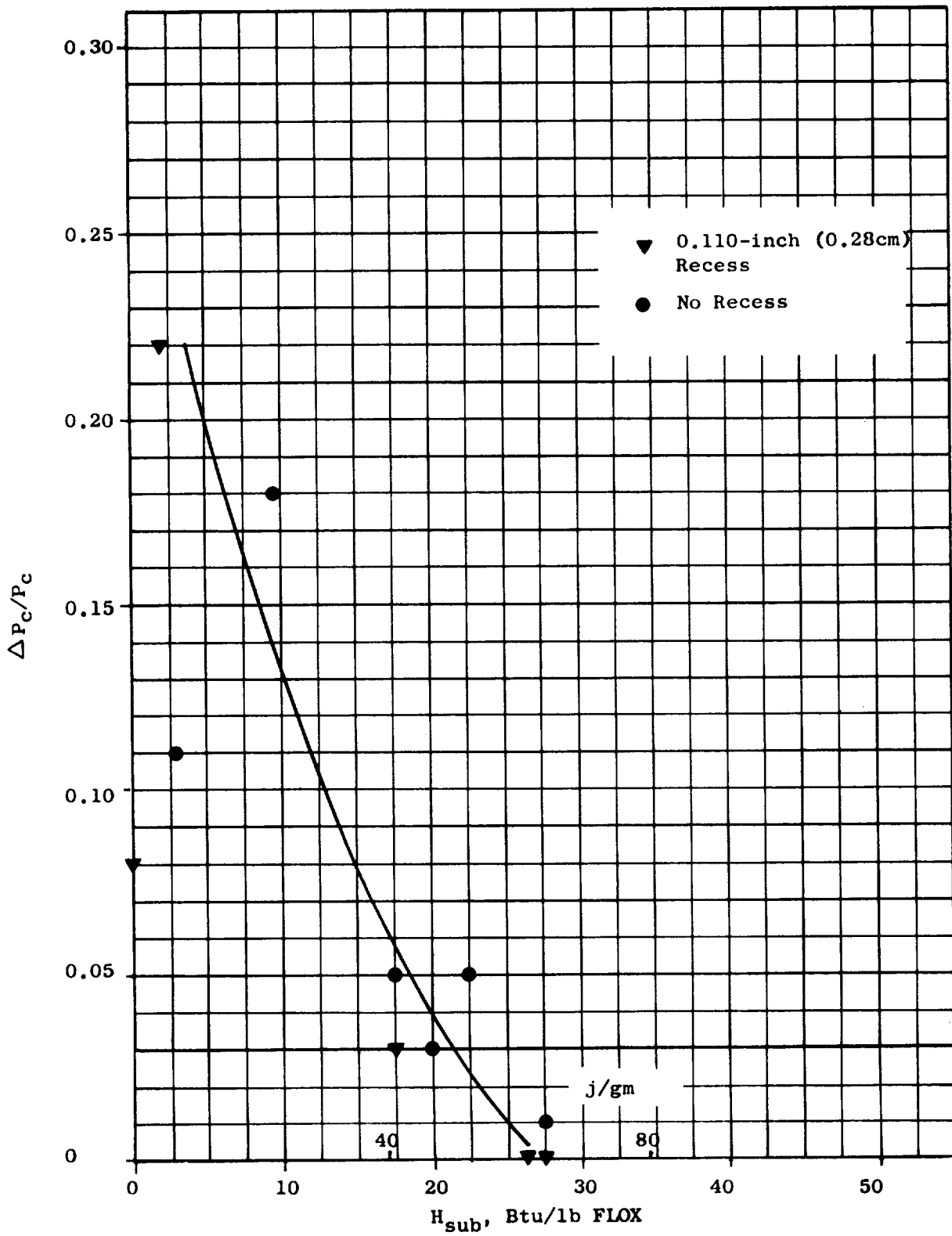


Figure 119. Correlation of Chugging Amplitude With FLOX Subcooling, Recessed Post Injector

3. Regenerative cooling with a nickel channel-wall chamber having a high area ratio nozzle is feasible at nominal mixture ratio down to approximately 50 psia (35 N/cm^2) chamber pressure if a very limited number of cycles is required. To provide for a longer life the following alternatives are available.
 - a. Throttle to no lower than approximately 100 psia (70 N/cm^2).
 - b. Reduce the propellant mixture ratio to 4.5.
 - c. Modify the peripheral elements of the injector to reduce the heat flux at low chamber pressures.

REFERENCES

1. NASA CR-72360, R7338, Space Storable Regenerative Cooling Investigation-Interim Report, Rocketdyne, A Division of North American Rockwell Corporation, Canoga Park, California, 25 September 1968.
2. NASA CR-54445, PWA FR1443, Investigation of Light Hydrocarbon Fuels With FLOX Mixtures as Liquid Rocket Propellants, Pratt and Whitney Aircraft, A Division of United Aircraft Corporation, West Palm Beach, Florida, 1 September, 1965.
3. Design Handbook For Liquid Fluorine Handling Equipment, AFRPL-TR-65-123, Second Edition, Edwards Air Force Rocket Propulsion Laboratory, Edwards, California, August 1965.
4. NASA CR-72559, R-7879, Space Storable Engine Characterization, Rocketdyne, March 1970.
5. Lambris, S., L. P. Combs, and R. S. Levine: Storable Combustion Processes In Liquid Propellant Rocket Engines, Fifth Colloquium of the Combustion and Propulsion Panel, Advisory Group for Aeronautical Research and Development, NATO, Braunschweig, Germany, April 1962.
6. NASA TR R-67, Propellant Vaporization as a Design Criterion for Rocket Engine Combustion Chambers, Priem, R. J., and M. F. Heidmann, 1960.
7. O395-04(18) SP, Kinetics, Mechanism, and Resultant Droplet Sizes of the Aerodynamic Breakup of Liquid Drops, Aerojet General Corporation, Downey, California, April 1964.
8. NASA CR-72695, R-8039, Lithium-Fluorine-Hydrogen Propellant Investigation, Rocketdyne, May 1970.
9. R-6028-2, Chamber Technology For Space Storable Propellants, Task II, Interim Report, Vol. 2, Rocketdyne, October 1965.
10. AFRPL TR-68-147, Correlation of Spray Injector Parameters With Rocket Engine Performance, Rocketdyne, June 1968.

11. JPL PR20-165, The Liquid Phase Mixing of a Pair of Impinging Streams, Rupe, J. H., Jet Propulsion Laboratory, Pasadena, California, August 1953.
12. R-5619-3, Applied Research Program To Evaluate the Feasibility of the Compound A/Hydrazine Propellant System, Part III, Third Quarterly Progress Report, Rocketdyne, October 1964.
13. Liquori, R. R. and J. W. Stephanson: The HEATING Program (Heat Engineering and Transfer in Nine Geometries), Report 417-5.0, ASTRA, Inc., Raleigh, North Carolina, January 1960.
14. Fluid Meters Handbook, Their Theory and Application, 5th Edition, ASME, 1939.
15. NASA CR-72542, R-6636-3, Fluorine-Hydrogen Performance Evaluation, Phase III: Space Storable Propellant Performance Demonstration, Rocketdyne, May 1970.

APPENDIX A

INJECTOR PERFORMANCE DESIGN ANALYSIS

Spray characteristics and their critical importance to injector design are basically defined by four classical processes which must take place for combustion to occur:

Atomization

Vaporization

Mixing (distribution)

Chemical reaction

The chemical reaction step is generally a function of the propellant combination. However, the rate of chemical reaction is very fast for most common propellants and is not considered to be overall rate controlling. The vaporization step is partly limited by the propellant combination because of its relationship to fluid properties. However, the rate of vaporization can be considerably enhanced if the droplet surface area to volume relationship is increased by the atomization step. Atomization and mixing (distribution) are controlled by the injector design. The two processes, atomization and distribution, were, therefore, the prime parameters considered in the selection of the injector design for application to this program.

ATOMIZATION

The one-dimensional, steady-state, combustion model computer program (Ref. 5) was used to predict combustion efficiency as a function of propellant dropsizes and combustion chamber geometry. Basically, the model accounts for the following processes:

1. Forced convection droplet vaporization
 - a. Changes in droplet temperature
 - b. Changes in droplet size due to vaporization
2. Droplet ballistics
 - a. Drag on droplets by moving combustion gas
 - b. Droplet breakup
3. Combustion gas dynamics
 - a. Instantaneous chemical reaction of vaporized propellants resulting in chemical equilibrium
 - b. Compressible fluid dynamics
 - c. Momentum interchange with propellant droplets

Physical equations describing all three processes are contained in the combustion model. The model applied the descriptive equations in an iterative manner to calculate the conditions incrementally from the injector face to the nozzle throat. The most important information which is calculated by the combustion model is the degree to which vaporization and combustion of liquid propellants are completed. For this application the combustion model calculates the percentage of oxidizer vaporized and reacted in the rocket engine combustion chamber (the fuel is injected as a gas). With this information the loss in combustion efficiency owing to incomplete oxidizer vaporization and reaction are calculated from the following equation (Ref. 6):

$$(\mathcal{N}_{c^*})_{D_{30}} = 1.0 - \frac{\dot{W}_{ov} + \dot{W}_{fi}}{\dot{W}_{oi} + \dot{W}_{fi}} \times \frac{c^*_v}{c^*_i} \quad (1)$$

where $(\mathcal{N}_{c^*})_{D_{30}}$ Combustion efficiency due to incomplete propellant vaporization and reaction

- \dot{W}_{oi} = weight flowrate of oxidizer injected
 \dot{W}_{ov} = weight flowrate of oxidizer vaporized
 \dot{W}_{fi} = total weight flowrate of fuel injected
 c^*_i = characteristic exhaust velocity corresponding to injection mixture ratio, $\dot{W}_{oi}/\dot{W}_{fi}$
 c^*_v = characteristic exhaust velocity corresponding to equivalent mixture ratio of reacted propellants, $\dot{W}_{ov}/\dot{W}_{fi}$

The loss in combustion efficiency due to incomplete vaporization and reaction was calculated for the FLOX/methane propellant combination using the above described combustion model, as a function of FLOX drop-sizes from 10 to 100 μ and chamber lengths from 5 to 12 inches (13 to 30 cm) and for a contraction ratio range from 2 to 6.

An estimate of the dropsize that would be expected employing the gaseous methane/FLOX propellant was calculated from equation (2). This equation, taken from Ref. 7, describes the relationship between the volume mean diameter of a spray field resulting from the secondary breakup of a liquid droplet into smaller droplets as a function of the physical properties and flow conditions.

$$\bar{D}_{30} = \phi \left[\frac{136 \sigma_L \mu_L^{3/2} D_L^{1/2}}{\rho_L^{1/2} \rho_g^2 \Delta V_g^4} \right]^{1/3} \quad (2)$$

where $\phi = \left[\frac{3\dot{W}_L/\dot{W}_g}{1 - (1 + \dot{W}_L/\dot{W}_g)^{-3}} \right]^{1/3}$

μ_L	=	liquid viscosity
σ_L	=	surface tension
ρ_g	=	density of gas
ρ_L	=	density of liquid
Δv_g	=	relative velocity of gas with respect to the large liquid droplet
D_L	=	diameter of the large liquid droplet which is to be atomized
\bar{D}_{30}	=	volume mean diameter of the small droplets which are produced by the atomization process
\dot{W}_L	=	liquid flowrate
\dot{W}_g	=	gas flowrate

To calculate the droplet size produced by injection of a liquid stream into a high-velocity gas jet, the characteristic diameter, D_L , in Equation (2) was replaced by the liquid jet orifice diameter.

Calculations of the mean dropsizes from Equation (2) indicate that a mean dropsizes of <10 can be achieved with the FLOX/methane propellants in any of the element designs which utilize the gaseous methane for atomization of impinging jets or fans. These results suggest that c^* performance for these conditions is primarily limited by propellant mixing.

MIXING (DISTRIBUTION)

Previous hot firing and cold flow spray analysis programs (Refs. 8 and 9) indicate that high-combustion efficiency in rocket engine thrust chambers occurs only when the initial local mixture ratio distribution is at or near the target chamber mixture ratio. This implies that the injector should provide a spray field having a uniform mixture ratio over the entire flow cross section.

The effect of mixing on combustion performance is determined employing a stream tube analysis program in which the chamber cross section is divided into discrete "tubes" of differing mixture ratio and percent mass. Overall performance is then defined as a function of departures from ideal distribution (mixing) by computing the integrated c^* levels obtainable, assuming no inter-stream-tube mixing. The resulting combustion c^* efficiency is calculated utilizing the following equation (Ref.10):

$$(\mathcal{N}_{c^*})_{E_m} = \frac{1}{c^*_T} \sum_{n=1}^I \frac{W_i}{W_t} c^*_i \quad (3)$$

where $(\mathcal{N}_{c^*})_{E_m}$ = combustion efficiency due to non-uniform mixing

c^*_T = theoretical c^* at the overall injected mixture ratio

W_i = local propellant mass

W_T = total injected propellant mass

c^*_i = local c^* at the local mixture ratio

I = total number of tubes

The mixing efficiency (K_m) is calculated (at the same conditions as for the c^* efficiency) employing a distribution index which describes the mass weighted deviation of local mixture ratio from the overall injected mixture ratio. The functional relationship is shown below (Ref.11).

$$K_m = 1 - \left[\sum_{r_i} \frac{W_i}{W_T} \frac{(R_T - r_i)}{R_T} - \sum_{\bar{r}_i} \frac{W_i}{W_T} \frac{(R_T - \bar{r}_i)}{1 - R_T} \right] \quad (4)$$

where K_m = mixing efficiency
 W_i = local mass
 W_T = total mass
 R_T = $\frac{\text{total oxidizer mass}}{\text{total oxidizer and fuel mass}}$
 r_i = $\frac{\text{local oxidizer mass}}{\text{local oxidizer and fuel mass}}$ for $r_i < R_T$
 \bar{r}_i = $\frac{\text{local oxidizer mass}}{\text{local oxidizer and fuel mass}}$ for $r_i > R_T$

For mathematical simplicity the subject analysis considered the mass distributed in two elements only, one with $r_i < R_T$ and one with $\bar{r}_i > R_T$. The analytical approach for the two-tube analysis is equally applicable to a multi-tube matrix. The ratio of total oxidizer mass to total oxidizer and fuel mass can be expressed as follows:

$$R_T = \frac{M_F}{A} r_A + \frac{M_F}{B} r_B \quad (5)$$

where R_T = $\frac{\text{total oxidizer mass}}{\text{total oxidizer and fuel mass}}$
 M_F = mass fraction in tube
 r = $\frac{\text{local oxidizer mass}}{\text{local oxidizer and fuel mass}}$
 A = tube A
 B = tube B

Specification of the total ratio R_T , one local mass fraction M_F and one local ratio r is sufficient to fix the values of the remaining variables.

For a two-tube analysis, Equation (4) reduces to

$$E_m = 1 - M_{F_A} \frac{(R_T - r_A)}{R_T} + M_{F_B} \frac{(R_T - r_B)}{1 - R_T} \quad (6)$$

where $r_A < R_T$

$r_B > R_T$

(other terms as previously defined)

Calculations were made at an overall mixture ratio of 5.7,

APPENDIX B

INJECTOR FACE HEAT TRANSFER ANALYSIS

Temperature profiles throughout an injector are dependent upon imposed heat load, propellant cooling capability, orifice spacing, and material thermal conductivity. There is some experimental evidence (Ref.12) to indicate that the average injector face heat flux level is about the same level as at the local chamber walls. The resulting face heat flux levels using this assumption were nominally 5 Btu/in.²-sec (0.74 KW/cm²) at P_c = 500 psia (F = 5000 pounds) and about 9 Btu/in.²-sec (1.3 KW/cm²) at a chamber pressure of 1000 psia (F = 10,000 pounds).

The cooling capability of the propellants was calculated from the semi-empirical relation

$$N_{Nu} = 0.025 N_{RE}^{0.8} N_{PR}^{0.4}$$

where the coolant properties were evaluated at a suitable film temperature.

The temperature profile determination for the injector requires the use of a thermal analyzer type program because of the three-dimensional nature of the problem. In this particular analysis, the HEATING program was utilized (Ref.13) for simplicity of input and the capability of a direct steady-state solution. The configurations analyzed are tabulated below.

TABLE VII

INJECTOR ELEMENT CONFIGURATIONS AND CONDITIONS

<u>Element Type</u>	<u>Face</u>	<u>Heat Flux</u>	<u>Figure</u>	<u>Thrust Level</u>	
				<u>Pounds</u>	<u>Newtons</u>
Pentad	Solid Copper	2X Nominal	B-1	5,000	22,000
Pentad	Solid Copper	2X Nominal	B-2	10,000	44,500
Pentad	Solid Nickel	2X Nominal	B-3	5,000	22,000
Pentad	Transpiration	2X Nominal	B-4	10,000	44,500
Concentric	Transpiration	2X Nominal	B-5	10,000	44,500
Concentric	Solid Copper	2X Nominal	B-6	10,000	44,500

A typical section was taken from the injector face pattern and analyzed. An enlarged view of a section from the pentad is shown in Fig. B-1. This section measures 0.250 x 0.250 inch (0.63 x 0.63 cm) and is 1.19 inches (3.0 cm) thick. The fuel orifice diameter was 0.055 inch and the oxidizer orifice diameter was 0.024 inch (0.061 cm). The cooling effect of the oxidizer manifolds was not included, and the methane temperature was assumed to be 660 F (612K). Cooling was accomplished by the FLOX in the orifices and behind the injector body.

The pentad section was analyzed at an oxidizer flowrate corresponding to a chamber pressure of 500 psia and thrust level of 5,000 pounds, assuming copper (OFHC) material. The heat flux level was taken as 10 Btu/in.²-sec (1.47 KW/cm²), which is about twice the expected value. The resulting temperatures at various points on the surface are denoted in Fig. B-1. The maximum copper temperature is about 954 F (790K).

$P_c = 500 \text{ psia (345 N/cm}^2\text{)}$
 $F = 5000 \text{ pounds (22,000 N)}$
 $Q/A = 10 \text{ Btu/in}^2\text{-sec (1.6 KW/cm}^2\text{-sec)}$

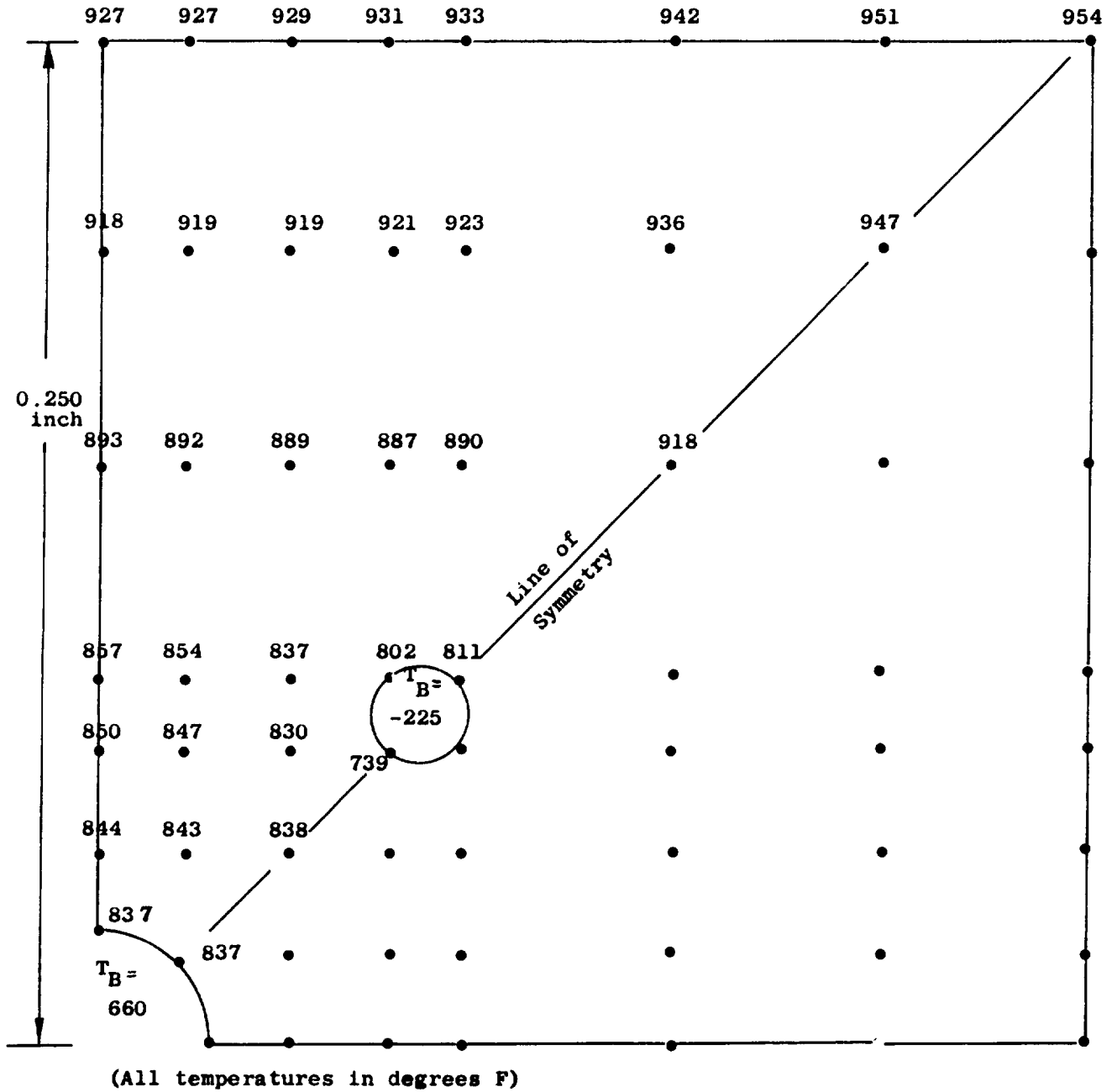


Fig. B-1 - Surface Temperature Distribution for Solid Copper Pentad Injector

The copper pentad injector was then analyzed at an oxidizer flowrate corresponding to a chamber pressure of 1000 psia and thrust level of 10,000 pounds. The heat flux level assumed was about 17 Btu/in.²-sec. (2.5 KW/cm²), again considerably higher than the nominal value. The resulting temperatures are shown in Fig. B-2, where the maximum value is seen to be 1202 F (913 K).

The use of nickel material for the pentad injector was also considered briefly. The resulting face temperature for flowrates corresponding to $P_c = 500$ psia (345 N/cm²) are shown in Fig. B-3. The maximum value is seen to be 2363 F (1570 K). The 1000 psia (690 N/cm²) case was not analyzed, but would be more severe than the 500 psia (345 N/cm²) case.

The use of a porous, transpiration-cooled (with methane) face surrounding the nickel pentad elements was also considered. (Porous face cooling on a copper body was not considered due to the difficulty of welding the porous material to the copper.) The temperature distribution for the reduced nickel face area is shown in Fig. B-4 for a 17 Btu/in.²-sec. (2.5 KW/cm²) heat flux with flowrates corresponding to $P_c = 1000$ psia (690 N/cm²). The maximum temperature for this configuration was 1996 F (1372 K).

The preceding results indicate that the nickel pentad with a solid face or with transpiration cooling is less desirable than the solid copper pentad. For this reason an alternate injector design was considered which could make better use of the Rigimesh concept. The coaxial injector configuration was deemed best for porous face cooling.

$P_c = 1000 \text{ psia } (690 \text{ N/cm}^2)$

$F = 10,000 \text{ pounds } (44,500 \text{ N})$

$Q/A = 17 \text{ Btu/in}^2\text{-sec } (2.5 \text{ KW/cm}^2\text{-sec})$

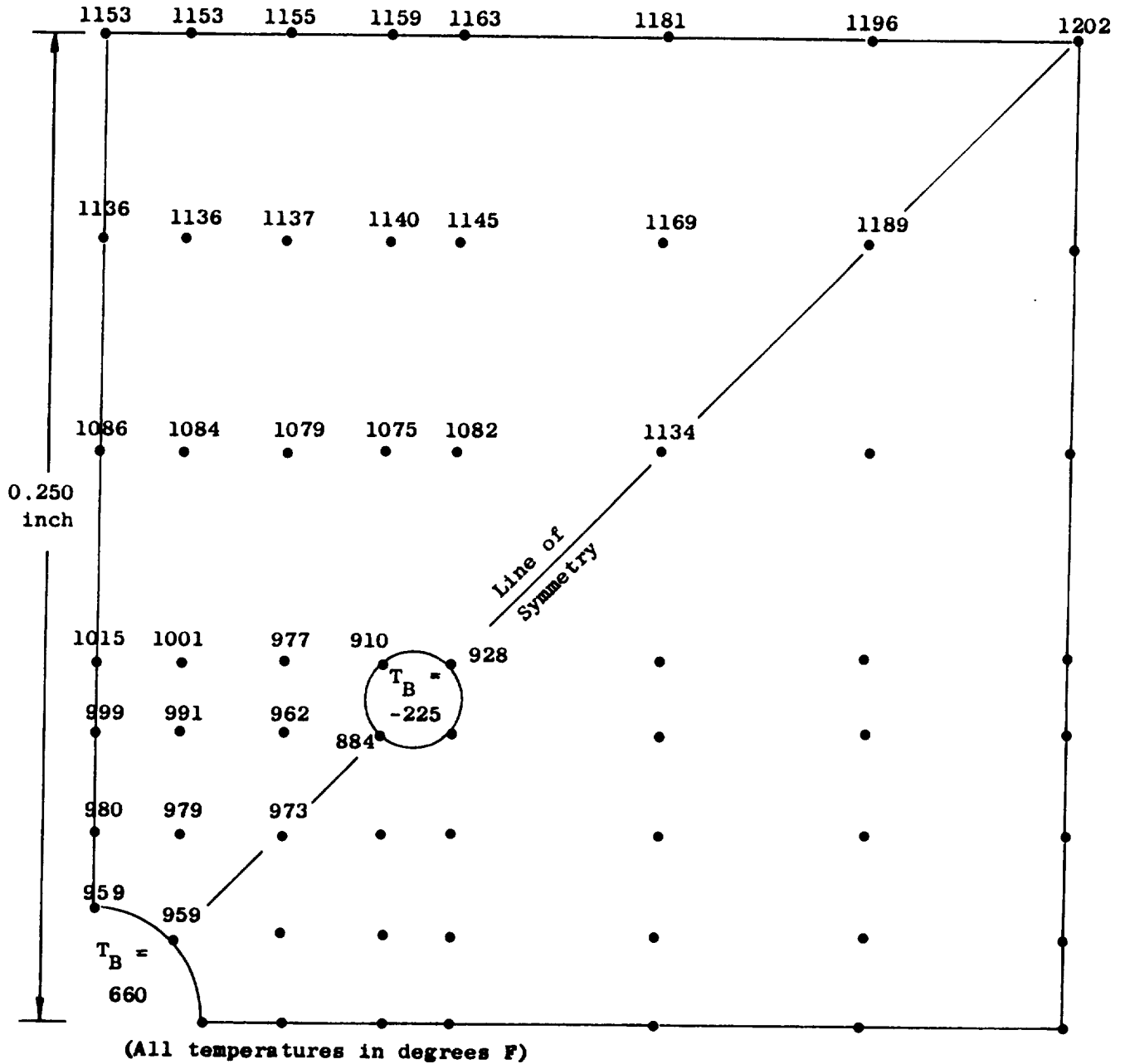
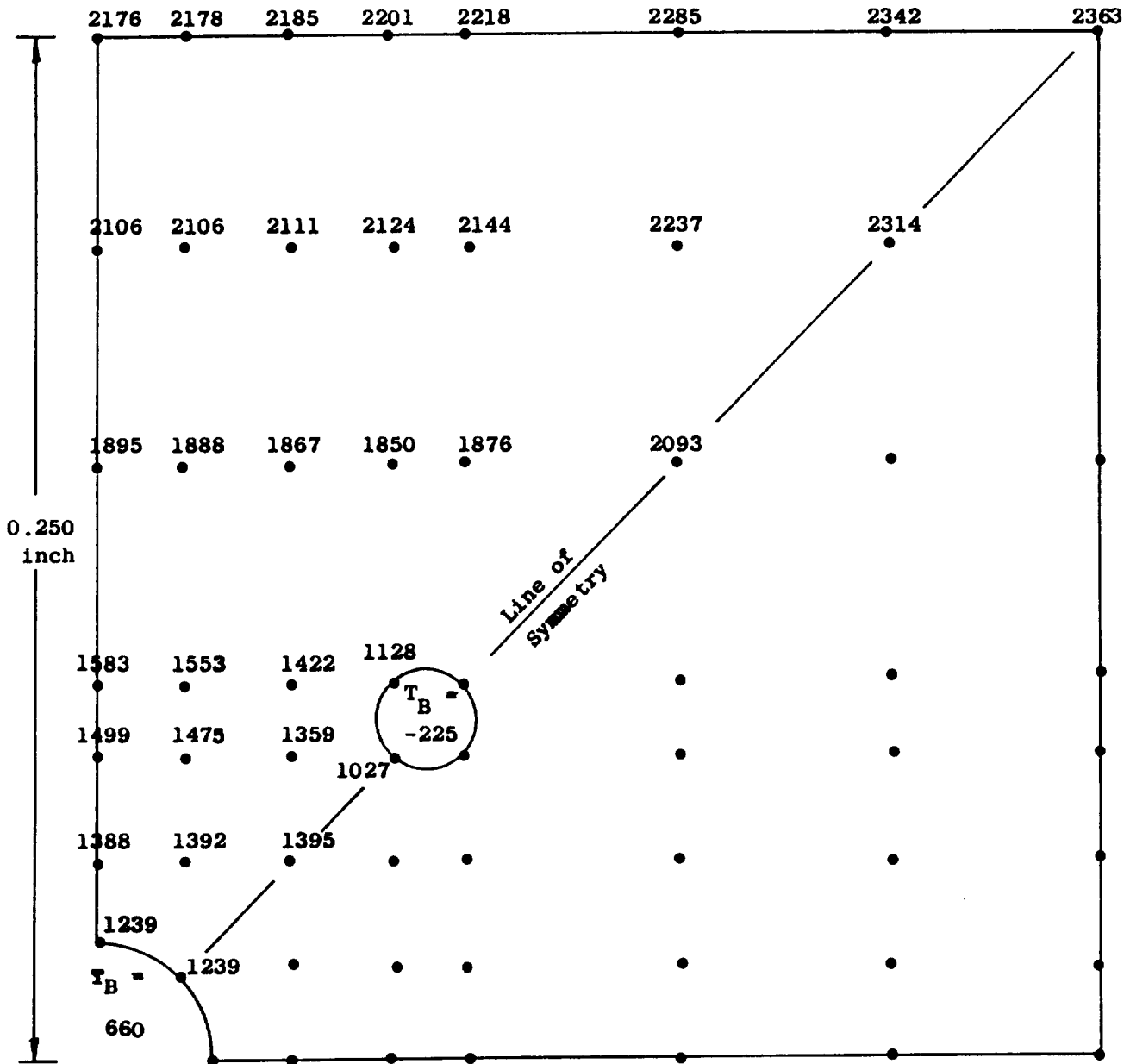


Fig. B-2 - Surface Temperature Distribution for Solid Copper Pentad Injector

$$P_c = 500 \text{ psia (345 N/cm}^2\text{)}$$

$$F = 5000 \text{ pounds (22,000 N)}$$

$$Q/A = 10 \text{ Btu/in}^2\text{-sec (1.6 KW/cm}^2\text{-sec)}$$



(All temperatures in degrees F)

Fig. B-3 - Surface Temperature Distribution for Solid Nickel Pentad Injector

$P_c = 1000 \text{ psia } (690 \text{ N/cm}^2)$
 $F = 10,000 \text{ pounds } (44,500 \text{ N})$
 $Q/A = 17 \text{ Btu/in}^2\text{-sec } (2.5 \text{ KW/cm}^2\text{-sec})$

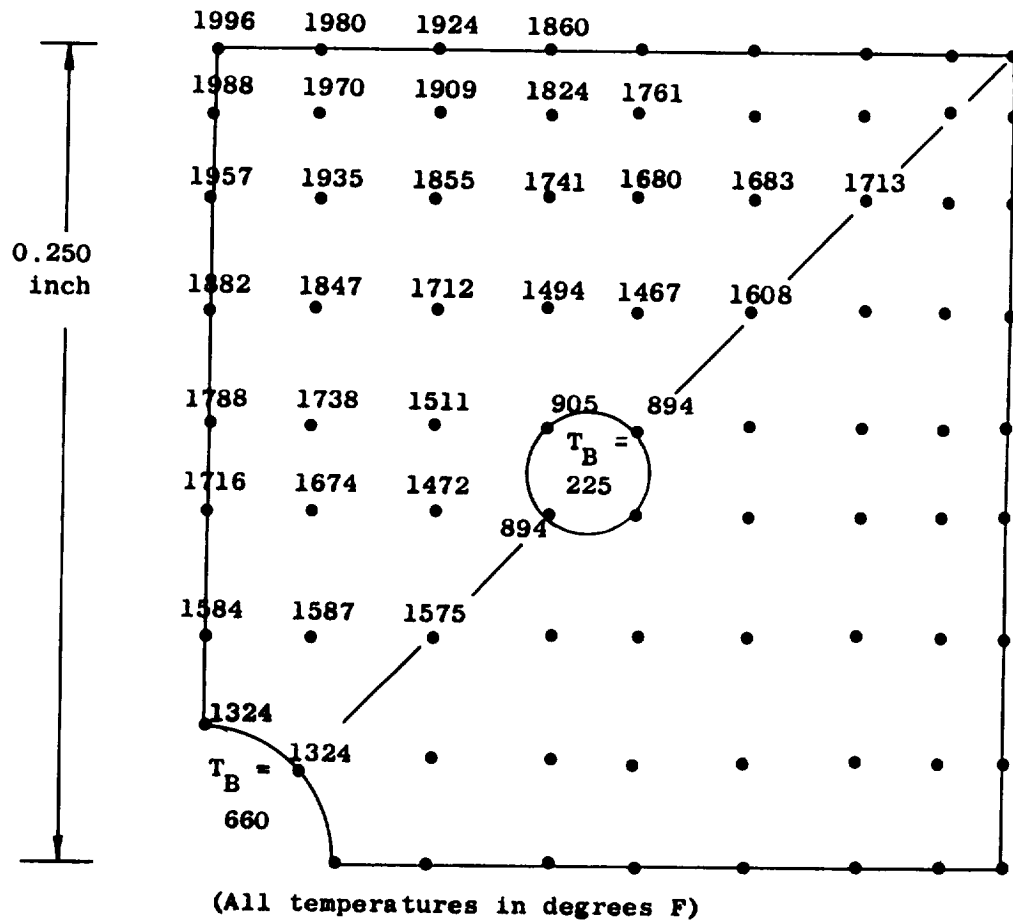
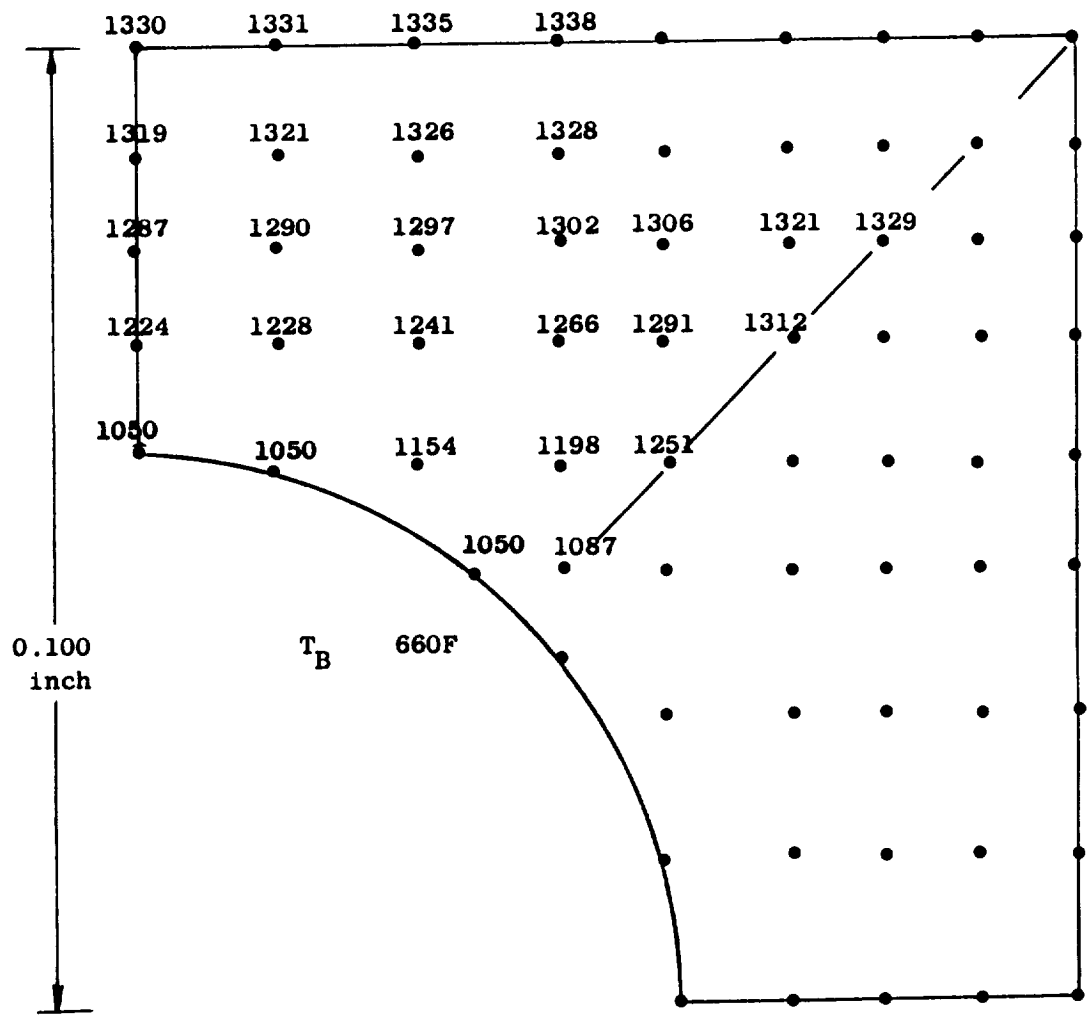


Fig. B-4 - Surface Temperature Distribution for Pentad Injector with Rigimesh

The coaxial injector studied also consisted of 91 elements, so that the spacing between elements remained unchanged. An enlarged view of a quarter-section of an element is shown in Fig. B-5. The resulting temperature profiles for the nickel with Rigimesh are shown. The peak nickel temperature was 1337 F (991 K). The actual number of elements is not critical because the highest temperature occurs, not in the Rigimesh between the elements, but in the small annular area around the element which is not transpiration cooled.

A solid-copper face concentric element injector with 91 elements was also analyzed because it presents a simpler design than the transpiration cooled face injector. The exposed surface between elements is slightly greater than for the pentad injector because of the smaller size of the concentric element. This, together with the fact that the fuel is outside of the oxidizer on the concentric element, resulted in maximum surface temperatures of 1970 F (1348 K) for 1000 psia (690 N/cm^2) flowrates with a $17 \text{ Btu/in.}^2\text{-sec}$ (2.5 KW/cm^2) heat flux as shown in Fig. B-6. Thus, the nickel concentric element injector with transpiration cooled face appears to be most satisfactory from the face heating standpoint. These results are based on the assumption of equal heat fluxes for the different element types. Test data comparing heat flux profiles for triplet and concentric element injectors used with GO_2/GH_2 propellants were generated under Contract NASS-20349. The heat flux level was lower at all locations for the concentric element injector. However, the reduction was particularly significant near the injector face where the concentric element injector resulted in heat fluxes approximately 50 percent lower than the triplet.

$P_c = 1000 \text{ psia (690 N/cm}^2\text{)}$
 $F = 10,000 \text{ pounds (44,500 N)}$
 $Q/A = 17 \text{ Btu/in}^2\text{-sec (2.5 KW/cm}^2\text{-sec)}$



(All temperatures in degrees F)

Fig. B-5 - Surface Temperature Distribution for Coaxial Injector with Rigimesh

$P_c = 1000 \text{ psia } (690 \text{ N/cm}^2)$
 $F = 10,000 \text{ pounds } (44,500 \text{ N})$
 $Q/A = 17 \text{ Btu/in}^2\text{-sec } (2.5 \text{ KW/cm}^2\text{-sec})$

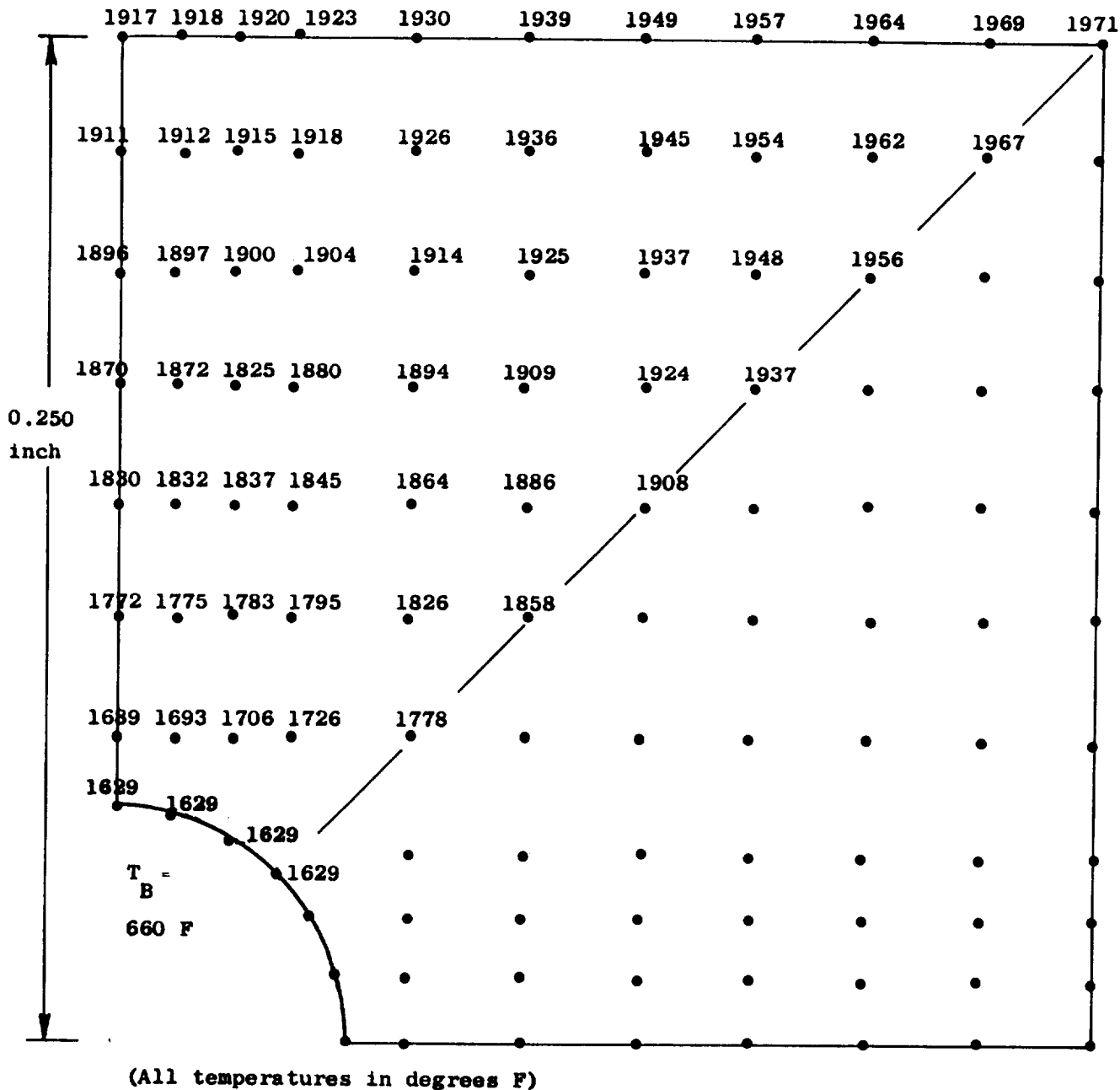


Fig. B-6 - Surface Temperature Distribution for Solid Copper Coaxial Injector

APPENDIX C

CORRELATION OF RECESSED POST INJECTOR DATA

Correlation of data from hot firing tests of recessed post injectors used on the J-2 engine resulted in pressure drops which were considerably higher than those predicted by the hydraulic "square law". The slope of the ΔP vs flowrate data (on a log-log plot) was less than 2. Cold flow tests of the injector resulted in pressure drops lower than the predictions based on the "square law".

To explain these anomalies consideration was given to conditions in the cup region, the region between the recessed FLOX post and the injector face. It was obvious that two extreme conditions could occur in the cup region: 1) the propellants could mix completely in the cup region, or 2) the propellants could remain completely unmixed (the wake at the tip of the FLOX post would tend to prevent mixing).

The static pressure drop in the cup region was determined for the complete-mixing model by solving continuity and conservation of momentum equations subject to the following assumptions:

- (1) The liquid phase is completely atomized in the cup
- (2) The liquid and gas phases are thoroughly mixed in the cup
- (3) None of the liquid phase is vaporized
- (4) The liquid and the gas phase leave the cup at the same velocity
- (5) The gas phase is treated as incompressible in the cup interaction region

(6) The static pressures of the liquid and gas phase are equal at the entrance and exit of the cup.

Although this model does account for the highest degree of mixing, it does not predict the highest possible values of pressure drop in the cup. This is because any vaporization or combustion will produce pressure losses in addition to those incurred from pure mixing.

The complete-mixing model need not always predict an increase in pressure drop. (A positive pressure drop is one for which the static pressure at the entrance to the cup is greater than chamber pressure.) At extremely high or low mixture ratios, the pressure recovery caused by the diffusion of the dominant fluid is sufficient to cause the exit momentum flux to be less than the total momentum flux entering the cup. The variation of predicted pressure drop with mixture ratio is presented in Fig. C-1. Here the static pressure variation across the cup is plotted against mass mixture ratio for fixed total flowrate. The curve represents the theoretical model for the J-2 hot fire conditions with chamber pressure equal to 1100 psia (758 N/cm^2) and total flowrate of 0.85 pounds per second (0.39 Kg/sec) of hydrogen/oxygen (per element).

Experimental hot firing data are plotted in Fig. C-2 together with pressure drop predictions based on zero-recess test data and also based on the complete-mixing model for mixture ratios of 4 and 6. The complete mixing model tends to predict the magnitude and slope of the data better than the hydraulic prediction. The data indicate less complete mixing at higher oxidizer flowrates, which is consistent with trends observed in cold flow studies.

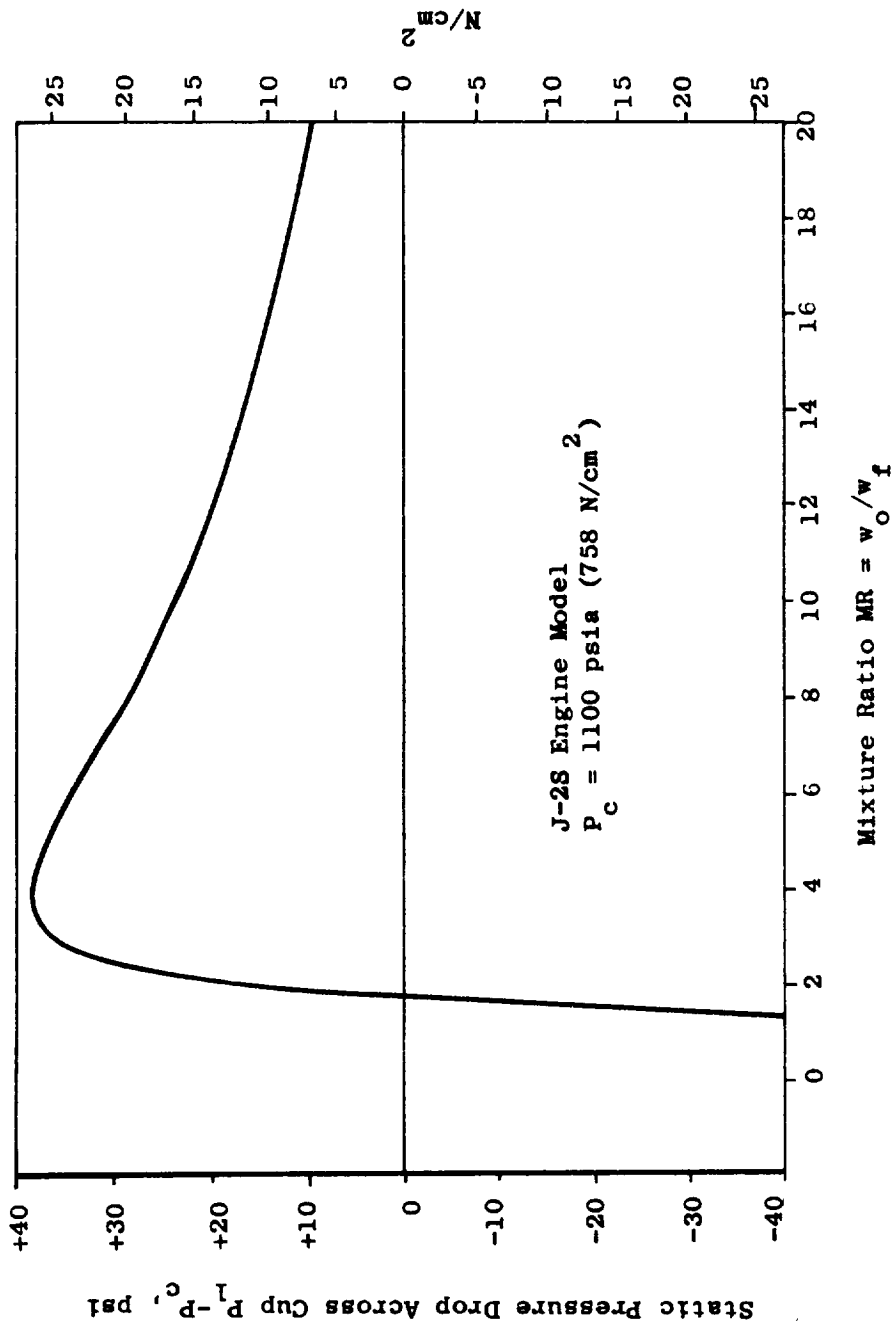


Figure C-1 - Complete Mixing Model - Variation of Static Pressure Drop Across Cup with Mixture Ratio

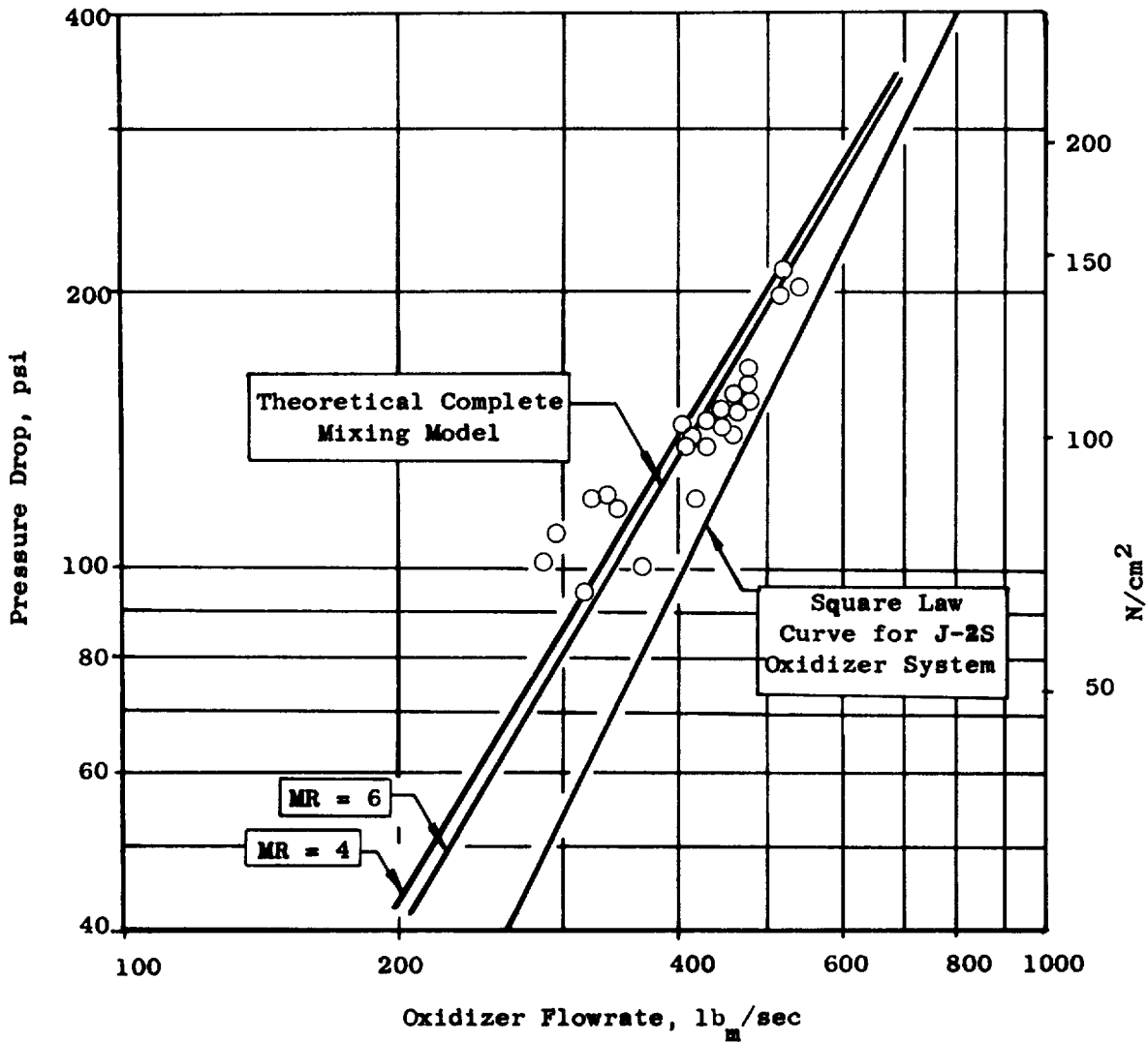


Figure C-2 - J-2S Hot-Fire Data - Oxidizer Flow Characteristics for Injectors With and Without Recess

The non-mixing model was developed by solving equations of continuity and conservation of mass and energy in the cup region subject to the following assumptions:

- (1) Oxidizer, fuel, and base static pressures may all be different.
- (2) Fuel and oxidizer static pressures are equal at the exit.
- (3) The fuel and oxidizer velocities may differ at the exit.
- (4) There is no shear between the fuel and oxidizer streams.

The non-mixing model correlated the cold flow data better than the complete-mixing model. This correlation is shown in Fig. C-3. The cold flow data indicated a pressure rise in the cup which was also predicted by the non-mixing model.

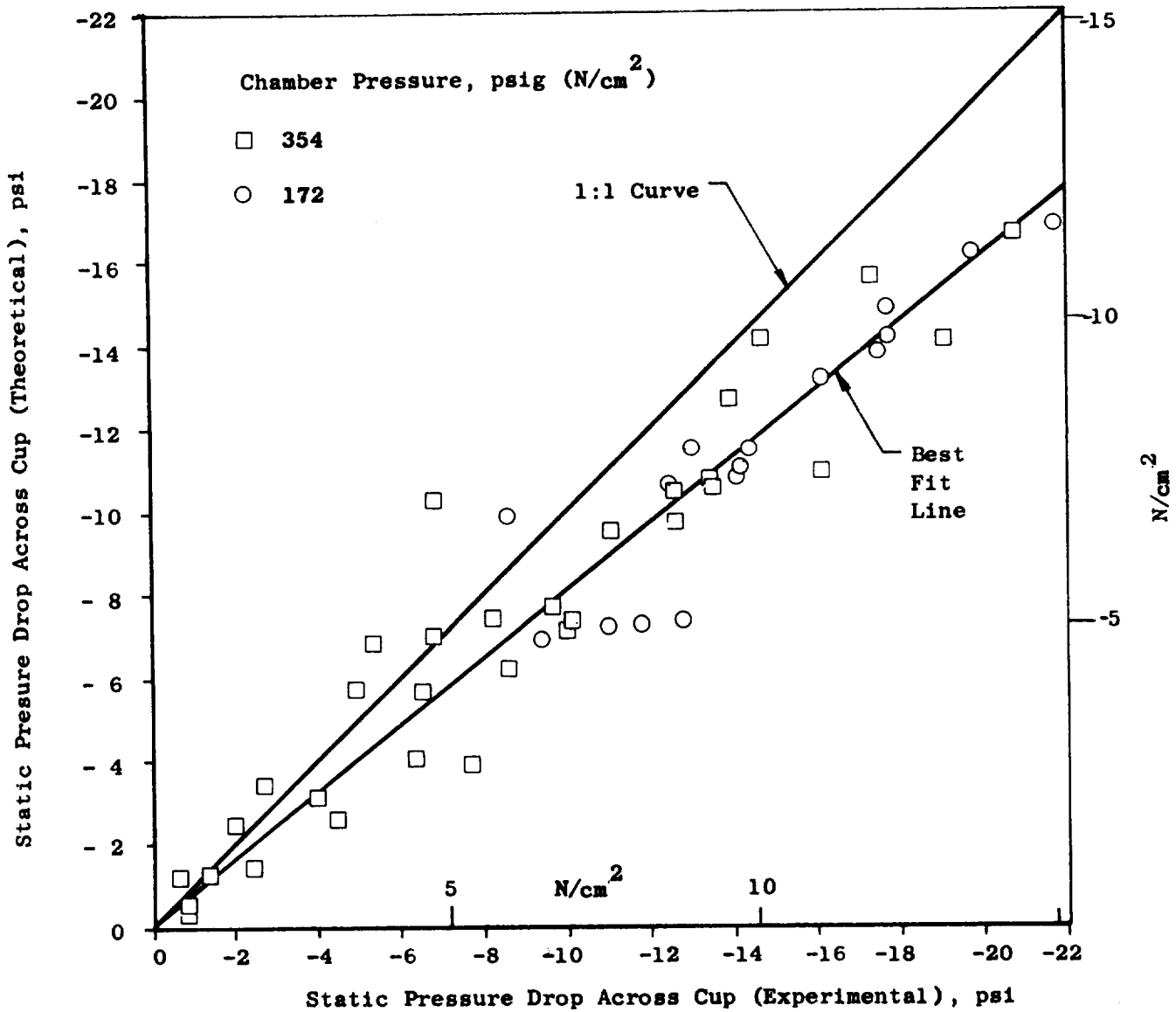


Figure C-3 - Comparison of Theoretical and Experimental Pressure Drop Results for J-2S Single Element Cold Flow

APPENDIX D

NOZZLE CONTOUR ANALYSIS AND DESIGN

An optimum nozzle was designed to attach to the existing thrust chamber at $\epsilon = 4$ to increase the area ratio to 60. The thrust chamber has a conical nozzle contour to $\epsilon = 4$. The cone angle, 36 degrees, was originally intended for use with an $\epsilon = 100$ extension. The optimum angle for an 80 percent length, $\epsilon = 60$ nozzle is approximately 34 degrees. The vacuum thrust coefficient for the existing chamber and best nozzle configuration is approximately 0.7 percent less than that of an optimum 80 percent length bell nozzle. The nozzle length for the present design is 67 percent (of an equivalent 15-degree cone length).

The starting flowfield for a method of characteristics analysis lies in the supersonic flow regime where hyperbolic partial differential equations of motion apply. The shape of the upstream chamber geometry, which lies in the subsonic flow regime, influences the gas properties in the starting supersonic flow regime. Gas flow properties in the subsonic flow regime are defined by elliptic partial differential equations where the method of characteristics does not apply. To solve the transonic flow problem a power series solution was used. Using the conditions of irrotationality and continuity the coefficients of the power series were determined. To assure accuracy, 35 terms in the power series were maintained.

A constant gamma or gas specific heat ratio of 1.16 was used for the transonic flow solution. This value corresponds to that of FLOX/CH₄ near a Mach Number of unity. The upstream chamber-side radius to throat radius ratio was 1.5. Prior to actual bell nozzle design, the flowfield within the fixed geometry conical expansion section was established. This preliminary flowfield extends downstream to where the bell nozzle control surface starts. This downstream gas expansion limit is represented by the last right running characteristic line which emanates from the conical section end point and extends to the axis. To ensure a high degree of computational accuracy, one hundred points were used on the transonic starting line. Also, instead of the commonly used Prandtl-Meyer turning around the downstream radius ($\rho/R_t = 0.615$) section, a fine characteristic net was utilized. This technique yields more accurate results than does the Prandtl-Meyer technique, which is strictly correct only for a two-dimensional, zero-radius (point) expansion.

Once the flowfield had been developed to the end of the conical section, a series of optimum thrust control surfaces were generated. These define the exit flowfields for different nozzle geometries (combinations of nozzle length and area ratio). This process is called mapping, and greatly facilitates selection of an optimum contour for a specified area ratio. The resulting optimum contour for $\epsilon = 60$, subject to the existing geometrical constraints, is shown in Fig. D-1. The wall pressure profile is shown in Fig. D-2. The inviscid value of $C_{F_{vac}}$, referenced to the geometric throat

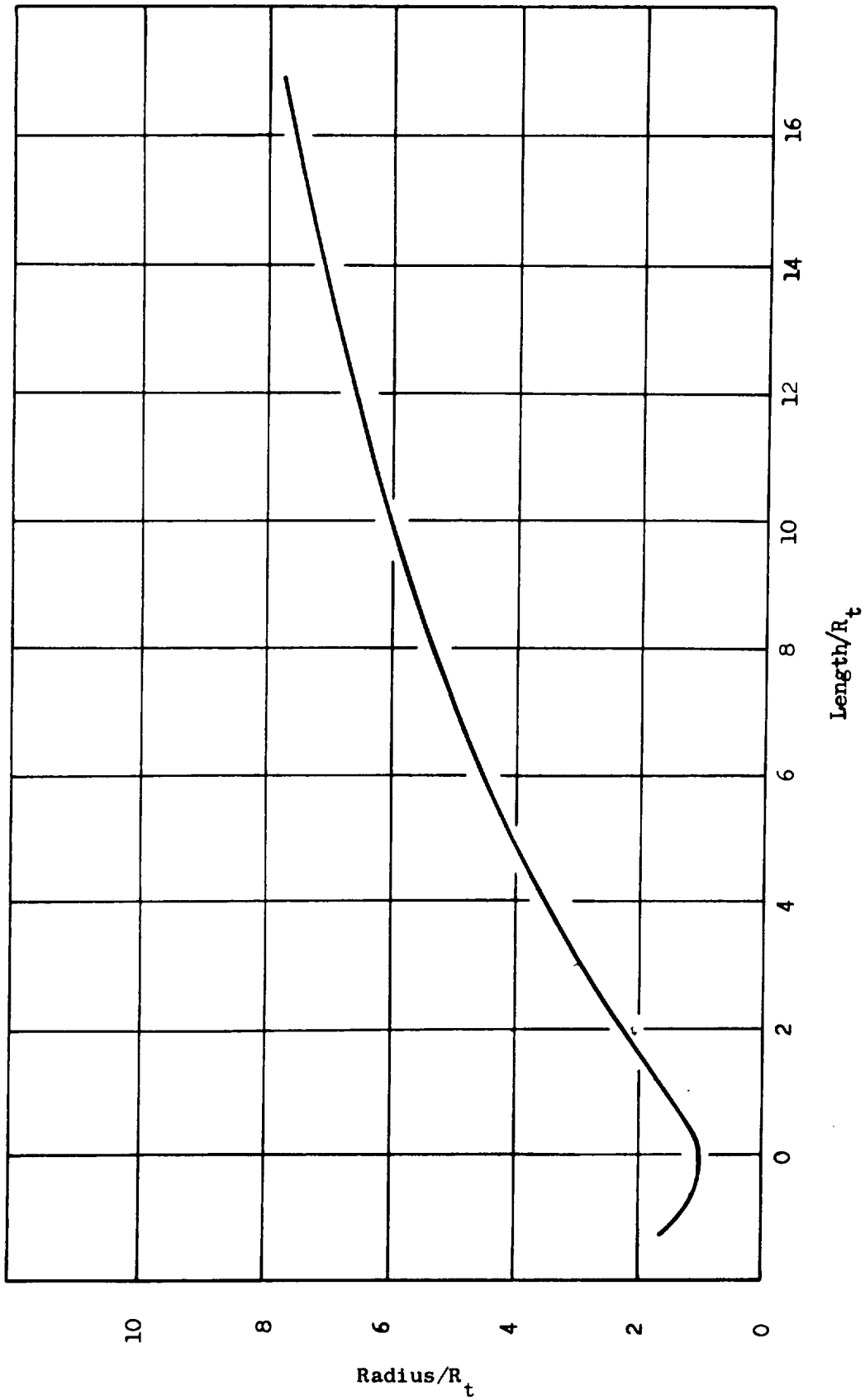


Fig. D-1 Contour for Bell Nozzle with $\zeta = 60$

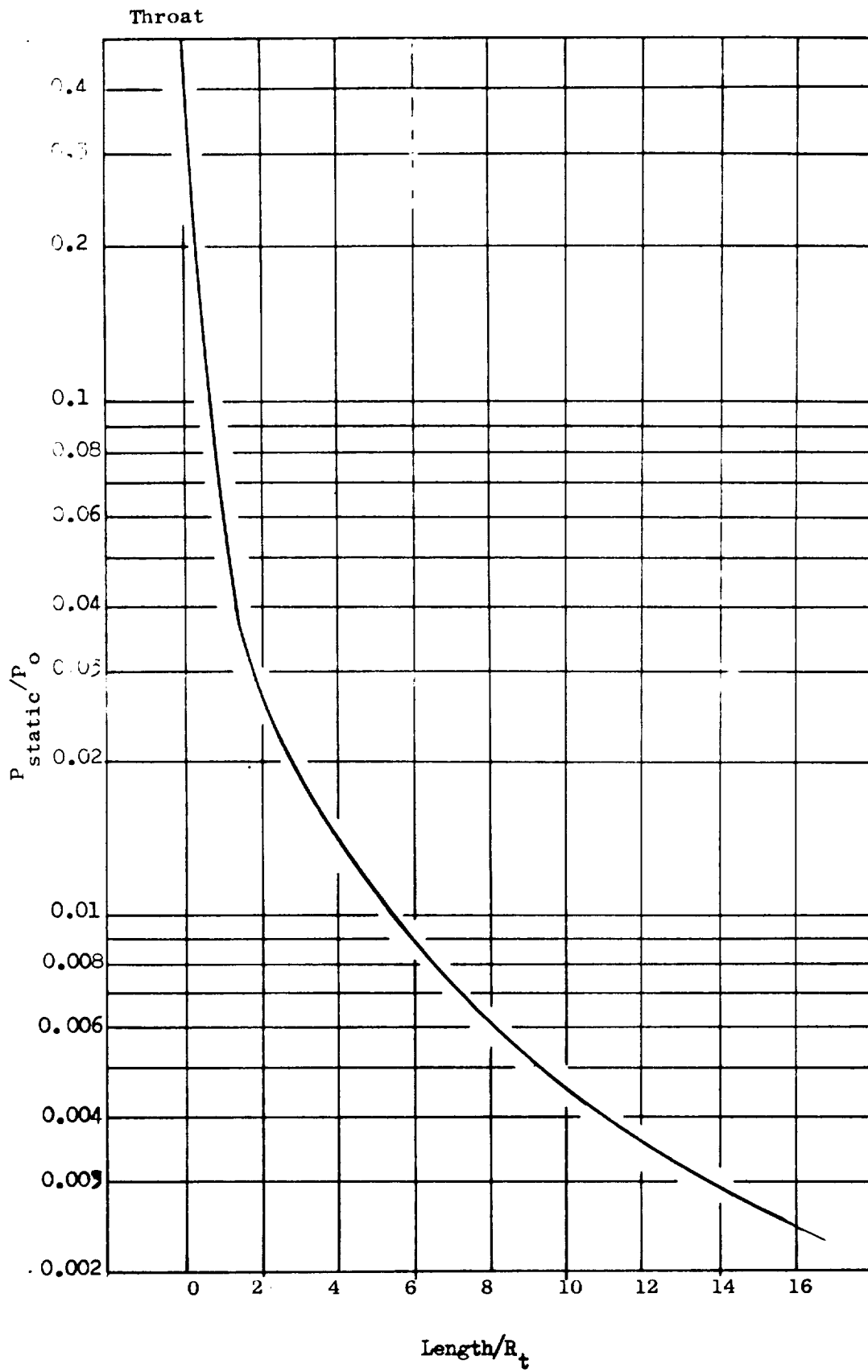


Fig. D-2 Wall Pressure Profile for $\epsilon = 60$ Nozzle

area, is 1.890. This corresponds to η_{C_f} of 0.979 and is based on a potential flow discharge coefficient of 0.994. The corresponding efficiency for an optimum 80 percent length nozzle (no existing geometrical constraints) would be 0.988, but boundary layer losses would be slightly greater than for the 67 percent length nozzle.

APPENDIX E

WATER-COOLED THRUST CHAMBER DESIGN ANALYSIS

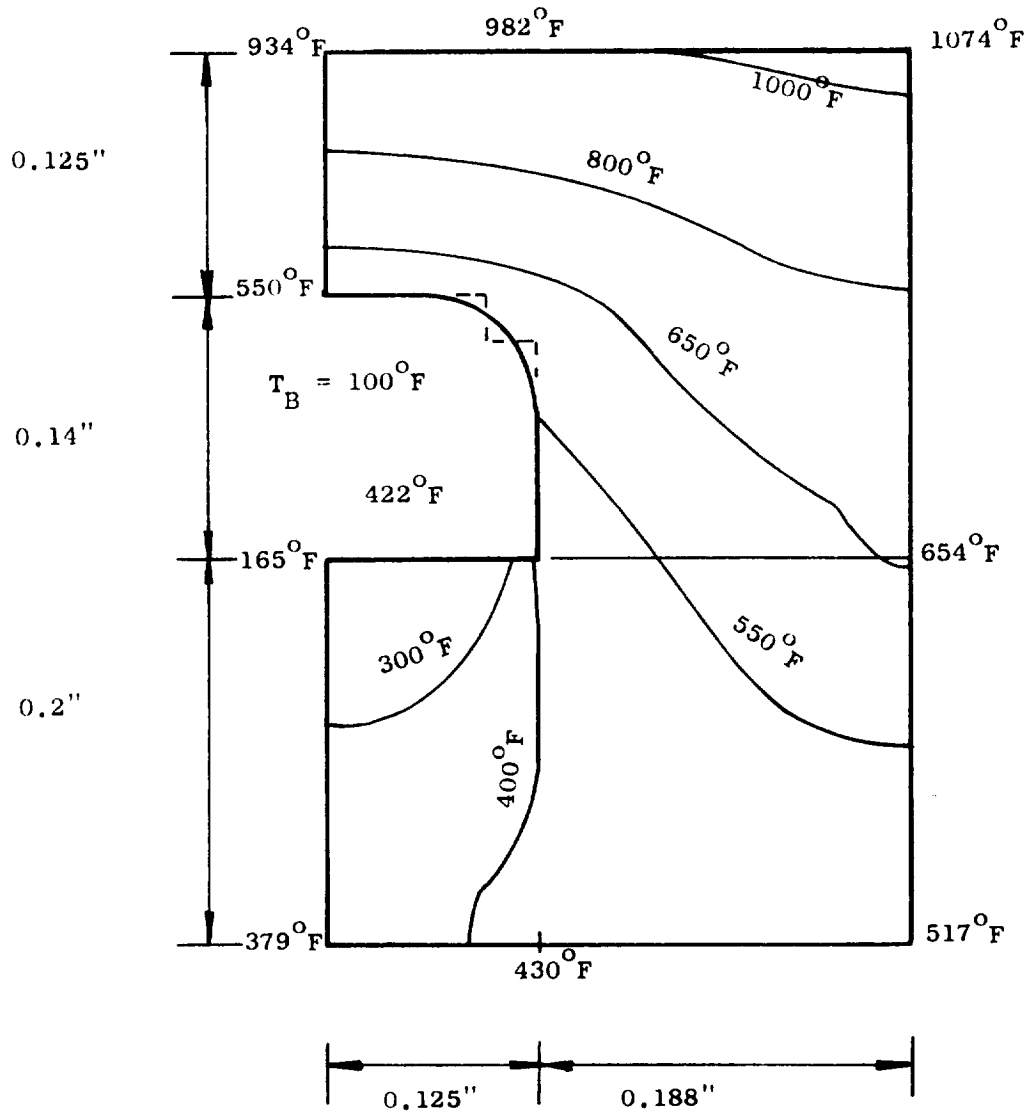
Thermal analyses were conducted to ascertain that the temperatures at various locations in the water-cooled thrust chamber were safe for the operating pressures involved. The combustion zone and throat region temperature profiles were determined using two-dimensional transient analysis methods.

Combustion Zone and Throat Region

The channel geometry analyzed for combustion zone heating is shown in Fig. E-1, which indicates the resulting isothermal temperature lines for steady-state conditions. The hot gas and coolant bulk parameters are also listed in Fig. E-1. The coolant film coefficient (h_c) given by

$$h_c = 0.023 \frac{K}{d_I} N_{RE}^{0.8} N_{PR}^{0.4}$$

where K is the thermal conductivity of the copper wall, d_I is the hydraulic diameter of the coolant passage, N_{RE} is the Reynolds number, and N_{PR} is the Prandtl number. Coolant velocities of 70 and 90 ft/sec (21.6 and 27.0 m/sec) were selected for the combustion zone and throat regions respectively to provide a bulk temperature rise of 50 F (28K) at a chamber pressure of 1000 psia (690 N/cm²).



$$P_c = 1000 \text{ Psia}; O/F = 5.7$$

$$h_g = 0.0021 \text{ Btu/in.}^2\text{-sec-}^{\circ}\text{F}$$

$$V_c = 70 \text{ ft/sec}; T_{\text{sat}} = 550^{\circ}\text{F}$$

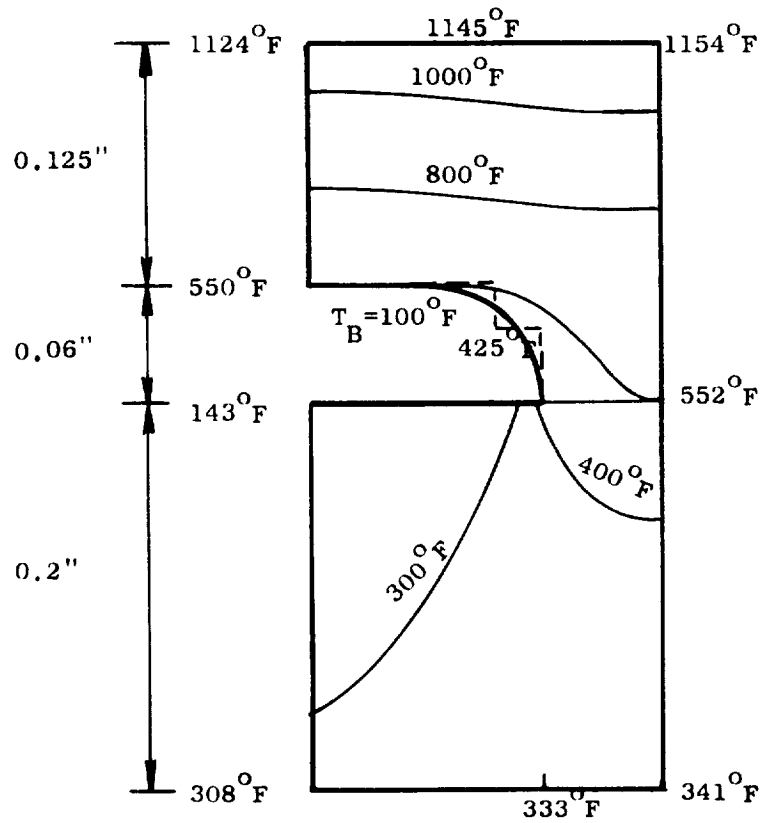
$$h_c = 0.0266 \text{ Btu/in.}^2\text{-sec-}^{\circ}\text{F}$$

Figure E-1. Steady State Isotherms in Combustion Zone

These temperatures were calculated by a multidimensional transient conduction computer program. Using the maximum conduction length in the one-dimensional conduction equation resulted in a maximum wall temperature of 1112F (875K) at these cooling conditions, which represents fairly accurate value by comparison with the program results. The maximum nickel temperature occurred at the interface, and was about 100 F (56K) above the coolant saturation temperature.

The geometry was determined to reach equilibrium in about 6 seconds heating duration by the standard one-dimensional transient solution for a slab. This type of analysis was used for the copper and nickel sections separately, which results in the prediction of maximum times to reach steady-state conditions. The copper material reached equilibrium in approximately one second.

A similar analysis was applied to a channel at the throat location for the conditions stated in Fig. E-2. The maximum wall temperature in a region of relatively high heat flux and close channel spacings may be closely approximated with the one-dimensional conduction equation utilizing the average conduction length because of the relatively flat temperature profiles, whereas the maximum length was more appropriate for the combustion zone channels. The approximate maximum wall temperature in the throat was 1120 F (880K), based on an average length, and the program prediction was 1154 F (893K). The interface temperature was closer to the coolant saturation temperature than in the combustion zone, due to the proximity of



$P_c = 1000 \text{ Psia} ; O/F = 5.7$
 $h_g = 0.00347 \text{ Btu/in.}^2\text{-sec-}^\circ\text{F}$
 $V_c = 90 \text{ ft/sec}$
 $T_{\text{sat}} = 550^\circ\text{F}$
 $h_c = 0.0324 \text{ Btu/in.}^2\text{-sec-}^\circ\text{F}$

Figure E-2. Steady State Isotherms in Throat Region

the channels to one another. In addition, the nickel was cooler by about 100 F (56K) in the throat region than the combustion zone, which is also caused by closer spacing of channels. Temperatures reach equilibrium in the throat region sooner than in the combustion zone because of the higher heat flux and closer spacing.

The nozzle hot gas seals are located at the junction of the nozzle exit section and the remainder of the thrust chamber. The upstream portion of the junction is depicted in Fig. E-3. Separate transient analyses were applied to the Cu, Ni, and 321 stainless steel components in the same manner as the examination of transients in the channel sections. The results of the 321 stainless steel analysis revealed that the seals would reach a temperature of 220 F (380K) in a minimum time of 20 seconds based on an initial temperature of 100 F (312K).

Nozzle

For the water-cooled nozzle design the channel width was assumed to be equal to the land width (channel spacing) as a first approximation. The combustion-side film coefficient profile was estimated using the Rocketdyne boundary layer calculation technique. The film coefficient for water was estimated from the relation

$$N_{Nu} = 0.023 N_{Re}^{0.8} N_{Pr}^{0.4}$$

assuming a nominal water velocity of 60 ft/sec (18 m/sec) and bulk temperature of 100 F (312K). The maximum allowable coolant-side

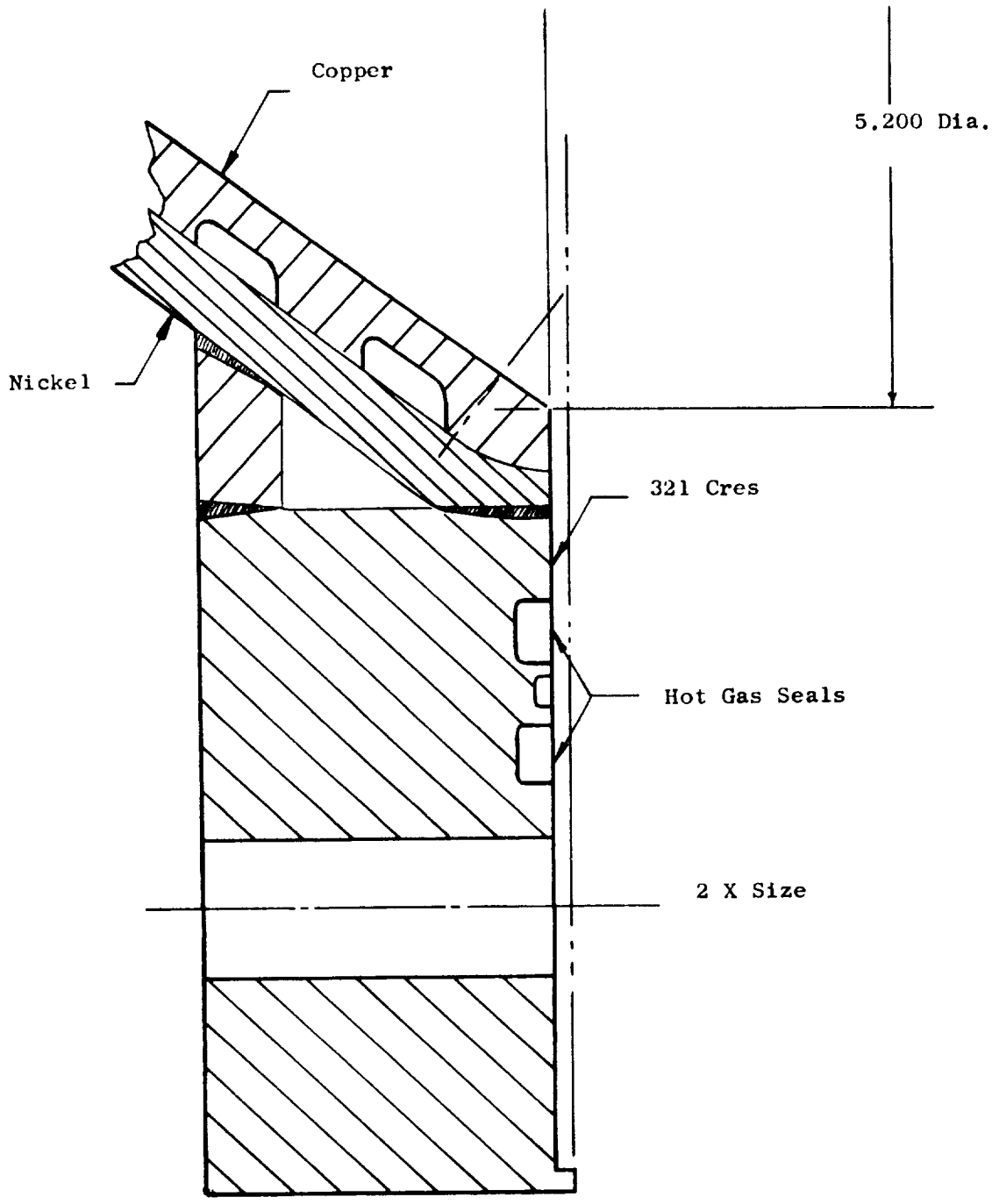


Figure E-3. Thrust Chamber Flange, $\xi = 4$

wall temperature was limited to about 500 F (535K) based on the saturation temperature of the water at a pressure of 500 psia (345 N/cm^2).

A two-dimensional analysis was then conducted to determine the midland combustion-side wall temperature as a function of channel width and spacing and the heat flux level (combustion-side film coefficient). The results of the two-dimensional analysis are shown in Fig. E-5.

Figures E-4 and E-5 were used to determine channel spacing and width based on a selected maximum wall temperature value. In order to minimize the fabrication time and cost, only two channel sizes were selected: (1) 0.250 x 0.100 inch (0.63 x 0.25 cm) at lower area ratios, and (2) 0.500 x 0.100 inch (1.27 x 0.25 cm) at higher area ratios. Channel spacings of 0.200, 0.300, and 0.500 inches (0.51, 0.76, and 1.27 cm) were utilized. The resulting channel coordinates are denoted in Table E-1. The channel closest to the attach point presents the most severe temperature condition because of the large reach and high heat flux involved. Reduction of the wall thickness to 0.050 inch (0.127 cm) for this channel would bring the maximum wall temperature to 1475 F (1070K) as shown in Fig. E-6. The two-dimensional analysis was repeated for the remaining channels using the finally selected channel widths and land widths. The results are presented in Table E-1. Channels 1 through 3 are cooled individually; channels 4 through 10 are cooled in series, as are channels 11 through 16 and 17 through 28. This grouping reduces

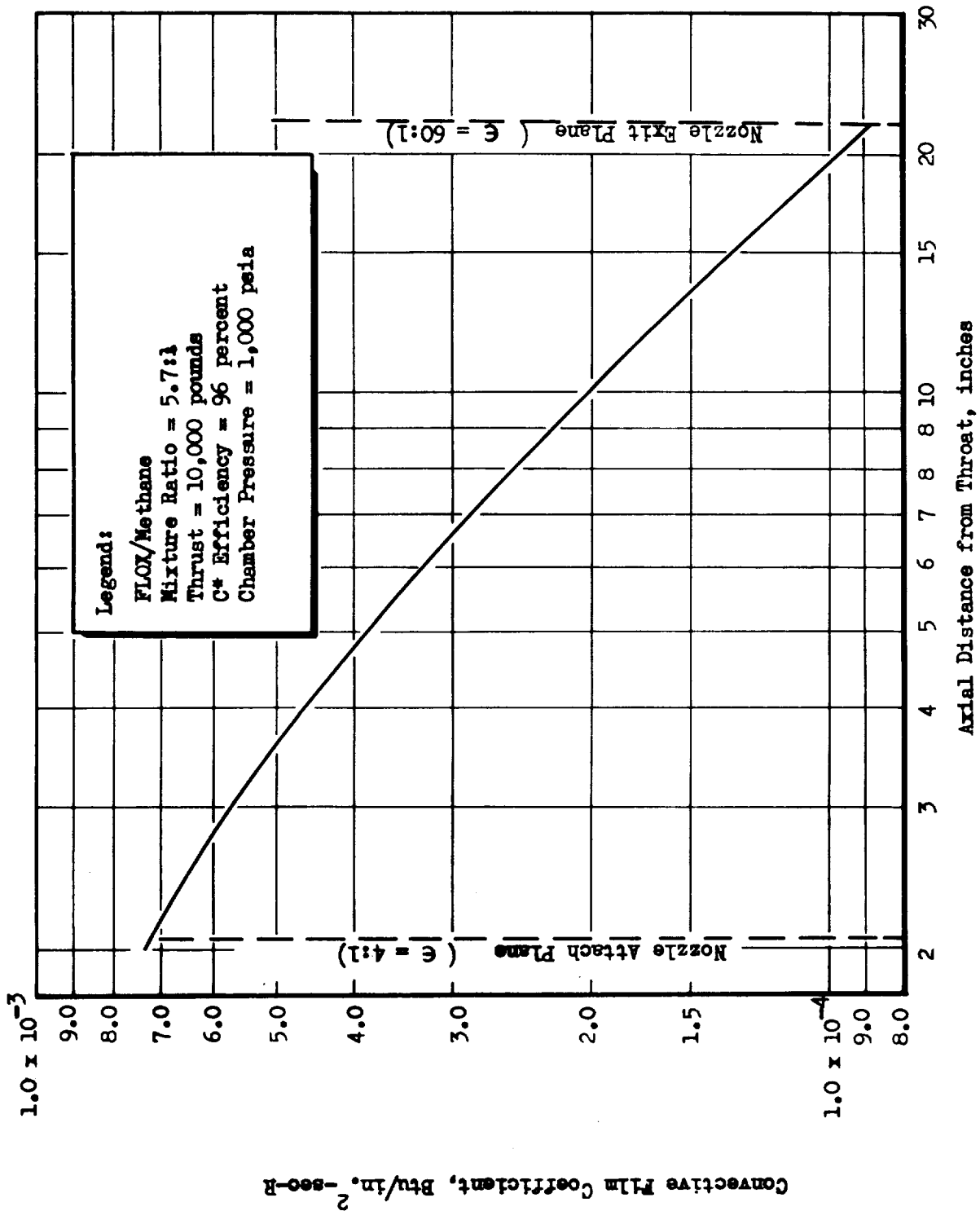


Figure E-4. Nozzle Convective Film Coefficient Profile

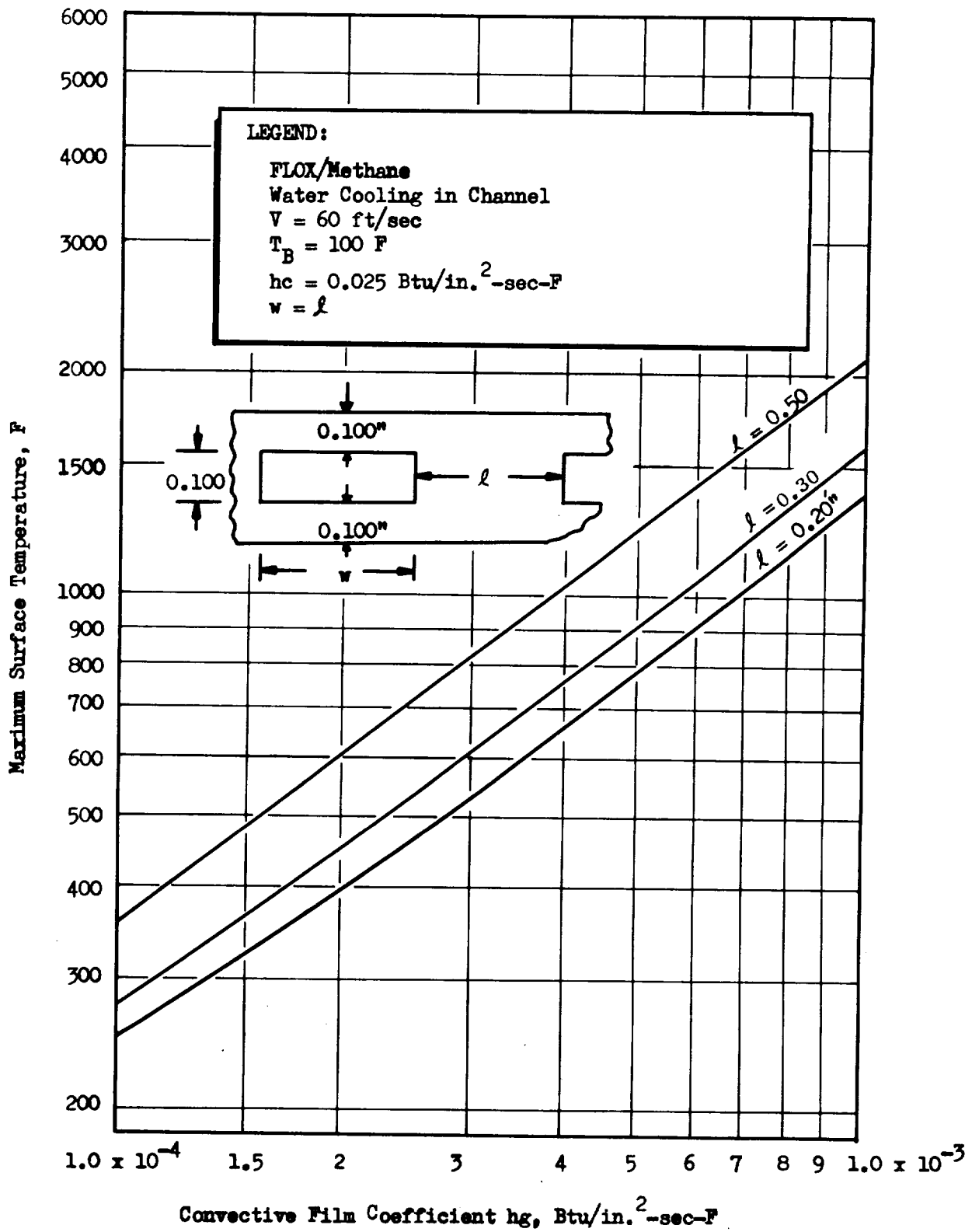


Figure E-5. Effect of Channel Spacing and Heating Rate on Maximum Nozzle Wall Temperature

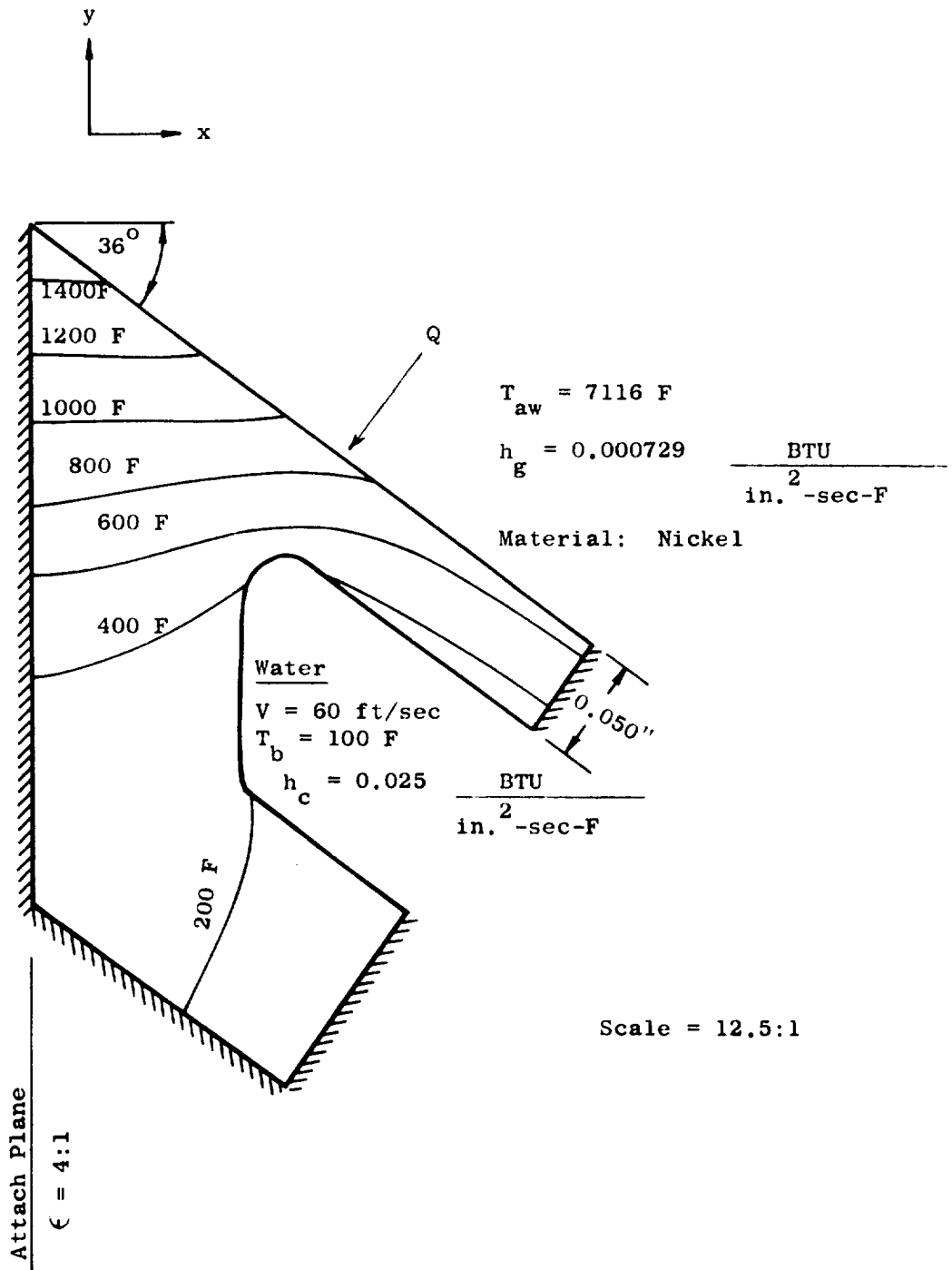


Figure E-6. Nozzle Isotherm Profiles in the Region of the Attach Plane.

TABLE E-1

NOZZLE COOLANT CHANNEL PARAMETERS

Channel No.	Slot* Width		Spacing Between		Axial Distance of Slot Center From Attach Plane		Maximum Surface Temp		Total Heat Input per Channel	
	in.	cm	in.	cm	in.	cm	F	K	Btu/sec	kW
1	0.250	0.638	0.100***	0.254	0.225	0.57	1475	1075	41	44
2	0.250	0.638	0.200	0.508	0.675	1.71	960	790	36	38
3	0.250	0.638	0.200	0.508	1.125	2.85			36	38
4	0.250	0.638	0.200	0.508	1.575	3.00			37	40
5	0.250	0.638	0.200	0.508	2.025	5.14			37	40
6	0.250	0.638	0.200	0.508	2.475	5.78			37	40
7	0.250	0.638	0.200	0.508	2.925	7.43			36	38
8	0.250	0.638	0.200	0.508	3.375	8.58			36	38
9	0.250	0.638	0.200	0.508	3.825	9.72			36	38
10	0.250	0.638	0.200	0.508	4.275	10.86	570	570	35	37
11	0.250	0.638	0.300	0.762	4.825	12.26	620	600	38	41
12	0.250	0.638	0.300	0.762	5.375	13.65	620	600	38	41
13	0.250	0.638	0.300	0.762	5.925	15.05			37	40
14	0.250	0.638	0.300	0.762	6.475	16.45			35	37
15	0.250	0.638	0.300	0.762	7.025	17.84			34	35
16	0.250	0.638	0.300	0.762	7.575	19.24	480	520	34	35
17	0.500	1.275	0.500	1.275	8.450	21.47	600	590	37	39
18	0.500	1.275	0.500	1.275	9.450	24.00			55	58
19	0.500	1.275	0.500	1.275	10.450	26.53			49	52
20	0.500	1.275	0.500	1.275	11.450	29.08			48	51
21	0.500	1.275	0.500	1.275	12.450	31.61			45	48
22	0.500	1.275	0.500	1.275	13.450	31.16			43	46
23	0.500	1.275	0.500	1.275	14.450	36.70			42	45
24	0.500	1.275	0.500	1.275	15.450	39.24			42	45
25	0.500	1.275	0.500	1.275	16.450	41.80			41	44
26	0.500	1.275	0.500	1.275	17.450	44.33			39	41
27	0.500	1.275	0.500	1.275	18.450	46.88			38	40
28	0.500	1.275	0.500	1.275	19.450	49.42	340	445	53	56

* Width is in axial direction

** Denotes spacing between given slot and previous (upstream) slot

*** Spacing between channel 1 and nozzle attach plane

Notes: Depths of all channels is 0.100 inches (0.254 cm).
Combustion-side wall thickness is 0.050 (0.127 cm) for channel
and 1 and 0.100 (0.254 cm) inches for channel 2 - 28.

the number of coolant lines as well as the number of water flowmeters required. The water bulk temperature rise and pressure drops for the series circuits were calculated to be less than 200 F (112K) and 1200 psi (820 N/cm²) respectively. The total water flowrate requirement was approximately 5.5 lb/sec (2.5 Kg/sec).

APPENDIX F

SOLUTION FOR THE PENETRATION OF A LIQUID STREAM INTO A GAS STREAM AT ARBITRARY ANGLES OF ATTACK

Data obtained from the cold flow jet penetration study conducted under Contract NAS3-7954 indicated that the physical mechanism primarily responsible for the limitation of liquid stream penetration into a flowing gas jet is the aerodynamically-caused breakup of the penetrating liquid stream into small fragments. Breakup of the liquid stream results in droplets (which are much smaller than the original diameter of the cylindrical stream) which are very rapidly turned in the direction of the gas flow and accelerated by the gas jet. As a result, their velocities become almost identical to the gas velocity very soon after they are formed. This rapid acceleration of the small droplets effectively prevents further liquid penetration and thereby limits the degree of mixing that will occur.

Since breakup of the liquid stream is the predominant mechanism limiting jet penetration, any correlation of the experimental data should be based on the "flight time" of the liquid (defined as the time during which it is exposed to the high velocity gas flow), and the calculated time required for the jet to break up due to the aerodynamic forces. The flight time of the liquid is given by the following equation:

$$t_f = \left[\frac{x_p}{V_L \cos \theta} \right]^{1/2} \quad (1)$$

where X_p = penetration distance

V_L = liquid injection velocity

θ = face angle of the liquid stream

($V_L \cos \theta$ gives the liquid velocity in the direction normal to the gas jet flow).

For the breakup time of the cylindrical liquid stream, the following expression, derived and experimentally verified for application to the breakup of relatively large spherical liquid droplets into small droplets (Ref. 5), was used:

$$t_b = \left[\frac{D_L}{V_g} \right] \cdot \left[\frac{\rho_L}{\rho_g} \right]^{\frac{1}{2}} \quad (2)$$

where t_b = breakup penetration time

D_L = diameter of liquid stream

V_g = gas velocity

ρ_L/ρ_g = ratio of liquid density to gas density

The value of t_b given in Equation (2) is the time between the first exposure of the liquid to the gas jet and the start of actual liquid breakup. This "dead time", or preparation time, is a result of the necessity first to generate disturbances (capillary waves) on the surface of the original liquid droplets. When the disturbances are critically large, liquid breakup begins. The time required for completion of the liquid breakup is approximately equal to the initial preparation period. The total time from initial exposure of the liquid to the gas to the completion of the breakup process

is therefore about twice the value of t_b given by Equation (2). Since this equation was originally developed to be applicable to liquid droplets rather than to cylindrical liquid streams, some modifications to it might be required to account for the difference between the two. However, because breakup time was used only as an empirical correlating parameter, no consideration was given to the geometrical difference between spheres and cylinders.

Equation (1) gives the exposed flight time of the liquid stream, which is equal to its total breakup time (or slightly more, due to continued penetration of the gas jet by the atomized liquid even after the actual cylindrical liquid stream has been completely broken up). For any particular situation, then, it should be expected that t_f will be slightly more than $2t_b$.

Data from Ref. 6 indicated that:

$$t_f = 2.5 t_b$$

which resulted in the following equation for jet penetration:

$$\frac{x_p}{D_L} = 2.5 \left[\frac{\rho_L}{\rho_g} \right]^{\frac{1}{2}} \left[\frac{v_L}{v_g} \right] \cos^2 \theta$$

APPENDIX G

DATA REDUCTION AND PERFORMANCE CALCULATIONS

DATA ACQUISITION

Transducer electrical signals were converted from analog to digital utilizing a Beckman 210 digital acquisition system. The digital data from the Beckman were recorded on IBM 729 tape. Selected digitized data were converted to analog signals, and a Brush recording was simultaneously made. Upon completion of each test firing, the Brush recording and magnetic tape were available for further processing. The IBM converted the raw digitized data to a graphical CRT output.

In addition to the Beckman Digital Acquisition System, oscillographs and direct inking graphic recorders (DIGR) were used to record thrust chamber and facility data. "Quick look" data, facility parameters, temperatures, pressures and flowmeter frequency were recorded on DIGR and oscillographs. The oscillograph served as backup to the Beckman recording system in addition to being a dynamic recording system for flowmeter frequency count.

Higher response transducer output, such as Photocon pressure measurements and accelerometer outputs, was recorded directly on magnetic tape for subsequent playback on an oscilloscope.

PERFORMANCE ANALYSIS

Data Reduction

A particular time slice of the raw digitized Beckman data was selected during steady-state operation for computer input to calculate on-site characteristic velocity and specific impulse.

The oxidizer flowrate was based upon the average output of two turbine-type flowmeters. Flowmeter calibrations were obtained on a water flow bench; corrections were applied to account for the viscosity and temperature differences between water and FLOX. An additional correction was made to adjust the flow for any oxidizer impurities as determined by periodic chemical analysis of the propellant. A turbine flowmeter was similarly used to determine the liquid methane flowrates.

The gaseous methane flowrate was obtained from venturi meters installed in parallel between the fuel heater and the thrust chamber. The size and number of venturi meters selected for each test was based upon the available methane bottle bank supply and predicted chamber injection pressures to provide quasi-sonic flow at the venturi throats.

For the determination of sonic flow, equation (1) was utilized (Ref. 14):

$$W_f = C_D A_2 \left[\frac{2gP_1 r^{2/\gamma} \left(\frac{\gamma}{\gamma-1}\right) \left(1-r \frac{\gamma-1}{\gamma}\right)}{1 - \frac{\gamma}{2} r^{2/\gamma}} \right]^{\frac{1}{2}} \quad (1)$$

where: C_D = venturi discharge coefficient
 A_2 = venturi throat area
 g = gravitational constant
 P_1 = upstream pressure
 γ = ratio of specific heats
 r = pressure ratio, P_2/P_1
 β = venturi area function (A_2/A_1)

For subcritical methane flow (as determined by the experimental pressure ratio r), the value was calculated from equation (2).

$$W_F = C_D A Y \frac{2 \rho_1 (P_1 - P_2)^{\frac{1}{2}}}{1 - \beta^4} \quad (2)$$

where: Y = compressibility factor ($P_2/P_1, \gamma, \beta$)
 P_2 = throat pressure

The value of the compressibility factor (Y) depends upon the venturi meter area ratio, pressure ratio, and the ratio of specific heats.

The flowrate thus determined by either equation (1) or equation (2) was corrected for impurities (percent non-combustibles as determined by chemical analysis). The impurities for either the fuel or the oxidizer never exceeded 0.7 percent and were usually much lower.

Static chamber pressure measurements were taken at several chamber locations upstream of the start of convergence and at the face of the concentric element injector. The value of throat stagnation pressure was calculated from nozzle inlet static pressure measurements with the injector face static measurement as a backup.

Throat stagnation pressure was calculated from the nozzle inlet static value using the assumption of isentropic flow in the nozzle. The static value was converted to stagnation based upon the Mach number corresponding to the chamber contraction ratio for isentropic flow.

The characteristic velocity based upon chamber pressure is defined by the following equation:

$$C^* = \frac{(P_c)_0 A^* g}{W_T} \quad (3)$$

where: $(P_c)_0$ = throat stagnation pressure
 A^* = chamber throat area
 W_T = total corrected propellant flow

The throat areas were corrected for pressure and thermal-induced strains. The throat area change was -0.4 percent for the solid chamber and 0.2 percent for the water-cooled chamber. Approximate calculations for the regeneratively cooled chamber indicated an area change of 0.5 percent.

The throat area is also corrected to the sonic area by means of a discharge coefficient which is determined by two effects. The first of these is the three-dimensional flow in the region of the nozzle throat. The sonic surface rather than being a plane at the minimum physical area actually is a curved surface starting in the nozzle contraction zone and extending out into the expansion region. The sonic point occurs at different local regions of the flow because the expansion of the exhaust gas flow is not one-dimensional but occurs at different rates throughout the flow.

The second mechanism affecting the discharge coefficient is the existence of a boundary layer near the wall in which velocities and densities differ greatly from those in the mainstream flow. Usually the boundary layer decreases the mass flowrate below that which would exist for inviscid flow. The value of the discharge coefficient was 0.992.

The C_p^* efficiency was calculated by dividing the experimental value of C_p^* by the theoretical C^* which was calculated for the chamber pressure, propellant mixture ratio (including FLOX composition) and propellant injection temperatures peculiar to each test.

The efficiency calculated in this manner includes injector losses and performance losses resulting from heat transfer to the chamber. The performance losses in the chamber are calculated by dividing the thrust chamber wall into two regions: the region between the injector and the point where boundary layer attachment occurs, and the region between this point and the nozzle exit. The region prior to boundary layer initiation is marked by the presence of violent turbulence. In this region it is assumed that the heat transferred to the thrust chamber wall is lost uniformly by all the gas: a molecule that transfers heat to the wall may reach the center of the flowfield or, by a series of collisions, receive some energy from the gas in the center of the flowfield. The reaction rates are high in this area and stay time is long; thus it can be deduced that the gas composition will achieve

the equilibrium associated with the reduced energy level. The gas will then proceed through the remaining length of the thrust chamber as though the lost heat had never been present. Therefore, in relation to the potential performance at the injector conditions, a heat loss has occurred.

The location of the boundary layer attachment point must be determined experimentally from an axial profile of the heat flux distribution. The water-cooled test data have indicated that this point is the start of convergence into the throat region. Measured heat fluxes in the cylindrical section of the chamber were used to compute the heat losses for the water-cooled tests. For the regeneratively cooled tests, the total measured heat load from the injector end of the chamber to $\epsilon = 4$ was divided in accordance with ratios established by water-cooled test data. The heat losses $(1 - \eta_H)$, varied from approximately 0.1 percent at high pressures to 1.5 percent at low pressures. The injector efficiency, $\eta_{C^*_{inj}}$, was calculated by increasing the C* efficiency by the amount of these losses:

$$\eta_{C^*_{inj}} = \eta_{C^*} + (1 - \eta_H)$$

Once the boundary layer is initiated, the heat transferred to the wall is lost entirely from the boundary layer. Cross diffusion, conduction and radiation between boundary layer and core gas are assumed to be negligible. The core gas proceeds through the nozzle without further loss of heat. As the heat is lost, the boundary layer grows to include an increasing portion of the total flow; but for any boundary layer thickness, the portion of the mass outside the boundary layer has lost no heat or it would become part of the boundary layer. The loss modes of heat transfer

and shear both occur exclusively in the boundary layer, once a well-defined boundary layer has begun to exist. The boundary layer analysis accounts for these shear and heat transfer losses and the interrelations between heat transfer and shear. The contribution of the boundary layer to the discharge coefficient is calculated by analyzing the region between the start of the boundary layer and the throat.

At Rocketdyne the boundary layer approach uses a finite difference solution of the integral momentum equations that includes terms to account for the effects of a pressure gradient, a compressible shape factor, a nonadiabatic wall condition, compressible flow condition, and a variable, turbulent boundary layer velocity profile. The computations use the Von Karman integral momentum equation which is valid for both laminar and turbulent boundary layer conditions. Further details of this method of analysis are contained in Ref.15 .

Injector performance was also calculated for the ambient pressure tests (tests with $\epsilon = 4$ or 6) from thrust measurements using

$$\eta_{C^*_F} = \eta_{I_{SV}} / \eta_{C_{FV}} = F_V / \dot{w}_t \eta_{C_{FV}} \quad I_{SV_{TH}} \quad (4)$$

where $\eta_{I_{SV}}$ is the vacuum specific impulse efficiency, $\eta_{C_{FV}}$ is the vacuum thrust coefficient efficiency; F_V is the vacuum thrust level; \dot{w}_t is the total propellant flowrate; and $I_{SV_{TH}}$ is the theoretical one-dimensional, isentropic vacuum specific impulse.

The calculation of η_{CFV} includes aerodynamic losses, kinetic losses and boundary layer losses. The methods of calculating the aerodynamic losses and geometric losses have been discussed. The calculation of reaction kinetic effects in the nozzle was performed by dividing the nozzle flow into a large number of streamtubes. The streamtubes are formed by streamlines derived from the aerodynamic analysis. The one-dimensional reaction kinetic analysis was then applied to the flow in each streamtube.

An exact reaction kinetic analysis was used to check limiting cases. These limiting cases were used to calibrate a sudden freezing point analysis method. The sudden freezing point method was then used to generate parametric data.

The sudden freezing point analysis depended upon the fact that the species composition of the actual reacting flow tends to remain in equilibrium during the early part of the expansion and then to become constant or frozen. The sudden freezing point method can, therefore, closely approximate the actual flow if the freezing point is carefully chosen. The use of the exact kinetic calculation to give guides to the selection of the freezing point ensures that the more approximate method accurately reflects the true flow conditions. The reaction kinetic loss for the nozzle was calculated by integrating the impulse function across the streamtubes at the nozzle exit for both equilibrium flow and for flow calculated using the calibrated sudden freezing model.

The effects of chamber pressure and propellant mixture ratio on η_{CP} are shown in Figs. G-1 and G-2.

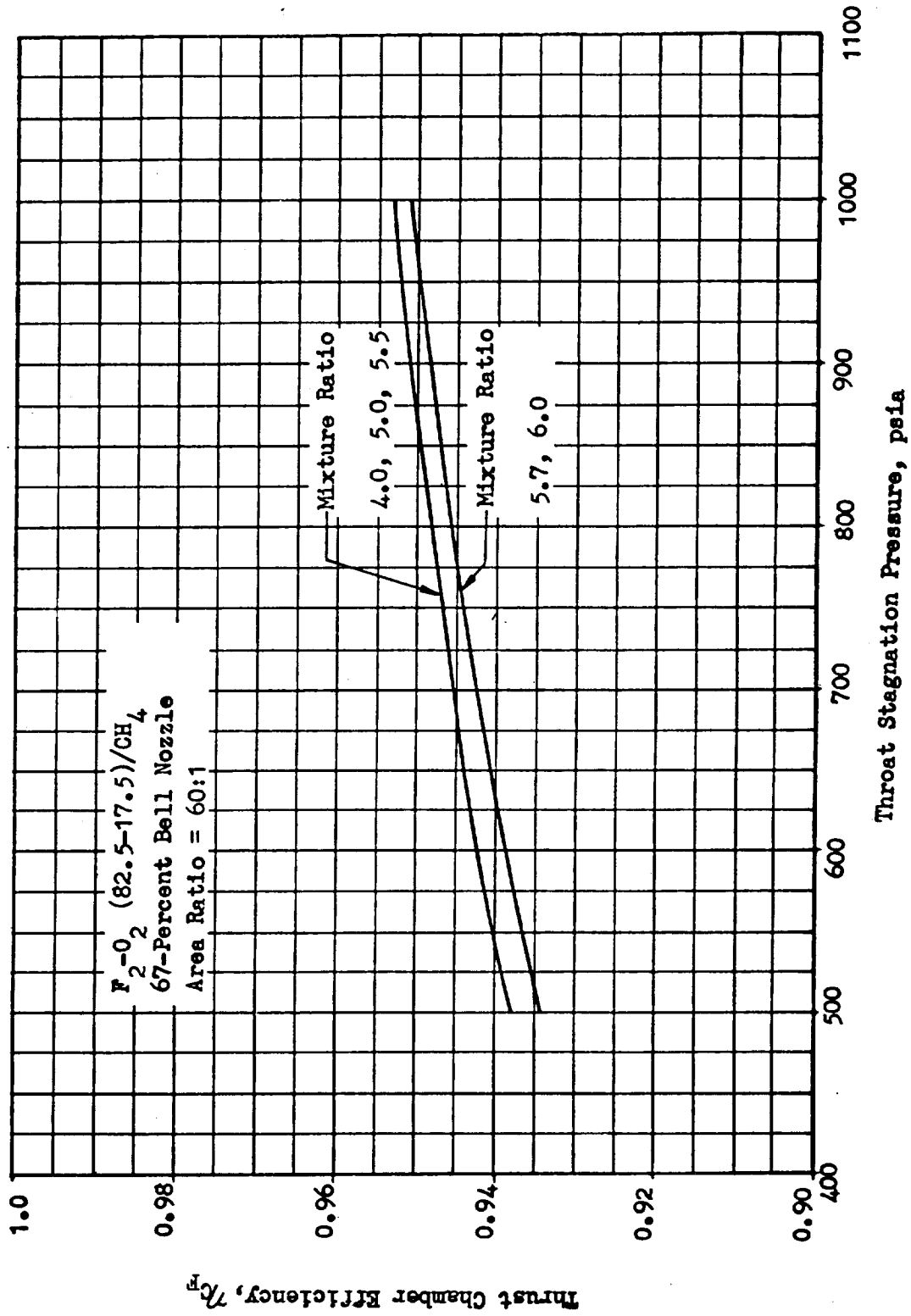


Figure G-1. Predicted Thrust Chamber Efficiency for 67-percent Bell Nozzle, Area Ratio = 60 Altitude Test Nozzle

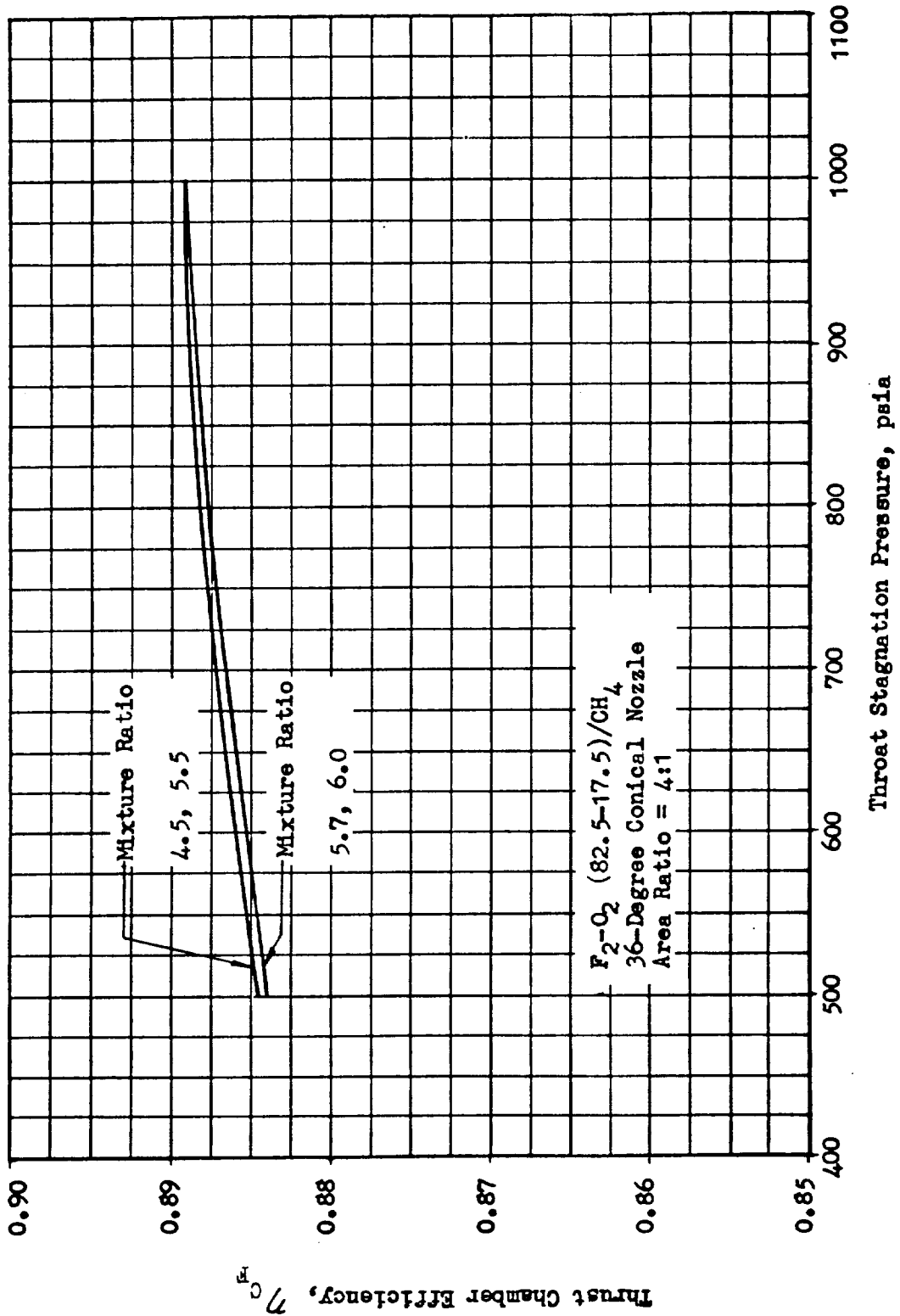


Figure G-2 . Predicted Thrust Chamber Efficiency for an Area Ratio of 4:1 Ambient Test Nozzle

The measured thrust at sea level conditions with the low expansion ratio chambers was corrected to vacuum conditions by the equation:

$$F_v = F_{\text{meas}} + P_a A_e \quad (5)$$

where: F_v = thrust corrected to vacuum conditions

F_{meas} = measured thrust

P_a = ambient pressure

A_e = nozzle exit area

A diffuser was used during the simulated altitude tests of the 60:1 expansion ratio nozzles. During these conditions the vacuum thrust was obtained from the following equation:

$$F_v = F_{\text{meas}} + P_a A_a - P_b A_b + F_b \quad (6)$$

where: A_a = area exposed to ambient pressure

P_b = base pressure on nozzle exit flange at altitude conditions

A_b = area of nozzle exit flange within the bellows

F_b = force imposed by bellows restraint and determined by calibration:

$$F_b = K_1 \Delta L + K_2 (P_a - P_b) \quad (7)$$

K_1 = bellows linear spring constant

ΔL = bellows deflection

K_2 = experimentally determined bellows constant

Vacuum specific impulse efficiency was calculated as

$$I_{SV} = F_v / w_t I_{SV_{TH}}$$

APPENDIX H

REGENERATIVE COOLANT FLOWRATE CHARACTERISTICS

During two tests of the regeneratively cooled thrust chamber the coolant flowrate increased while the coolant jacket pressure drop actually decreased slightly. A brief analysis of the conditions which lead to this apparently anomalous behavior are presented in this appendix. These tests were conducted in a system in which the coolant flowrate was determined by the fuel tank and thrust chamber pressures and by the system resistance. The coolant jacket resistance was the major part of the system resistance.

The pressure drop in a thrust chamber regenerative coolant circuit varies in a manner approximately proportional to the square of the coolant flowrate and inversely proportional to the average coolant density. This is given by the relation

$$P = K \frac{\dot{w}_c^2}{\rho} \quad (1)$$

where K is a proportionality constant. The methane is operating in the region of a nearly perfect gas such as that for a fixed ΔP (i.e., average pressure is constant) and the average density is inversely proportional to the average methane bulk temperature. That is

$$\rho \propto \frac{1}{\bar{T}} \quad (2)$$

so that Equation (1) becomes

$$\Delta P = K' \dot{w}_c^2 \bar{T} \quad (3)$$

The average bulk temperature is approximately proportional to the total heat input and inversely proportional to the coolant flowrate.

$$\bar{T} \propto \frac{Q}{\dot{w}_c} \quad (4)$$

Equation (3), therefore, can be written

$$\Delta P = K' \dot{w}_c^2 \frac{Q}{\dot{w}_c} = K' \dot{w}_c Q \quad (5)$$

The above relation indicates that for a fixed heat input the coolant pressure drop varies nearly linearly with flowrate. This is typical of most engine systems operating over a range of mixture ratios. In the case of the FLOX/methane, however, the heat input has been found to be almost proportional to the mixture ratio for mixture ratios of 1.5 to 5, as shown in Fig. 86. The heat input is therefore given by the approximate

$$Q \propto \frac{1}{\dot{w}_c} \quad (6)$$

for nearly constant chamber pressure. Relation (5) therefore reduces to the form

$$\Delta P \approx K''$$

indicating that the coolant pressure drop is essentially independent of coolant flowrate. Conversely, for a fixed ΔP the coolant flowrate can vary widely and is dependent primarily on restrictions upstream of the thrust chamber.

APPENDIX I

DISTRIBUTION

REPORT
COPIES
R D

RECIPIENT

DESIGNEE

	National Aeronautics & Space Administration	
	Lewis Research Center	
	21000 Brookpark Road	
	Cleveland, Ohio 44135	
1	Attn: Contracting Officer, MS 500-313	
5	Liquid Technology Branch, MS 500-209	
1	Technical Report Control Office, MS 5-5	
1	Technology Utilization Office, MS 3-16	
2	AFSC Liaison Office, 501-3	
2	Library	
1	Office of Reliability & Quality Assurance,	
	MS 500-111	
1	D. L. Nored, Chief, LRTB, MS 500-209	
3	J. W. Gregory, Project Mgr., MS 500-209	
1	E. W. Conrad, MS 500-204	
1	R. H. Kemp, MS 49-1	
1	R. H. Knoll, MS 501-2	
1	W. Tomazic, MS 500-203	
2	Chief, Liquid Experimental Engineering, RPX	
	Office of Advanced Research & Technology	
	NASA Headquarters	
	Washington, D. C. 20546	
2	Chief, Liquid Propulsion Technology, RPL	
	Office of Advanced Research & Technology	
	NASA Headquarters	
	Washington, D. C. 20546	
1	Director, Launch Vehicles & Propulsion, SV	
	Office of Space Science & Applications	
	NASA Headquarters	
	Washington, D. C. 20546	
1	Chief, Environmental Factors & Aerodynamics	
	Code RV-1	
	Office of Advanced Research & Technology	
	NASA Headquarters	
	Washington, D. C. 20546	

REPORT
COPIES
R D

RECIPIENT

DESIGNEE

1	Chief, Space Vehicles Structures Office of Advanced Research & Technology NASA Headquarters Washington, D. C. 20546	
1	Director, Advanced Manned Mission, MT Office of Manned Space Flight NASA Headquarters Washington, D. C. 20546	
6	NASA Scientific & Technical Information Facility P.O. Box 33 College Park, Maryland 20740	
1	Director, Technology Utilization Division Office of Technology Utilization NASA Headquarters Washington, D. C. 20546	
1	National Aeronautics & Space Administration Ames Research Center Moffett Field, California 94035 Attn: Library	Hans M. Mark Mission Analysis Division
1	National Aeronautics & Space Administration Flight Research Center P.O. Box 273 Edwards, California 93523 Attn: Library	
1	National Aeronautics & Space Administration Goddard Space Flight Center Greenbelt, Maryland 20771 Attn: Library	Merland L. Moseson Code 620
1	National Aeronautics & Space Administration John F. Kennedy Space Center Cocoa Beach, Florida 32931 Attn: Library	Dr. Kurt H. Debus
1	National Aeronautics & Space Administration Langley Research Center Langley Station Hampton, Virginia 23365 Attn: Library	E. Cortwright Director
1	National Aeronautics & Space Administration Manned Spacecraft Center Houston, Texas 77001 Attn: Library	J. G. Thiobodaux, Jr. Chief, Propulsion & Power Division

REPORT
COPIES
R D

RECIPIENT

DESIGNEE

1	National Aeronautics & Space Administration George C. Marshall Space Flight Center Huntsville, Alabama 35812 Attn: Library	Hans G. Paul Leon J. Hastings James Thomas Dale Burrows I. G. Yates Clyde Nevins J. Blumrich
1	Jet Propulsion Laboratory 4800 Oak Grove Drive Pasadena, California 91103 Attn: Library	Henry Burlage, Jr. Duane Dipprey
1	Defense Documentation Center Cameron Station Building 5 5010 Duke Street Alexandria, Virginia 22314 Attn: TISIA	
1	Office of the Director of Defense Research & Engineering Washington, D. C. 20301 Attn: Office of Att. Dir. (Chem. Technology)	
1	RTD (RTNP) Bolling Air Force Base Washington, D. C. 20332	
1	Arnold Engineering Development Center Air Force Systems Command Tullahoma, Tennessee 37389 Attn: Library	Dr. H. K. Doetsch
1	Advanced Research Projects Agency Washington, D. C. 20525 Attn: Library	
1	Aeronautical Systems Division Air Force Systems Command Wright Patterson Air Force Base Dayton, Ohio Attn: Library	D. L. Schmidt Code ARSCNC-2
1	Air Force Missile Test Center Patrick Air Force Base, Florida Attn: Library	L. J. Ullian

REPORT
COPIES

R D

RECIPIENT

DESIGNEE

1	Air Force Systems Command Andrews Air Force Base Washington, D. C. 20332 Attn: Library	Capt. S. W. Bowen SCLT
1	Air Force Rocket Propulsion Laboratory (RPR) Edwards, California 93523 Attn: Library	
1	Air Force Rocket Propulsion Laboratory (RPM) Edwards, California 93523 Attn: Library	
1	Air Force FTC (FTAT-2) Edwards Air Force Base, California 93523 Attn: Library	Donald Ross
1	Air Force Office of Scientific Research Washington, D. C. 20333 Attn:	SREP, Dr. J. F. Masi
1	Space & Missile System Organization Air Force Unit Post Office Los Angeles, California 90045 Attn: Technical Data Center	
1	Office of Research Analyses (OAT) Holloman Air Force Base, New Mexico 88330 Attn: Library RRRD	
1	U. S. Air Force Washington, D. C. Attn: Library	Col. C. K. Stambaugh Code AFRST
1	Commanding Officer U.S. Army Research Office (Durham) Box CM, Duke Station Durham, North Carolina 27706 Attn: Library	
1	U.S. Army Missile Command Redstone Scientific Information Center Redstone Arsenal, Alabama 35808 Attn: Document Section	Dr. W. Wharton
1	Bureau of Naval Weapons Department of the Navy Washington, D. C. Attn: Library	J. Kay Code RTMS-41

REPORT
COPIES
R D

RECIPIENT

DESIGNEE

1	Commander U.S. Naval Missile Center Point Mugu, California 93041 Attn: Technical Library	
1	Commander U.S. Naval Weapons Center China Lake, California 93557 Attn: Library	
1	Commanding Officer Naval Research Branch Office 1030 E. Green Street Pasadena, California 91101 Attn: Library	
1	Director (Code 6180) U.S. Naval Research Laboratory Washington, D. C. 20390 Attn: Library	H. W. Carhart J. M. Krafft
1	Picatinny Arsenal Dover, New Jersey 07801 Attn: Library	I. Forsten
1	Air Force Aero Propulsion Laboratory Research & Technology Division Air Force Systems Command United States Air Force Wright Pattern AFB, Ohio 45433 Attn: APRP (Library)	R. Quigley C. M. Donaldson
1	Electronics Division Aerojet General Corporation P.O. Box 296 Azusa, California 91703 Attn: Library	W. L. Rogers
1	Space Division Aerojet General Corporation 9200 E. Flair Drive El Monte, California 91734 Attn: Library	S. Machlowski
1	Aerojet Ordnance and Manufacturing Aerojet General Corporation 11711 S. Woodruff Avenue Fullerton, California 90241 Attn: Library	

**REPORT
COPIES**

R D

RECIPIENT

DESIGNEE

1	Aerojet Liquid Rocket Company P.O. Box 13222 Sacramento, California 95813 Attn: Technical Library 2484-2015A	R. Stiff
1	Aeronutronic Division of Philco Ford Corp. Ford Road Newport Beach, California 92663 Attn: Technical Information Department	Dr. L. H. Linder
1	Aerospace Corporation 2400 E. El Segundo Blvd. Los Angeles, California 90045 Attn: Library-Documents	I. G. Wilder
1	Arthur D. Little, Inc. 20 Acorn Park Cambridge, Massachusetts 02140 Attn: Library	A. C. Tobey
1	Astropower Laboratory McDonnell-Douglas Aircraft Company 2121 Paularino Newport Beach, California 92163 Attn: Library	
1	ARO, Incorporated Arnold Engineering Development Center Arnold AF Station, Tennessee 37389 Attn: Library	
1	Susquehanna Corporation Atlantic Research Division Shirley Highway & Edsall Road Alexandria, Virginia 22314 Attn: Library	
1	Beech Aircraft Corporation Boulder Facility Box 631 Boulder, Colorado Attn: Library	Douglas Pope
1	Bell Aerosystems, Inc. Box 1 Buffalo, New York 14240 Attn: Library	T. Reinhardt W. M. Smith

REPORT
COPIES
R D

RECIPIENT

DESIGNEE

1	Bendix Systems Division Bendix Corporation 3300 Plymouth Street Ann Arbor, Michigan Attn: Library	John M. Beneger
1	Bellcomm 955 L'Enfant Plaza, S.W. Washington, D. C. Attn: Library	H. S. London
1	Boeing Company Space Division P.O. Box 868 Seattle, Washington, 98124 Attn: Library	J. D. Alexander C. F. Tiffany
1	Boeing Company 1625 K Street, N.W. Washington, D. C. 20006	
1	Boeing Company P.O. Box 1680 Huntsville, Alabama 35801	Ted Snow
1	Chemical Propulsion Information Agency Applied Physics Laboratory 8621 Georgia Avenue Silver Spring, Maryland 20910	Tom Reedy
1	Chrysler Corporation Missile Division P.O. Box 2628 Detroit, Michigan Attn: Library	John Gates
1	Chrysler Corporation Space Division P.O. Box 29200 New Orleans, Louisiana 70129 Attn: Librarian	
1	Curtiss-Wright Corporation Wright Aeronautical Division Woodridge, New Jersey Attn: Library	G. Kelley
1	University of Denver Denver Research Institute P.O. Box 10127 Denver, Colorado 80210 Attn: Security Office	

REPORT
COPIES
R D

RECIPIENT

DESIGNEE

1	Fairchild Stratos Corporation Aircraft Missiles Division Hagerstown, Maryland Attention: Library	
1	Research Center Fairchild Hiller Corporation Germantown, Maryland Attn: Library	Ralph Hall
1	Republic Aviation Fairchild Hiller Corporation Farmington, Long Island, New York	
1	General Dynamics/Convair P.O. Box 1128 San Diego, California 92112 Attn: Library	Frank Dore
1	Missiles and Space Systems Center General Electric Company Valley Forge Space Technology Center P.O. Box 8555 Philadelphia, Penna. 19101 Attn: Library	A. Cohen F. Schultz
1	General Electric Company Flight Propulsion Laboratory Department Cincinnati, Ohio Attn: Library	D. Suichu
1	Grumman Aircraft Engineering Corporation Bethpage Long Island, New York Attn: Library	Joseph Gavin
1	Hercules Powder Company Allagheny Ballistics Laboratory P.O. Box 210 Cumberland, Maryland 21501 Attn: Library	
1	Honeywell, Inc. Aerospace Division 2600 Ridgeway Road Minneapolis, Minnesota Attn: Library	
1	IIT Research Institute Technology Center Chicago, Illinois 60616 Attn: Library	C. K. Hersh

REPORT
COPIES
R D

RECIPIENT

DESIGNEE

1	Kidde Aer-Space Division Walter Kidde & Company, Inc. 567 Main Street Bellville 9, New Jersey	R. J. Hanville
1	Ling-Temco-Vought Corporation P.O. Box 5907 Dallas, Texas 75222 Attn: Library	
1	Lockheed Missiles and Space Company P.O. Box 504 Sunnyvale, California 94087 Attn: Library	
1	Lockheed Propulsion Company P.O. Box 111 Redlands, California 92374 Attn: Library, Thackwell	H. L. Thackwell
1	Marquardt Corporation 16555 Saticoy Street Box 2013, South Annex Van Nuys, California 91409	L. R. Bell, Jr.
1	Martin-Marietta Corp. (Baltimore Division) Baltimore Maryland 21203 Attn: Library	
1	Denver Division Martin-Marietta Corporation P.O. Box 179 Denver, Colorado 80201 Attn: Library	Dr. Morganthaler F. R. Schwartzberg
1	Orlando Division Martin-Marietta Corporation Box 5827 Orlando, Florida Attn: Library	J. Fern
1	Western Division McDonnell Douglas Astronautics 5301 Bolsa Avenue Huntington Beach, California 92647 Attn: Library	R. W. Hallet G. W. Burge P. Klevatt

REPORT
COPIES
R D

RECIPIENT

DESIGNEE

1	McDonnell Douglas Aircraft Corporation P.O. Box 516 Lambert Field, Missouri 63166 Attn: Library	R. A. Herzmark
1	Space & Information Systems Division North American Rockwell Corporation 12214 Lakewood Blvd. Downey, California Attn: Library	
1	Northrop Space Laboratories 3401 West Broadway Hawthorne, California Attn: Library	Dr. William Howard
1	Purdue University Lafayette, Indiana 47907 Attn: Library (Technical)	Dr. Brude Reese
1	Radio Corporation of America Astro-Electronics Products Princeton, New Jersey Attn: Library	
1	Rocket Research Corporation Willow Road at 116th Street Redmond, Washington 98052 Attn: Library	F. McCullough, Jr.
1	Stanford Research Institute 333 Ravenswood Avenue Menlo Park, California 94025 Attn: Library	Dr. Gerald Marksman
1	Thiokol Chemical Corporation Redstone Division Huntsville, Alabama Attn: Library	John Goodloe
1 1	TRW Systems, Inc. 1 Space Park Redondo Beach, California 90278 Attn: Tech. Lib. Doc. Acquisitions	D. H. Lee H. Burge
1	United Aircraft Corporation Corporation Library 400 Main Street East Hartford, Connecticut 06108 Attn: Library	Dr. David Rix Erle Martin Frank Owen

REPORT
COPIES
R D

RECIPIENT

DESIGNEE

1	1	United Aircraft Corporation	R. J. Coar
	1	Pratt & Whitney Division	T. E. Bailey
	1	Florida Research & Development Center	Dr. Schmitke
		P.O. Box 2691	
		West Palm Beach, Florida 33402	
		Attn: Library	
1		United Aircraft Corporation	Dr. David Altman
		United Technology Center	
		P.O. Box 358	
		Sunnyvale, California 94038	
		Attn: Library	
1		Vickers Incorporated	
		P.O. Box 302	
		Troy, Michigan	
1		Vought Astronautics	
		Box 5907	
		Dallas, Texas	
		Attn: Library	

